LUND UNIVERSITY

Efficient Quantum Memories Based on Spectral Engineering of Rare-Earth-Ion-Doped Solids

Sabooni, Mahmood

2013

Link to publication

Citation for published version (APA):
Sabooni, M. (2013). *Efficient Quantum Memories Based on Spectral Engineering of Rare-Earth-Ion-Doped Solids*. [Doctoral Thesis (monograph), Atomic Physics].

Total number of authors:
1

LUND UNIVERSITY

PO Box 117
221 00 Lund
+46 46-222 00 00

Efficient quantum memories based on spectral engineering of rare-earth-ion-doped solids

Mahmood Sabooni

Doctoral Thesis
2013

Lund University

EFFICIENT QUANTUM MEMORIES BASED ON SPECTRAL ENGINEERING OF RARE-EARTH-ION-DOPED SOLIDS

Printed in Sweden by Media-Tryck, Lund 2013

Division of Atomic Physics
Department of Physics
Faculty of Engineering, LTH
Lund University
P.O. Box 118
SE–221 00 Lund
Sweden

http://www.atomic.physics.lu.se
http://www.atomic.physics.lu.se/research/quantum_information/

ISSN 0281-2762
Lund Reports on Atomic Physics, LRAP-472

ISBN 978-91-7473-480-5

ABSTRACT

The main aim of the present thesis is to demonstrate the efficient quantum memories for light employing coherent processes in rare-earth-ion-doped crystals.

Rare-earth (RE) ions between lanthanum, with atomic number 57, and lutetium, with atomic number 71, have a partly filled 4f shell, which is spatially inside the full shells 5s, 5p, and 6s. Therefore, 4f-4f transitions are shielded from environmental noise. Less noise means longer lifetime and coherence times and, when the crystals are cooled down to ∼4 K, these can be ∼ 8 orders of magnitude longer than what is typical for electronic transitions in solids. In quantum information processing, we are looking for physical systems which are isolated from the environment and consequently have good coherence properties. The long coherence time of both optical and spin transitions, is the main attraction of rare-earth ions for quantum information processing.

In the present thesis, we map a quantum state of light employing a 4f-4f transition of praseodymium doped in yttrium silicate. We mainly employed the ensemble approach and the atomic frequency comb (AFC) protocol for quantum memory demonstrations. Among several parameters that define quantum memory performance, we mostly focused on quantum memory efficiency. The overall memory efficiency is simply defined as the energy of the pulse recalled from the memory divided by the energy of the pulse sent in for storage in the memory.

To maximize quantum memory efficiency, most protocols require high optical depth, αL. This is a limitation for materials with rather good coherence properties but low optical depth. In the research described in the present thesis, we combined the use of a low finesse cavity and the ensemble approach and designed an impedance-match cavity to obtain the advantages of both approaches and thereby to implement an efficient quantum interface in a weakly absorbing solid-state medium. Based on the cavity configuration, we obtained 56% storage and retrieval efficiency, which is the highest storage and retrieval efficiency based on the AFC protocol reported in the research so far.

In the present thesis, we demonstrated a narrow-band ($\sim$2 MHz) spectral filter with a >30 dB intensity absorption/transmission ratio, which is based on the large (6 orders of magnitude) ratio between the inhomogeneous and homogeneous broadening of $Pr^{3+} : Y_2SiO_5$. Slow-light effects due to the strong dispersion created by the spectral filter improved the suppression of the filter by also utilizing the time domain. As an application, we detected weak diffuse light shifted by ultrasound from the carrier $\sim$2 MHz, after a 9 cm thick biological tissue.

The coupling between light and matter is directly related to the relative direction of the light polarization and transition dipole moment of atoms. I developed a simulation program that was able to investigate the polarization direction and ellipticity of polarization of optical radiation propagating through the crystal. This might open up new opportunities for the investigation of interesting physics regarding propagation effects and for the improvement of spectral engineering of RE ions in the future.

In order to deal with the sharp homogeneous transitions of the RE ions, the frequency of our dye laser was stabilized against a highly stabilized Fabry-Pérot cavity using the Pound-Drever-Hall locking scheme.

POPULAR SCIENCE DESCRIPTION

Have you ever looked at a flame dancing in the air and asked yourself what a flame really is? For instance, what happens when we burn firewood (matter) and thus change it to light and heat (energy). Simply speaking, when you ask such questions you are wondering about two physical quantities, light and matter. Clearly many over the history of time have thought about the interaction between light and matter, and some have thought more in depth in order to understand the basic phenomenon related to this interaction. One approach is to analyze the building blocks of light and matter. In physics, a quantum is regarded as the minimum amount of any physical entity involved in an interaction. For instance, the *photon* is introduced as a single quantum of light, and is referred to as a "light quantum". The *photon* is one of the key quantities that we are dealing with in the present thesis.

The speed of light c ($\approx 300,000$ km/s), in the famous equation of mass-energy equivalence $E = mc^2$, is considered as the maximum speed at which all energy, matter, and information in the universe can travel. In the research described in the present thesis, we are trying to control and store the fastest quantity in the physical world, the *photon*, in matter and release an identical *photon* after some on-demand time. A device with this capability is called a quantum memory for light and this thesis describes an investigation towards developing such quantum memories. There are several applications for a component with the possibility to store a light quantum and retrieve it on-demand. One application which has attracted a great deal of attention recently is *quantum cryptography.*

Cryptography is a technique that enables secure communication in the presence of third parties. In simple words, cryptography can be described as the conversion of information from a readable state to apparent nonsense. Afterwards, the encrypted message is sent to the intended recipient and the decoding technique needed to recover the original information is shared only with the intended recipients. Therefore, the sender precludes unwanted persons from understanding the secret message. In ancient cryptography, many different practical methods already existed for encoding secret messages. Modern cryptography employs mathematics, computer science, and electrical engineering to encrypt messages and is applied, for example, with ATM cards, computer passwords, and electronic commerce. The more complicated cryptographic algorithms of today are more difficult to break down but fundamentally it is not impossible to do so.

Lately, it has been realized that nature offers a property within the quantum world for data encryption which is fundamentally impossible to break by a third party. This impossibility to break information coded by *quantum cryptography* comes from a property of nature, not from the computational ability or intelligence. The special property, ensuring fully secure information encryption, is called *entanglement* and it could be an important resource for the 21^{st} century.

To somewhat understand *entanglement*, let us consider a source which emits a pair of particles such that one particle goes to the right and the other one leaves the source to the left. This means that these particles have opposite momenta. Therefore, if one finds the first particle in the upper right corner, it can be predicted that the second particle is in the lower left corner. This illustrates that there is a correlation between the behavior of the two particles and the results of the measurements performed on such pairs. In a similar way, we can prepare two entangled photons and, for instance, transfer one to the moon and keep one at earth. Surprisingly, however, experiments have shown that the photon on the moon will be instantaneously affected by changes carried out on the earth photon. (Note that the effect occurs instantaneously although the earth-moon distance is on average about 380,000 km. Therefore light, as the fastest quantity in the world, can travel this distance in about a second.) This instantaneous effect, which Einstein called “spooky action at a distance”, can be used to enable a sender and receiver to share secret information because whenever a third party tries to extract information from such a connection, the sender and receiver will be able to detect the presence of an eavesdropper.

Quantum cryptography has been demonstrated for distances below $\sim$170 km using commercial equipment. The losses in optical fibers prevent the distance from being extended significantly beyond this limit. In the classical world, the problem of losses in communication channels is solved by adding amplification stages, but this approach does not work in the quantum world because of the inherent noise sensitivity of quantum states. To overcome this difficulty, a protocol is proposed to employ quantum memories to extend the communication channels. A large part of the present thesis has been devoted for developing memories that can store and recall entangled photon and thus enable long distance quantum cryptography.

LIST OF PUBLICATIONS

This thesis is based on the following papers, which will be referred to by their roman numerals in the text.

I **Towards an efficient atomic frequency comb quantum memory**
A. Amari, A. Walther, M. Sabooni, M. Huang, S. Kröll,
M. Afzelius, I. Usmani, B. Lauritzen, N. Sangouard,
H. de Riedmatten, N. Gisin.
Journal of Luminescence **130**, 1579−1585 (2010).

II **Storage and Recall of Weak Coherent Optical Pulses with an Efficiency of 25%**
M. Sabooni, F. Beaudoin, A. Walther, N. Lin, A. Amari,
M. Huang, and S. Kröll.
Phys. Rev. Lett. **105**, 060501 (2010).

III **Hyperfine characterization and spin coherence lifetime extension in $Pr^{3+} : La_2(WO_4)_3$**
M. Lovrić, P. Glasenapp, D. Suter, B. Tumino, A. Ferrier,
P. Goldner, M. Sabooni, L. Rippe, and S. Kröll.
Phys. Rev. B **84**, 104417 (2011).

IV **Slow light for deep tissue imaging with ultrasound modulation**
H. Zhang, M. Sabooni, L. Rippe, C. Kim, S. Kröll,
L. V. Wang, and P. R. Hemmer.
Appl. Phys. Lett. **100**, 131102 (2012).

V **Cavity enhanced storage-preparing for high efficiency quantum memories**
M. Sabooni, S. T. Kometa, A. Thuresson, S. Kröll, and
L. Rippe.
New Journal of Physics **15**, 035025 (2013).

VI **Efficient Quantum Memory Using a Weakly Absorbing Sample**
M. Sabooni, Qian Li, S. Kröll, and L. Rippe.
Phys. Rev. Lett. **110**, 133604 (2013).

ABBREVIATIONS

AFC	Atomic Frequency Comb
CRIB	Controlled Reversible Inhomogeneous Broadening
CQED	Cavity Quantum Electrodynamics
DDS	Direct Digital Synthesizer
EIT	Electromagnetic Induced Transparency
EOM	Electro-Optical Modulator
FID	Free Induction Decay
FPD	Free Polarization Decay
FWHM	Full Width at Half Maximum
GEM	Gradient Echo Memory
HYPER	HYbrid Photon Echo Rephasing
NMR	Nuclear Magnetic Resonance
PBS	Polarization Beam Splitter
PD	Photo Diode
PDH	Pound-Drever-Hall frequency locking
PSHB	Persistent Spectral Hole Burning
QIP	Quantum Information Processing
RASE	Rephased Amplified Spontaneous Emission
RE ions	Rare-Earth ions
RF	Radio Frequency
ROSE	Revival Of Silenced Echo
RWA	Rotating Wave Approximation
UOT	Ultrasound Optical Tomography
ZEFOZ	ZEro First Order Zeeman

CONTENTS

Papers

Chapter 1

Introduction

The laws that govern the behavior of the smallest components of our universe, such as fundamental particles, atoms and molecules, are described by “quantum physics”. In the quantum world, in contrast to the world of classical physics, things can be in two places at once or can even be two things at once and have many other (from our classical world point of view) strange properties. In the late 20th century, scientists in the area of information science began thinking about how to take advantage of the strange properties described by quantum mechanics. They proposed that understanding the rules of the quantum world could aid us with tasks which are not possible to perform in the world as described by classical physics. One such task was the unconditionally secure transmission of information. In addition, in 1994 Peter Shor proposed an algorithm with possibility to perform prime number factorization in exponentially fewer steps than classical algorithms [1]. Further, Lov K. Grover suggested a search algorithm that would offer a quadratic improvement over the best classical algorithm [2].

In addition to the unique opportunities of quantum information mentioned above, there are many other reasons to push towards increasing our understanding of quantum information. As a first reason, we know that the reduction of the size of transistors is key for improvement of classical computer performance [3]. If transistors become much smaller, however, the strange effects of quantum mechanics will begin to strongly affect their performance. It would therefore seem that these effects could present a fundamental limit to our classical computer technology and we need to be prepared to move towards quantum computers. A second reason is that, according to Landauer’s principle [4], erasing a single bit of information is equivalent to energy dissipation, and this dissipated energy will be converted to heat. We know quantum computer operations are *reversible* while some classical operations are not.

Reversibility of an operation means we are not erasing any information during the operation. No loss in information processing means no energy dissipation. Therefore, moving towards quantum information could be an important issue from the energy consumption point of view.

In quantum information processing, a *qubit* as a unit of quantum information, the quantum analogue of the classical bit, represents a two-state quantum system. A qubit should have the ability to represent a quantum state which is either at 0, 1 or at a superposition between 0 and 1. In classical computers, parallel computing is performed by having several processors linked together. As an analogy, in a quantum computer, a single quantum processor is able to perform multiple computations on its own by utilizing the fact that the qubit exists in a superposition state. Therefore, superposition could be considered as an important resource for quantum computing. Let us move on from a single qubit to a multi-qubit regime and suppose that these qubits are correlated. By employing multi-correlated-qubits, we can take advantage of another resource granted by nature, called *entanglement*.

Quantum information could be encoded on a stationary qubit such as an atom or a flying qubit such as a photon or even sometimes in superposition between both. Therefore, it appears that we need a quantum interface between light and matter with a possibility of dealing with *superposition* and *entanglement* properties.

The ability to map, store, and later retrieve quantum states of light from matter is an inherently very interesting topic from the point of view of basic science. The main objective of the present thesis is development of efficient storage media for light (at the quantum level). Such a device is called a quantum memory for light and it will be an important building block in quantum information processing (QIP) [5].

1.1 Quantum memories

Quantum memories are expected to become vital elements for future quantum communication [6] in quantum repeaters for long distance quantum key distribution [7, 8], although there have also been some proposals for quantum communication without the necessity of quantum memories [9]. Quantum computing (QC) is another target application for quantum memories, where they may improve gate operation time [10]. As a specific example, quantum memories are one of the most important components of quantum computing based on the linear optics QC scheme [11]. Other applications of quantum memories include Signal synchronization in optical quantum processing [12, 13], the implementation of a deterministic single-photon source [14], and precision measurements based on mapping of the quantum properties of an optical state onto atomic ensembles [15]. For most of the applications just mentioned, high performance will be required in terms of high efficiency [16, 17], on-demand long storage time [18, 19], multi-mode storage capacity [20, 21] and broad bandwidth [22].

So far several protocols in a variety of physical systems are proposed for quantum memory demonstration. Detailed quantum memory properties are discussed in Chapter 6.

1.2 Spectral engineering

The physical system used in the present thesis is based on rare-earth (RE) ions doped in a number of specific host crystals, although, in most experiments described, praseodymium doped in yttrium silicate (Y_2SiO_5) is used. The relatively long coherence time of RE ions, which is discussed in Chapter 2, is the main attraction of these materials. In addition, different RE ions inside the host crystal experience different fields from the environment, therefore the ensemble of ions will be inhomogeneously broadened. The combination of narrow homogeneous line-width (∼1 kHz for $Pr^{3+} : Y_2SiO_5$) and broad inhomogeneous broadening (∼5 GHz for $Pr^{3+} : Y_2SiO_5$) provide a possibility to spectrally engineer the absorption profile for specific applications. For such applications, a stable laser is required with a frequency line-width of the same order as the homogenous line-width (∼1 kHz for $Pr^{3+} : Y_2SiO_5$). Details about the coherent light source that we developed for this purpose are discussed in Chapter 4. In the present thesis, the inhomogeneous broadening of $Pr^{3+} : Y_2SiO_5$ is tailored for quantum memory application. In addition, a narrow-band spectral-temporal filter is demonstrated for application in biological tissue imaging in Paper **IV**.

1.3 Aims and outline of the thesis

Three general aims of the present research are stated below, along with reference to the papers describing the research:

(i) Improvement of the storage and retrieval efficiency of quantum memories. Investigation of improving the efficiency of quantum memories is the main aim of the research described in Paper **I**, Paper **II**, Paper **V**, and Paper **VI**.

(ii) Development of means to increase the storage time of quantum memories. The intention to create quantum memories with longer storage time is the reason for investigation in Paper **III**.

(iii) Exploring of new applications for spectral engineering in rare-earth-ion-doped crystals. A spectral-temporal filter is constructed for biological tissue imaging in Paper **IV**.

Detailed discussion of the scientific contributions are found in the peer-reviewed scientific articles fund at the end of the thesis. The purpose of the thesis chapters is to provide a more thorough understanding of the methods used.

The thesis chapters, and their connections to the papers are outlined below

Chapter 2 The main physical resource for all experiments in the present thesis is based on employing rare-earth-ion-doped crystals. The properties of rare-earth-ion-doped crystal are discussed in this chapter.

Chapter 3 Coherent manipulation of the interaction between light and matter is the main target of this chapter. Light is treated classically based on Maxwell's equations, while matter is discussed quantum mechanically based on Bloch equations.

Chapter 4 An overview of the experimental setup including the cavity assisted laser frequency stabilization setup is discussed in this chapter.

Chapter 5 Understanding the properties of light polarization during propagating through a medium is the main topic in this chapter.

Chapter 6 In this chapter, we discuss different aspects of quantum memory and also different proposals related to quantum memory demonstration.

Chapter 7 We discuss the feasibility of engineering a narrowband ($\sim$ 2 MHz) spectral-temporal filter with sharp edges based on the properties of rare-earth ions. Improving the filtering process in the time domain is discussed based on taking advantage of the slow light effect. We employed the demonstrated spectral-temporal filter for biological tissue imaging based on the ultrasound optical tomography (UOT) technique.

CHAPTER 2

RARE-EARTH IONS TRAPPED IN CRYSTALS

The discovery of rare-earth (RE) elements dates back to 1794 when Gadolin found a black metal mineral called Yttria in Ytterby (a village in the Swedish archipelago close to Stockholm), which was a mixture of several elements. In the early twentieth century, spectroscopic investigations of rare-earth (RE) compounds showed very sharp spectral lines, comparable to the spectra of single atoms or molecules. This meant that, compared to the other elements in the periodic table, the interaction between RE ions and their environment is fairly weak. Much later, investigations on RE elements led to the narrowest spectral lines ever observed in solids [23]. The sharp spectral lines originated from the shielding of the 4f electrons by the 5s, 5p and 6s electrons, (see Fig. 2.1). The order of filling of the electron shells is illustrated by the red arrows, and starts with the $1s^2$ orbital and ends at $5d^j$, where i and j denote the number of electrons in sub-shells 4f and 5d, respectively, for the lanthanides. From this schematic figure, it can clearly be seen that the 4f orbital is shielded by higher energy levels and the spatially outer-lying 5s, 5p and 6s shells.

The radial charge density, $P^2(r)$, as a function of the radius, r, for 4f, 5s, 5p, and 6s orbitals of Gd^+ is shown more clearly in Fig. 2.2 [24]. Actually, we should bear in mind that the lowest-energy electrons are the 4f electrons, which are not the outermost electrons in this case. On the other hand, elements with 5d electrons should be less shielded and have broader spectral lines. In fact, the shielding effect decouples the 4f level from environmental noise, making the 4f level a good candidates for quantum manipulation.

The procedure of adding tiny amounts of RE ions to transparent crystals, ceramics, or glasses is called doping, and is used to produce the active medium for solid-state lasers. The same idea

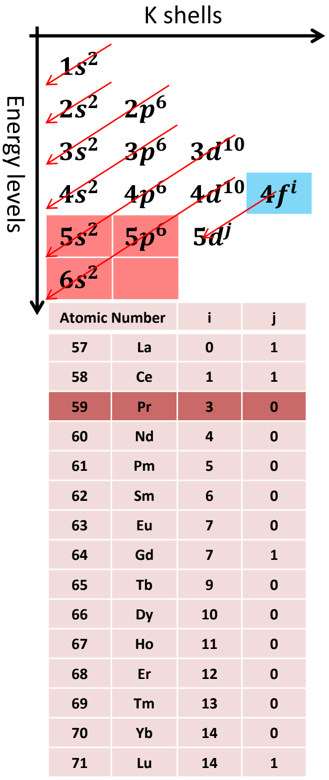

Atomic Number		i	j
57	La	0	1
58	Ce	1	1
59	Pr	3	0
60	Nd	4	0
61	Pm	5	0
62	Sm	6	0
63	Eu	7	0
64	Gd	7	1
65	Tb	9	0
66	Dy	10	0
67	Ho	11	0
68	Er	12	0
69	Tm	13	0
70	Yb	14	0
71	Lu	14	1

Figure 2.1. *Electron configuration of the lanthanides. The order of filling of the electron shells is shown by the red arrows, and starts with the 1^{st} energy level and ends at the 6^{th} energy level. For the lanthanides, the 4f shell is shielded by the 5s, 5p, and 6s electrons.*

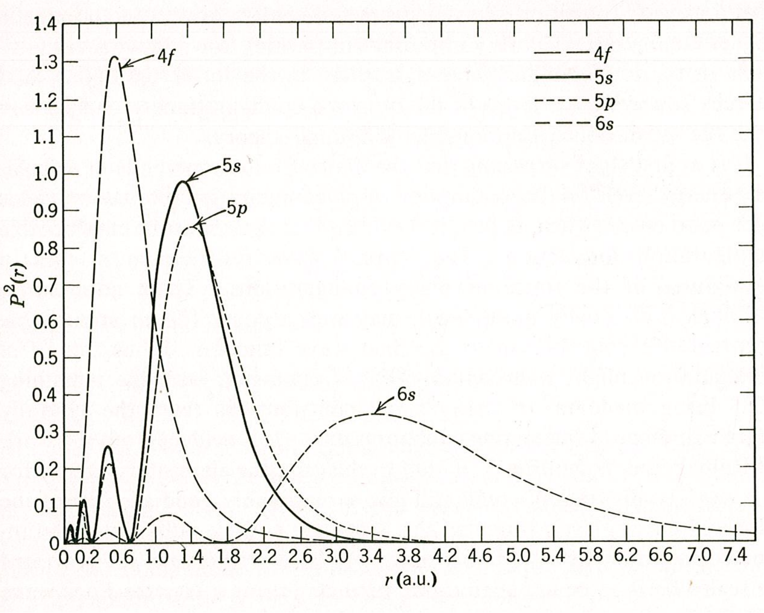

Figure 2.2. *Radial charge density, $P^2(r)$, as a function of radius, r, for the 4f, 5s, 5p, and 6s orbitals of Gd^+ [24]*

can be used employing different crystalline materials as hosts for RE ions to achieve a physical system for quantum computing and quantum information processing. Actually, RE ions trapped in crystals offer some advantages as a quantum computing material [25, 26] compared to other quantum computing schemes. The aim of this chapter is to introduce the different aspects of RE ions trapped in dielectric solids, particularly praseodymium doped in yttrium silicate ($Pr^{3+} : Y_2SiO_5$).

The electron configuration in the ground state of an atom will minimize the energy of the whole atom. Following the Pauli exclusion principle (two identical electrons can not occupy the same quantum state simultaneously) and Hund's rule of maximum multiplicity (multiplicity is equal to the number of unpaired electrons plus one), electrons will fill up higher shells as the atomic number, Z, increases. To understand the spectra of any atomic structure, start with one-electron systems such as hydrogen and hydrogen-like atoms, where a single electron is circulating around a central field, and the eigenvalues are inversely proportional to the square of n (principal quantum number). To go further in the periodic table, the second step will be to include angular momentum, **L**, and the magnetic moment, μ_L, of the orbital electron. Additionally, because of the spin properties of the electron, one should consider the spin angular momentum, **s**, and the associated magnetic moment, μ_s, and, finally, the spin-orbit interaction. There are two main approximations for the spin-orbit interaction: LS coupling (Russell-Sunders approximation) and jj coupling. LS coupling is more valid for the outer shells of light elements, whereas jj coupling typically dominates for inner shells of heavy atoms [27]. However, a large number of atoms (some RE elements) follow an intermediate coupling scheme.

The work presented in this thesis is related to the interaction of light with RE ions, and it is therefore relevant to describe their energy level structure. The energy level structure of the $4f^n$ configuration of a typical RE ion (R^{3+}) doped in LaF_3 based on the free-ion and the crystal-field splitting approximation (see Eq. 2.2) has been calculated by Carnall et al. as shown in Fig. 2.3 [28]. Principal transitions for spectral hole burning and quantum information processing are shown in Fig. 2.3 by the solid green arrows, while the dashed red arrows show the commercially available solid state lasers based on RE materials.

2.1 Rare-earth ion interactions

Different host crystals such as $Y_3Al_5O_{12}$ (yttrium aluminum garnet, YAG), Y_2SiO_5 (yttrium silicate), and $La_2(WO_4)_3$ (tungstate) could slightly affect the properties of the RE ions but in most cases the effect of the free ion Hamiltonian ($\hat{H}_{FI}$) is more dominant than the crystal field Hamiltonian ($\hat{H}_{CF}$). The total Hamiltonian for the RE ions trapped in a crystal can be decomposed in the following way:

$$\hat{H} = \hat{H}_0 + \hat{H}_1(t) + \hat{H}_P \tag{2.1}$$

where $\hat{H}_0$ and $\hat{H}_1(t)$ are the time-invariant and time-dependent parts of the atomic Hamiltonian, respectively. The $\hat{H}_P$ term is related to the phonon interaction which can be eliminated by employing cryogenic temperatures for the crystal ($< 4K$). The time-invariant part of the atomic Hamiltonian can be written as follows [29, 30]:

$$\hat{H}_0 = [\hat{H}_{FI} + \hat{H}_{CF}] + [\hat{H}_{HF} + \hat{H}_Q + \hat{H}_z] \tag{2.2}$$

where $\hat{H}_{FI}$ is the free-ion Hamiltonian, and $\hat{H}_{CF}$ is related to the crystal field. The remaining terms, which make smaller contributions, are $\hat{H}_{HF}$, which represents hyperfine coupling, ($\hat{H}_Q$ denotes the nuclear electric quadrupole interaction), and finally $\hat{H}_z$ is for both nuclear and electronic Zeeman interactions.

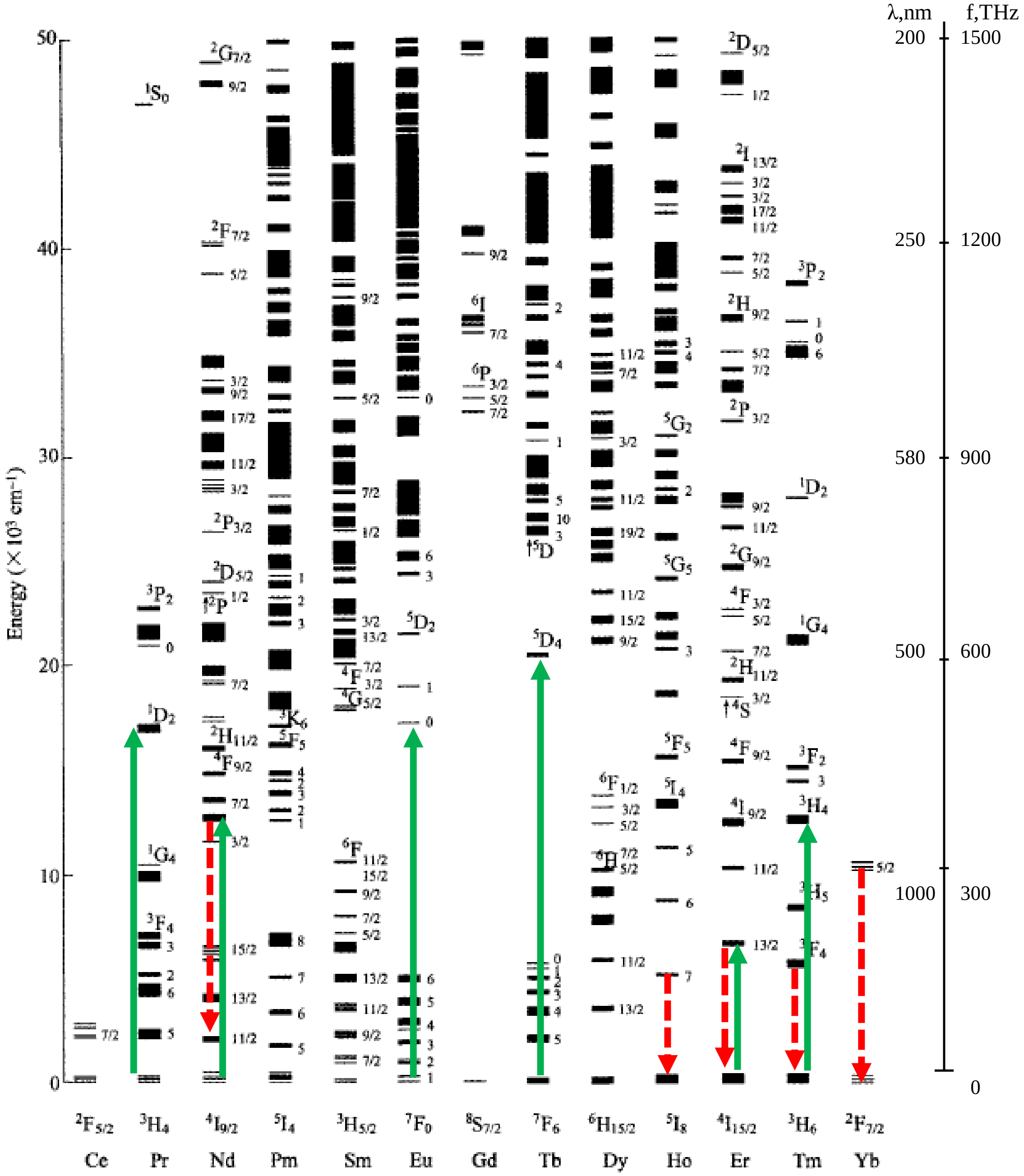

Figure 2.3. *Energy level structure of* R^{3+} : LaF_3 *based on calculated free-ion and crystal-field splitting [28]. The solid green arrows show principal transitions for spectral hole burning and quantum information processing, while the dashed red arrows show the commercially available solid state lasers.*

The $\hat{H}_{FI}$ Hamiltonian, which is the dominating term in Eq. 2.2, corresponds to $\hat{H}_C$ and $\hat{H}_{SO}$ for the Coulomb interaction and the spin-orbit interaction of the 4f electrons. Based on the selected rare-earth, the Russell-Sanders approximation ($\hat{H}_C \gg \hat{H}_{SO}$), the jj coupling regime ($\hat{H}_C \ll \hat{H}_{SO}$), or an intermediate condition ($\hat{H}_C \approx \hat{H}_{SO}$) can be used [29].

Actually, the scale of crystal field splitting ($\approx 10^{12} Hz$) is smaller than that of the free-ion splitting ($\approx 10^{15} Hz$), while the hyperfine energy splitting ($\approx 10^6 - 10^9 Hz$) is even smaller, thus it would be a good approximation to employ perturbation theory to calculate crystal field splitting and hyperfine structures. The Zeeman term will be considered when applying a static magnetic field [29]. Following Eq. 2.1, the dynamic interactions can be listed as follows:

$$\hat{H}_1(t) = [\hat{H}_{SI}(t) + \hat{H}_{TLS}(t)] + [\hat{H}_{NQP}(t) + \hat{H}_{EFS}(t)] \tag{2.3}$$

where the energy shift of these interactions is in the range of kHz. Therefore, one can apply perturbation theory to estimate the effects of all these Hamiltonians. The terms in the first bracket are related to the intrinsic properties of the crystal, while those in the second are related to extrinsic properties such as the incident light. $\hat{H}_{SI}(t)$ represents the interaction of the RE ion with the host nuclear spin, while $\hat{H}_{TLS}(t)$ describes the interaction of the RE ion with the ensemble of the two-level system around the target ion. In the extrinsic part, $\hat{H}_{NQP}(t)$ represents non-equilibrium phonons, which are related to the non-thermally activated phonons. $\hat{H}_{EFS}(t)$, which can range from a few kHz to several GHz [26], arises from the excitation induced frequency shift from ion-ion interactions.

2.2 Hyperfine structure

Since the experiments presented in this thesis deal with hyperfine structure, it is worth while to describe the physics behind hyperfine structure. For a more detailed discussion the reader is referred to Refs. [27, 31]. Hyperfine structure is explained by the presence of nuclear magnetic and electric moments, interacting with the electronic shell. In the magnetic hyperfine structure, the interaction between nuclear spin angular momentum, **I**, and electronic angular momentum, **J**, will create a new angular momentum **F** and this gives the following eigenvalues for the Hamiltonian, which is $H_{hfs} = a\mathbf{I}.\mathbf{J}$:

$$E_{hfs} = \frac{a}{2}[F(F+1) - I(I+1) - J(J+1)] \tag{2.4}$$

$$\Delta E_{hfs(F,F-1)} = aF \tag{2.5}$$

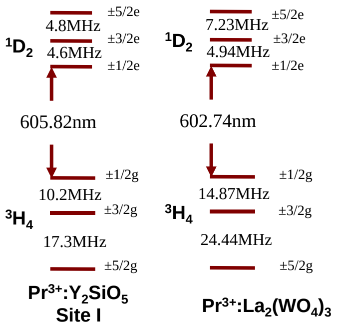

Figure 2.4. *Two different host materials doped with Pr have two different hyperfine structures for the* $^3H_4 - {}^1D_2$ *transition*

where a is the magnetic dipole interaction constant, and $|I + J| \geq F \geq |I - J|$ [27]. The electric hyperfine structure is related to the deformation of the nucleus. This deformation is described by the electronic quadrupole moment, Q (prolate:$Q > 0$; oblate $Q < 0$)[27]. In the case of no nuclear spin (I=0) there is no magnetic or electronic hyperfine structure. The magnetic interaction will be present for $I \geq 1/2$, whereas for the electronic hyperfine structure $I \geq 1$ and $J \geq 1$ must be satisfied. Any external magnetic field source could affect the hyperfine splitting. Actually, this "external knob" is very helpful in controlling the properties of predefined states as shown in Paper **III**. In that experiment, mostly weak external magnetic fields (leading to a Zeeman effect) were applied. The last and normally smallest splitting in the hyperfine levels is the result of isotopic effects, which depend on the variation in mass and volume of the nuclei in different isotopes.

The hyperfine structure of praseodymium (Pr), the main dopant studied in this thesis, must be investigated in more detail. The element Pr has only one naturally abundant isotope (A = 141). ^{141}Pr has nuclear spin $I = 5/2$, and electric quadrupole moment $Q = -8 \times 10^{-26} cm^2$ [32]. In the absence of an external magnetic field, the second-order hyperfine and nuclear electric quadrupole interactions in a crystal-field singlet will split the lowest crystal field state of the $^3H_4$ ground state into three levels with $m_I = \pm 5/2, \pm 3/2$, and $\pm 1/2$. Since the crystal field is an important term as can be seen in the Hamiltonian in Eq. 2.2, the splitting of Pr hyperfine levels in Eq. 2.5 will be different in different host materials. For instance, two different host materials doped with Pr, have two different hyperfine structures for the $^3H_4 - {}^1D_2$ transition, as shown in Fig. 2.4. Typically, RE materials are used to be doped in the solid state crystal as a trivalent ions such as Pr^{3+}, but divalent Pr^{2+} ions are also used [29].

2.3 Dipole moment orientation

Yttrium silicate (Y_2SiO_5) was extensively employed as a host material for Pr ions in this work, belongs to the monoclinic crystal system, and the $C^6_{2h}(C2/c, number 15)$ class based on the Schönflies classification [33]. The monoclinic cell of (Y_2SiO_5) has the dimensions a=10.410 Å, b=6.721 Å, c=12.490 Å, and $\beta = 102.39°$, where β is the angle between a and c, giving a unit-cell volume of V =853.51 Å^3. The unit cell contains 16 Y^{3+} ions, and the total Y^{3+} density is $1.83 \times 10^{22} cm^{-3}$ [34, 35]. A RE ion, such as Pr^{3+} (with a 1.82Å atomic radius) can be used as a dopant instead of Y^{3+} ions (with a 1.8Å atomic radius) to achieve a naturally trapped ion quantum information system. Yttrium silicate is a biaxial, and has three principal axes of polarization, D_1 ,D_2, and b which are defined in Fig. 2.5 [36]. X-ray measurements have enabled the exact determination of their directions with respect to the crystallographic axes (a, b, c) as shown in Fig. 2.5.

Based on the dipole moment approximation, which is valid when the wavelength of the field is greater than the distance between the electrons and nuclei, the interaction Hamiltonian of any two-level system can be written as follows:

$$\hat{H} = \mathbf{p}.\mathbf{E} \tag{2.6}$$

where $\mathbf{p}$ is the electrical dipole moment with components $p_{ij} = \langle i|p|j\rangle$, and $\mathbf{E}$ is the optical electric field vector [37]. The diagonal elements of the dipole moment matrix represent the static dipole moment, while the off-diagonal terms represent transition dipole moments. Eq. 2.6 can be written using the Rabi frequency notation ($\Omega = \mathbf{p}.\mathbf{E}/\hbar$), which shows that the Rabi frequency is determined by the magnitude of the transition dipole moment and the optical field, and also by the projection of one onto the other. To reduce the complexity and make use of the advantages of having a single-Rabi frequency response, it is important to align the light polarization along one of the principal axes of the crystal.

The optical transition of any two-level system can be described by the energy difference between the two levels and a transition dipole moment. This is very simple for an individual ion, but to achieve the same simplicity in a crystalline environment, one needs to find a symmetrical direction in the crystal along which to align the incident $\mathbf{E}$ vector such that all excited dipoles project identically onto it. An extensive study of all possible combinations of 32 point groups and the 230 space groups has been performed by Sun et al. [38]. This paper shows that there is at least one solution for all physically allowed combinations providing single Rabi frequency temporal behavior.

As we wish to maximize the interaction between the laser light and matter, and also want single-Rabi frequency behavior, it is important to know the symmetrical orientation of the doped ion transition dipole moment in relation to the three principal axes of polarization. The general symmetry consideration for a four transition dipole moment versus three principal axes of polarization for Y_2SiO_5 is shown in Fig. 2.6. For site I in $Pr^{3+} : Y_2SiO_5$, four transition dipole moments can be reduced to two as $\theta = \pi/2$ and $\phi = \pi/2 - 15.5°$ according to the absorption measurement in table 7.6 of Ref. [29]. The actual transition dipole moment direction is shown in Fig. 2.7.

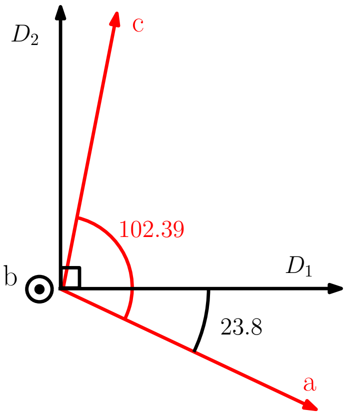

Figure 2.5. *Orientations of the crystal and principal directions of the optical indicator in* (Y_2SiO_5)*[36].*

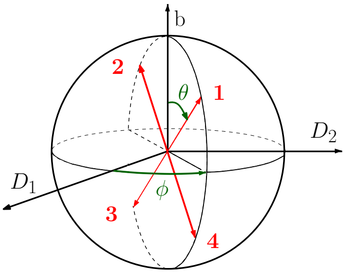

Figure 2.6. *Symmetry considerations regarding light propagation and light polarization for coherent interactions with ions in the* Y_2SiO_5 *crystal. 1.*(θ, ϕ), *2.*$(\theta, \phi + \pi)$,*3.*$(\pi - \theta, \phi + \pi)$,*4.*$(\pi - \theta, \phi)$.

2.4 Homogeneous and Inhomogeneous line-widths

Generally, a spectral line-width originates from two main contributions: homogeneous and inhomogeneous line-width broadening.

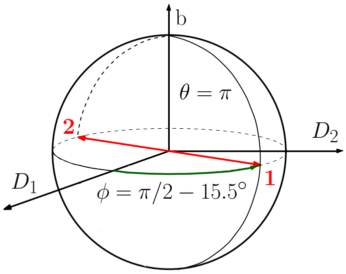

Figure 2.7. *Transition dipole moment direction in site I of* $Pr^{3+}: Y_2SiO_5$.

Line-width broadening can take place in an optical transition or a transition between hyperfine states. The intrinsic properties of ions usually lead to homogeneous broadening while inhomogeneous broadening is caused by the extrinsic properties.

In order to obtain a pure homogeneous line-width, we should consider an isolated, non-interacting atom or ion. The homogeneous transition is the result of the broadening of the transition due to the finite lifetime of the excited state. The natural spectral width of an emission, $\Delta\nu_N$, due to the finite lifetime ,τ, of any excited dipole moment, is limited to $\frac{1}{2\pi\tau}$, due to the uncertainty principle between energy and time. From the classical point of view, a Fourier transform of an exponential decay (atomic dipole moment) with a finite lifetime τ will be a Lorentzian function with full width at half-maximum of $\Delta\nu = \frac{1}{2\pi\tau}$.

This ion transition lifetime can be affected by the ion-phonon interaction (single- or two-phonon interaction), the ion-ion interaction, or the ion spin-nuclear spin interaction [29]. Dynamic processes, such as those involving lattice phonons, and fluctuating nuclear or electron spins, are the phenomena mainly responsible for homogeneous line-width broadening. To suppress thermally induced phonons, the experiments described in this thesis were performed at cryogenic temperatures ($\sim$ 2K). Spontaneous phonon emission dominates over thermally induced phonons in interactions at cryogenic temperatures [32].

Phenomenologically, there are two different decay times describing the decay (T_1) and decoherence (T_2) processes in atomic physics. The decay time T_1 (also called the longitudinal homogeneous lifetime) is mainly related to the population decay of the excited state, whereas the coherence time T_2 (the transverse homogeneous lifetime) is also related to the dephasing of the state. The distinction between population decay and dephasing will be discussed in Chapter 3 where the Bloch sphere concept is introduced. The homogeneous line-width, Γ_h, is associated to the phase memory or coherence time, T_2, through a time-frequency Fourier transform:

$$\Gamma_h = 1/\pi T_2 \tag{2.7}$$

Dephasing processes can originate from two different sources. As shown in Eq. 2.8, T_2' represents pure homogeneous dephasing, where T_2^* is the ensemble-averaged transverse dephasing time, which is related to the inhomogeneous effect [37].

$$1/T_2 = 1/T_2' + 1/T_2^* \tag{2.8}$$

The decoherence time T_2, is limited by both spin-flip and dephasing processes, and can be much smaller than T_1, although its upper bound is $T_2 = 2T_1$.

Based on the calculation of the Y^{3+} density in Section 2.3, if Y_2SiO_5 is doped with 0.05% Pr^{3+}, this will give about a million Pr^{3+} ions in a μm^3 laser beam spot. The atoms in a group of identical atoms or ions, all with a defined homogeneous line-width, inside a solid-state crystal, will experience different environments (strain, local electric and magnetic fields). Therefore, the resonance frequency of these identical ions will show a slight Stark shift. Defects or disorder, which are unavoidable in crystal growth, will affect the environments of the ions differently. The atomic radius mismatch for instance between Y(180 pm), Pr(182 pm), Ce(181.5 pm), and Er(176 pm) is unavoidable, and increases the inhomogeneous line-width [39]. Inhomogeneous broadening can also arise due to the statistical distribution of isotopes of the host ions. The overall transition frequency distribution of all these ions, which experience different electric fields resulting from their crystalline environment, is called the inhomogeneous line-width. This effect has been employed in a quantum computing proposal [25, 26] to address millions of qubits within a μm^3 laser beam spot by selecting a specific (but arbitrary) frequency window. In the present work, inhomogeneous broadening was manipulated coherently, and collective emission from an atomic or ionic ensemble was employed to construct a quantum memory unit.

Let us now compare the size of homogeneous and inhomogeneous line-widths of different RE materials. One of the sharpest homogeneous line-widths is 50 Hz, found in $Er^{3+} : Y_2SiO_5$, [40] which is limited by the excited state lifetime (about 10 ms). One of the sharpest inhomogeneous line-widths is found in low doping concentration of $Nd^{3+} : YLiF_4$ with $\sim$ 10 MHz inhomogeneous broadening in presence of an external magnetic field [41]. This sample contained about 1-10 ppm Nd^{3+} ions. At the other end of the scale, 0.15% $Pr^{3+} : Sr_{0.6}Ba_{0.4}Nb_2O_6$ has a sub-GHz homogeneous line-width and 2.7 THz inhomogeneous line-width [42]. A very good survey of the key properties of selected RE activated optical materials has been presented by Thiel et al. [42].

Nonlinear spectroscopy [43, 44] has been employed using two main modes of operation (time and frequency) to distinguish between homogeneous and inhomogeneous contributions. The optical properties of some selected ions have been studied using frequency domain techniques. Such techniques include fluorescence line narrowing (FLN) [45], and spectral hole burning (SHB) [46]. In the other mode, pulses of light in the time domain were employed to investigate the coherence properties of the ion ensemble. Examples of time domain techniques include the photon echo technique [47], and optical free induction decay (FID) [48], which we will discuss it in Section 3.4.

2.5 Dephasing and Spectral Diffusion

Two main process responsible for optical dephasing are phonon-ion interactions and spin-flips. Phonon-ion interactions can take place via direct (resonant) or indirect (Raman) processes. The contribution of direct processes to the homogeneous line-width (Γ_h), follows $(e^{\frac{\Delta_g}{kT}} - 1)^{-1}$ where Δ_g is the energy gap of the two level system and T is the temperature. For energy level separations much larger than the phonon energy, the contribution of Raman processes is characterized by $\Gamma_h \sim T^7$ [29].

The RE ions will be affected via spin-spin interactions with the host ions. Any spin changes (spin-flips) of the surrounding ions will affect the optical dephasing time of the target RE ions through spin-spin interactions [29]. The dephasing behavior of the target RE ions will change with time, mainly due to the so called "frozen core" effect. According to this, the spin-flip perturbation of surrounding ions is different when the RE ion is in the ground state or an excited state [32].

The equivalent of the optical dephasing concept in the time domain is line-width broadening in the frequency domain. Therefore, the same mechanism that causes dephasing will create dynamic absorption line-width broadening, which is called spectral diffusion. Actually, electric and magnetic dipole interactions between the RE ions and its surroundings could be affected by the excitation pulse itself. Spectral broadening that depends on the laser pulse intensity is called instantaneous spectral diffusion (ISD). Spectral diffusion can be reduced by decreasing the doping density (i.e. increasing the ion-ion interaction distance), and by reducing the intensity of the excitation pulse. Further details are discussed in Ref. [29] and references therein.

CHAPTER 3

LIGHT-MATTER INTERACTION

In quantum information processing, quantum states are encoded in quantum bits, called qubits. Essentially, the qubit is a classical binary bit with an additional property called superposition, allowing information to be encoded in Hilbert space. Actually, quantum superposition is one of the fundamental principles of quantum mechanics. It means that a physical system (say, an atom) exists partly in all configurations of its properties (states) simultaneously; but, when measured, the result corresponds to only one of the possible configurations (states). From a mathematical point of view, any linear combination of solutions will also be a solution, since the Schrödinger equation is linear. Such solutions are often constrained to be orthogonal, such as the energy eigenstates of an electron in an atom. This property can be used to extract phase information from the atom. Another fundamental quantum resource is quantum entanglement. Quantum entanglement is actually a form of quantum superposition. Let us consider a source that emits a pair of particles in such a way that one particle goes to the right and the other goes to the left. These particles then have opposite momenta. Therefore, if one particle is found in the upper right corner, the other particle will probably be found in the lower left corner. This illustrates the correlation between the results of measurements performed on the two particles in such pairs. In quantum mechanics an entangled pair is defined in the following way:

$$(|0\rangle_1|1\rangle_2 + |1\rangle_1|0\rangle_2)/\sqrt{2} \tag{3.1}$$

A two-level atomic state could be a very good candidate for a stationary qubit, while a photon acting as a flying qubit is a good candidate for transferring a quantum state between two stationary qubits (atoms). Coherent quantum state mapping between stationary and flying qubits requires investigation of the coherent interaction between photons and atoms. Without loosing the generality of the problem, it is sufficient to treat light as a classical electromagnetic wave based on Maxwell's equations, while the two-level atomic state is treated quantum mechanically based on the Bloch equations. In this chapter, Maxwell's equations are first briefly discussed, followed by a discussion of some of the coherent transient phenomena based on the Bloch equations.

3.1 Maxwell's equations

Maxwell's equations as a classical approach can be considered for investigating the propagation of electromagnetic waves in an atomic medium. Maxwell's equations expressed in SI units are:

$$\nabla \times \mathbf{H} = \mathbf{j} + \frac{d\mathbf{D}}{dt} \tag{3.2}$$

$$\nabla \times \mathbf{E} = -\frac{d\mathbf{B}}{dt} \tag{3.3}$$

$$\nabla \cdot \mathbf{D} = \rho_f \tag{3.4}$$

$$\nabla \cdot \mathbf{B} = 0 \tag{3.5}$$

where **E** and **H** are electric and magnetic fields, respectively [49]. **D** and **B** are electric displacement and magnetic induction, respectively, ρ_f is the free charge and **j** is current density. The *constitutive relations* connect material properties to the field properties as follows:

$$\mathbf{D} = \epsilon\mathbf{E} + \mathbf{P} \tag{3.6}$$

$$\mathbf{P} = \chi\epsilon\mathbf{E} \tag{3.7}$$

$$\mathbf{B} = \mu\mathbf{H} + \eta \tag{3.8}$$

where **P** the is macroscopic electric dipole moment, χ is the electric susceptibility, η is the magnetization, and ϵ and μ are the dielectric permittivity and magnetic permeability, respectively. For simplicity, we can assume that there is no magnetization ($\eta = 0$) and no free charge ($\rho_f = 0$). Another reasonable assumption in this case is that there is no electric conductivity, σ, due to ohmic losses. Therefore, the current density ($\mathbf{j} = \sigma\mathbf{E}$) will be eliminated. Based on Maxwell's equations (3.2-3.5) and *constitutive relations* (3.6-3.8) together with the assumptions mentioned above, gives the second-order differential equation, called Maxwell's wave equation in a medium:

$$\nabla^2\mathbf{E} - \frac{n^2}{c^2}\frac{d^2\mathbf{E}}{dt^2} = \mu\frac{d^2\mathbf{P}}{dt^2} \tag{3.9}$$

where $n = \sqrt{1+\chi}$ is the refractive index and c is the speed of light in vacuum ($c = 1/\sqrt{\epsilon\mu}$).

3.2 The Bloch equations

In the interaction between light and an atom, it may be appropriate to consider any atom as a two-level atom if a monochromatic wave is on or near resonance with two specific levels, and far off resonance with the rest of the atomic levels. In this case, the Hamiltonian of the system can be written as follows:

$$H = H_0 + H_I(t) \tag{3.10}$$

where H_0 is the stationary part, and the time-dependent part, expressed as a perturbation term, is called the interaction Hamiltonian (H_I). The wave function of an unperturbed atomic state is:

$$|\Psi(\mathbf{r},t)\rangle = c_1(t)|1\rangle e^{-i\omega_1 t} + c_2(t)|2\rangle e^{-i\omega_2 t} \tag{3.11}$$

where $\omega_0 = \omega_2 - \omega_1$ corresponds to the energy level of the atomic state, as shown in Fig. 3.1. The related density matrix for this wave function is:

$$|\psi\rangle\langle\psi| = \begin{pmatrix} |c_1|^2 & c_1 c_2^* \\ c_2 c_1^* & |c_2|^2 \end{pmatrix} \tag{3.12}$$

where the diagonal and off-diagonal elements represent populations and coherences, respectively.

We now apply an electromagnetic field to the atoms, based on dipole moment approximation:

$$H_I(t) = e\mathbf{r} \cdot \mathbf{E_0} \cos(\omega t) \tag{3.13}$$

where $e\mathbf{r}$ represents the dipole moment of the electron with respect to the atom's center of mass. Assuming that the atomic dipole moment and electric field are along $\hat{\mathbf{e}}_x$, and employing the time-dependent Schrödinger equation gives:

$$i\hbar\frac{\partial\Psi}{\partial t} = H\Psi \tag{3.14}$$

In conjunction with Eqs. 3.11, the time evolution of the density matrix components can be expressed as follows:

$$\begin{cases} i\dot{c}_1 = \Omega\cos(\omega t)e^{-i\omega_0 t}c_2 \\ \\ i\dot{c}_2 = \Omega^*\cos(\omega t)e^{-i\omega_0 t}c_1 \end{cases} \tag{3.15}$$

where $\Omega = \frac{e\mathbf{X_{12}}\cdot\mathbf{E_0}}{\hbar}$ is called the *Rabi* frequency, and $X_{12} = \langle 1|x|2\rangle$. Applying the rotating-wave approximation (RWA) [31] to Eq. 3.15 leads to the more compact form:

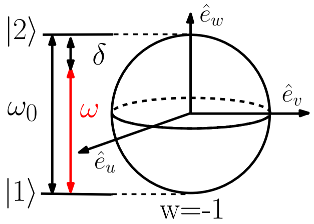

Figure 3.1. *Bloch sphere representation for on- or near-resonance two-level atoms. $\omega_0 = \omega_2 - \omega 1$ is the atomic resonance frequency and $\delta = \omega_0 - \omega$ is the detuning frequency between the applied electromagnetic field and the atomic transition. When the decay of the atomic levels is neglected, the Bloch vector is limited to the surface of the Bloch sphere. Including, decay as in Eq. 3.28 causes the Bloch vector will to shrink inside the sphere.*

$$\begin{cases} i\dot{c}_1 = \frac{\Omega}{2} c_2 e^{i\delta t} \\ \\ i\dot{c}_2 = \frac{\Omega^*}{2} c_1 e^{-i\delta t} \end{cases} \tag{3.16}$$

where $\delta = \omega - \omega_0$, as illustrated in Fig. 3.1.

Let us now define a new set of variables that is useful in the case of detuning, δ.

$$\begin{cases} \tilde{c}_1 = c_1 e^{-i\delta t/2} \\ \\ \tilde{c}_2 = c_2 e^{i\delta t/2} \end{cases} \tag{3.17}$$

and then we can define the time differentiation of Eq. 3.17 as follows:

$$\begin{cases} \dot{\tilde{c}}_1 = \dot{c}_1 e^{-i\delta t/2} - i\frac{\delta}{2} c_1 e^{-i\delta t/2} \\ \\ \dot{\tilde{c}}_2 = \dot{c}_2 e^{i\delta t/2} + i\frac{\delta}{2} c_2 e^{i\delta t/2} \end{cases} \tag{3.18}$$

We can now use Eqs. 3.16, 3.17, and 3.18 to give the time evolution equation for the probability coefficients:

$$\begin{cases} i\dot{\tilde{c}}_1 = \frac{\delta}{2}\tilde{c}_1 + \frac{\Omega}{2}\tilde{c}_2 \\ \\ i\dot{\tilde{c}}_2 = \frac{\Omega}{2}\tilde{c}_1 - \frac{\delta}{2}\tilde{c}_2 \end{cases} \tag{3.19}$$

We can write the real and imaginary parts of the off-diagonal elements of the density matrix as follows:

$$\begin{cases} u = \tilde{c}_1\tilde{c}_2^* + \tilde{c}_2\tilde{c}_1^* \\ v = -i(\tilde{c}_1\tilde{c}_2^* - \tilde{c}_2\tilde{c}_1^*) \\ w = \tilde{c}_1\tilde{c}_1^* - \tilde{c}_2\tilde{c}_2^* \end{cases} \tag{3.20}$$

Actually, by introducing u, v, w we have translated the density matrix (Eq. 3.12) to the rotating frame, which is called the Bloch frame. Here we introduce the Bloch vector:

$$\mathbf{R} = u\hat{\mathbf{e}}_u + v\hat{\mathbf{e}}_v + w\hat{\mathbf{e}}_w \tag{3.21}$$

where u, v are the phase quadrature components of the dipole in the Bloch sphere, as shown in Fig. 3.1, and w represent the difference in population between the two atomic states. The Bloch sphere (Fig. 3.1) is a suitable representation of on- or near-resonance two-level atoms. (Feynman diagrams [50, 51] are more appropriate for multi-level systems including off-resonance transitions. This, however, is beyond scope of this thesis.) Differentiating Eq. 3.20 and applying Eqs. 3.16 and 3.19 to it, leads to a compact form of the optical Bloch equations:

$$\begin{cases} \dot{u} = \delta v \\ \dot{v} = -\delta u + \Omega w \\ \dot{w} = -\Omega v \end{cases} \tag{3.22}$$

By introducing a vector called a pseudo vector, $\mathbf{W} = \Omega \hat{\mathbf{e}}_u + \delta \hat{\mathbf{e}}_w$, it is possible to write the Bloch equations in the vector notation:

$$\begin{pmatrix} \dot{u} \\ \dot{v} \\ \dot{w} \end{pmatrix} = \begin{pmatrix} \hat{i} & \hat{j} & \hat{k} \\ u & v & w \\ \Omega & 0 & \delta \end{pmatrix} \tag{3.23}$$

$$\dot{\mathbf{R}} = \mathbf{R} \times \mathbf{W} \tag{3.24}$$

So far, we have not considered any decay constant in the equations, therefore, the Bloch vector, $\mathbf{R}$, will survey only the surface of the Bloch sphere. From the constraint of Eq. 3.24 it is clear that the Bloch vector will precess about the pseudo vector, $\mathbf{W}$.

A more realistic set of equations could be obtained by considering spontaneous decay of the atomic state. Here we consider the exponential decay of the c_2 coefficient as follows:

$$c_2(t) = e^{-\Gamma t/2} c_2(0) \tag{3.25}$$

and no decay for the c_1 coefficient. Considering excited state spontaneous decay (Eq. 3.25) in Eqs. 3.20 leads to the final version of the optical Bloch equations including the decay term:

$$\begin{cases} \dot{u} = \delta v - \frac{\Gamma}{2} u \\ \dot{v} = -\delta u + \Omega w - \frac{\Gamma}{2} v \\ \dot{w} = -\Omega v - \Gamma(w+1) \end{cases} \tag{3.26}$$

In practice, it may be necessary to know the Bloch equations when applying a complex form of the Rabi frequency,

$$\Omega = \Omega_{Re} + i\Omega_{Im} \tag{3.27}$$

Considering the complex form of the Rabi frequency in all the calculations above will give the Bloch equations as follows:

$$\begin{cases} \dot{u} = \delta v - \frac{\Gamma}{2} u + \Omega_{Im} w \\ \dot{v} = -\delta u + \Omega_{Re} w - \frac{\Gamma}{2} v \\ \dot{w} = -\Omega_{Re} v - \Gamma(w+1) - \Omega_{Im} u \end{cases} \tag{3.28}$$

When considering a complex Rabi frequency, the pseudo vector must be rewritten:

$$\mathbf{W} = -\Omega_{Re} \hat{\mathbf{e}}_u + \Omega_{Im} \hat{\mathbf{e}}_v + \delta \hat{\mathbf{e}}_w \tag{3.29}$$

Eq. 3.28 is a useful equation that can be used to predict many interesting phenomena by inserting different optical or radio frequency (RF) pulses with different Rabi frequencies.

3.3 The definition of pulse area

The excitation pulse interacting with a resonant two-level atom may have different shapes in the time domain. The excitation pulse area (Θ) is used as a dimensionless quantity, and is defined as the integration of the Rabi frequency of this pulse over time:

$$\Theta = \int \Omega(t)dt \tag{3.30}$$

For instance, any pulse with the ability to excite atoms from the $w = -1$ to the $w = 1$ state has a pulse area $\Theta = \pi$, and is simply called a π pulse (see Fig. 3.1).

The simplest case is zero detuning ($\delta = 0$) and a real Rabi frequency, for instance, a square pulse with a fixed frequency matched to the energy separation of a two-level atom. In this case, according to Eq. 3.29, the pseudo vector will be along $-\hat{e}_u$. Thus, a pulse that excites atoms from the $w = -1$ to the $w = 1$ state is called a square π pulse. A $\pi/2$ pulse is a pulse with the ability to excite atoms from the ground state to a superposition state which is shown as the $(\hat{e}_u, \hat{e}_v)$ plane in Fig. 3.1.

3.4 Free polarization decay

One of the first phenomena that was interpreted via the Bloch equations was free polarization decay (FPD), which is the optical analogy to free induction decay (FID) in the NMR (nuclear magnetic resonance) technique. FPD experiments belong to the time domain implementations of non-linear spectroscopy experiments (see Section 2.4) and an FPD signal indicates that the system is coherent. Applying an excitation pulse with duration T, which is shorter than T_2, can excite atoms from the $w = -1$ state to the $(\hat{e}_u, \hat{e}_v)$ phase plane as shown in Fig. 3.2a. A $\pi/2$ pulse gives the maximum FPD signal. Leaving atoms in the $(\hat{e}_u, \hat{e}_v)$ plane, allows atoms to start to oscillate with the same phase which leads to coherent emission in the propagation direction of the excitation pulse. After a while, the atoms start to dephase because they are oscillating at different frequencies. Therefore, the FPD signal will decrease in a manner proportional to the transverse relaxation time (T_2) of the target atoms. A more thorough model for the decay rate of FPD at low Rabi frequency (Ω) is given by Macfarlane et al. [32]:

$$\tau_{FPD} = \frac{T_2}{1 + \sqrt{\Omega^2 T_1 T_2 + 1}} \tag{3.31}$$

where T_2 and T_1 are the transverse (coherence) time and longitudinal relaxation time, respectively.

3.5 Photon echo effect

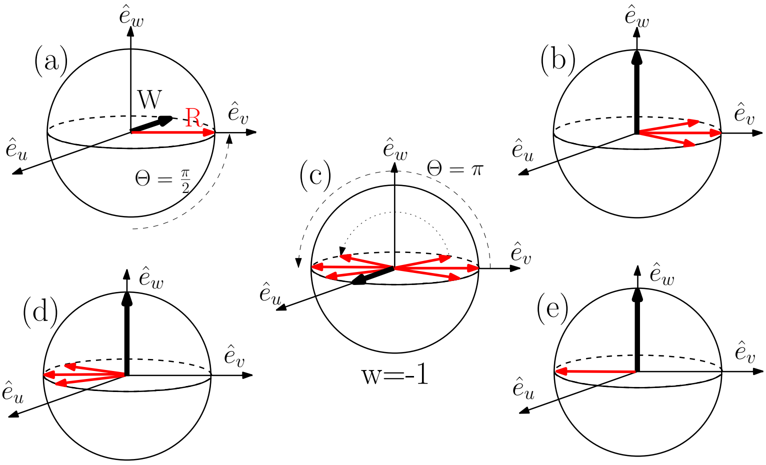

Figure 3.2. *The photon echo effect introduced by the Bloch sphere representation. (a) The first pulse is applied at $t = 0$ and excites the Bloch vector, R, from the ground state to the $(\hat{e}_u, \hat{e}_v)$ plane, creating a superposition. Here we assume there is no detuning, δ, therefore the pseudo vector, $\mathbf{W} = -\Omega\hat{e}_u$. (b) The waiting time, $t = t_{21} < T_2^*$, leads to dephasing of ions with different frequencies. At this stage, $\mathbf{W} = \delta\hat{e}_w$. (c) A π pulse with $\mathbf{W} = \Omega\hat{e}_u$ is applied to add a π phase to the evolved superposition state. (d) A waiting time of $t = t_{21}$ leads to rephasing of the superposition state. (e) The superposition state is refocused along $R = -v\hat{e}_v$ at time $t = 2t_{21}$.*

A short excitation pulse in the FPD experiment enables measurement of the coherence time, T_2. In the case of individual atoms, a much longer coherence time, T_2, can be measured. This raises the question of whether it would be possible to coherently re-phase all the oscillating dipoles and detect a coherent burst of constructive interference. The *photon echo* experiment was aimed to achieving this goal. Actually, most of the optical coherent transient phenomena were first discovered in the radio frequency region. A photon echo is the optical analogy of the spin echo in NMR [52]. A photon echo was first reported by Kurnit et al [47] in ruby crystal.

Following the first pulse at $t = 0$ in FPD experiment and applying a π pulse, after a time $T_2^* < t = t_{21} < T_2$ to an inhomogeneously broadened medium, one could rephase the coherent dipole emissions. In the Bloch vector picture, this corresponds to employing a $\pi/2$ pulse to excite ions from $\mathbf{R} = (0, 0, -1)$ to $\mathbf{R} = (0, 1, 0)$ (see Fig. 3.2a). By waiting

$$T_2^* < t = t_{21} < T_2$$

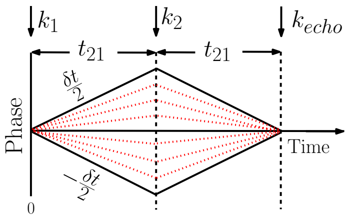

Figure 3.3. *Phase diagram representation of two pulse photon echo. Pulse sequences are denoted by k_1, k_2, and k_{echo} at times $t = 0$, $t = t_{21}$, and $t = 2t_{21}$. For further discussion see text.*

different ions will precess differently and spread over the $(\hat{e}_u, \hat{e}_v)$ plane. Applying a π pulse to rotate the Bloch vector, $\mathbf{R}$, about $\hat{e}_u$ corresponds to adding a π phase to the ions spread in the $(\hat{e}_u, \hat{e}_v)$ plane. The Bloch vectors of all the ions become aligned with the $-\hat{e}_v$ axis at time $t = 2t_{21}$ and the echo signal is emitted, as shown in Fig. 3.2e.

Coherent transient phenomena can be presented using phase diagrams [53, 54]. In the phase diagram representation shown in Fig. 3.3 time is plotted on the horizontal axis, while the phase of the atoms in the field interaction representation is plotted on the vertical axis (see Section 2.5 of Ref. [54]). Following Eq. 3.17, the phase associated with state $|1\rangle$ is $-\frac{\delta t}{2}$ while state $|2\rangle$ is $\frac{\delta t}{2}$, where δ is a general term corresponding to all phases associated with the atom. This could come from frequency detuning of the atoms in inhomogeneously broadened solids, or Doppler shift caused by movement in gases. The red dashed lines in Fig. 3.3 represent ions with different dephasing rates.

In the phase diagram representation, the duration of the applied laser pulse is considered to be sufficiently short that it appears to be instantaneous. The photon echo starts at t=0 by applying a pulse with a wave-vector $\mathbf{k}_1$ that creates a coherent superposition of two states. The phase evolution of the two states over time, which is shown by solid black lines in Fig. 3.3, will be $\frac{\delta t}{2}$ and $-\frac{\delta t}{2}$ within time $t = 0$ and $t = t_{21}$. Different dephasing rates in inhomogeneously broadened media are shown by the red dashed lines with different slopes in Fig. 3.3. It is possible to calculate the relative phase of any state relative to the zero phase in any time slice of Fig. 3.3. The π pulse applied at time $t = t_{21}$ will turn the phase symmetry of the dephased states by the amount π. This pulse is a π pulse in the Bloch representation rotating the Bloch vector about $\hat{\mathbf{e}}_u$. At $t = 2t_{21}$ the phases of the atomic states will interfere constructively, and individual phase differences will refocus to zero, and the echo signal will appear.

Phase matching

A nonlinear dielectric medium is characterized by the nonlinear relation between polarization density, $\mathbf{P}_{NL}$, and electric field $\mathbf{E}$:

$$\mathbf{P}_{NL} = a_1\mathbf{E} + a_2\mathbf{E}^2 + a_3\mathbf{E}^3 \tag{3.32}$$

where a_1 is the linear coefficient, and a_2, a_3 denote the second- and third-order nonlinearities, respectively. The polarization density of the photon echo signal can be considered to be a plane wave, $P_{2PE} \propto e^{i(\mathbf{k}_{echo}\cdot\mathbf{r})-\omega t} + c.c.$, while for two input pulses the electric field is:

$$E_j = E_0 e^{i(\mathbf{k}_j\cdot\mathbf{r})-\omega t} + c.c, \quad j = 1, 2 \tag{3.33}$$

To fulfill the phase matching condition for a two-pulse photon echo, $\mathbf{E}_1 + \mathbf{E}_2$ from Eq. 3.33 can be inserted into the right-hand side of Eq. 3.32. It is necessary to find the equivalent term when the left-hand side of Eq. 3.32 is P_{2PE} (the echo signal). Satisfying these conditions requires going beyond the second-order nonlinear effect, and third-order terms must be considered. This is the reason why the photon echo is a third-order nonlinear effect. Following the calculation above will give the phase matching condition for the two pulse photon echo [55]:

$$\mathbf{k}_{echo} = -\mathbf{k}_1 + 2\mathbf{k}_2 \tag{3.34}$$

Therefore, $\mathbf{k_1}$ and $\mathbf{k_2}$ in Fig. 3.3 should satisfy the phase matching condition described above.

3.6 Conventional photon echo limitations for quantum state storage

Two pulse photon echo has been used extensively as a sensitive spectroscopic tool [47]. Because of the inherent properties of the photon echo, it has been considered for classical light storage. One of the most important parameters governing light storage is the efficiency of storage, which is defined as the ratio between the echo signal and the input pulse energy. High efficiencies have been predicted and observed experimentally, in some cases greater than the unity [56–58]. In addition, the photon echo approach has good potential for storing several photonic states with different spectral, spatial, or temporal characteristics. These properties make it very promising for quantum state storage. Early in the 21st century, attention was turned to employ this coherent transient effect in the quantum domain. However, the simple two photon echo has some limitations on the quantum level. In this section, the obstacles preventing the use of two pulse photon echo for quantum state storage will be briefly discussed.

Quantum state storage for light, requires either a single photon Fock state [59], or a coherent state [59] attenuated to single photon level. For instance, Paper **II** describes a coherent state with an average photon number < 1 stored in the memory. There has been some interest in determining why the conventional two-photon echo cannot be used for quantum state storage [60]. In a two pulse photon echo, the second pulse is aiming for rephasing through population inversion. Therefore, a bright (π) pulse is required, which creates spontaneous emission. The amplitude of this spontaneous emission is comparable to or even higher than the amplitude of the retrieved echo. A single photon as a storage pulse was compared with no photon (vacuum state) in the two pulse photon echo scheme by Ruggiero et al. [60]. They calculated that the probability of photon emission at the echo time for a single photon input was twice as high as in the case with no input. This corresponds to a signal-to-noise ratio of one. This could be characterized as the first limitation of the two pulse photon echo.

The second limitation concerns propagation effects inside the medium. Propagation of the rephasing pulse inside the medium could stretch the pulse and produce a tail between the rephasing and the echo pulses. The amplitude of this tail is not negligible compared to the echo amplitude. This is a coherent propagation effect [61], and it is a fundamental limitation. This should not be confused with the noise induced by fluorescence.

The third limitation can also be connected to the propagation effect, but from a different viewpoint. It is related to the population inversion induced by the optical rephasing pulse, leading to medium amplification. This could explain the greater than unity predicted and observed efficiency [56–58]. The amplification itself is a clear sign of quantum state fidelity reduction because of the no-cloning theorem [4]. Based on these limitations, one could draw the conclusion that conventional photon echo is not suitable for quantum state storage. However, coherent rephasing processes in general are a promising basis for several quantum state storage protocols, as will be described in Chapter 6.

Let us now consider two pulses ($\pi/2$,π) in a two photon echo with separation τ. The second pulse (π pulse) is then divided into two $\pi/2$ pulses separated by an arbitrary time, T. This will lead to three $\pi/2$ pulses at $t = 0$, $t = \tau$, and $t = \tau + T$. The echo will be emitted at time $t = 2\tau + T$, which is called the stimulated, or three-pulse photon echo effect. An explicit calculation of the three pulse photon echo in both two- and three-level systems, shows that the conventional three pulse photon echo cannot be successfully employed for quantum state storage either [62]. The reason is that the rephasing pulses used in this scheme will induce spontaneous emission, which produces noise comparable to the retrieved signal. In the same way as for the two photon echo, it has been shown that the pulse propagation inside the medium will limit the possibility of employing conventional three-pulse photon echoes for quantum state storage [60].

CHAPTER 4

EXPERIMENTAL SETUP

To perform an experimental light-matter manipulation in the quantum regime, we need adequate and sometimes rather sophisticated equipment. In the present chapter, I discuss the equipments required for the experiments performed under the course of this thesis. In this discussion, I focus mainly on the light source needed to interact with material with long coherence properties (RE ions). The properties of the RE ion are discussed in Chapters 2 and 5.

4.1 Light source

The main scope of this thesis is the investigation and utilization of the coherent properties of the praseodymium ion $^3H_4 - {}^1D_2$ transition (see Fig. 2.4), which is about 606 nm. To have access to a proper coherent light source at this wavelength, We paid attention to the frequency stability of the selected laser. Since the narrow line-width of Pr is the main noteworthy property of interested, the frequency line-width of this laser had to be at least in the same level as the homogenous broadening of praseodymium ($\sim$ 1 kHz). Lacking a proper solid state laser within the target wavelength led us to employ a dye laser. The frequency stability of a typical commercial dye laser ($\sim$ 1 MHz) is about three orders of magnitude higher than the stability needs for our praseodymium sample. Thereby, an extra frequency stabilization setup is needed to reduce the dye laser line-width to the phase stability level of the atom.

A 6 Watt $Nd:YVO_4$ coherent Verdi-V6 laser at 532 nm was used which pumps a Coherent 699-21 dye laser and generates about 600 mW laser radiation at 606 nm. The Verdi-V6 laser is constructed based on pumping the $Nd:YVO_4$ crystal using arrays of diode lasers that emit light at 808 nm with 20 W power. The advantage of a dye laser is its broad frequency tuning range (from

400-700 nm). On the other hand, it is constructed by having a liquid dye flow as an active medium and the mechanical oscillation in this liquid makes it unstable compared to solid state lasers. In addition, to cover the entire frequency span, one needs to change the dye material. We are running our dye laser on the Rhodamin 6G dye, which has a maximum output power of about 590 nm and can be tuned from 570 nm to 640 nm [27]. Rhodamin 6G was dissolved in Ethylene-glycol with at the concentration of 1 $gr/liter$.

To prepare a stable dye flow at the nozzle, one needs a stable dye flow pressure and temperature. The dye pressure is kept at about 4.2 bar (Micropump GJN25-JF1SJ) while the temperature is controlled by a feedback loop heat exchanger about at about $8°C$. The dye flow setup is shown in Fig. 4.1. The interaction between the pump laser and the dye solution inside the dye laser ring cavity takes place just after the nozzle exit. A filter with a $0.1 \mu m$ hole size (Cole Parmer:EW-06479-48) was used to eliminate small air bubbles at the nozzle. A pressure transducer (PCB piezotronics:113B28) was utilized to monitor pressure variation. The dye nozzle from the original dye laser was replaced by a new one (RDSN02) from Radiant Dye Laser.

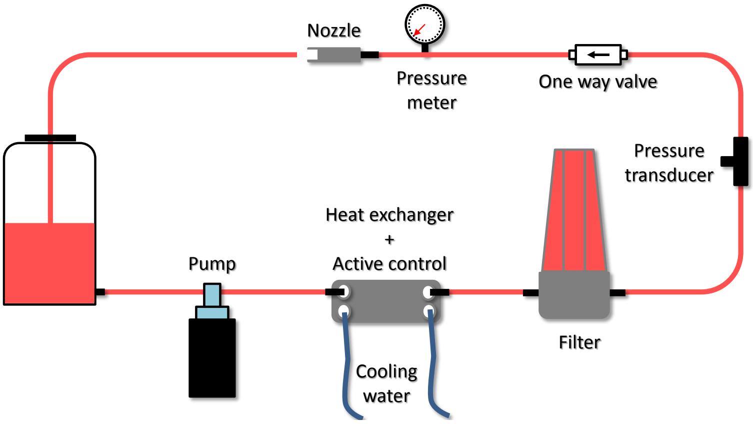

Figure 4.1. *Dye circulation setup to maintain stream stability. Additional details are given in the text.*

4.2 Frequency stabilization

The main advantages of the RE ions that we are dealing with is their very long coherence time or very well defined transition frequency, as discussed in Chapter 2. Interaction with these sharp atomic transitions requires a laser source narrow in frequency. However, if there is no inherent narrow bandwidth laser at the transition frequency of interest, one could consider employing a feedback loop and trying to lock the laser frequency to a stable reference. This is the concept, which is discussed in this section.

As a frequency locking reference for the dye laser, two different techniques are employed in the experiments carried out in this thesis. Firstly, a persistent spectral hole in $Pr^{3+} : Y_2SiO_5$ was employed for the experiments described in Paper **I** to Paper **V**. For details about this technique the reader is referred to [63, 64]. Secondly, the periodic spacing of highly stabilized Fabry-Pérot cavity resonances was utilized [65–69] in the experiments described in Paper **V** and Paper **VI**. Both techniques employ the Pound-Drever-Hall locking scheme [70–72] which we will discuss briefly in this section.

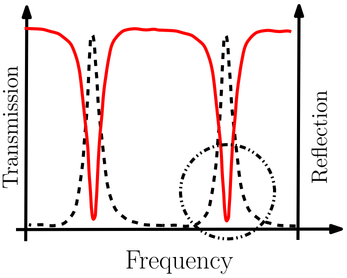

Figure 4.2. *Free spectral range of a Fabry-Pérot cavity. The black dashed and red solid lines are the transmitted and reflected light from the cavity, respectively. A near resonance spot is indicated by a circle and discussed in Fig. 4.3.*

4.2.1 Theoretical overview

In many applications, laser frequency jittering is the experimental limitation and a great deal of effort has been devoted to remove this boundary. As a general conceptual model, we need to consider two factors to be able to achieve a more stable laser frequency. Firstly, we must have a measurement tool as a reference to measure the laser frequency with sufficient accuracy. Secondly, we need to have the ability to adjust the laser frequency. The frequency adjustment is possible in most laser setups by feeding an electric signal controlling the appropriate actuators.

A Fabry-Pérot cavity would be a good candidate for measuring the laser frequency. The standing wave condition between the two mirrors in the Fabry-Pérot cavity puts constraints on the transmitted light frequency. Actually, in the Fabry-Pérot cavity, only light of wavelengths that are integer multiples of 2L (L is the cavity length) can pass through undisturbed. This property means that by scanning the frequency across the cavity we will have a transmission frequency with a free spectral range of $\Delta\nu_{FSR} = \frac{c}{2L}$ as shown in Fig. 4.2. If one considers the operation frequency on the side of one of the transmission peaks in Fig. 4.2, then any frequency variation will result in amplitude variations in the transmitted field. As a consequence, any compensation for amplitude variation could end up at the frequency compensation. The weak point in this scheme is thus the difficulty of distinguishing between frequency fluctuation and the laser intensity variation.

Employing a reflected beam from the cavity, instead of the transmitted one, will decouple the intensity and frequency noise. Actually, One could consider the Fabry-Pérot cavity in any optical setup as a frequency filtering device. From an energy conservation point of view, the full transmission of the light beam occurs when there is no reflected power. This condition is called the impedance-matched condition and can be considered as the heart of the Pound-Drever-Hall locking method [70–72]. Based on this method, one can measure the reflected intensity and hold it at zero. By this method we gain two properties. First, the laser intensity noise is decoupled from the frequency fluctuation. Second, we can fix faster frequency fluctuation since we do not need to wait for the field build-up in the cavity, a period of time which is considerably longer than that of the optical and electronic delay in the feedback setup.

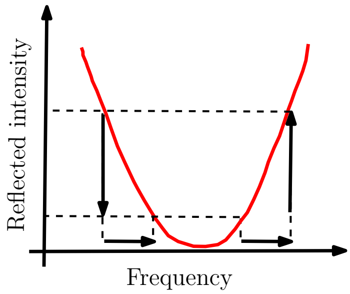

Figure 4.3. *The reflection from a Fabry-Pérot cavity near resonance. A laser frequency modulation will creates an intensity modulation. The phase of the modulated intensity below and above resonance gives us the sign of the error signal.*

Let us consider one of the reflected peaks in Fig. 4.3, and compare the reflected intensity for the lower and higher frequency sides. Because of their symmetry, the two sides are not immediately distinguishable. If one, on purpose, modulate the laser frequency over a small frequency range, then it is possible to determine the direction of the frequency detuning from the resonance. As shown in Fig. 4.3, the slope (the frequency derivative of the intensity) of the reflected field will be negative, zero, or positive, depending on whether the frequency is below, at, or above the resonance point, respectively. In other words, any input local oscillation with well-defined phase will be reflected from the right (left) side of the resonance peak with zero (π) phase change. This can thus be a good signal to use to push the actual laser frequency to the center of the resonance (Zero reflected intensity). This is the main idea behind the Pound-Drever-Hall frequency locking scheme.

The basic set up of Pound-Drever-Hall frequency locking is shown in Fig. 4.4. An electro-optical modulator (EOM) driven by a direct digital synthesizer (DDS) creates the modulation frequency ω_m and sends it to the cavity. A polarizing beam splitter followed by a $\lambda/4$-plate will separate the input light to the cavity and the reflected light from the cavity. The error signal is created by multiplying the second channel of the DDS and the light signal reflected after the photodiode at the mixer. The output of the two channels of the DDS should be identical except for the phase, which can be tuned to compensate for the phase shift in the two paths. Then the laser actuators need a proper amplification and filtering to tune the laser frequency with appropriate speed. There is an element in Fig. 4.4 which is called a Faraday rotator and it is not necessary for understanding the Pound-Drever-Hall frequency locking but it needs to be there in practice. The Faraday rotator will block reflected light back from the cavity. In fact, the small amount of reflected light, which passes through the Faraday rotator, could be enough to unlock the laser [72].

The frequency stability that can be obtained by locking the laser is directly limited by the steepness of the prepared reference peak. As a consequence, in practice a high finesse cavity is needed. Using the Fabry-Pérot cavity is not the only way to prepare a reference peak. The narrow spectral transition of atoms is also employed for laser frequency stabilization in semi-conductor lasers [73–75], Ti:Sapphire [76], and dye lasers [77]. For this purpose narrow line-width materials, for instance RE ions, are promis-

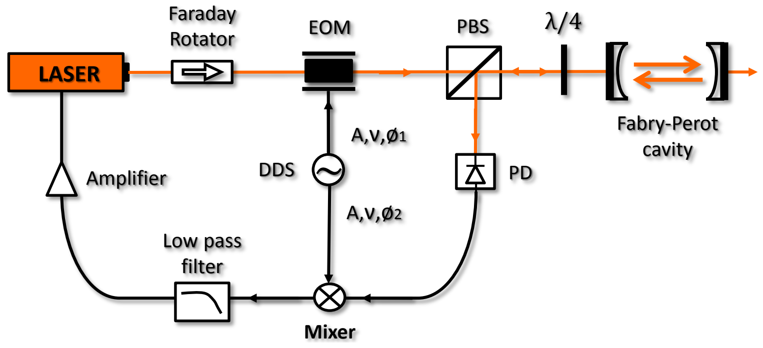

Figure 4.4. *The basic setup of the Pound-Drever-Hall frequency locking technique. The cavity reflection is employed as a reference signal. A combination of a polarizing beam splitter (PBS) and a $\lambda/4$-plate is employed to separate the input beam from the reflected beam. The reflected beam impinges on the photodiode (PD) and is then multiplied by the second channel of the direct digital synthesizer (DDS) signal at the mixer. A low pass filter and a servo amplifier act as a regulating system. The Faraday rotator will block the reflected back light from the cavity to the laser. In the present setup, the DDS channels are identical except that the relative phase ($\phi_2 - \phi_1$) between the two outputs can be adjusted. Tuning the $\phi_2 - \phi_1$ acts as a phase shift compensation for the two arms.*

ing candidates. Frequency-locking based on spectral hole burning employs transmitted light. One of the main differences between these techniques is the use of transmitted light in the spectral hole burning compared to the Fabry-Pérot cavity. Two-stage laser stabilization based on a combination of Fabry-Pérot and spectral-hole burning techniques to reach to sub-Hertz frequency stability has also been suggested [68].

4.2.2 Feedback loop setup

The main discussion in this section is about the actual frequency stabilization setup based on the Fabry-Pérot cavity technique employed in the present thesis. The schematic drawing of the entire laser frequency stabilization setup is shown in Fig. 4.5 and the specific components are listed in Section 4.5. Fig. 4.5 is a modification of Fig. 8.2 in Ref. [64], which shows the setup used for frequency stabilization based on spectral hole burning. Here, we describe the parts which are replaced from spectral hole burning to the Fabry-Pérot cavity stabilization scheme. There are several noise sources that need to be eliminated for the frequency stabilization setup to work as it should.

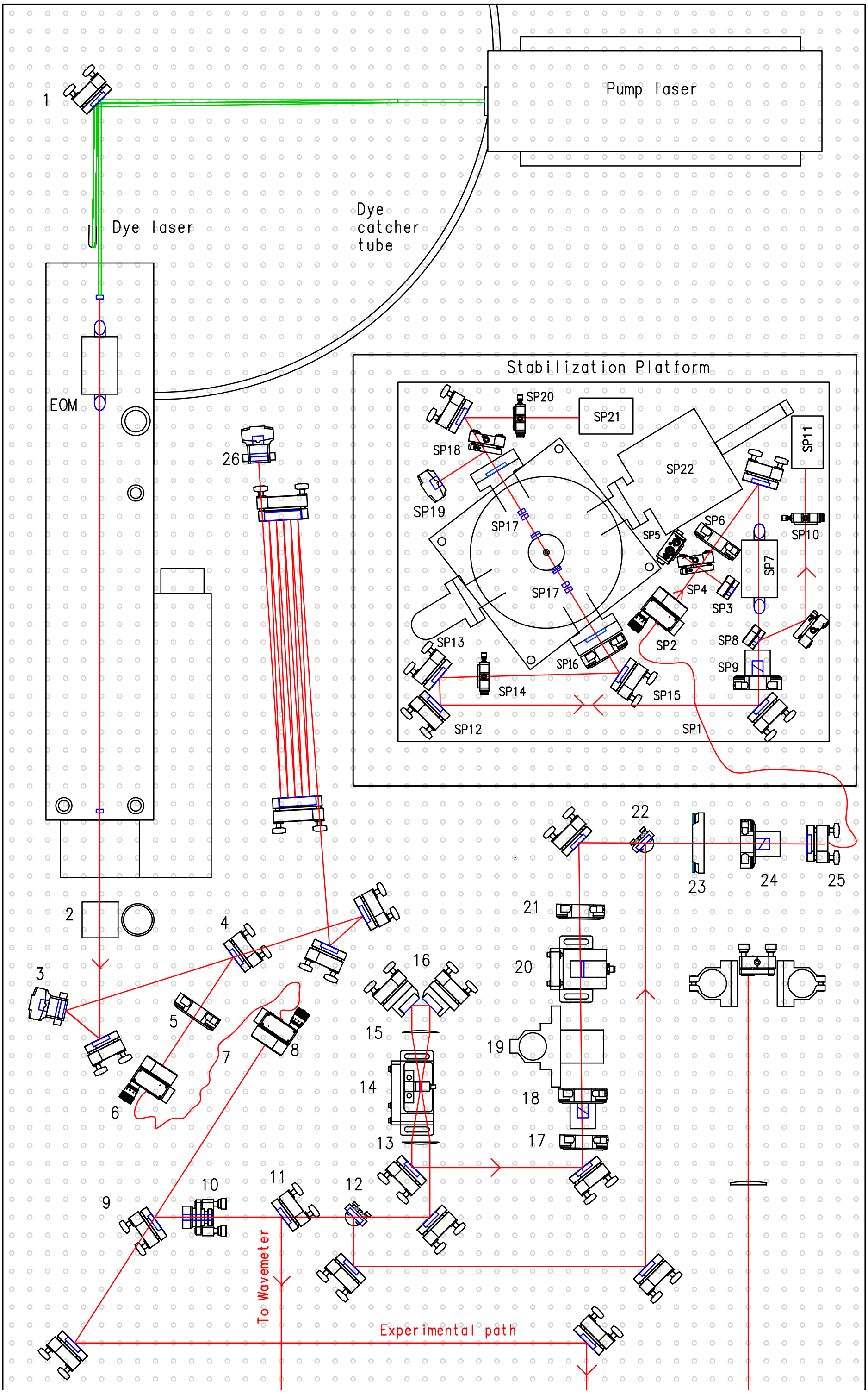

Figure 4.5. *Layout of the stabilization setup for the frequency stabilization platform. The specific components are listed in the section 4.5.*

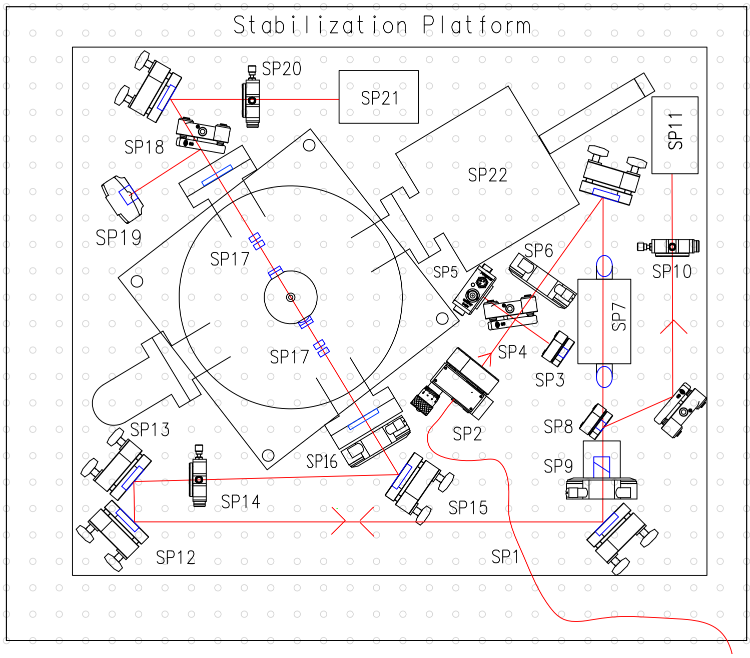

Figure 4.6. *Layout of the frequency stabilization platform. The specific components are listed in the section 4.5.*

To eliminate vibrational noise from the environment, part of the setup is placed on an active vibration isolated platform (HWL:TS-150), which is referred to as a stabilization platform in Fig. 4.5 and shown separately in Fig. 4.6. The light is coupled to the stabilization platform via a short (50 cm) polarization-maintaining fiber. The components list is starts with SPxx in Section 4.5 belongs to the stabilization platform. A Fabry-Pérot cavity with a length of 4.87 cm length and a finesse of $\sim$150000 in the wavelength range of 580-606 nm is embedded in the vacuum chamber ($\sim 6 \times 10^{-9} mbar$) which is shown in Fig. 4.6. This Fabry-Pérot cavity is employed as a frequency reference and it is the heart of the frequency stabilization feedback loop. Figs. 4.7 and 4.8 shows a photograph of the laser stabilization setup and the frequency stabilization platform, respectively. A more detailed discussion is given in Ref. [78].

The electro-optic modulator (EOM)

As stated in the theoretical discussion in section 4.2.1, an electro-optic modulator (EOM) is needed for light modulation in the PDH locking technique. An electro-optic modulator (EOM)

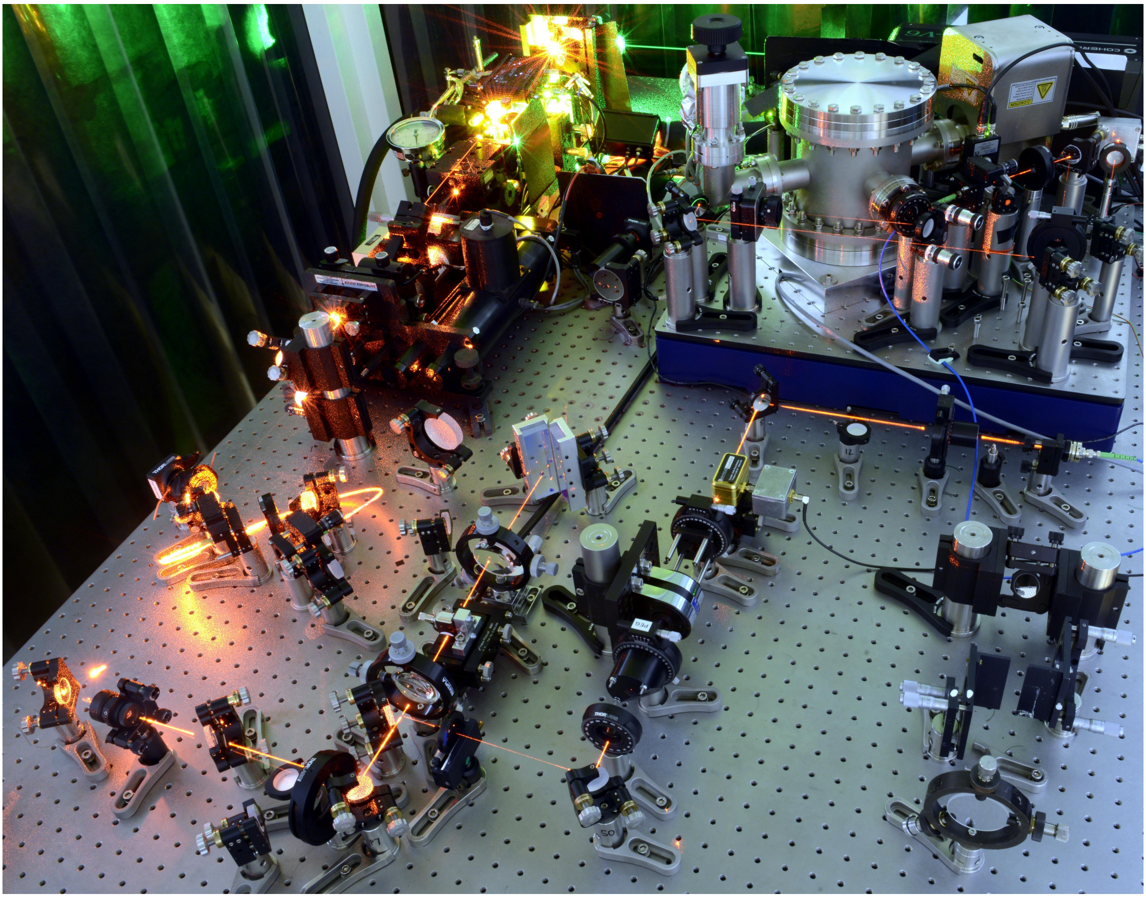

Figure 4.7. *Photograph of the laser stabilization setup.*

consists of an electro-optical crystal with the ability to change the optical path length by changing an applied external electric field. The refractive index change is linear in the applied electric field (called Pockels effect). The linear relation between applied electric field E and the induced refractive index changes, Δn, has the form:

$$\Delta n = \frac{1}{2} n_e^3 r_{33} E \tag{4.1}$$

where n_e is the unperturbed index of refraction and r_{33} is the appropriate element in the electro-optic tensor. For the phase modulators, one could consider the phase of the light field $\Delta\phi = k\Delta n l$, where k is the wave number and l is the crystal length. The light E-field will be modulated by $\Delta\phi$ (modulation index) at modulation frequency ω_m:

$$E = E_0 e^{i[\omega_0 t + \Delta\phi \sin(\omega_m t)]} \tag{4.2}$$

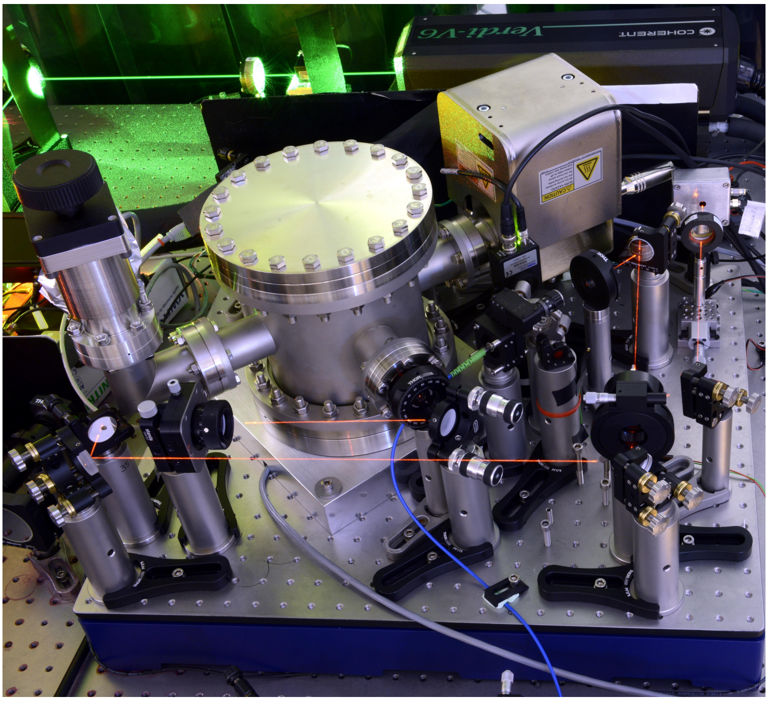

Figure 4.8. *Photograph of the frequency stabilization platform.*

If one consider a crystal of length, l, with electrodes separated by the crystal thickness, d, and applies an electric field along a crystal axis transversal to the direction of the optical propagation, then the phase modulation will be:

$$\Delta\phi = \frac{2\pi}{\lambda}[\frac{1}{2}n_e^3 r_{33}]\frac{l}{d}V_{pp} \tag{4.3}$$

This means that by exposing this crystal to an electric field, the speed of light will change in the crystal. The output light phase depends on the phase velocity in the crystal. Thereby, we can modulate the output phase of the light by applying an external voltage.

The phase modulation EOM (Qioptiq : PM25) is employed in the frequency stabilization setup in Fig. 4.6. The required peak to peak voltage for π phase shift is called a half-wave voltage (V_π). The V_π of the present EOM at 606 nm is 956 V, which is quite large and thus needs a huge radio frequency (RF) amplification. From an electronic point of view, the present EOM could be realized as a 30 pF capacitor. Therefore, for running at a single modulation frequency, it is possible to design a resonant circuit for the specific

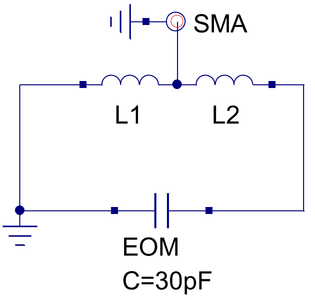

Figure 4.9. *Resonate circuit for the EOM (Qioptiq : PM25). To achieve a resonance frequency at 20 MHz a 1.5 mm wire diameter was selected. The diameter of both coils is 13.5 mm and the number of turns are n_1= 20, n_2= 9. The lengths of the coils are l_1=10 cm and l_2=4 cm.*

frequency corresponding to a 30 pF capacitor. The circuit designed for a 20 MHz modulation frequency (ω_m) is shown in Fig. 4.9. Considering the effect of the resonance circuit, the applied average RF power (P) across the EOM will be enhanced as follows:

$$\Delta\phi = \frac{2\pi}{\lambda}[\frac{1}{2}n_e^3 r_{33}]\frac{l}{d}\sqrt{2PQ\sqrt{\frac{L}{C}}} \tag{4.4}$$

where L is the coil inductance and C is the crystal capacitance. This resonance circuit will have a quality factor (Q) which is the ratio of stored energy over the input energy.

In PDH locking technique the error signal, depends on the cavity finesse, the laser wavelength, and the power in the carrier and sidebands, to the first order [72]. The ratio between the power in the sidebands and the carrier is equivalent to the modulation index ($\Delta\phi$). In practice, one needs to measure the modulation index versus the input RF power to obtain the scale factor in Eq. 4.5 such that the error signal can be optimized. To this end, an experimental setup was designed. The EOM with the resonance circuit is placed in the zero order arm of an AOM. Then, the beating between the EOM output and the first order of the AOM signal were overlapped on a fast photo-detector. A Fourier transform of the beating pattern gives us the carrier and sideband voltage amplitudes which are directly proportional to the respective E-fields.

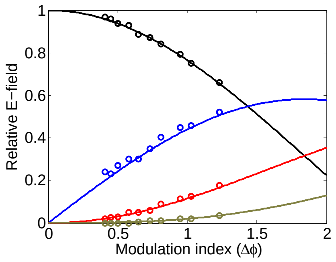

Figure 4.10. *The E-field distribution between carrier and sidebands follows four different Bessel functions. The lines represent theoretical Bessel functions and the circles are modulation index measurements.*

For a specific input power across the EOM, one specific modulation index was measured. Measuring the modulation index was accompolished by fitting the area below the carriers and sidebands and then considering it to be a coefficient of the corresponding Bessel functions. The measured modulation indices fitted to Bessel functions are shown in Fig. 4.10. A transfer coefficient between the RF power (in watts) applied across the EOM and the achieved modulation index (in radians) for the designed resonance circuit (Fig. 4.9) is:

$$\Delta\phi = \frac{3.2e^{-7}}{\lambda}\sqrt{P} \tag{4.5}$$

where λ is the light wavelength (in meters). The optimum modulation index in Ref. [72] is calculated to be at 1.08 which requires an RF power of about 4.2 W. The properties of the designed coil in the resonant circuit will be affected by the temperature instability which is produced by the high RF power. For the present resonance circuit, the temperature stability ($< 1°C$) was measured at 2W input power.

Coupling to the cavity

One of the vital steps towards designing the PDH locking setup construction is to couple the Gaussian TEM00 mode resonance frequency into the cavity. The beam is supposed to be collimated after the fiber (SP1 in Fig. 4.6). The lens SP14 in Fig. 4.6 is responsible for the divergence of the beam while the sets of mirrors (especially SP12, and SP15) are employed to correct the beam direction to the cavity mirrors. In addition to the spatial alignment, we need to consider alignment in the frequency domain by scanning the laser over at least one free spectral range (the mode-spacing of the present cavity is ~3 GHz) to find the TEM00 of the Gaussian beam at the transmission camera (SP19). The beam divergence have to be designed such that we have the same curvature for the beam and the cavity mirrors at the location of the mirrors. Any mismatch could end up producing high order Hermite-Gaussian spatial modes. The typical high order Hermite-Gaussian modes are shown in Fig. 4.11. To estimate our cavity mode structure, one can employ equation (See page 761 Ref. [79]):

$$\nu_{qnm} = [q + (n + m + 1)\frac{arccos(\pm\sqrt{g_1 g_2})}{\pi}] \times \frac{c}{2L} \tag{4.6}$$

where q represents the longitudinal modes and n and m stand for the transverse modes. The present Fabry-Pérot cavity is designed using parameters $g_1 = 1 + \frac{L}{R_1} = 0.9026$, $g_2 = 1 + \frac{L}{R_2} = 1$, where the cavity length L = 4.87 cm and R_1 and R_2 stand for the first and second mirror radii, respectively. Eq. 4.6 together with the values for the cavity above give a transverse mode frequency separation of about 300 MHz, which is shown in Fig. 4.12 for two longitudinal modes separated by about 3 GHz. The purpose of the spatial cavity alignment is to suppress the transverse modes (by at least a factor of 10 in the detected intensity) compared to the longitudinal modes in the transmitted signal.

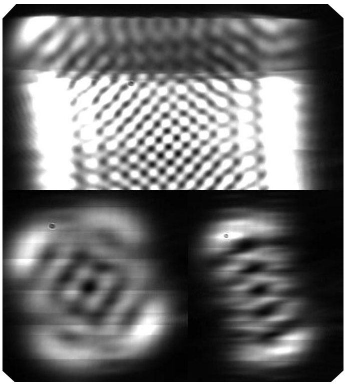

Figure 4.11. *Three typical high order Hermite-Gaussian cavity mode transmission patterns.*

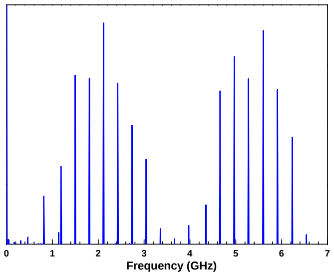

Figure 4.12. *Scanning the frequency across the Fabry-Pérot locking cavity gives two longitudinal modes with a separation of about 3 GHz in addition to several transverse modes with separations of about 300 MHz.*

Two channels of the direct digital synthesizer (DDS) in Fig. 4.4 were used to construct the PDH error signal. The first channel was employed to provide the RF signal to the EOM in Fig. 4.4 in order to create a sideband signal at the desired modulation frequency. The reflected signal from the Fabry-Pérot cavity is detected at the photodiode and then multiplied by the second output channel of the DDS that provides the same frequency as modulation frequency, ω_m, as a reference. Based on frequency modulation spectroscopy approach [80], by controlling the phase of the second channel of the DDS, we can decide to have our system in either "dispersion" or "absorption" mode. The response signal versus detuning, in both the dispersion and absorption modes, achieved by controlling the phase differences between two channels of the DDS are shown in Fig. 4.13, and 4.14, respectively. In practice, the phase differences between the two output channels of the DDS should be set to have the dispersion mode in the error signal as shown in Fig. 4.13. Further information and more details about these steady response signals are provided in Ref. [71, 72].

The error signal obtained, after passing through electronic filtering and amplification, is applied to different actuators inside the

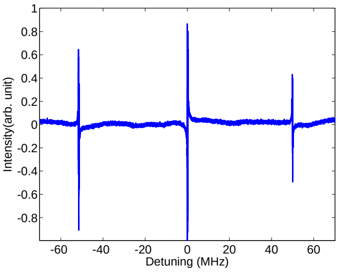

Figure 4.13. *A typical response signal versus the detuning in the dispersion mode.*

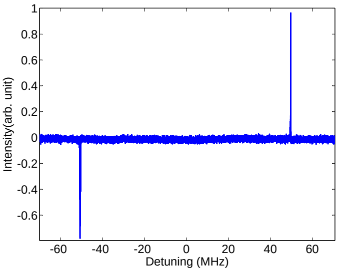

Figure 4.14. *A typical response signal versus the detuning in the absorption mode.*

dye laser ring cavity as shown in Fig. 4.15. Different actuators will change the dye laser ring cavity length on different time scales, as shown in Fig. 4.15.

4.3 Pulse Preparation

For all experiments related to the present thesis, we needed to design different complicated optical pulses. These light pulses were engineered by employing two acousto-optic modulators (AOM) in the setup. In this section, we discuss in more detail the principles on which the AOM is based on.

The acousto-optic modulator

Applying sound as a mechanical wave to an optical medium can affect the refractive index of the medium. The dynamic Bragg grating created by the sound wave can be employed to create diffraction of the light impinging on this grating. This is the main physics behind acousto-optic modulation. The acousto-optic modulator as a general piece of optical equipment consists of a radio-frequency (RF) source driving a piezo-electric transducer, attached to a crystal. The dynamical grating mentioned above is created inside the crystal. Any incident laser beam will be diffracted by this grating. The intensity of the diffracted light is proportional to the sound intensity. Additionally, the light frequency undergoes a frequency shift equal to the sound frequency. Therefore, any modulation on the input RF signal to the AOM will be mapped onto the light.

The double pass AOM

Since the beam diffraction angle is a function of the modulation frequency, changing the RF frequency shifts the propagation direction of the first-order diffracted beam. To eliminate this unwanted spatial movement, a double-pass AOM configuration is employed. To this end, one can consider using a retro-reflected mirror configuration for the first-order diffracted beam and sending it back through the AOM. The output beam after the second pass through the AOM will be shifted in frequency twice with respect to the input beam. In this arrangement, scanning the RF frequency, and consequently the output light frequency, does not cause any steering of the first order output of the second pass. In fact, the output of the second pass counter-propagates with the original input beam. Whilst this is desirable, as it allows the frequency to be changed without any steering of the output beam, it poses the problem of how to separate the path of the output beam from that of the input beam. To solve this issue, one could employ a polarizing beam splitter (PCB) and a $\lambda/4$ plate. As a second alternative, which is the one applied in our setup, one can design a butterfly configuration for the first and second beams through the AOM. Looking at the AOM from the side, it becomes apparent that one can send the input beam at a small angle with respect to the horizon. Then the retro-reflected mirror configuration can change the beam height and overlap the second beam with the first beam at the AOM. The butterfly configuration will separate the incoming and outgoing beams spatially (due to the difference in their heights).

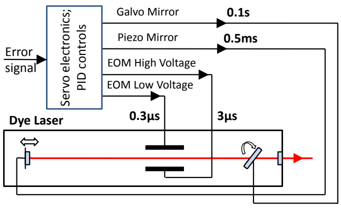

Figure 4.15. *Four different actuators inside a dye laser ring cavity correct the cavity length and consequently the laser frequency.*

An acousto-optic modulator (AA. opto-electronics St.200/B100/A0.5-VIS, AOM) with a 200 MHz center frequency is employed in the double pass configuration to achieve a 200 MHz bandwidth after the second pass. A second AOM (AA. opto-electronics St.360/B200/A0.5-VIS) is used in the setup in a single pass configuration with a center frequency at 360 MHz and a bandwidth of 200 MHz. After the AOM's the laser mode is cleaned by passing through a single-mode fiber (PMC-630-3.8-NA012-3-APC-2500-P;Schäfter-Kirchhoff). An extensive MATLAB code, via a two channel 1-GS/s arbitrary waveform generator (Tektronix AWG520), generates the driving RF signal needed for the AOMs.

4.4 Cryostat

A cryostat (from cryo meaning cold and stat meaning stable) is an equipment that can prepare a cryogenic environment. There are several types of cryostat based on the various refrigeration methods employed to keep the sample cold enough. Within the framework of the present thesis, we mainly used an Oxford Spectromag. This cryostat has a 20-liters built-in liquid helium reservoir. As the helium boils within the sample chamber, it is continuously replenished by a steady flow from the liquid helium reservoir. Temperature control of the sample within the cryostat is typically performed by controlling the flow rate of liquid helium into the sample chamber, controlling the pressure inside the sample chamber by a vacuum pump together with a heating wire attached to a PID temperature control loop. In addition, due to the scarcity of liquid helium, the out going helium gas was recovered in a central system belonging to Lund University. The Oxford Spectromag allows optical measurements to be performed in the temperature range of 1.5 - 300 K with magnetic fields up to 7 teslas (at a temperature of 4.2 K) or 8 teslas (at a temperature of 2.2 K).

In the experiments related to Paper **IV**, a Janis cryostat (Model: STVP-400) was used mainly because of its larger beam acceptance angle to the sample compared to the Oxford Spectromag cryostat. This is related to the property called *etendue* which is discussed in detail in Section 7.3.1.

4.5 Table components

1. High-power mirror, CVI
2. Periscope, from 135 mm coming from the laser to 75.4 mm which is the beam height for the rest of the set-up.
3. Alignment camera, Thorlabs, DCC1545
4. Mirror, polished backside, Thorlabs
5. $\lambda/2$ plate, Thorlabs
6. Z-Axis Translation Mount, Thorlabs, SM1Z and CP02T
7. Fiber, Thorlabs, PM460-HP-FC/APC both ends
8. Z-Axis Translation Mount, Thorlabs, SM1Z and CP02T
9. Beam splitter, $\approx 5\%$ reflection
10. Telescope(ϕ=2 mm $\rightarrow$ ϕ=1 mm)
11. Beam splitter, $\approx 5\%$ reflection
12. Flip Mirror, Newport, 9891-M
13. Lens, Thorlabs, LA1145-A
14. AOM, frequency shifter, Brimrose, GPF-1500-10
15. Lens, Thorlabs, AL50100-A
16. Retro-reflector mirror, Altechna, custom order
17. $\lambda/2$ plate, Thorlabs
18. Polarizer, FocTek, GPB7008
19. Faraday rotator, Leysop, FOI 5/57
20. AOM, fiber noise cancelation, Isomet, 1205C-x
21. Polarizer, FocTek, GLP6310
22. Flip Mirror, Newport, 9891-M
23. $\lambda/2$ plate, Thorlabs
24. Polarizer, FocTek, GLP6310
25. Fiber coupler, Schäfter Kirchhoff, 60SMS-1-4-M5-33
26. Alignment camera, Thorlabs, DCC1545

Stabilization platform components

SP1. Fiber, Thorlabs, PM460-HP-FC/APC both ends

SP2. Z-Axis Translation Mount, Thorlabs, SM1Z and CP02T

SP3. Mirror for fiber noise cancelation, Thorlabs, FL05635-10

SP4. Beam splitter, CVI, BS1-633-20-1012-45S

SP5. Detector, Thorlabs, PDA36A

SP6. $\lambda/2$ plate, Thorlabs

SP7. EOM, Qioptiq , PM25

SP8. Mirror Throlabs BB05-E02 mounted on Thorlabs MA45-50/M to impinge the reflected beam from the cavity to the detector **SP11**

SP9. Polarizer, FocTek, GPB7008

SP10. Lens, Thorlabs, f= 50 mm

SP11. Error photo-detector, Home built, photodiode: Hamamatsu S5905, trans-impedance amplifier: MAX3658

SP12. Cavity coupling mirror, Thorlabs, BB1-E02

SP13. Cavity coupling mirror, Thorlabs, BB1-E02

SP14. Cavity coupling lens, Eksma, AR@430-960nm, f= 400 mm, mounted on Eksma optics 840-0210

SP15. Cavity coupling mirror, Thorlabs, BB1-E02

SP16. $\lambda/4$ plate, Thorlabs

SP17. Fabry-Pérot cavity mirrors, Thin films,V6-488+V6-489

SP18. Beam splitter, CVI, $\approx 5\%$ reflection

SP19. Camera, Point Grey, FFMV-03M2M-CS

SP20. Lens, Thorlabs, f= 50 mm

SP21. Transmission detector, Home built, photodiode: Hamamatsu S5971, trans-impedance amplifier: Texas Instruments THS4631

SP22. Ion pump, Titan

CHAPTER 5

LIGHT PROPAGATION IN AN ANISOTROPIC MEDIUM

Understanding the properties of light propagating through a medium is one of the interesting challenges of studying electromagnetic wave theory. Explaining experimentally observed phenomena related to light propagation in terms of electromagnetic theory is quite complex due to the interaction of light with matter taking place during the propagation. One could reduce this complexity without loosing the generality of the solution by considering a simplification based on the properties of the medium. We start the simplification by considering a plane-stratified medium, which is a valid assumption for the materials investigated in our case. The assumption of plane-stratified media is a proper approximation for materials that show variation in the propagation direction (z-axis) and no variation in the lateral (x-y plane) direction. In other words, we have homogeneity in the x-y plane and inhomogeneity along the z-axis. The main theoretical concept of the calculations in this chapter is discussed with more details in Ref. [81].

5.1 Basic equations

For macroscopic media, Maxwell equations describe the dynamics of the fields as follows:

$$\begin{cases} \bigtriangledown \times \mathbf{E}(\mathbf{r},\omega) = ik_0(c_0\mathbf{B}(\mathbf{r},\omega)) \\ \bigtriangledown \times \eta_0\mathbf{H}(\mathbf{r},\omega) = -ik_0(c_0\eta_0\mathbf{D}(\mathbf{r},\omega)) \end{cases} \tag{5.1}$$

where c_0 and k_0 are the speed and wave-number of light in a vacuum, respectively. In addition, **E**, **B**, **H**, and **D** are the electric field, magnetic induction, magnetic field, and the displacement electric field, respectively. In order to apply Maxwell's macroscopic equations, it is necessary to specify the relations between

D, **E**, **H**, and **B**. These equations are called *constitutive relations.*

$$\begin{cases} \mathbf{D}(\mathbf{r}) = \epsilon_0[\boldsymbol{\epsilon}(z,\omega)\cdot\mathbf{E}(\mathbf{r},\omega) + \eta_0\boldsymbol{\xi}(z,\omega)\cdot\mathbf{H}(\mathbf{r},\omega)] \\ \mathbf{B}(\mathbf{r}) = \frac{1}{c_0}[\boldsymbol{\zeta}(z,\omega)\cdot\mathbf{E}(\mathbf{r},\omega) + \eta_0\boldsymbol{\mu}(z,\omega)\cdot\mathbf{H}(\mathbf{r},\omega)] \end{cases} \tag{5.2}$$

where $\mathbf{r} = x\hat{\mathbf{x}} + y\hat{\mathbf{y}} + z\hat{\mathbf{z}}$ and ω is the angular frequency. $\boldsymbol{\epsilon}$ and $\boldsymbol{\mu}$ are the *permittivity* and *permeability* of the medium, respectively, while $\boldsymbol{\xi}$ and $\boldsymbol{\zeta}$ are called crossed magneto-electric dyadics.

In a single crystal, the physical and mechanical properties can often be orientation dependent. When the properties of a material vary with orientation, the material is said to be *anisotropic*. Alternatively, when the properties of a material are the same in all directions, the material is said to be *isotropic*. *Bi-anisotropic* media may be characterized as a general class of linear media which exhibit so-called magnetoelectric coupling between the electric and magnetic fields [81].

Based on the plane-stratified assumption, it is natural to decompose the electromagnetic field into tangential (x-y plane) and normal components. Considering this lateral homogeneity and substituting the constitutive relations (Eq. 5.2) into the Maxwell equations (Eq. 5.1) gives a system of ordinary differential equations (ODEs) with the variable z.

$$\frac{d}{dz}\begin{pmatrix} \mathbf{E}_{xy}(z) \\ \eta_0\mathbf{J}\cdot\mathbf{H}_{xy}(z) \end{pmatrix} = ik_0\mathbf{M}(z)\cdot\begin{pmatrix} \mathbf{E}_{xy}(z) \\ \eta_0\mathbf{J}\cdot\mathbf{H}_{xy}(z) \end{pmatrix} \tag{5.3}$$

where **J** is a two-dimensional rotation dyadic (rotation of $\pi/2$ in the x-y plane) as follows:

$$\mathbf{J} = \begin{pmatrix} 0 & -1 \\ 1 & 0 \end{pmatrix} \tag{5.4}$$

and

$$\mathbf{J}\cdot\mathbf{J} = -\mathbf{I_2} = \begin{pmatrix} -1 & 0 \\ 0 & -1 \end{pmatrix} \tag{5.5}$$

in addition

$$\mathbf{M} = \begin{pmatrix} \mathbf{M}_{11} & \mathbf{M}_{12} \\ \mathbf{M}_{21} & \mathbf{M}_{22} \end{pmatrix} \tag{5.6}$$

For a more detailed discussion of how to obtain Eq. 5.3, which is beyond the scope of this thesis, the reader is referred to Ref. [81]. We will discuss the matrix elements of $\mathbf{M}(z)$ for $Pr^{3+} : Y_2SiO_5$ in Section 5.2.2.

5.2 Light propagation in the $Pr^{3+}:Y_2SiO_5$ crystal

In this section the light propagation inside a 0.05% $Pr^{3+}:Y_2SiO_5$ crystal is discussed. We start by calculating the permittivity tensor and employing the theoretical approach discussed in Section 5.1 to achieve the light polarization direction while propagating through this specific medium.

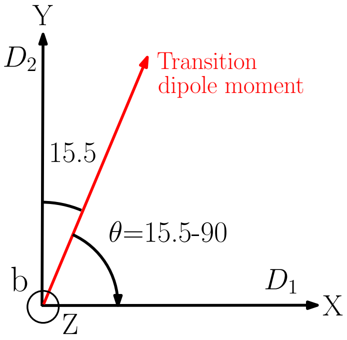

Figure 5.1. *Transition dipole moment direction versus principal axis for* $Pr^{3+}:Y_2SiO_5$.

5.2.1 Defining the permittivity tensor in the principal axis coordinate system

To define the permittivity tensor for $Pr^{3+}:Y_2SiO_5$, one could start by deriving the relation between permittivity and susceptibility for the host material (Y_2SiO_5) and the absorber (Pr) separately as follows:

$$\boldsymbol{\epsilon} = n^2\epsilon_0 = (1+\boldsymbol{\chi})\epsilon_0 = (1+\boldsymbol{\chi}_{host}+i\boldsymbol{\chi}_{abs})\epsilon_0 \tag{5.7}$$

The imaginary part of the susceptibility is proportional to the absorption, while the real part of the susceptibility is proportional to the real refractive index. $\boldsymbol{\chi}_{abs}$ is directly connected to the absorption coefficient (α), in the medium as follows [82]:

$$\chi_{abs} = \frac{n_b c_0}{\omega}\alpha \tag{5.8}$$

where $n_b \approx 1.8$ as a background refractive index and $\omega \approx 2\pi.494$ THz. The anisotropic absorption coefficients for the two sites of a nominally 0.05% $Pr^{3+}:Y_2SiO_5$ crystal at the ${}^3H_4 - {}^1D_2$ transition is measured as shown in the Table 7.6 in the Ref. [29]. Based on this measurement the absorption for site I (605.977 nm) is about 3.6 ± 0.5 along the D_1, 47 ± 5 along the D_2, and < 0.1 along the b axis, all in the unit cm^{-1} (See Fig. 5.1, where b, D_1, and D_2 are crystal principal axes.) Therefore, following Eq. 5.8 we obtain:

$$\chi_{abs} = 8.2\times10^{-4} \tag{5.9}$$

in the direction of the transition dipole moment shown in Fig. 5.1. χ_{abs} is a unitless quantity which represents the imaginary part of the susceptibility.

To be able to perform the summation in Eq. 5.7 for different susceptibilities, we have rotated the $\boldsymbol{\chi}_{abs}$ coordinate about the b axis to the principal axis coordinate. According to Fig. 5.1 the rotation angle in the case of $Pr^{3+}:Y_2SiO_5$ is $\theta = 15.5 - 90$.

$$\boldsymbol{\chi}_{abs} = \mathbf{R_z}\cdot\boldsymbol{\chi}_{abs}.\mathbf{R_z}^{-1} = \chi_{abs}\begin{pmatrix} \cos^2\theta & \sin\theta\cos\theta & 0 \\ \sin\theta\cos\theta & \sin^2\theta & 0 \\ 0 & 0 & 0 \end{pmatrix} \tag{5.10}$$

The next step is to calculate $\boldsymbol{\chi}_{host}$ based on the Sellmeier dispersion and the measured coefficients from Table 7.1 and Eq. 7.2 in Ref. [29].

$$\boldsymbol{\chi}_{host} = \begin{pmatrix} 2.1989 & 0 & 0 \\ 0 & 2.2744 & 0 \\ 0 & 0 & 2.1883 \end{pmatrix} \tag{5.11}$$

Adding up all calculations, the final results for the permittivity tensor in the principal axis coordinate will be:

$$\bar{\bar{\epsilon}} = \begin{pmatrix} \epsilon_{xx} & \epsilon_{xy} & \epsilon_{xz} \\ \epsilon_{yx} & \epsilon_{yy} & \epsilon_{yz} \\ \epsilon_{zx} & \epsilon_{zy} & \epsilon_{zz} \end{pmatrix} \tag{5.12}$$

$$= \begin{pmatrix} 1 + \chi_{xx} + i\chi_{abs}\cos^2\theta & i\chi_{abs}\sin\theta\cos\theta & 0 \\ i\chi_{abs}\sin\theta\cos\theta & 1 + \chi_{yy} + i\chi_{abs}\sin^2\theta & 0 \\ 0 & 0 & 1 + \chi_{zz} \end{pmatrix} \epsilon_0 \tag{5.13}$$

$$= \begin{pmatrix} 3.1989 + 5.85e^{-5}i & -2.11e^{-4}i & 0 \\ -2.11e^{-4}i & 3.2744 + 7.6e^{-4}i & 0 \\ 0 & 0 & 3.1883 \end{pmatrix} \epsilon_0 \tag{5.14}$$

5.2.2 Defining the M tensor based on the permittivity tensor

According to the main assumption of this chapter (the plane-stratified media assumption), the four dyadics $\boldsymbol{\epsilon}(z), \boldsymbol{\xi}(z), \boldsymbol{\zeta}(z)$, and $\boldsymbol{\mu}(z)$ in Eq. 5.2 depend only on the spatial variable, z, which describes the propagation direction. The second assumption in our case is to consider all four dyadics to be independent of angular frequency (ω).

The $Pr^{3+} : Y_2SiO_5$ crystal, which is our medium, is modeled as a non magnetic anisotropic medium with zero crossed magneto-electric dyadics. Therefore, as a third assumption, we consider there to be no crossed magneto-electric dyadics ($\boldsymbol{\xi} = \boldsymbol{\zeta} = 0$) in Eq. 5.2. There exists a general sets of equations for the connection between the fundamental matrix $\mathbf{M}(z)$ and the four main dyadics in Ref. [81], but based on the three assumptions described above, a normal incident, non-magnetic, and anisotropic medium, we can simplify the $\mathbf{M}(z)$ for our case as:

$$\mathbf{M} = \begin{pmatrix} \bar{\bar{\mathbf{0}}} & -\bar{\bar{\mathbf{I}}}_2 \\ -\bar{\bar{\epsilon}}_{\perp\perp} + \frac{1}{\epsilon_{zz}}\bar{\epsilon}_{\perp}\bar{\epsilon}_z & \bar{\bar{\mathbf{0}}} \end{pmatrix} \tag{5.15}$$

where

$$\bar{\bar{\epsilon}}_{\perp\perp} = \begin{pmatrix} \epsilon_{xx} & \epsilon_{xy} \\ \epsilon_{yx} & \epsilon_{yy} \end{pmatrix}, \quad \bar{\epsilon}_{\perp} = \begin{pmatrix} \epsilon_{xz} \\ \epsilon_{yz} \end{pmatrix}, \quad \bar{\epsilon}_{z} = \begin{pmatrix} \epsilon_{zx} & \epsilon_{zy} \end{pmatrix}, \bar{\bar{\mathbf{I}}}_2 = \begin{pmatrix} 1 & 0 \\ 0 & 1 \end{pmatrix} \tag{5.16}$$

5.2.3 M tensor eigenvalues

Following Eq. 5.3, we need to investigate the eigenvalues and eigenvectors of the M tensor (Eq. 5.15) in order to calculate the tangential components of the electric and magnetic field. The eigenvectors $\bar{u}_i$ and $\bar{v}_i$ correspond to the eigenvalues $+\lambda_i$ and $-\lambda_i$ $(i = 1, 2)$ for the forward and backward waves, respectively:

$$\begin{cases} \bar{u}_i = \{E_{xi}, E_{yi}, -\eta_0 H_{yi}, \eta_0 H_{xi}\} \\ \\ \bar{v}_i = \{-E_{xi}, -E_{yi}, -\eta_0 H_{yi}, \eta_0 H_{xi}\} \end{cases} \quad \text{for i=1,2} \tag{5.17}$$

5.2.4 E-field evolution in the propagation direction

To understand the E-field and H-field properties while the wave is propagating in the z direction, we can employ the fundamental equation for one-dimensional wave propagation (Eq. 5.3). By considering the eigenvectors and eigenvalues of the M matrix (Eq. 5.17), the wave properties along the propagation (z) direction is calculated for the forward wave:

$$\frac{d}{dz}\bar{u}_i = ik_0\lambda_i\bar{u}_i \Longrightarrow \bar{u}_i(z) = \bar{u}_i(0)e^{ik_0\lambda_i z} \tag{5.18}$$

it is possible to calculate the backward wave $(\bar{v}_i(z))$ in the same way.

By convention, the polarization of light is described by specifying the orientation of the wave's electric field at a point in space over one period of the oscillation. Therefore, to understand the polarization direction inside the medium it is enough to drive only the E-field. The initial light polarization before interaction with the medium could be driven by the E-field direction:

$$E_0 = E_{0x}\hat{x} + E_{0y}\hat{y} \tag{5.19}$$

In addition, the electric field inside the medium could be written as a superposition of the E-field of two eigenvectors:

$$\begin{aligned} E_{inside} &= \alpha\bar{E}_1(z) + \beta\bar{E}_2(z) \\ &= \alpha(E_{x1}\hat{x} + E_{y1}\hat{y}) + \beta(E_{x2}\hat{x} + E_{y2}\hat{y}) \end{aligned} \tag{5.20}$$

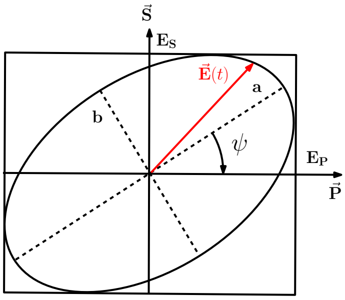

Figure 5.2. *Different representation for $\hat{\bar{E}}(t)$ as a complex amplitude vector which is rotating in the polarization plane which is perpendicular to the propagation direction. More discussion is in the text.*

based on the boundary condition for the tangential E-fields at the interface:

$$\begin{cases} \hat{x} : E_{0x} = \alpha E_{x1} + \beta E_{x2} \\ \hat{y} : E_{0y} = \alpha E_{y1} + \beta E_{y2} \end{cases} \tag{5.21}$$

Therefore

$$\begin{cases} \alpha = \frac{E_{0x}E_{y2} - E_{0y}E_{x2}}{E_{x1}E_{y2} - E_{y1}E_{x2}} \\ \beta = \frac{1}{E_{x2}}[E_{0x} - \alpha E_{x1}] \end{cases} \tag{5.22}$$

Now, based on the knowledge from input E-field E_0 (Eq. 5.19), we can calculate the E-field inside the medium (E_{inside}) from Eq. 5.20. Later, we can extend our knowledge to different slabs in the propagation direction using Eqs. 5.18 and 5.20 as follows:

$$\bar{u}(z) = \alpha \bar{u}_1 e^{ik_0\lambda_1 z} + \beta \bar{u}_2 e^{ik_0\lambda_2 z} \tag{5.23}$$

5.2.5 Major and minor elliptical polarization calculation

So far, we have calculated $\bar{u}(z)$, which is connected to the E-field according to Eq. 5.17. The next step, could be to map $\bar{u}(z)$ to the world of polarization. In this section, we introduce the polarization definition from two different perspectives and then connect it to $\bar{u}(z)$.

One of the solutions for the wave equation will be $\mathbf{E}(\mathbf{r}, t) = \hat{\bar{E}}e^{-i(\omega t - \mathbf{k}\cdot\mathbf{r})}$ with a complex amplitude vector $\hat{\bar{E}}$. This complex vector, which is in the plane perpendicular to the propagation direction, could be written in two different notation which are equivalent:

$$\begin{cases} \hat{\bar{E}} = E_P\mathbf{P} + E_S\mathbf{S} \\ \hat{\bar{E}} = \bar{E}_r + i\bar{E}_i \end{cases} \tag{5.24}$$

In the first notation, E_P and E_S are two complex scalers while $\mathbf{P}$ and $\mathbf{S}$ are two orthogonal unit vectors, as shown in Fig. 5.2. Actually, the letters $\mathbf{P}$ and $\mathbf{S}$ have a German origin, where $\mathbf{S}$ stands for "Senkrecht", which means perpendicular, and $\mathbf{P}$ stands for parallel. This is equivalent to the convention for p-polarized and s-polarized light. The p-polarized light is understood to have an electric field direction parallel to the plane of incidence on a surface, and the s-polarized light has the electric field oriented perpendicular to that plane. The phase differences ($\phi = \phi_P - \phi_S$) between $E_P = |E_P|e^{i\phi_P}$ and $E_S = |E_S|e^{i\phi_S}$ define the linear ($\phi = 0, n\pi$; n is an integer number), circular($\phi = \pm(2n+1)\frac{\pi}{2}$), or elliptical polarization (see Eq. 5.26).

In the second notation, the real vectors, $\bar{E}_r$ and $\bar{E}_i$, span the same plane as $\hat{\bar{E}}(t)$, but they would generally not be orthogonal. The calculations for $\bar{u}_i$ and $\bar{v}_i$ in Eq. 5.17, follows the second convention. However, in many practical contexts it is preferable to work with orthogonal vectors. We therefore propose using vectors $\bar{E}_r$ and $\bar{E}_i$ as a basis for constructing two new real vectors $\bar{a}$ and $\bar{b}$, which are perpendicular to and existing in the same plane as vectors $\bar{E}_r$ and $\bar{E}_i$. To express the optical field as components along the major and minor polarization axes, a linear transformation is written as follows:

$$\begin{cases} \bar{\mathbf{a}} = \bar{E}_r \cos\psi + \bar{E}_i \sin\psi \\ \bar{\mathbf{b}} = -\bar{E}_r \sin\psi + \bar{E}_i \cos\psi \end{cases} \tag{5.25}$$

where ψ, is shown in Fig. 5.2, is defined by:

$$\tan(2\psi) = \frac{2|\bar{E}_r||\bar{E}_i|}{|\bar{E}_r|^2 + |\bar{E}_i|^2} \cos\left(\widehat{\bar{E}_r, \bar{E}_i}\right) \tag{5.26}$$

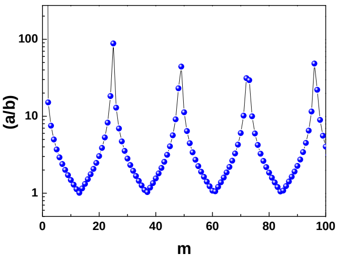

Figure 5.3. *Wave retardation for a pure Y_2SiO_5 crystal. The input polarization $\alpha = 45°$ relative to D_2 while the propagation direction is along the b-axis. The ellipticity $\frac{a}{b} = 1$ at m=12 shows the circular polarization.*

5.3 Simulation results

The main purpose of the simulation in this chapter is to determine the precision required in our setup to minimize the polarization rotation of the field while the wave is propagating through the medium. For this purpose, one needs to monitor the magnitude and the direction of vectors $\bar{\mathbf{a}}$ and $\bar{\mathbf{b}}$ inside the medium. To this end, the sample is divided into several slabs along the propagation direction (z) and then Eqs. 5.25 and 5.26 are employed to calculate vectors $\bar{a}(z)$ and $\bar{b}(z)$ and polarization angle $\psi(z)$. The length of each slab in our simulation is $m = \frac{606}{1.8}$ nm.

5.3.1 Understanding retardation in a Y_2SiO_5 crystal

Different refractive indices ($n_b = 1.7856$, $n_{D1} = 1.7886$, $n_{D2} = 1.8095$) along the principal axes in the Y_2SiO_5 crystal causes the crystal to be a birefringent [83]. The propagation phase, ϕ, can be written as $\phi = \omega\frac{L}{c}$ radians per meter, so that a wave of frequency ω will experience a phase shift of ϕ radians in traveling a distance L through the crystal. The difference between two phase shifts along D_1 and D_2 is termed the retardation $\Delta\phi = 2\pi\frac{\Delta n L}{\lambda}$. The final equation for retardation considering the crystal length $L = m\lambda$ will be:

$$\Delta\phi = 2\pi\Delta n.m \qquad m \in \mathbf{N} \tag{5.27}$$

Let's calculate the crystal length needed to obtain a quarter wave plate. Quarter wave plates are used to turn plane-polarized light into circularly polarized light and vice versa. To do this in our case, we must orient the input polarization at $\alpha = 45°$ relative to D_2. In the case of a pure Y_2SiO_5 crystal without any absorber and propagation direction along the b axis, the m is calculated to be about 12 based on Eq. 5.27 for $\Delta\phi = \frac{\pi}{2}$. This is about $4\,\mu m$ for a wavelength of about $\frac{606}{1.8}$ nm, which fits very well with the simulation results shown in Fig. 5.3

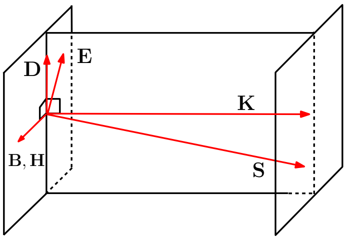

Figure 5.4. *The* **H**, **B** *are normal to the plane which contain the vectors* **D**, **E**, **S**, *and* **k**. $\mathbf{D} \perp \mathbf{k}$ *and* $\mathbf{E} \perp \mathbf{S}$.

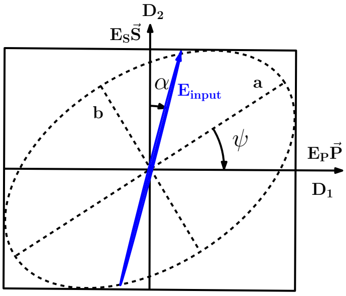

Figure 5.5. $\mathbf{E}_{input}$ *is a theoretically perfect linear input light polarization with an angle* α *relative to the* D_2 *axis.*

5.3.2 Polarization rotation in a $Pr^{3+} : Y_2SiO_5$ crystal

The characterization of an electromagnetic wave is based on understanding the wave-vector, **k**, the field vectors, **E**, **D**, **H**, **B**, and the complex Poynting vector, $\mathbf{S} = \frac{1}{2}\mathbf{E} \times \mathbf{H}$ (direction of power flow). These vectors should obey Eq. 5.1. Therefore, considering $\bigtriangledown = i\mathbf{k}$ we can show the **D** vector should be normal to **k** and **H**. In the same way the two parallel vectors **B** and **H** are perpendicular to **k** and **E**. In fact, the relation between **D** and **E** depends on the presence of the polarization in the medium, which is $\mathbf{D} = \varepsilon_0\mathbf{E} + \mathbf{P}$. Based on this criteria, the differences between Poynting vector **S** and wave-vector **k** are shown in Fig. 5.4. In other words, in a medium where polarization direction **P** is not normal to wave-vector **k**, the direction of the poynting vector and wave-vector will be different, as shown in Fig. 5.4. In our case the transition dipole moment direction of the absorption site is equivalent to polarization direction **P**. The transition dipole moment direction of Pr ions doped in Y_2SiO_5 is in the $(\widehat{D_1, D_2})$ plane, as shown in Fig. 5.1. Thereby, in the case of $Pr^{3+} : Y_2SiO_5$, the logical choice seems to be to keep the propagation direction along the b-axis.

In the simulations discussed below the permittivity tensor in Eq. 5.14 is employed with the input E-field polarization direction along D_2 ($\alpha = 0$ in Fig. 5.5) and the input wave propagation direction, k, is along the b axis according to Fig. 5.1. As we discussed earlier, the medium is divided into several slabs (m) along the propagation direction. In Fig. 5.6a, polarization angle ψ and ellipticity $\frac{a}{b}$ are shown for 100 slabs. The magnitude of $\bar{\mathbf{a}}$ and $\bar{\mathbf{b}}$ for 100 slabs is shown in Fig. 5.6b.

Case I

In the same way, as described above, it is possible to extend the propagation length to m = 3000 ($\approx$ 1 mm 0.05% $Pr^{3+} : Y_2SiO_5$ crystal), which is shown in Fig. 5.7. Fig. 5.7a shows the angle of the light polarization relative to the D_1 axis as a function of propagation length m. As seen in Fig. 5.7b, the polarization ellipticity varies between a minimum and maximum value while propagating through the medium. The variation of the major ($\bar{\mathbf{a}}$) and minor ($\bar{\mathbf{b}}$) axes of the polarization is shown in Fig. 5.7c,d. The main oscillation is related to the minor ($\bar{\mathbf{b}}$) axis of the polarization as shown in Figs. 5.6b and 5.7d.

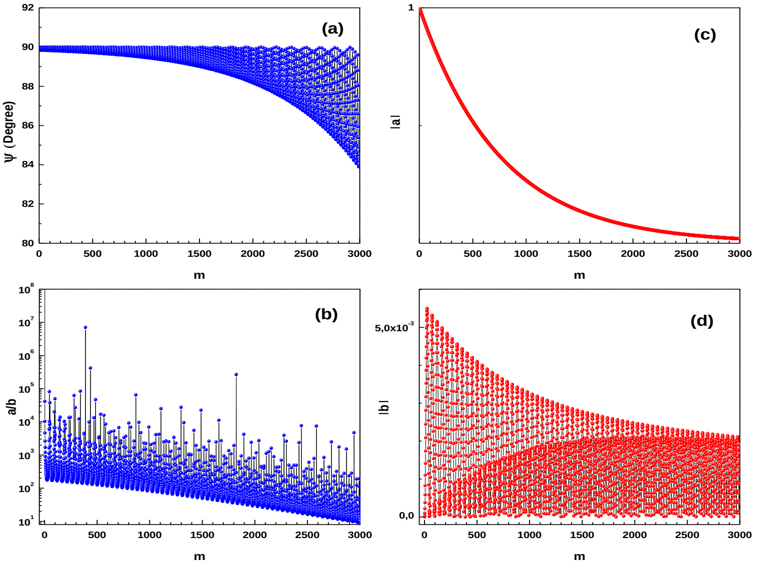

Figure 5.7. *Polarization properties versus m (number of slabs) for the initial polarization angle, $\alpha = 0$, and a 0.05% $Pr^{3+} : Y_2SiO_5$ crystal. (a) polarization direction defined by angle ψ. (b) polarization extinction in logarithmic scale, (c,d) magnitude of polarization along* **a**, *and* **b**, *respectively.*

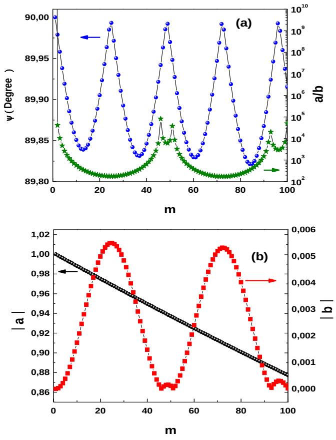

Figure 5.6. *Polarization properties versus m (number of slabs) for the initial polarization angle $\alpha = 0$ and a 0.05% $Pr^{3+} : Y_2SiO_5$ crystal. (a) polarization direction defined by the angle ψ. (b) polarization extinction in logarithmic scale. (c,d)magnitude of polarization along* **a**, *and* **b** *respectively.*

Case II

Let's go further and investigate an even longer crystal. A polarization direction ψ and ellipticity $\frac{a}{b}$ for the initial polarization angle $\alpha = 0$ and an extinction ratio higher than 10^6 is simulated for m = 20000 ($\approx$ 7 mm 0.05% $Pr^{3+} : Y_2SiO_5$ crystal) in Fig. 5.8. This simulation shows that, even when we start with a very pure linear polarization along D_2, there is a turning point for the polarization direction at m $\approx$ 4800. Further simulation shows that by mis-aligning input polarization angle α, the turning point will occur after a shorter propagation length. Therefore, because of the polarization rotation inside the crystal, ions in different slabs of the crystal will not experience the same Rabi frequency. In addition, if we take a long enough crystal ($> 4\,mm$) and set the input polarization along D_2, the output polarization should be almost along D_1 and this occur regardless of the input polarization. A preliminary experiment has confirmed this effect, but further investigations needs to be performed to ascertain that this indeed is the case.

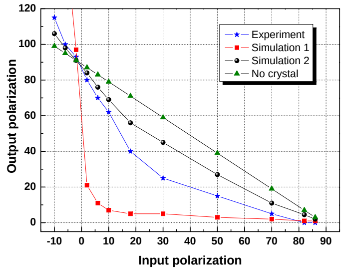

Figure 5.9. *Output polarization versus input polarization direction after a 1 mm long $Pr^{3+} : Y_2SiO_5$. An experiment (blue star), simulation1 (red square), results of polarization direction after 3000 slabs (≈ 1 mm $Pr^{3+} : Y_2SiO_5$) considering $\chi_{abs} = 8.2 \times 10^{-4}$, simulation2 (black circle), results of polarization direction after 3000 slabs (≈ 1 mm $Pr^{3+} : Y_2SiO_5$) considering $\chi_{abs} = 1 \times 10^{-4}$, compared to no crystal case (green triangle).*

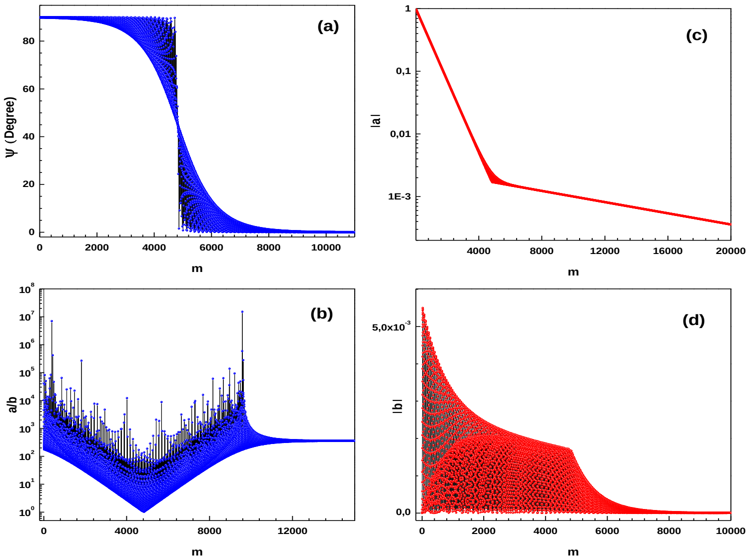

Figure 5.8. *Polarization properties versus m (number of slabs) for the initial polarization angle, $\alpha = 0$ (see Fig. 5.5) and a 0.05% $Pr^{3+} : Y_2SiO_5$ crystal. (a) polarization direction defined by angle ψ. (b) polarization extinction in logarithmic scale. (c,d) magnitude of polarization along* **a**, *and* **b**, *respectively. There is a turning point for polarization direction at m ≈ 4800*

Case III

To understand how precisely we need to align the input linear polarization, one could run the simulation with mis-aligned input polarization. The mis-aligned input polarization from the D_2 axis and inside the $(\widehat{D_1, D_2})$ plane is called α as shown in Fig. 5.5. After propagation of the light through a medium of about 3000 slabs we calculate the polarization angle (ψ). The output polarization versus input polarization is shown in Fig. 5.9. The green trace in Fig. 5.9 shows the case when we do not have any crystal while the blue shows the experimental measurement in a 1 mm long $0.05\% Pr^{3+} : Y_2SiO_5$ crystal. Two sets of simulations with different χ_{abs} are shown in Fig. 5.9. In the first simulation, which is shown by the red trace, $\chi_{abs} = 8.2 \times 10^{-4}$ according to Eq. 5.9. In the second simulation, which is shown by the black trace, $\chi_{abs} = 1 \times 10^{-4}$. The mismatch between the simulation and the experiment is originated from χ_{abs} coefficient in Eq. 5.9. Actually, by employing the present theoretical model it is possible to reverse the process and measure the absorption of the material by measuring the polarization angle after the crystal.

In conclusion, in this chapter, we developed a simulation program able to investigate the polarization direction ψ and ellipticity $\frac{a}{b}$ (see Fig. 5.5) while propagating through the crystal. This will open up a new opportunity to investigate more interesting physics regarding to the propagation effects in RE ions in the future.

CHAPTER 6

QUANTUM MEMORIES

Quantum information is a general term that describes the physical information contained in the state of a quantum system. The qubit, used as a unit of quantum information, is a two-level quantum system that can actually be a superposition of the two states at any given time. In the quantum world, the phase angles between the components of a system in a quantum superposition needs to be well defined, otherwise the quantum state will collapse. Keeping track of phase information is required to maintain "quantumness", and is what makes quantum systems different from systems in the classical world. Phase preservation is related to "coherence", which is at the heart of all the discussions in this thesis. The longer the coherence time, the longer the phase preservation, and consequently the quantum state will live longer. In the case of a single photon, the qubit can be represented in several different ways, using different physical quantities, such as the polarization of a single photon, the photon number [84], the photon path [12], or a separation in time (time-bin) [85] to encode information. But in all cases, the photon plays the role of a flying qubit. Therefore, the requirement of having a stationary qubit (like matter) and map on the encoded quantum state from flying qubit to stationary qubit is perceived. Such a quantum interface between light and matter, with an ability to map onto, store in, and later retrieve the quantum state of light from matter, is vital in quantum information processing [5]. A device capable of this can be called a quantum memory for light, and will be discussed in detail in this chapter.

6.1 Why is there a need for a quantum memory?

In the most proposed quantum computation schemes, decoherence destroys the information in a superposition of states, thus making long computations impossible. It is possible to reduce the effects of decoherence by storing information in a quantum memory, assuming that the decoherence process acts independently on each of the bits stored in the memory [10]. For example, the quantum memory is one of the most important components in quantum computing based on linear optics. In this scheme, when the probability of a successfully teleported gate or addition to a cluster state becomes small, photons that are part of the circuit must be stored for a considerable time while the off-line preparation of entangled photons is taking place [11].

Signal synchronization in optical quantum computation, is one of the applications of a quantum memory. Several parallel qubits, must be synchronized at each step in time, and a quantum memory acting as an identity quantum gate with a delay that leaves any state unchanged, could be useful in this way [12]. Another application of a quantum memory is the implementation of a deterministic single-photon source. In this application it may be possible to couple one of the entangled photons produced, for example, from parametric down conversion, to a quantum memory, and use the other as a heralded photon. Thus, the stored photon could be released on demand and act as a deterministic single photon source [14]. It should be noted that such schemes require efficient coherent exchange of the photon state to the stored state, and back, as well as long-lived storage. For a comparison, the reader is referred to a review by Eisaman et al. [86], which describes several other schemes which are competing in the implementation of a deterministic single photon source.

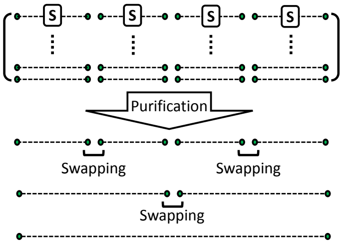

Figure 6.1. *The basic idea of quantum repeaters. 1) entanglement is generated via the source (S) shown by the dashed line. 2) Improved entangled states are generated by purification procedure. 3) Entanglement is distributed across the longer distance via swapping procedure.*

The quantum memory plays a vital role in long-distance quantum communication [87], although there are proposals for quantum communication without the necessity of quantum memories [9]. Extension of the quantum communication channel length (beyond 170 km [88]) is limited by optical losses. For instance, the probability of both absorption and depolarization of a photon (i.e., the qubit) in fiber optics increase exponentially with the length of the fiber. Therefore, the optical transmission probability will decrease exponentially with length. Actually, the number of transmitted photons will be reduced by absorption, while the fidelity of the transmitted photons will be reduced by depolarization or decoherence [6]. To overcome these difficulties, the concept of quantum repeaters can be used by combining quantum teleportation and quantum state storage [6, 7].

The basic idea is to divide the transmission channel into many segments as shown in Fig. 6.1. The length of each segment is of the order of the channel attenuation length. In the first step, entanglement is generated in each segment. Then, the entangled state is purified. Entanglement purification is a way of extracting a subset of states with higher entanglement from a large set of less entangled states. In the third step, the beams from two adjacent segments are overlapped on a beam splitter to swap their entanglement and extend the segment length [87]. To achieve almost perfect entanglement, further purification needs to be done after swapping again. The principle of entanglement purification using linear optics has been explained by Pan et al. [89]. Since entanglement purification is a probabilistic operation, employing a quantum memory in each arm of the entangled state will increase the transfer rate [6].

Furthermore, quantum memories for light are also employed for precision measurements based on mapping the quantum properties of an optical state to the atomic ensembles. This will reduce the level of quantum noise in the measured observable [15, 90].

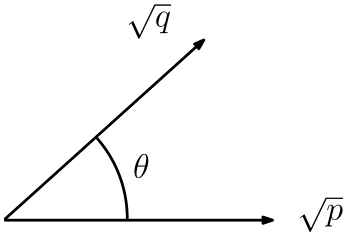

Figure 6.2. *The fidelity of two probability distributions* p *and* q *can be interpreted geometrically as the inner product of two normalized vectors* $\sqrt{p}$ *and* $\sqrt{p}$ *like* $F(p,q) = \sqrt{p}.\sqrt{q} = \cos\theta$

6.2 Different aspects of quantum memory

A quantum memory for light is an interface that should receive a photonic quantum state, characterized for instance, by an amplitude, phase, polarization, direction, and after a time, retrieve an ideally identical quantum state. To be able to distinguish a quantum memory from a classical memory, it is necessary to define concrete quantities by which it can be characterized. In this section, these definitions will be discussed, in addition to the figure of merit needed for different applications.

6.2.1 Fidelity

Several definitions have been proposed to obtain a quantitative answer to the question regarding the similarity of two information items in an information processing operation (classical or quantum). Among these definitions, we will discuss the *fidelity* which seems the most relevant to the work presented in this thesis. For other definitions, the reader is referred to Ref. [4]. Let us assume we have two probability distributions, $\{p_x\}$ and $\{q_x\}$, in the classical world. The fidelity of these two probability distributions is defined as:

$$F(p_x, q_x) = \sum_x \sqrt{p_x q_x} \tag{6.1}$$

This definition is very similar to the inner product of two normalized vectors $\sqrt{p}$ and $\sqrt{q}$ as shown in Fig. 6.2. When the probability distributions are identical, the fidelity will be unity, and in the case of two orthogonal probability distributions it will be zero. Therefore, in general we have the condition $0 \le F(p_x, q_x) \le 1$.

In the quantum world, the general definition of the fidelity for two quantum states ρ and σ will be [4]:

$$F(\rho, \sigma) = Tr\sqrt{\rho^{1/2}\sigma\rho^{1/2}} \tag{6.2}$$

Let us be more specific by discussing some examples. First, consider $[\rho, \sigma] = 0$, which means one could write the quantum states in an orthogonal basis $|i\rangle$ as follows:

$$\rho = \sum_i r_i |i\rangle\langle i| \, , \; \sigma = \sum_i s_i |i\rangle\langle i| \tag{6.3}$$

The fidelity will then be given by:

$$F(\rho, \sigma) = Tr\sqrt{\sum_i r_i s_i |i\rangle\langle i|} = \sum_i \sqrt{r_i s_i} = F(r_i, s_i) \tag{6.4}$$

Therefore, when $[\rho, \sigma] = 0$ the quantum fidelity $F(\rho, \sigma)$ will be very similar to the classical fidelity $F(r_i, s_i)$.

In the second example, let us assume that one of the states is pure, then it can be described by a single ket vector, $\rho = |\psi\rangle\langle\psi|$. In this case the fidelity will be:

$$F(\rho, \sigma) = Tr\sqrt{|\psi\rangle\langle\psi|\sigma|\psi\rangle\langle\psi|} = \sqrt{\langle\psi|\sigma|\psi\rangle} \tag{6.5}$$

In the third example, we consider two pure states $\rho = |\psi\rangle\langle\psi|$ and $\sigma = |\phi\rangle\langle\phi|$, in which case the fidelity will be $F(\rho, \sigma) = |\langle\psi|\phi\rangle|$. The fidelity is also limited to $0 \leq F(\rho, \sigma) \leq 1$ in the quantum world.

For comparison, we will now consider the fidelity between an input state, ρ, to the quantum memory and an output state, σ, from the quantum memory. The fidelity is simply defined as the overlap of the quantum state wave function of the recalled wave packet with that of the one originally sent in for storage. In the case of optimum fidelity, the wave functions of the input and output photons are identical. An alternative definition is conditional fidelity, i.e. the overlap is conditional on that the photon was emitted by the memory [91].

In quantum information processing, for instance, we could evaluate the preservation of the information in the memory interface by measuring the fidelity between the input and output states. However, in order to ensure that the interface is working in the quantum regime, it is necessary to define a border between the classical and quantum regimes, i.e., the highest classical fidelity possible. A large number of studies have been carried out to define this border for different input states and different measurement methods. For instance, for a coherent state in the case of continuous variable measurements (i.e. homodyne measurements), the critical fidelity has been shown to be $F_{class} = 1/2$ [92]. The boundary fidelity by performing a discrete variable measurement (i.e. a photon counting measurement) on a coherent state, lead to $F_{class} = 2/3$ [93].

6.2.2 Efficiency

The overall memory efficiency is simply defined as the energy of the pulse recalled from the memory divided by the energy of the pulse sent in for storage in the memory. At the quantum level (weak coherent pulses), storage efficiency basically corresponds to the probability that the stored information is retrieved. To be able to discuss the efficiency in detail, the overall efficiency is divided to several parts as follows:

$$\eta_{overall} = P_{abs} P_{emi} P_{dep} P_{re-abs} P_{loss} \tag{6.6}$$

where $P_{abs} = 1 - e^{-\alpha L}$ is the probability of the absorption of the photon by the quantum memory, and αL is the optical depth of the sample. P_{emi} is the opposite operation, and gives the probability of photon emission by the memory.

There are several practical obstacles for realizing the quantum memory for light as a basic quantum gate. Quantum memories must be isolated from the environment as much as possible so that the stored qubits are not destroyed by environmental influences. On the other hand, quantum memories have to be able to exchange information with the environment by writing qubits into the memory and reading them out again. Thus, finding the optimum will restrict practical implementation to a limited number of physical systems, which are discussed in this section. In reality, during and between the absorption and re-emission procedures there is a possibility of decoherence due to the interaction of the quantum memory with the environment. P_{dep} represents a general dephasing process which could arise from either an individual atom or an atomic ensemble. We can write $P_{dep} = e^{-\gamma t}$, where γ is a general dephasing rate coefficient. P_{dep} is the probability that must be considered in order to extend the storage time of a quantum memory. In three-level atoms, which are called Λ systems (see Fig. 6.3), this is achievable via storage in a shelving state, which has a longer coherence time (T_2). For certain systems, a longer storage time can be achieved by applying external compensation during storage, as will be discussed in Section 6.2.3.

In an ensemble approach when we have a thick sample, the emitted photon from the early slices in the sample could be absorbed by the rest of the sample. This is represented by P_{re-abs} in Eq. 6.6. Therefore, there is a trade off between the optical depth needed for maximizing the absorption and minimizing the re-absorption. This will limit the overall quantum memory efficiency to 54% [94, 95]. Two ways of circumventing this problem have been suggested. One is to force the output state to be emitted from the opposite direction [96, 97], called the backward direction scheme. The other is the forward direction scheme, performed by spectrally removing the atoms in the rest of the sample by applying an electric or magnetic field [98]. This will be discussed in more detail in Section 6.3.5. P_{loss} is related to the absorbers that do no participate in the memory procedure, e.g. the background absorption by the sample.

It should be noted that high overall efficiency is not always necessary, and that efficiency is very application dependent. In some applications such as unknown state teleportation, a memory with unconditional high fidelity is required. In other words, the product of fidelity and efficiency must be higher than the classical limit [91]. The efficiency requirements for the quantum repeater application are discussed in Ref. [99].

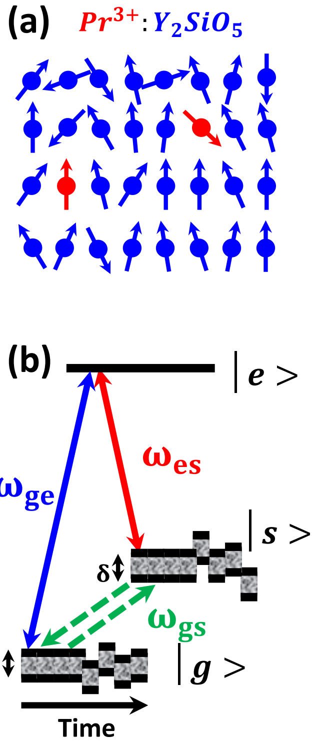

Figure 6.3. *An example of decoherence sources for protocols based on a* Λ *system in a RE doped crystals. (a) Nuclear spin fluctuation of the surrounding ions (*Y_2SiO_5*) which is changing with time. (b) Due to the fluctuation in nuclear spin two effects occur. First, hyperfine inhomogeneous broadening* δ *and second, fluctuation of the energy separation* $|g\rangle \mapsto |s\rangle$*.*

6.2.3 Storage time

Based on the application, there will also be requirements on storage time and on-demand retrieval of the stored input field [18, 19, 100–103]. In some applications, for instance, in long-distance quantum communication, when one of the entangled states is distributed across the distance L, the second state must be stored in a memory with a storage time longer than $\frac{L}{c}$ where c is the speed of light in the transmission channel [99]. In addition, we should be able to "push a button" to retrieve the stored state, which means the scheme must be "on-demand". In other applications, a long storage time is not necessary, e.g. signal synchronization in optical quantum processing [12, 13], the implementation of a deterministic single-photon source [14], and precision measurements based on mapping of the quantum properties of an optical state onto an atomic ensemble [15].

As discussed above (Eq. 6.6), the overall efficiency is exponentially related to the dephasing rate. This means, that isolating the memory from the environment (statically or dynamically) is key in ensuring a high overall efficiency for long times. For example, in the protocols based on the Λ system at cryogenic temperatures, the coherence time of the shelving state (T_2^{hyp}) is usually longer than the optical one (T_2^{opt}). In RE ions, excited state coherence times (T_2^{opt}) range from tens of μs to 6 ms [40] and hyperfine coherence times as long as 30 s [104] have been demonstrated. Therefore, transferring the information from the optical excited state to the shelving state will extend the storage time. This could be a first step towards extending the memory storage time. The next step may be to investigate the possibility of increasing the coherence time of the shelving state (T_2^{hyp}).

To improve T_2^{hyp}, it is necessary to find the source of decoherence and try to suppress it. The hyperfine structure is, in principle, explained by the presence of nuclear magnetic and electric moments interacting with the electronic shell. Therefore, small fluctuation in the surrounding nuclear spin, will cause hyperfine level broadening. The surrounding nuclear spin fluctuation of $Pr^{3+}:Y_2SiO_5$ is shown schematically in Fig. 6.3a. This broadening is illustrated schematically in Fig. 6.3 by δ. Typically, the hyperfine inhomogeneous broadening of RE ions is on the order of tens of kHz, e.g. 30-80 kHz for $Pr^{3+} : Y_2SiO_5$ [105], 20-30 kHz for $Eu : YAlO_3$ [106], and about 70 kHz for $^{153}Eu^{3+} : Y_2SiO_5$ [107].

Two sources of disturbance are included in Fig. 6.3b. The first is the inhomogeneous broadening of the states $|g\rangle$ and $|s\rangle$, which is shown by δ in Fig. 6.3b. The second is the fluctuation of the frequency separation between the states $|g\rangle$ and $|s\rangle$ in time (see Fig. 6.3b). These are two important dephasing mechanisms that must be suppressed to achieve long T_2^{hyp}. Let us first discuss the hyperfine inhomogeneous broadening. Any quantum state mapped on the ions experiencing the inhomogeneous broadening will start dephasing at a rate that is inversely proportional to the broadening δ. This can be externally rephased, for instance, via a pair of radio-frequency (RF) π pulses which is on-resonance with ω_{gs}, shown by dashed vectors in Fig. 6.3b. These RF pulses should be able to transfer the whole storage pulse bandwidth between two shelving states. In the phase diagram in Fig. 6.4, the time sequence of the procedure is shown as a type of refocusing scheme.

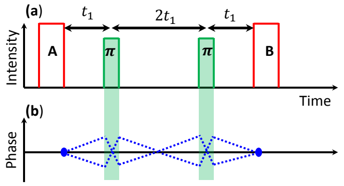

Figure 6.4. *Applying a pair of radio-frequency (RF) pulses between two optical transfer pulses (A,B) to compensate for dephasing due to hyperfine inhomogeneous broadening.*

In the next step, a general and promising method of improving the coherence properties of any quantum state, known as the dynamical decoupling (DD) method, can be employed [108]. This method, initially developed for NMR spectroscopy, can be applied to selectively counteract random perturbations induced by some of the spin Hamiltonian terms [52]. However, it was later proposed that the coherence property could be improved by reducing the dephasing rate for an open system [108]. This method is based on applying a periodic series of inversion pulses to the quantum state stored in the matter. To obtain efficient DD pulses, the rate of the DD pulses ($\frac{1}{t_1}$) should be higher than the dephasing rate ($\frac{1}{t_2}$) of the quantum state as shown in Fig. 6.5.

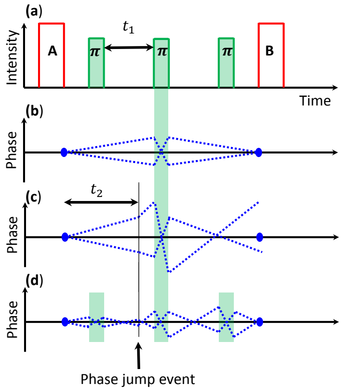

Figure 6.5. *The principle of dynamical decoupling (DD) pulses principles. For further discussion see text.*

Let us consider the phase diagram for one of the shelving states as shown in Fig. 6.5. To be more specific, pulses a and b are the pulses that can be used to transfer the quantum state from, for instance, optical state $|e\rangle$ to the shelving state $|s\rangle$, and vice versa, in Fig. 6.3b. To improve, T_2^{hyp} one could apply a series of π pulses with a bandwidth at least as large as δ, which is the inhomogeneous broadening of the state $|s\rangle$. As an example, three π pulses are shown between transfer pulses A and B in Fig. 6.5a. The continuous phase diagram of the shelving state $|s\rangle$ without any phase jump, and the method of correction with a single π pulse are shown in Fig. 6.5b. In Fig. 6.5c, a single π pulse is applied in the presence of the phase jump that arises from environmental noise. Finally, phase correction using three DD pulses in the presence of a single phase jump is shown in Fig. 6.5d. The number of DD pulses can be increased to hundreds or thousands to maintain a very narrow phase variation about the central phase. For more details and a review, the reader is referred to Refs. [108–110].

The hyperfine levels in the presence of the nuclear spin $(I > 1)$

will be degenerated (doubly) and they can be split by applying an external static magnetic field through the Zeeman shift, as illustrated in Fig. 6.6. A relevant practical problem is to find the direction and magnitude of the static magnetic field required to achieve the best isolation from environmental noise. Because of the anti-crossing effect of the split hyperfine states at a particular magnetic field, [27], we can find an energy separation ($\hbar\omega$) that is less sensitive to the variation in the magnetic field. As shown in Fig. 6.6, the first-order estimate is obtained when the transition frequency between the two states is insensitive to the fluctuation in the magnetic field ($\frac{\partial\omega}{\partial B} = 0$). This particular magnetic field gives a zero first order Zeeman shift (ZEFOZ) [18, 19], which can improve T_2^{hyp} by about $4-5$ orders of magnitude. The ZEFOZ approach was used in this work to extend T_2^{hyp} in $Pr^{3+} : La_2(WO_4)_3$ (Paper **III**).

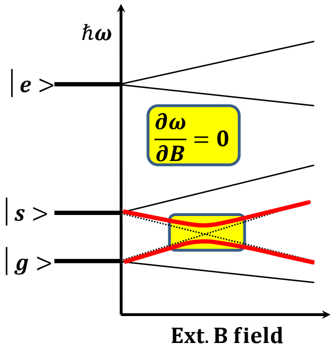

Figure 6.6. *Property of a ZEFOZ point. Insensitivity of the energy separation* $|g\rangle \mapsto |s\rangle$ *to the surrounding nuclear spin fluctuation by applying a particular external* $\mathbf{B} = (B_x, B_y, B_z)$ *to the sample.*

DD pulses can be used to improve the coherence of an open quantum system with an unknown disturbance. The ZEFOZ technique is being used in an attempt to isolate the quantum system from the surrounding environment by applying static compensation. The ideal solution would be a combination of these two techniques to improve the coherence, as demonstrated in Refs. [18, 19, 104, 111].

6.2.4 Bandwidth and mode capacity

The memory bandwidth is the maximum spectral width of the memory that can store an input quantum state efficiently. In other words, the memory bandwidth will define how short the pulses are that can be stored. In addition, for most applications, the storage time of the memory must be several times longer than the storage pulse duration. A more stringent figure of merit is thus the time-bandwidth product (TBP) of the memory defined as the product of the memory storage time and the storage pulse bandwidth.

We will now introduce another concept, called the memory mode capacity, which is used in some of the literature to indicate the performance of memories. The memory mode capacity, as a consequence of the high TBP, indicates how many independent pulses (modes) can be stored efficiently in the memory. These pulses may be independent in time, frequency, or even the spatial domain. Multimode storage is crucial in probabilistic applications to boost the occurrence rate of events [20, 21, 112]. Among the ensemble approaches for quantum memories, it has been shown that the atomic frequency comb (AFC) is the best technique for multimode applications, since it is not limited by the optical depth, αL [113, 114]. Multimode memories in atomic ensembles are discussed in detail by Nunn et al. by comparing the multimode properties of different quantum memory protocols [114].

6.2.5 Wavelength

The operational wavelength of a quantum memory could be a crucial figure of merit in some applications, but it is normally not the first priority for optimization. This could be an issue, for instance, in fiber optics based, long-distance quantum communication since the losses in the fiber are much lower in the telecommunication wavelength [115, 116]. The demonstration of a deterministic single photon source by combining the quantum memory and a heralded single photon source is another application. It is necessary to choose a suitable quantum memory operation wavelength Based on the specific application for the single photon source. An extensive and practically useful review of different single photon sources, including the quantum memory approach, is discussed by Eisaman et al. [86].

6.2.6 Linearity

To demonstrate a memory for optical quantum state storage, it is necessary to test it with low photon numbers to ensure that it operating in the quantum regime. The simplest quantum state may be the attenuation of coherent light to the single photon level. In practice, testing and optimizing quantum memories in the quantum regime will be more difficult. Therefore, one could show theoretically or experimentally that the protocol is linear with light amplitude. It may then be possible to optimize the quantum memory parameters with classical light, making the extension of the results to the quantum regime straightforward. This is the case for the experiments preformed within the scope of this thesis. In all quantum memory demonstrations presented in this thesis, the AFC protocol was employed, which is discussed below in Section 6.3.5. The results presented in Paper **II** support the linearity of the AFC technique, which was used in the rest of the experiments. In the study described in Paper **II**, the storage pulse is attenuated to the single photon level, or to a coherent pulse with an average of 0.1 photons/pulse. The 25% storage and retrieval efficiency obtained (Paper **II**) is almost comparable with the classical pulse described in Paper **I**. It should be borne in mind that a classical pulse still means a regime where the average photon number is much less than the number of absorbers involved.

6.3 Different implementations for quantum memories

The interaction between an atom and a photon at the quantum level is the central issue in demonstrating a quantum memory for light. High storage and retrieval efficiency are the main targets of quantum memories, and requires strong coupling between light and matter [5]. There are several ways of enhancing the coupling between light and matter, which will be described in this section.

An early approach related to quantum information in the study of atom-light interactions was within the framework of cavity quantum electrodynamics (CQED). In the CQED approach, light can be efficiently coupled via a high finesse cavity to a few atoms, or even to a single atom [117]. Another approach, which is practically less complex than CQED, is based on an optically thick, free-space atomic ensemble [5]. A third option involves an ensemble in a low-finesse cavity, and has been found to be very efficient for quantum memories.

The main principles of each approach are presented below. A more detailed description of the scheme employed in the experiments described in this thesis is also given.

6.3.1 The high-finesse cavity and single atom approach

Cavity quantum electrodynamics is based on the study of the interaction between light confined in a high-finesse cavity and atoms, where the quantum nature of light (photons) is significant. This set-up provides the opportunity to enhance the quantum properties of light. CQED could, in principle, be used to construct a quantum memory. Based on the dipole moment approximation ($\hat{H} = \hat{d}.\hat{E}$), it is possible to obtain a strong interaction in the single-atom single-photon experiment by placing a high-quality-factor (Q) cavity around the photon, or by using an atom with a large atomic dipole moment ($\hat{d}$). For example, Rydberg atoms [118] can exhibit very large electric dipole moments due to their large size.

An atom in an optical cavity is a good example of a two-level system coupled to a quantized field. The interaction Hamiltonian of this system, based on the dipole moment approximation and the rotating wave approximation (RWA), is formulated in the Jaynes-Cummings model as follows [59]:

$$\hat{H} = (1/2)\hbar\omega_0\hat{\sigma}_3 + \hbar\omega\hat{a}^\dagger\hat{a} + \hbar\lambda(\hat{\sigma}_+\hat{a} + \hat{\sigma}_-\hat{a}^\dagger) \tag{6.7}$$

where $\hat{a}$ and $\hat{a^\dagger}$ are the annihilation and creation operators, and $\hat{\sigma}_+ = |e\rangle\langle g|$, $\hat{\sigma}_- = |g\rangle\langle e|$, and $\hat{\sigma}_3 = |e\rangle\langle e| - |g\rangle\langle g|$ are the so-called atomic transition operators, which obey Pauli spin algebra, and λ is the coupling amplitude [59]. The first term in Eq. 6.7 is related to the atoms, whereas the second term represents the quantized field, and the third term describes the interaction between light and matter.

One of the first attempts towards the quantum memory construction was to made using optical delay lines, such as optical fibers. This approach has been used for photon synchronization

[119]. The storage time of an optical delay is limited by the losses in the fiber, and it is determined by the delay length, which can be a practical limitation. Alternatively, light can be injected into a high-Q cavity and later recalled through an electro-optical switch [120]. The same coupling can be made from a stored photon in a high-Q cavity to a single atom passing through a cavity [121]. making use of the tunability of the Q factor in high-Q photonic crystal cavities is another alternative for this type of quantum memories [122], although this is outside the scope of the present thesis. For more information on this, the reader is referred to the review paper by Raimond et al. [117]. Other work related to quantum memories is presented in Refs. [121, 123–125].

6.3.2 The ensemble approach

A large collection of atoms, an atomic ensemble, can be efficiently coupled to quantum states of light when a collective superposition state of many atoms is utilized for coupling. The atomic ensemble approach, in contrast to the cavity-enhanced interaction of light with single atoms, is motivated by the fact that collective effects, related to the large number of atoms in the ensemble, make it much easier to achieve a strong and controllable coupling between the atoms and the photons.

A quantum state of light, expressed as a general term, $|\psi_L\rangle$, can be mapped onto a quantum state of atoms, $|0_A\rangle$, in the Schrödinger representation $\hat{U}|\psi_L 0_A\rangle \mapsto |0_L \psi_A\rangle$. Equivalently, the operator transformation $\hat{U}^\dagger \hat{a}_A \hat{U} = a_L$ can be in the Heisenberg representation. In the case of an ensemble, $|0_A\rangle$ and $|\psi_A\rangle$ can be written as follows:

$$|0_A\rangle = |0_1 \dots 0_N\rangle \tag{6.8}$$

$$|\psi_A\rangle = \frac{1}{\sqrt{N}} \sum_j |0_1 \dots e_j \dots 0_N\rangle \tag{6.9}$$

where N is the number of the atoms in the ensemble, and equivalently, in the Heisenberg representation:

$$a_A^\dagger |0_1 \dots 0_N\rangle = \frac{1}{\sqrt{N}} \sum_j |0_1 \dots e_j \dots 0_N\rangle \tag{6.10}$$

Since most of the work described in this thesis is based on an ensemble of atoms, ensemble-based light-matter interactions will be discussed in more detail below.

6.3.3 Off-resonant storage

A wave packet can be defined by its amplitude and phase. When the frequency of the wave packet is detuned from the resonance of a two-level atomic transition by an amount greater than the atomic line-width, the phase of the wave packet will be mapped onto the atoms without photon absorption. In this way, the photonic quantum state is not collapsed, but part of the photonic quantum state information is mapped onto the atom. The phase of the quantum state of the atoms could be transferred to the photon afterwards. This provides a non-destructive photon-atom interaction that is suitable for quantum memory applications. This is very similar to the quantum non-demolition (QND) measurement technique.

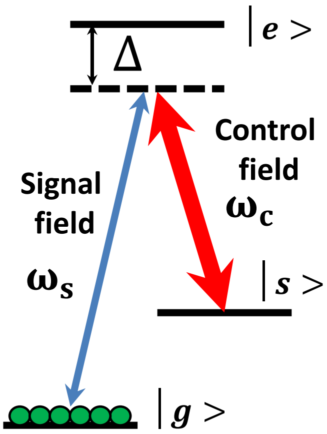

Figure 6.7. *Typical Λ system.*

In quantum mechanics, performing measurements on a system to obtain information will disturb the quantum state of the system, unless the system is in an eigenstate. A QND measurement minimizes this disturbance by using a particular system-detector interaction that preserves the eigenstates of a suitable operator of the quantum system. This actually leads to an ideal projective measurement. Let us assume we have a system in state $|\psi\rangle$, and measurement apparatus $|M\rangle$, and the dynamics of this state measurement can be given in terms of the Hamiltonian:

$$H = H_{self} + H_{int} \tag{6.11}$$

where H_{self} describes the Hamiltonian of the system and H_{int} denotes the interaction between the measurement apparatus and the system. This measurement is a QND measurement if $[H_{self}, H_{int}] = 0$.

One of the first demonstration of a quantum memory for light that beats a classical benchmark is done based on the off-resonance Faraday interaction in a cesium vapor in a paraffin-coated glass cell, by Julsgaard et al. [126].

6.3.4 The Raman and EIT approach

The Raman quantum memory protocol [127] and the electromagnetic induced transparency (EIT) do not compete, but actually complement one another. Each protocol has certain advantages in its area of applicability. In the EIT scheme, it is preferable to ensure that the storage pulses have a sharp frequency and are close to the resonance frequency to give a longer storage time. In the Raman scheme, the pulse spectrum should be concentrated close to, but outside, the absorption peak. Thus, the Raman protocol can be designed for larger bandwidth memory [128].

These types of schemes rely on a three-level system, for instance a Λ system, as shown in Fig. 6.7, with some specific restrictions. The $|g\rangle \mapsto |e\rangle$ and $|s\rangle \mapsto |e\rangle$ transitions must be "dipole allowed", while $|g\rangle \mapsto |s\rangle$ is not allowed. The state $|e\rangle$ is simultaneously connected to states $|g\rangle$ and $|s\rangle$ by the two optical fields ω_s and ω_c, respectively. The dephasing rates of the individual states are important, particularly the dephasing of state $|s\rangle$, which in the ideal case should be a metastable state.

The main objective of the electromagnetic induced transparency (EIT) approach, as the name implies, is to eliminate the effect of absorption in a medium during light propagation. In other words, although the photon transition frequency is exactly on resonance with an atomic transition, excitation will not occur. In atomic physics, a non-absorbing system of this type is referred to as a dark state. This can occur in a Λ system, as illustrated in Fig. 6.7. According to the classical explanation, electrons inside the medium are responsible for light propagation resulting from changes in the dielectric constant. If it were possible to stop the movement of the electrons at the frequency of the incident light, the effect of the medium would be eliminated. when the phase of the two sinusoidal waves ω_c and ω_p in Fig. 6.7 is properly adjusted this condition can be satisfied.

It is possible to interpret the EIT phenomenon, based on quantum mechanics, by means of destructive quantum interference between two fields with frequencies ω_c and ω_s (see Fig. 6.7). The form of the Hamiltonian for a Λ system will be $H = H_0 + H_{int}$, where H_0 is the bare atom Hamiltonian and H_{int} is the Hamiltonian taking the interaction with the fields into consideration. Following the dipole approximation, the atom-light interaction can be written $H_{int} = \boldsymbol{\mu}.\mathbf{E}$, where $\boldsymbol{\mu}$ is the transition dipole moment between two atomic states, and $\mathbf{E}$ is the amplitude of the electric field. In other words, this is equivalent to the definition of the Rabi frequency, $\Omega = \boldsymbol{\mu}.\mathbf{E}/\hbar$. H_{int} of the Λ system illustrated in Fig. 6.7, which is interacting with two laser fields in the rotating frame:

$$H_{int} = -\frac{\hbar}{2}\begin{pmatrix} 0 & 0 & \Omega_s \\ 0 & 0 & \Omega_c \\ \Omega_s & \Omega_c & -2\Delta \end{pmatrix} \tag{6.12}$$

where Ω_s and Ω_c are real Rabi frequencies related to the signal and control field, respectively, and $\Delta = \omega_{31} - \omega_s = \omega_{32} - \omega_c$ is the detuning of the excited state $|e\rangle$ from the Λ transition. One of the eigenstates of H_{int} can be written in terms of the bare atomic state:

$$|\psi\rangle = \cos\theta|g\rangle - \sin\theta|s\rangle \tag{6.13}$$

where $\sin\theta = \frac{\Omega_s}{\sqrt{\Omega_s^2+\Omega_c^2}}$ and $\cos\theta = \frac{\Omega_c}{\sqrt{\Omega_s^2+\Omega_c^2}}$.

The expectation value related to the eigenstate $|\psi\rangle$ and the state $|e\rangle$ through the interaction Hamiltonian H_{int} will be:

$$\langle e|H_{int}|\psi\rangle = \Omega_s\cos\theta - \Omega_c\sin\theta \tag{6.14}$$

The eigenstate $|\psi\rangle$ has no contribution from $|e\rangle$ and is called a dark state.

After entering the sample, the signal field photons will start to establish coherence between the states $|g\rangle$ and $|e\rangle$. The wave of flipped atomic spin state and the optical wave are now strongly coupled, and propagate through the medium. This combination of photons and spins can be described as a quasi-particle called a dark-state polariton [129]. After a certain time, which can be calculated using the photonic and atomic properties, the dark-state polariton will be transformed into a photonic state. The velocity of the light pulse that undergoes transformation to a polariton, and vice versa, is smaller than the speed of a light pulse in vacuum, and is proportional to the group velocity of the pulse. Actually, the dark-state polariton concept is an ideal scenario for storing a quantum state that is represented by the signal field, while a classical field is employed as the control field to manipulate the atomic ensemble.

The quantum state in terms of a signal field entering the atomic ensemble will be spatially compressed and, in the ideal case, fully transferred to the dark-state polariton. At this point in time, the classical control field can be turned off to freeze the quantum state as a spin-wave atomic ground state coherence between $|g\rangle$ and $|s\rangle$. The reverse process is possible by turning on the control field, i.e. the transfer of the spin-wave atomic ground state coherence to the dark-state polariton, and finally to the photonic state. For a more detailed review of EIT theory, see e.g. Refs. [5, 130–132].

6.3.5 The photon echo approach

The coherent rephasing first observed between spin levels and was called “spin echo” [52]. It was later demonstrated in the optical domain and was then called a “photon echo” [47]. However, in 2001 a highly efficient quantum memory scheme based on photon echo was proposed [96]. Generally, the photon echo approach is based on mapping an optical pulse on to a collective atomic excitation. As shown in Fig. 6.7, a weak optical pulse can be absorbed by an atomic ensemble in the ground state $|\psi_g\rangle = |g_1 \ldots g_N\rangle$ at time $t = 0$, after which the collective atomic excitation will be:

$$|\psi_e\rangle = \sum_j c_j e^{-i\delta_j t} e^{ikz_j} |g_1 \ldots e_j \ldots g_N\rangle \tag{6.15}$$

where N is the number of atoms in the ensemble and k is the wave vector of the optical field. In addition, δ_j and z_j are the detuning and the position of the j^{th} atom, and c_j is the probability amplitude. In all photon echo based approaches, the idea is to rephase the collective atomic coherence and enhance the constructive interference between all constituents of the atomic ensemble at some later time, $t = t_e$. Here, different proposals based on photon echo for quantum memory application will be discussed in detail.

CRIB

The way suggested to achieve the rephasing of the collective atomic coherence, in the controlled reversible inhomogeneous broadening (CRIB) protocol [96, 97], is based on the reversing the detuning of each atom at a given time τ after absorption. The collective atomic state after reversing the atomic detuning will change from Eq. 6.15 to:

$$|\psi_e\rangle = \sum_j c_j e^{-i\delta_j t} e^{i\delta_j \tau} e^{ikz_j} |g_1 \dots e_j \dots g_N\rangle \tag{6.16}$$

All the atoms will then have the same phase, and collective emission will take place at time $t = \tau$, after reversing the atomic detuning, or $t_e = 2\tau$, after sending in the storage pulse. In addition, the direction of propagation of the collective atomic coherence can be reversed from forward-traveling to a backward-propagating emission by reversing the spatial phase shift from e^{ikz_j} to e^{-ikz_j} (see Section 3.5).

The steps suggested and demonstrated in solid-state materials in Refs. [97, 133, 134] based on the CRIB approach are presented below.

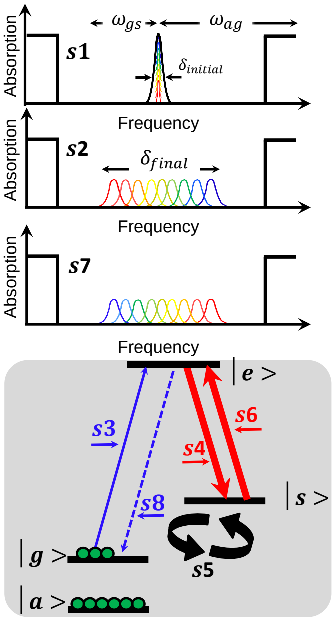

Figure 6.8. *Steps required for quantum memory demonstration based on the original CRIB protocol. The spatial direction of the optical beams* (**k**) *is shown by small arrows in the* Λ *system diagram. s3 and s4 are in the forward direction while s6 and s8 are in the backward direction. For further details see text.*

1. Consider an absorption line of an inhomogeneously broadened ensemble of atoms and then prepare a transmission window with the possibility to remove the atoms from states $|g\rangle$ and $|s\rangle$ by optical pumping, as shown in Fig. 6.8. Then prepare a narrow absorption peak with full width at half-maximum (FWHM) $\delta_{initial}$ in state $|g\rangle$ (s1 in Fig. 6.8).

2. Apply an external DC electric field that varies along the direction of propagation through the sample with the aim of broadening the line to a width, δ_{final}, (s2 in Fig. 6.8).

3. The medium is now ready to accept a weak storage pulse with resonance frequency ω_{ge}, with a bandwidth smaller than δ_{final} and greater than $\delta_{initial}$. Such a pulse, which is shown as s3 in Fig. 6.8, is sent in at time $t = 0$, and collective atomic coherence is created between states $|g\rangle$ and $|e\rangle$. At time $t = T_e$ the external DC electric field is turned off.

4. Apply a bright classical π pulse, shown as s4 in Fig. 6.8, at the resonance frequency ω_{es}, with the same direction (forward direction) as the storage pulse ($k\mathbf{z}$). At this step an atomic coherence between states $|s\rangle$ and $|g\rangle$ is created.

5. Apply a pair of π pulses, which is shown as s5 in Fig. 6.8, at resonance frequency ω_{sg} which is in the radio frequency (RF) region. These pulses will compensate for related to

the hyperfine inhomogeneous broadening discussed in Section 6.2.3. The ZEFOZ technique and DD pulses, as also discussed in Section 6.2.3, can be employed to improve T_2^{hyp} significantly.

6. Apply a bright classical π pulse, shown as s6 in Fig. 6.8, at the resonance frequency ω_{es}, with the opposite direction to the storage pulse ($-k\mathbf{z}$) i.e. the backwards direction. This causes the atomic coherence to be mapped back to the states $|g\rangle$ and $|e\rangle$.

7. Turn on the same external DC electric field with the opposite polarity, as shown by s7 in Fig. 6.8.

8. The recall pulse, shown as s8 in Fig. 6.8, will be emitted at time T_e in the backward direction after turning on the external DC electric field.

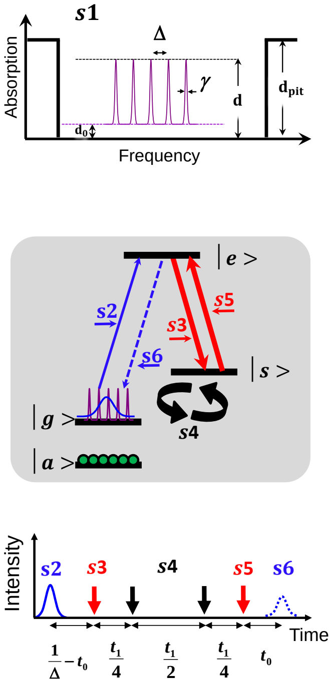

Figure 6.9. *Steps required for quantum memory demonstration based on an on-demand AFC protocol. The spatial direction of the optical beams ($\mathbf{k}$) is shown by small arrows in the Λ system diagram. s3 and s4 are in the forward direction while s6 and s8 are in the backward direction. For further details see text.*

AFC

As discussed above, the key point in photon-echo-based quantum memories is to employ a suitable technique for rephasing the collective atomic coherence. The AFC technique, which is proposed by Afzelius et al. [113], employs a separately prepared periodic comb-like absorption structure with peak separation Δ to rephase the atomic dipole after a defined time $t = 1/\Delta$. This periodic structure offers some advantages compared to line broadening by a linear DC Stark shift in the CRIB approach, as will be discussed below.

An AFC structure consists of a series of (artificially created) absorbing peaks with equidistant frequency spacing Δ and peak width γ (see Fig. 6.9). An input (storage) field (at time $t = 0$) which spectrally overlaps the AFC structure will be absorbed, leaving the absorbers in a superposition state [113]. If the coherence time is long compared to $1/\Delta$, collective emission will occur at time $t_{echo} = 1/\Delta$ due to constructive interference (similar as for the modes in a mode-locked laser). On-demand retrieval of the stored input field is possible by transferring the ground-excited state superposition to a spin-level superposition, as demonstrated in Ref. [100].

The steps required to demonstrate a quantum memory based on the AFC approach, where the emitted field propagates in the backward direction, are given below.

1. Consider an absorption line of an inhomogeneously broadened ensemble of atoms and then prepare a transmission window by removing the atoms from states $|g\rangle$ and $|s\rangle$ employing optical pumping, as shown in Fig. 6.9. Then prepare

a set of N narrow absorption peaks with FWHM of γ separated by Δ in state $|g\rangle$ (s1 in Fig. 6.9). The peaks may have different line shapes and, interestingly, comparisons between square, Gaussian and Lorentzian AFC peaks show significantly higher storage and retrieval efficiency for square-like AFC peaks [135].

2. Send a quantum state storage pulse with resonance frequency ω_{ge} and bandwidth smaller than $(N-1)\Delta$ and greater than Δ in to the material at time $t = 0$. A typical Gaussian storage pulse is shown as the solid blue line in Fig. 6.9(s2). The shape of the storage pulse can be optimized to give the best absorption. The objective is to transfer all the energy from the quantum state storage pulse to the distribution of ions, $|g_1 \dots g_N\rangle$, in the spectral grating with defined finesse ($F = \Delta/\gamma$). After the light-matter interaction, the initial state of the N atoms will develop into the state [113]:

$$|\alpha\rangle_A = |g_1 \dots g_N\rangle + \sum_{j=1}^{N} c_j e^{i(\delta_j t - kz_j)} |g_1 \dots e_j \dots g_N\rangle \quad (6.17)$$

where z_j is the spatial position of the j^{th} atom, k is the wave number of the storage pulse and c_j is the amplitude. The AFC is a well-separated periodic structure with frequency detuning, $\delta_j = 2\pi m_j \Delta (m_j$ is an integer). The periodicity, Δ, of the AFC structure will give rise to constructive emission exactly after a time $t = 1/\Delta$ (Eq. 6.17). Waiting longer than $t = 1/\Delta$ will lead to echo detection in the forward direction. However, to achieve an on-demand quantum memory it is necessary to transfer the stored quantum state to another emptied spin state before time $t = 1/\Delta$, as discussed in the next steps.

3. Apply a π pulse, shown as s3 in Fig. 6.9, as a control field after a time $t = 1/\Delta - t_0$ at the resonance frequency ω_{es}, with the same direction as the storage pulse ($k\mathbf{z}$) called the forward direction. This step creates atomic coherence between states $|s\rangle$ and $|g\rangle$.

4. Apply a pair of π pulses, shown as s4 in Fig. 6.9, at the resonance frequency ω_{sg}, which is in the RF region. (See the discussion in Section 6.2.3 on extending the hyperfine coherence time, T_2^{hyp}.) The ZEFOZ technique and DD pulses can be applied to enhance the coherence properties of the material, instead of a pair of RF π pulses. This is a very relevant and interesting research topic for the future, in attempts to combine high efficiency and long storage times in RE materials.

5. Apply a π pulse, shown as s5 in Fig. 6.9, as a control field at the resonance frequency ω_{es}, with the opposite direction to the storage pulse ($-k\mathbf{z}$) i.e. the backward direction. This causes the atomic coherence to be mapped back to the states $|g\rangle$ and $|e\rangle$.

6. The recall pulse, shown as s6 in Fig. 6.9, is emitted in the backward direction at time $t = 1/\Delta + t_1$.

The theoretical predictions of storage and retrieval efficiency, based on the AFC technique in the backward direction, assuming a comb structure with Gaussian peaks, is given by [113]:

$$\eta_b^{AFC} = (1 - e^{-\frac{d}{F}})^2 e^{-\frac{7}{F^2}} e^{-d_0} \tag{6.18}$$

where d ($=\alpha L$, α is the absorption coefficient and L the sample length) is the optical depth of the AFC peak, and $F = \frac{\Delta}{\gamma}$ is the AFC finesse. From Eq. 6.6, it can be seen that the first term in Eq. 6.18 is related to the coupling between light and atoms. The second term is related to the dephasing factor, and the last term is included to address an additional loss factor due to an absorbing background, d_0, which often occurs due to imperfect preparation of the comb (see Fig. 6.9).

Based on the assumptions discussed above, and running all the beams in the forward direction, the maximum storage and retrieval efficiency will be limited to 54% [113]:

$$\eta_f^{AFC} = (-\frac{d}{F})^2 e^{-\frac{d}{F}} e^{-\frac{7}{F^2}} e^{-d_0} \tag{6.19}$$

One of the main advantages of AFC compared to CRIB is that the available optical depth of the material is used more efficiently. The multimode capacity is another advantage of the AFC over CRIB and EIT. For comparison, the number of modes that can be stored is proportional to $\sqrt{d}$ in EIT and off-resonant Raman interactions, and to d in CRIB [113]. This means that the optical depth must be increased when using the EIT and CRIB techniques to be able to store many modes, while for AFC the multimode capacity is not dependent on the optical depth.

GEM

One of the experimental challenges in the original CRIB approach is the necessity of backward demonstration to eliminate re-absorption [96, 97]. It was later realized that when applying a longitudinal electric field in the CRIB protocol, as originally suggested by Nilsson et al. [97], the re-absorption of the forward direction output pulse was eliminated [98, 136]. This is very similar to the gradient-echo technique used in nuclear magnetic resonance

(NMR) technique. Therefore, this type of CRIB is called longitudinal CRIB (LCRIB) or simply a gradient-echo memory (GEM) [16, 17, 98]. To clarify this important point, it is useful to divide the sample into several slices in the propagation direction (z), and consider all beams propagating in the forward direction ($+\mathbf{k}z$). In the transverse CRIB (TCRIB) configuration, the electric field is applied transversally to the sample as shown in Fig. 6.10. In transverse broadening CRIB, the atomic absorption line is equally broaden for each position z. Therefore, the echo emitted from earlier slices will be absorbed in the rest of the sample. The electric field configuration can be changed from transverse to longitudinal, as shown in Fig. 6.11, in which case, ions in different slices will be shifted differently in frequency. Using this configuration the echo emitted from the first slice of the sample will be absorbed by the last few slices. Using a longitudinal electric field significantly simplifies the experiments. In addition, GEM opens the way for new features, such as changing the time order of the input pulse sequence in the medium, as discussed in detail in Ref. [137].

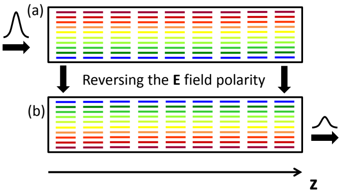

Figure 6.10. *(a) Absorption line broadening (δ_{final}) according to step s2 in Fig. 6.8 for different ions along the direction of propagation (z) according to the transverse CRIB (TCRIB) configuration. (b) Reversing the polarity of the electric field in the TCRIB protocol.*

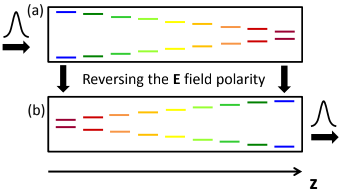

Figure 6.11. *Absorption line broadening (δ_{final}) according to step s2 in Fig. 6.8 for different ions along the direction of propagation (z) according to the longitudinal CRIB (LCRIB) configuration. (b) Reversing the polarity of the electric field in the LCRIB protocol.*

Recently, other photon-echo-based protocols proposed for quantum memory demonstration, such as revival of silenced echo (ROSE) [138], hybrid photon echo rephasing (HYPER) [139], and rephased amplified spontaneous emission (RASE) [140, 141]. No need for spectral engineering preparation is one of the main advantages of these new protocols, in contrast to other protocols mentioned above.

6.3.6 The low finesse cavity and the ensemble approach

Optical cavity systems have a variety of applications, for example, increasing atom-light coupling efficiency [142], as spectral filters [143], as etalons to construct single-mode lasers [144], and in laser frequency stabilization [69, 70]. In gravitational wave detection, a Fabry-Pérot cavity is used to store photons for almost a millisecond while they "bounce" up and down between the mirrors [145]. In this section, cavity-assisted quantum memory is introduced, which is the heart of the efficient quantum memory described in Paper **V** and Paper **VI**.

In Sections 6.3.1 and 6.3.2, improving the light-matter coupling based on the high-finesse cavity-enhanced interaction of light with a single atom [117], and the use of an optically thick, free-space atomic ensemble [5, 146] were discussed, respectively. A third alternative is to combine the advantages of both these approaches in an intermediate approach to implement an efficient quantum interface in a weakly absorbing solid-state medium. In this approach, an ensemble of atoms inside a low-finesse cavity can be used to enhance the coupling efficiency between light and matter. A general theoretical discussion on the ability of this intermediate approach in the demonstration of an efficient quantum memory is discussed in Refs. [147, 148].

The impedance-matching condition

In 2010, a specific criterion (the impedance-matching condition) for application in quantum memories was introduced at the same time by two research groups [149, 150]. According to this criterion, complete absorption of the input pulse can be obtained for weakly absorbing materials if they are placed in a cavity [149, 150]. The absorption during one round trip of the cavity should be exactly equal to the transmission of the input coupling mirror, and there should be no other losses during the cavity round trip. Obtaining this condition, which is called impedance-matched condition, is a vital step towards efficient quantum memories using weakly absorbing media.

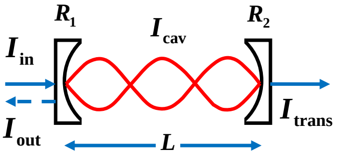

Figure 6.12. *The impedance-matched condition in the absence of any absorber in a symmetric ($R_1 = R_2$) Fabry-Pérot cavity will provide $I_{trans} = I_{in}$ and $I_{out} = 0$.*

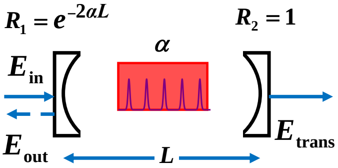

Figure 6.13. *The impedance-matched condition in the presence of an absorber αL in an asymmetric ($R_1 = e^{-2\alpha L}$ and $R_2 = 1$) Fabry-Pérot cavity will provide $E_{out} = 0$, while E_{in} is fully coupled to the absorber inside the cavity.*

This criterion can be clarified by comparing two cases. Let us first consider a Fabry-Pérot cavity with identical mirror reflectivities ($R_1 = R_2$), and no absorber or losses inside. At the resonance frequency of the cavity, the input and output intensities will be equal ($I_{\text{in}} = I_{\text{trans}}$), while the reflected intensity vanishes ($I_{\text{out}} = 0$), as illustrated in Fig. 6.12. In the second case, an absorber with absorption coefficient α is inserted into a Fabry-Pérot cavity with an output mirror reflectivity $R_2 = 1$. This cavity will satisfy the impedance-matched condition if $R_1 = e^{-2\alpha L}$ (where L is the cavity length) there are no other losses during the cavity round trip. This condition is shown schematically in Fig. 6.13.

The impedance-matching condition can be also described based on the different fields inside the cavity. Consider part of the incoming field $\overrightarrow{E}_{\text{in}}$ which is directly reflected ($\overrightarrow{E}_{\text{refl}}$) at the first mirror surface (R_1), (see Fig. 6.13). The field leaking out from the cavity through R_1 ($\overrightarrow{E}_{\text{leak}}$), is coherently added to $\overrightarrow{E}_{\text{refl}}$ such that $\overrightarrow{E}_{\text{out}} = \overrightarrow{E}_{\text{refl}} + \overrightarrow{E}_{\text{leak}}$. At the impedance-matched condition, $\overrightarrow{E}_{\text{refl}}$ and $\overrightarrow{E}_{\text{leak}}$ differ in phase by π, but have the same amplitude $\mid \overrightarrow{E}_{\text{refl}} \mid=\mid \overrightarrow{E}_{\text{leak}} \mid$. This means that $\overrightarrow{E}_{\text{out}}$ should ideally vanish if the impedance-matching condition is satisfied.

Using this configuration, the input light will be completely absorbed by the absorber inside the cavity, in the ideal case. To use this configuration as a quantum memory, the next step is to keep track of the quantum state phase (coherence property) in the atomic ensemble. This is possible by preparing the absorption distribution based on one of the schemes discussed in Section 6.3.5. Regardless of the quantum memory scheme employed, the background absorption should be minimized. In Paper **V** and Paper **VI**, a cavity configuration was employed around the absorber material, and more than one order of magnitude improvement in memory efficiency, compared to that obtained without the cavity, was demonstrated. The praseodymium absorption line in $Pr^{+3}:Y_2SiO_5$ was tailored using the AFC protocol [113], and an impedance-matched cavity configuration [149] was employed to enhance the quantum memory efficiency.

A theoretical prediction of the storage and retrieval efficiency based on the AFC technique inside an impedance-matched cavity is given by [149]:

$$\eta_{cavity}^{AFC} = [\frac{2(1-R_1)\sqrt{R_2}}{(1-\sqrt{R_1R_2}e^{-\frac{d}{F}})^2}]^2(\frac{d}{F})^2 e^{-\frac{2d}{F}} e^{-\frac{7}{F^2}} e^{-d_0} \tag{6.20}$$

where d, d_0, and F are the AFC peak absorption, background absorption, and the AFC finesse ($\frac{\Delta}{\gamma}$), as shown in Fig. 6.9, respectively. The reflectivity of the mirrors are R_1 and R_2, as shown in Fig. 6.13. Based on Eq. 6.20, the efficiency of an AFC-cavity quantum memory with AFC finesse $F = 10$ and background absorption $d_0 = 0$ in an asymmetric cavity ($R_2 = 0.997$), as a function of the input mirror reflectivity R_1, is shown in Fig. 6.14. Different traces belong to the available AFC peak absorption (d) inside the cavity. The best memory efficiency ($\eta \approx 92\%$) was obtained at the impedance-matched condition $R_1 = e^{-\frac{2d}{F}} = e^{-0.2} \approx 0.82$.

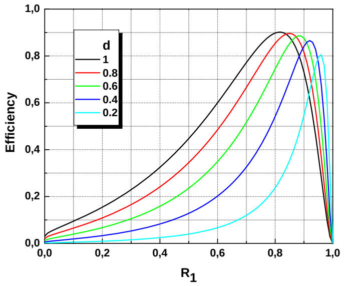

Figure 6.14. *The efficiency of an AFC-cavity quantum memory. Different traces belong to the available AFC peak absorption (d) inside the cavity. For further details see text.*

Strong dispersion and cavity free spectral range

The cavity transmission line-width and mode separation are vital parameters in all cavity-based applications. The relation between these two cavity parameters and the medium dispersion is presented here, and finally the medium absorption structure is discussed [151, 152]. To this end, we will start with the mode spacing calculation in the absence of ion absorption inside the cavity. A cavity without any absorber inside is henceforth called a "cold cavity". According to the round-trip phase condition, constructive interference between all plane waves inside the cavity is required for on-resonance transmission through the cavity needs:

$$\phi(\nu) = \frac{2\pi\nu n_r(\nu)2L}{c_0} = 2\pi q \tag{6.21}$$

where ν is the frequency, n_r is the real refractive index, $2L$ is the round-trip distance inside the cavity, c_0 is the speed of light in vacuum, and q is an integer. The frequency mode spacing is then given by:

$$\Delta\nu_{mode} = \nu_{q+1} - \nu_q = \frac{c_0}{2Ln_r(\nu)} \tag{6.22}$$

Introducing an ion absorption frequency distribution $\alpha(\nu)$ to the cavity will affect the real refractive index $n_r(\nu)$. Indeed, the relation between the absorption coefficient and the refractive index is a result of the Kramers-Kronig relations, which relate the real (k_r) and imaginary (k_i) parts of the susceptibility of a medium (Eq. 5.5.13 in Ref. [49]):

$$k_r(\nu) = \frac{2}{\pi}\int_0^\infty \nu' \frac{k_i(\nu')}{\nu'^2 - \nu 2} d\nu' \tag{6.23}$$

$$k_i(\nu) = \frac{2}{\pi}\int_0^\infty \nu' \frac{k_r(\nu')}{\nu'^2 - \nu 2} d\nu' \tag{6.24}$$

.

Suitable approximations are needed to extract the frequency mode spacing relation in presence of a dispersive medium. The small fractional frequency spacing and the variation in refractive index with frequency between the modes motivate the use of Taylor expansion about the central mode ν_q. Taylor expansion to the first order gives an approximate expression for the real refractive index:

$$n_r(\nu_{q+1}) \approx n_r(\nu_q) + \frac{dn_r(\nu_q)}{d\nu}(\nu_{q+1} - \nu_q) \tag{6.25}$$

Recalculating the frequency mode spacing from Eq. 6.22 in a dispersive medium according to Eq. 6.25 leads to:

$$\begin{aligned} \Delta\nu_{mode} &= \nu_{q+1} - \nu_q \\ &= \frac{c_0}{2L}[\frac{q+1}{n_r(\nu_{q+1})} - \frac{q}{n_r(\nu_q)}] \\ &\approx \frac{c_0}{2L}\frac{1}{n_r(\nu) + \nu\frac{dn_r(\nu)}{d\nu}} \end{aligned} \tag{6.26}$$

The definition of the group velocity of light

$$\nu_g^{-1} = \frac{1}{2\pi}\frac{dk}{d\nu} = \frac{1}{c_0}\frac{d(\nu n_r(\nu))}{d\nu} = \frac{1}{c_0}[n_r(\nu) + \nu\frac{dn_r(\nu)}{d\nu}] = \frac{n_g(\nu)}{c_0} \tag{6.27}$$

where k is the wave number, together with Eq. 6.26, gives a simple equation for the frequency mode spacing in the cavity in the presence of dispersion.

$$\Delta\nu_{mode} \approx \frac{c_0}{2L}\frac{1}{n_g(\nu)} = \frac{\nu_g(\nu)}{2L} \tag{6.28}$$

The Eq. 6.28 shows the possibility of controlling the cavity mode spacing by controlling the group refractive index ($n_g(\nu)$). On the other hand, manipulation of the ion absorption frequency distribution, $\alpha(\nu)$, will affect the dispersion via the Kramers-Kronig relations. Therefore, the possibility of engineering the ion absorption frequency distribution allows the cavity mode spacing to be engineered.

Based on Eq. 6.26 there are four different regimes for the group velocity and, consequently, the frequency mode spacing.

1. If $n_r(\nu) \gg \nu\frac{dn_r(\nu)}{d\nu}$ then Eq. 6.26 is almost the same as Eq. 6.22 when there is no dispersion relation.

2. If $n_r(\nu) \ll \nu\frac{dn_r(\nu)}{d\nu}$ the group velocity is decreased and, according to Eq. 6.28, the frequency mode spacing in the cavity will be closer. This regime is called the slow light regime.

3. If $n_r(\nu) \approx -\nu\frac{dn_r(\nu)}{d\nu}$ the denominator in Eq. 6.26 will be very small and the group velocity is much higher than phase velocity, leading to the fast light regime.

4. If $n_r(\nu) < -\nu\frac{dn_r(\nu)}{d\nu}$ then the group velocity has the opposite direction to the phase velocity.

Chapter 7

Spectral-temporal filters

The combination of large inhomogeneous broadening and narrow homogenous broadening of RE ions, which is discussed in Section 2.4, could be used with advantage to engineer a very narrow-band spectral filter. In practice, this filter is made possible by employing a laser with a frequency stable narrow line-width of the order of the homogenous line-width. Then, through optical pumping, one can remove a subset of ions in the inhomogeneous profile and create a sharp spectral hole or spectral edge. Sharpness refers here to the difference between the maximum and minimum absorption within a certain frequency window $\nu - \nu_0$ as shown in Fig. 7.1. One of the inherent properties of spectral filtering with a sharp absorption edge is a strong dispersion through the Kramers-Kronig relation. Therefore the output signal after the filter will experience a delay in the time domain. In this chapter, we will discuss the design of a spectral filter in a particular crystal ($0.05\% Pr^{3+} : Y_2SiO_5$), and describe the slow light effects that are exhibited by such a spectral filter and then try to optimize its performance by combining spectral and temporal (slow light) filtering. At the end of this chapter, some applications of such spectral-temporal filters are discussed.

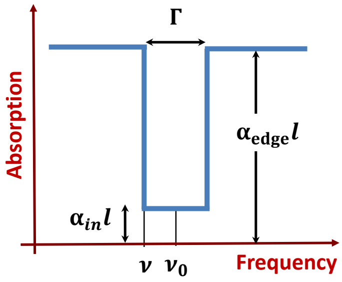

Figure 7.1. *Schematic for a typical spectral filter.*

7.1 Spectral filter design

In this section we discuss the use of the $^3H_4 - {}^1D_2$ transition of a $0.05\% Pr^{3+} : Y_2SiO_5$ crystal as an example of a spectral filter design, but the main idea could be extended to other RE ion doped crystals. In $Pr^{3+} : Y_2SiO_5$, the sharp edge spectral filters are created by taking advantages of the large ratio between the ion's inhomogeneous broadening (∼5 GHz) and its homogeneous broadening (∼1 kHz). To be able to use the advantage of narrow line-width in practice, the frequency stabilized laser is used that is discussed in Chapter 4.

In this section, we take up the specific approaches to maximize the edge absorption, α_{edge}, minimize the transmission window absorption, α_{in}, and possibly minimize Γ (see Fig. 7.1). Typically, we are dealing with Γ on the order of 1-2 MHz. The spectral filter is produced using spectral hole burning (SHB) technique. SHB can be started by simply shining the laser beam onto the inhomogeneous profile, optically pumping and removing ions from one of the hyperfine ground states (for instance $\pm 1/2g$ of $Pr^{3+} : Y_2SiO_5$ in Fig. 2.4) and putting them somewhere else (for instance in the $\pm 5/2g$, Fig. 2.4). To maximize α_{edge}, obviously we have to place the laser frequency at the center of the inhomogeneous profile. This will be the frequency position of our spectral filter and it is considered as the center frequency ν_0 afterwards. However, is it possible to increase the absorption of the crystal even more than the absorption at the center of inhomogeneous profile? Here, I suggest a pulse sequence which can give a positive answer to this question. To accomplish this goal, we designed an erasing sequence which must be applied before the actual hole burning sequence. The erasing pulses pump the ions back into an absorbing state at the frequency of interest, in our case ν_0. In fact by pumping the ions into a particular initial state we maximize the optical absorption at that particular state.

In a typical experiment our purpose was to prepare a spectral filter that would be transparent from -1 MHz to 1 MHz about $\nu_0 = 0$ MHz. To do this, the erasing sequence was as follows:

1. Chirp the laser from 16 MHz to 20 MHz for t_{E1} ($\sim 86\,\mu s$) and wait for t_{E2} ($\sim 500\,\mu s$, roughly 3 times the optical T_1^{opt}, or long enough for excited state population relaxation)

2. Chirp from -20 MHz to -16 MHz, with erasing and waiting time the same as in step (1)

3. Repeat (1) and (2) many times, but each time increase the erasing frequency outward away from the central frequency by a step of 4 MHz, so that the there is no spectral overlap between consecutive pulses. For example, the second repetition would chirp from 20 MHz to 24 MHz and -24 MHz to -20 MHz. This was repeated until finally the total frequency range spanned by the erasing pulses was -40 MHz to -16 MHz and 16 MHz to 40 MHz.

4. Repeat the previous sets of erasing pulses, as described in (1), (2), (3), typically 150 times.

The sequence above provides an example of how to improve the absorption at the frequency of interest. For a specific application, we can use the same scheme but we need to optimize the Rabi frequency and number of pulses. The numbers above are

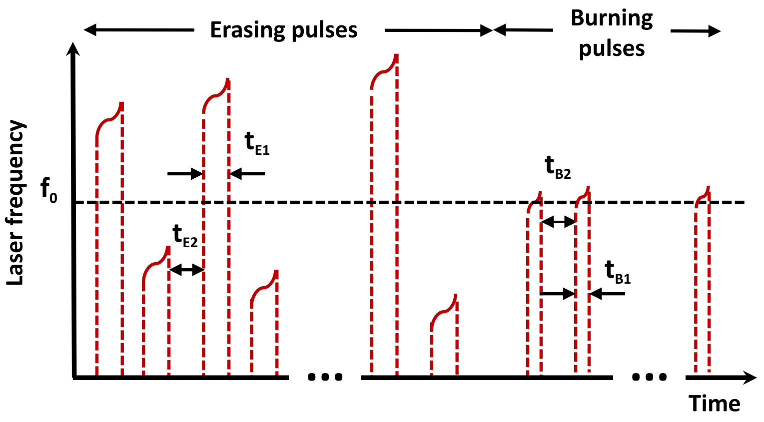

Figure 7.2. *Pulse sequences for spectral-temporal filter demonstration versus frequency. For more discussion see the text.*

used to demonstrate a spectral filter while the beam diameter at the crystal was ≈ 3 mm and we were therefore limited by the available Rabi frequency. This is the reason that we used so many pulses to achieve the best construction. For these pulses a specially designed frequency chirp is used. This chirp is a mixture of a linear sweep and a complex hyperbolic secant, or Sechyp [153]. The linear sweep function is added at the center of the Sechyp frequency chirp function (Eq. 2 in Ref. [153]) while ensuring that the first and second derivatives are continuous. This special type of chirped pulse, which may be denoted Sechyp-scan, optimizes population transfer efficiency and keeps unwanted excitations to a minimum level [154, 155]. We did not use a continuous chirp from 16 MHz to 40 MHz, because in this range the ions need time to relax from the excited state between excitations cycles in order to achieve efficient ground state population redistribution.

After the erasing procedure, we start the hole burning sequences by means of a series of sechyp-scan pulses which scan about the center frequency from -1 MHZ to 1 MHz. This spectral hole was burned with 80 μs pulses (t_{B1} in Fig. 7.2), consecutive pulse separations of 500 μs (t_{B2} in Fig. 7.2), and repeated 1000 times. To make a symmetric spectral hole, the scanning direction was flipped for every other burning pulse, i.e. -1 MHz to +1 MHz then +1 MHz to -1 MHz and so on.

I then felt that it would be interesting to compare the spectral filter obtained with and without the suggested erasing procedure. To this end, two sets of simulations were carried out. The results are presented in Fig. 7.3. These simulations are based on the assumption that the initial absorption profile, within the range

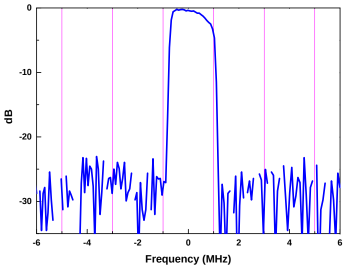

Figure 7.4. *Transmitted intensity versus detuning. Top-hat shaped spectral filter demonstrated in a 1.2 cm 0.05%* $Pr^{3+}:Y_2SiO_5$ *at cryogenic temperature (~3 K).*

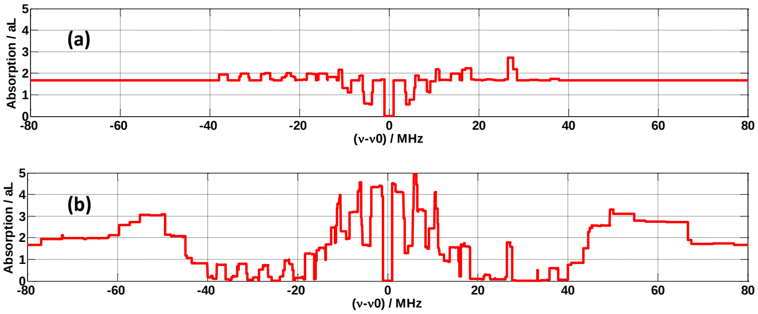

Figure 7.3. *Hole burnig simulation. (a) No eraser and then a 2 MHz hole burning. (b) Suggested eraser procedure and then a 2 MHz hole burning at frequency* $\nu_0 = 0$.

considered, is independent of frequency. Then ions are repopulated between the $Pr^{3+}:Y_2SiO_5$ energy levels based on the input pulses and by considering the actual branching ratios. For the comparison, two different cases were defined:

1. No eraser, 2 MHz hole burning as shown in Fig. 7.3a
2. The suggested eraser procedure and then a 2 MHz hole burning, shown in Fig. 7.3b.

We can compare the relative absorption at the side of the 2 MHz hole burnt at center frequency $\nu_0 = 0$ as shown in Figs. 7.3a and 7.3b. This comparison shows a clear improvement of the absorption edge, α_{edge}, for the spectral hole created at $\nu_0 = 0$, when the eraser pulses is employed.

With the above preparation procedure, we were able to create in an efficient manner a 2 MHz wide approximately "top-hat" shaped spectral hole as shown in Fig. 7.4. The transmitted intensity inside the transparent spectral region was attenuated less than 3dB. However, at $\nu = 2$ MHz away from the center it was more than 45 dB when measured with a collimated laser beam and 33 dB when measured with highly scattered light, respectively. Thus the on/off ratio was ~30 dB for diffuse light and ~42 dB for collimated light.

7.2 Temporal filtering

The phenomenon of slow light attracted many interests in the past decade because of the successful early demonstrations of very slow propagation speeds [156] and even stopped light [157]. In addition, slow light was observed in a solid using a $Pr^{3+}:Y_2SiO_5$ crystal

[158]. Since then slow light has been employed for numerous applications such as classical and quantum information storage, synchronization of optical pulses, high-precision spectroscopy, radar beam steering, etc. [159]. In this section, we discuss the role of the slow light effect on improving the overall filter suppression.

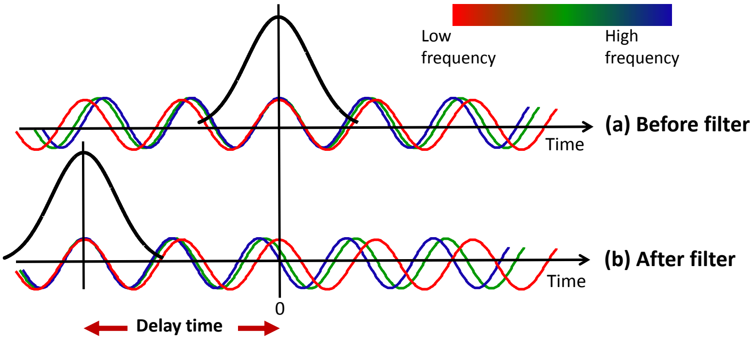

Figure 7.5. *A schematic illustration of the effect of different phase velocities of different frequency components in a pulse (a) the input pulse to the spectral filter. (b) the delayed pulse after the spectral filter.*

An intuitive picture for understanding the time delay created by a spectral filter can be obtained by decomposing the input pulse into several frequency components. A typical pulse is shown simply in Fig. 7.5a using three frequency components . In the case of the input pulse passing through a sharp spectral filter, different frequency components experience different propagation speeds. Therefore, the summation of the frequency components after passing through the spectral filter will be constructive at a different time. The envelope of a delayed pulse is shown schematically in Fig. 7.5b.

Let us now calculate the effect of the spectral filtering on the group velocity for a typical pulse which passes through the spectral filter. According to the definition of group velocity:

$$v_g^{-1} = \frac{1}{2\pi}\frac{dk}{d\nu} = \frac{1}{c}\frac{d(\nu n_r(\nu))}{d\nu} = \frac{1}{c}[n_r(\nu)+\nu\frac{dn_r(\nu)}{d\nu}] = \frac{n_g(\nu)}{c} \quad (7.1)$$

One can see the spectral filter as an ion absorption frequency distribution $\alpha(\nu)$ which is related to the imaginary part of the susceptibility, $k_i(\nu)$, of the medium. It is possible to calculate the real part of the susceptibility, $k_r(\nu)$, based on Kramers-Kronig relations (Eq. 5.5-13 in Ref. [49]):

$$k_r(\nu) = \frac{2}{\pi}\int_0^\infty \nu' \frac{k_i(\nu')}{\nu'^2 - \nu^2} d\nu' \quad (7.2)$$

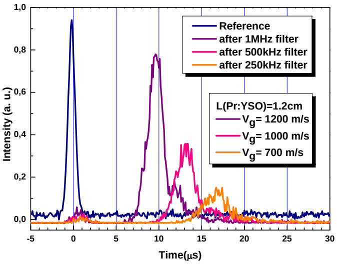

Figure 7.6. *Slow light effect. The input optical Gaussian pulse with* $t_{fwhm} = 1\,\mu s$ *(black trace) sent to the center frequency of a spectral filters with different widths,* Γ, *demonstrated in a 1.2 cm long* $Pr^{3+} : Y_2SiO_5$ *crystal. The longest delay is* $\sim 17\,\mu s$ *shown in the orange trace which is equivalent to a group velocity of* v_g*=700 m/s.*

$$k_i(\nu) = \frac{2}{\pi} \int_0^\infty \nu' \frac{k_r(\nu')}{\nu'^2 - \nu^2} d\nu' \tag{7.3}$$

and we know the real part of the susceptibility is related to the real refractive index, $n_r(\nu)$. Therefore, one can measure $\alpha(\nu)$ experimentally and then calculate $n_r(\nu)$ based on Kramers-Kronig relations and finally also the group velocity as follows:

$$v_g = \frac{c}{n_g} = \frac{1}{n_r(\nu) + \nu \frac{dn_r(\nu)}{d\nu}} \tag{7.4}$$

Based on Eq. 7.4, we have the possibility to control the group velocity of the input pulse by engineering real refractive index $n_r(\nu)$ through the absorption frequency distribution $\alpha(\nu)$. The results in Paper **IV** show the possibility to design the spectral filter in the regime when $n_r(\nu) \ll \nu \frac{dn_r(\nu)}{d\nu}$, which is called the slow light regime. The different regimes of this phenomenon are discussed in Section 6.3.6.

For the case that the spectral filter width, Γ, is much narrower than the inhomogeneous broadening and much wider than the laser line-width, we can (approximately) write the group velocity, v_g, for a pulse propagating through the spectral filter as follows [160, 161]:

$$v_g = \frac{2\pi\Gamma}{\alpha} \tag{7.5}$$

where Γ is the spectral filter width and $\alpha = \alpha_{edge} - \alpha_{in}$ as shown in Fig. 7.1.

Let us now calculate the relevant time delay for a Fourier limited pulse with a spectral width in the order of γ in a crystal with length L:

$$t_{delay} = \frac{L}{v_g} = \frac{\alpha L}{2\pi\Gamma} \tag{7.6}$$

which means that we will have a delay of more than the pulse duration if $\alpha L > 2\pi$. The absorption depth $\gg 2\pi$ is realistic to achieve in $Pr^{3+} : Y_2SiO_5$ crystal.

Once the spectral filter was demonstrated, it was possible to take the next step: the optimization of the temporal filtering based on the slow light effect. A typical spectral filter such as the one shown in Fig. 7.4 was demonstrated experimentally using a 1.2 cm long $Pr^{3+} : Y_2SiO_5$ crystal with $\Gamma = 1$ MHz. A Gaussian pulse of light with $t_{fwhm} = 1\,\mu s$ sent through the center frequency of the spectral filter. The output Gaussian pulse was delayed by about $10\,\mu s$ (see the purple trace in in Fig. 7.6). A set of experiments with different spectral filter widths Γ are also shown in Fig. 7.6. Measurments for all three conditions show a significant time separation between the input pulse to the spectral filter and the delayed pulse afterwards. Therefore, employing this spectral filter also provides another degree of freedom, in the time domain, for filtering purposes.

7.3 Applications

Based on the demonstrated spectral-temporal filter which is shown in Fig. 7.4, we can selectively filter out one of two optical pulses (at $\lambda \approx 606$ nm) which are separated about 2 MHz by an approximately 30 dB suppression. A variety of applications could be suggested for such a narrow-band and sharp edge spectral-temporal filter such as the one demonstrated using the $Pr^{3+} : Y_2SiO_5$ crystal. In this section, we will discuss some applications in more details.

7.3.1 Ultrasound Optical Tomography

In this section, we describe the use of our prepared spectral-temporal filter in an environment which is essentially outside of the scope of the present thesis. However, it is interesting to see how broad the applications of such a filter can be. We will discuss the application of the present spectral filter for optical imaging of biological tissue. The technique is called ultrasound optical tomography (UOT) because we take advantage of the interaction between ultrasound and light.

Generally, in an imaging process we need to optimize both the contrast and the resolution of the image. Having both properties in imaging biological tissue is a challenging task because of the relatively high scattering in the medium. The contrast is defined as the ratio between the brightest color (white) to the darkest color (black). This property has similarities with dynamic range, which is the ratio between the largest and smallest possible values of a changeable quantity. Light can have relatively good contrast in a biological tissue. Resolution, on the other hand, is the ability of an imaging system to make distinguishable details in the object that is being imaged. The resolution properties of light are very poor in a highly scattering medium such as biological tissue. Ultrasound, on the other hand, propagates almost ballistically with a scattering coefficient three orders of magnitude smaller than visible light. Therefore, ultrasound can provide relatively good resolution, but unfortunately it has a poor contrast property. One can thus think about combining light and ultrasound to get the advantages of both.

Having both light and ultrasound inside a scattering medium, such as biological tissue, causes amplitude and phase modulation of the probe illumination, ν_l, by ultrasound, ν_s. This produces new optical frequencies shifted from the original by +/- the ultrasound frequency ν_s. In principle these modulation sidebands, $\nu_l \pm \nu_s$, can be filtered out from the unmodulated scattered light, ν_l, to reveal the UOT signal. The interaction between pulsed ultrasound and a light pulse in biological tissue is shown schematically in Fig. 7.7a. After the interaction in the tissue, the carrier and sidebands are

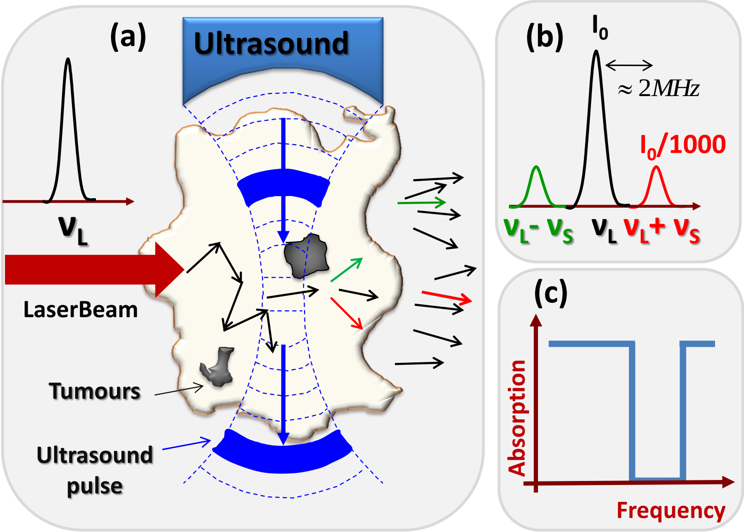

Figure 7.7. *A schematic illustration of the ultrasound optical tomography (UOT) principle. (a) Ultrasound shifted light (sidebands) are created by an interaction between the laser beam and pulsed ultrasound in the tissue. Black, green, and red arrows represent the spatial distribution of the carrier frequency and lower and higher frequency sidebands, respectively. (b) Comparison between the intensity and frequency separation of the carrier (black) and sidebands (green and red). (c) Schematic of a spectral filter with capability of filtering out either green or red sideband.*

shown in Fig. 7.7b. For filtering purposes it is much easier to increase the ultrasound frequency and thereby separate the carrier and sidebands. On the other hand, the ultrasound modulation efficiency will decrease at higher frequencies. Therefore, because of the trade off between these two quantities, the ultrasound frequency in Paper **IV** was set to ν_s =2.3 MHz. A well-functioning spectral filter, which is shown in Fig. 7.7c, needed to suppress the carrier signal, which is ~three orders of magnitude larger than the sideband. Monitoring the intensity of the light shifted by the ultrasound while scanning the ultrasound focus on the sample then produces an image of the interior of the object.

The main technical challenges for deep tissue imaging and other demanding applications of optically detected ultrasound are due to the sidebands, $\nu_l \pm \nu_s$, being typically many orders of magnitude weaker than the carrier signal, ν_l. Therefore the key task is filtering out these relatively weak sidebands from the much stronger carrier signal.

The main attempt of the UOT experiment in Paper **IV** is to go to deep (>5 cm) tissue imaging. Light leaving a thick biological tissue has a large etendue, which is defined by the product of the light solid angle and area [162]. The reason for large etendue is that, the light is fully diffused and emerges with essentially a 4π solid angle. Combining this with the large size (∼10 cm) of tissue samples used in medical or biological applications, gives a very large etendue ∼100,000 $sr - mm^2$ (see Fig. 1b of Paper **IV**). For fully diffused light, the etendue of the detection system approximately determines the fraction of ultrasound shifted photons that can be collected. To get a feel for the magnitude of this problem, consider that typical interference-based optical color filters have orders of magnitude smaller than the etendue ∼100, and versions of these that are narrow-band enough (∼1 MHz confocal Fabry-Pérot) to filter out ultrasound modulated photons have etendue < 1 (see Fig. 1b of Paper **IV**). The prepared spectral-temporal filter based on the persistent spectral hole burning (PSHB) technique in Paper **IV** clearly achieved much better etendue compared to other filtering schemes in the type of applications proposed so far. Actually, by far the largest etendue yet reported is with spectral hole burning (SHB) materials [163, 164].

Pulsed ultrasound excitation is generally preferred over continues wave due to its high resolution in the ultrasound propagation direction, faster imaging speed and compatibility with the well-established conventional ultrasound imaging techniques [165, 166]. A schematic illustration of pulsed ultrasound is shown in Fig. 7.7 by solid blue, which moves in the same direction as the ultrasound propagation direction. A tumor in the tissue will absorb much more light than other parts of the tissue. Therefore, the presence of a tumor in the tissue will be detected by the absence of the whole or part of the sideband signal. This is discussed more in greater detail in Paper **IV**.

In addition to the spectral filtering, the sideband signal is delayed due to the slow light created through the persistent spectral hole burning and this in turn improved the performance of the ultrasound modulated optical tomography such that it was possible to image up to a 9 cm thick tissue phantom, as described in Paper **IV**. The unprecedented performance of this filtering combination comes from the fact that slow light provides an additional temporal degree of freedom that enhances the spectral selectivity of the hole burning filter. Projections based on straightforward improvements in the experimental apparatus show that imaging in even thicker phantoms should be possible. Here we note that even though this demonstration was carried out at a wavelength of 606 nm, slow light has also been observed in materials that work in the therapeutic window (for example Tm:YAG [167] at 800 nm). Thus slow light may find an application in early cancer detection via UOT. The UOT technique has potential applications to biological and medical imaging, for example early tumor detection, as well as non-contact ultrasound imaging for a variety of commercial, government, and research applications.

7.3.2 Quantum memories

The discussion in this section also has interesting implications for the possible application of the demonstrated spectral-temporal filter to the development of quantum memories.

As we discussed in Section 3.5, one of the fundamental limitations of conventional photon echo for quantum memory applications is the spontaneous emission from strong rephasing pulses at the same time as the echo emission. The spontaneous emission is actually much larger than the single photon level echo emission. The strong rephasing pulse is replaced by switching for instance an electric field in CRIB or GEM protocol to avoid the strong spontaneous emission as discussed in Section 6.3.5. The strong rephasing is not needed in AFC protocol [113], because of the inherent rephasing process between AFC peaks. However, for all mentioned protocols, to extend the storage time (or to obtain on-demand storage with the AFC technique) we need to employ a pair of bright optical transfer pulses to map the quantum state from the optical state to the shelving state and vice versa. These pulses are separated out from the echo emission by ground state hyperfine state separation, for instance ≈10.2 MHz in the $Pr^{3+}:Y_2SiO_5$ crystal. In addition, the time separation between the second bright transfer pulse and the echo emission is short ($\sim$ several μs). The transfer pulse can disturb the emitted echo through off-resonance excitation or a scattering procedure. Therefore, it would be important to find a way to circumvent this problem.

Let us now be more specific and talk about quantum memory preparation based on an on-demand AFC protocol in a $Pr^{3+}:Y_2SiO_5$ crystal. In this case, the ground state hyperfine separations are 10.2 MHz and 17.3 MHz (see Fig. 2.4). According to the AFC protocol, which is discussed in Section 6.3.5, we can use the $\pm 1/2$ and $\pm 3/2$ states for the memory. This will lead to a 10.2 MHz frequency separation between the strong transfer pulse and the echo emission. Therefore, we can easily modify the demonstrated spectral filter for the UOT experiment in Paper **IV** to render them useful for quantum memory application. Actually, the larger frequency separation between two pulses in the quantum memory application provides less constraint for the spectral filter preparation. We can even think of creating an absorption edge to have a low-pass or high-pass spectral filter instead of narrowband spectral filter. This could be an option, in case the spectral filtering limits the mode capacity of the AFC technique.

OUTLOOK

In 2008, as this thesis work was starting, quantum memory was a quite new topic for the experimental quantum information community. Soon, different protocols in different materials were proposed, thus promoting the growth of this new-born infant. Several experimental groups started to demonstrate and improve different aspects of quantum memories. Fidelity, storage and retrieval efficiency, storage time, bandwidth, multi-mode storage, and operational wavelength were the main properties of concern.

During the course of the research described in the present thesis, we focused mostly on optimization of the storage and retrieval efficiency. We moved toward our goal by construction of a frequency stabilized laser source in combination with employing the pulse shaping setup that enable us to obtain about 1% accuracy over a range of more than six orders of magnitude in intensity. This high efficiency is mainly a product of our highly controllable and precise spectral engineering techniques.

Most quantum memory protocols require relatively high optical depth to increase light-matter coupling efficiency and finally overall storage and retrieval efficiency. But in 2010, new proposals from the research community suggested combining a low finesse cavity and ensemble approaches for efficient quantum memory construction in the weakly absorbing media. Based on these proposals and using $Pr^{3+} : Y_2SiO_5$, we demonstrate the highest storage and retrieval efficiency based on the AFC protocol achieved so far. The low finesse cavity configuration, with advantages of having the quantum memory in a weakly absorbing media, opens up the possibility of utilizing materials with low optical depth but good coherence properties (e.g. $Eu^{3+}\!:\!Y_2SiO_5$). This creates a promising future for combining high efficiency and multi-mode capacity.

Another benefit of the low finesse cavity configuration compared to the single-pass crystal, is demonstrating a high overall efficiency in the short crystal length and consequently small physical storage volume. This cavity configuration can simplify the implementation of long-term storage in the hyperfine levels. Storage in the hyperfine levels requires a radio frequency (RF) signal to drive the spin state transition to compensate for the spin inhomogeneous broadening. Quantum memories demonstrated in a smaller physical volume require lower RF power. This property may in practice significantly simplify the process of having long storage time and high efficiency quantum memories.

Most quantum memory protocols based on rephasing, such as the photon echo effects, which are proposed for long storage time, suffer from the background light noise emitted at the same time as the echo emission. This background light would, however, normally have a different frequency compared to the quantum memory output signal. Based on spectral engineering of the inhomogeneous broadening of Pr^{3+} : Y_2SiO_5 , we designed and demonstrate a narrow-band (~2 MHz) spectral-temporal filter for biological tissue imaging purposes. The same spectral-temporal filtering technique can also be applied for quantum memory construction in the future. Indeed, this spectral-temporal filter can suppress background noise and helps to distinguish the output single photon level signal emitted from the quantum memory. As a second suggestion, we can employ an efficient second memory, which involves just using a two-level system and does not have any transfer pulses to the shelving state, after the main quantum memory. The second memory can delay the emission from the first memory and consequently suppress the background noise originated from the transfer pulses in the first memory.

For the future of quantum memories, we can expect development should move towards combining different aspects in a single physical system. For instance, as we discuss in the present thesis, having a high storage and retrieval efficiency and long storage time simultaneously would create a bright future for quantum memories based on photon-echo-like effects. This could happen in the cavity configuration. In addition, the multi-mode capacity of quantum memories based on photon-echo-like effects is limited by the hyperfine separation of the materials used. Therefore, there is a need to investigate other materials with larger hyperfine separations, for instance, extending the work on $Eu^{3+}:Y_2SiO_5$.

COMMENTS ON THE PAPERS

I **Towards an efficient atomic frequency comb quantum memory**
A. Amari, A. Walther, M. Sabooni, M. Huang, S. Kröll,
M. Afzelius, I. Usmani, B. Lauritzen, N. Sangouard,
H. de Riedmatten, N. Gisin.
Journal of Luminescence **130**, 1579–1585 (2010).

In this paper, the possibility to achieve relatively high efficiency quantum memory based on the atomic frequency comb (AFC) technique is demonstrated. The inhomogenously broadened line of a 0.05% $Pr^{3+}:Y_2SiO_5$ crystal with a length of 2 cm is employed to achieve a storage and retrieval efficiency of 35% after 1 μs. At the time of publication, this was the highest quantum memory efficiency demonstrated based on the AFC technique.
I participated in the planning, demonstration of the AFC structure, and took part in all the experiments.

II **Storage and Recall of Weak Coherent Optical Pulses with an Efficiency of 25%**
M. Sabooni, F. Beaudoin, A. Walther, N. Lin, A. Amari,
M. Huang, and S. Kröll.
Phys. Rev. Lett. **105**, 060501 (2010).

The experimental realization of a single photon level quantum state storage based on the AFC technique is the main target of this paper. To demonstrate a memory for optical quantum state storage, one needs to test it with a low photon number to ascertain that it operates in the quantum level. The same quantum efficiency achieved at the single photon level and the classical light level is called linearity response of the memory. This paper supports the linearity of the AFC technique which is used for the rest of the papers.
I participated in the planning, took part in all the experiments and wrote the manuscript as a corresponding author.

III **Hyperfine characterization and spin coherence lifetime extension in $Pr^{3+} : La_2(WO_4)_3$**
M. Lovrić, P. Glasenapp, D. Suter, B. Tumino, A. Ferrier, P. Goldner, M. Sabooni, L. Rippe, and S. Kröll.
Phys. Rev. B **84**, 104417 (2011).

In this paper, the praseodymium hyperfine interaction of $Pr^{3+} : La_2(WO_4)_3$ is characterized and the spin Hamiltonian parameters are determined by numerical analysis of Raman-heterodyne spectra collected over a range of static external magnetic-field strengths and orientations. The potential of $Pr^{3+} : La_2(WO_4)_3$ for quantum memory applications is shown by measuring the spin coherence lifetime in a magnetic field that is chosen such that small additional magnetic fields, to first order, do not shift the transition frequency. Experimental results demonstrate a spin coherence lifetime of 158 ms which is almost 3 orders of magnitude longer than in zero field.
I participated in the planning, took part in all the experiments and was involved in the interpretation of part of the experimental results.

IV **Slow light for deep tissue imaging with ultrasound modulation**
H. Zhang, M. Sabooni, L. Rippe, C. Kim, S. Kröll, L. V. Wang, and P. R. Hemmer.
Appl. Phys. Lett. **100**, 131102 (2012).

In this paper, persistent spectral hole burning (PSHB) in $Pr^{3+} : Y_2SiO_5$ is employed to demonstrate a narrow-band spectral filter of $\sim$ 2 MHz with a suppression of $\sim$30 dB for diffuse light. In addition, the strong dispersion within the spectral filter frequency region provide a time delay based on the slow-light effect. The slow light gives complete temporal discrimination and improves the performance of the narrow-band spectral filters. This narrow-band spectral filter is used to optically detect ultrasound from deep inside highly scattering tissue. We demonstrate this capability with a 9 cm thick tissue phantom, having 10 cm^{-1} reduced scattering coefficient, and achieve an unprecedented background-free signal.
I participated in the planning, designing, and took part in all the experiments and wrote part of the manuscript.

V **Cavity enhanced storage-preparing for high efficiency quantum memories**
M. Sabooni, S. T. Kometa, A. Thuresson, S. Kröll, and L. Rippe.
New Journal of Physics **15**, 035025 (2013).

This paper shows the first experiment of using a low finesse cavity and weakly absorbing materials to demonstrate an efficient quantum memory. Using this approach, we experimentally demonstrate a significant ($\sim$ 20-fold) enhancement in quantum memory efficiency compared to the no cavity case. A strong dispersion, originating from absorption engineering inside the cavity was observed. This directly affected the cavity line-width. A more than 3 orders of magnitude reduction of cavity mode spacing and cavity line-width from GHz to MHz was observed. We are not aware of any previous observation of several orders of magnitudes cavity mode spacing and cavity line-width reduction due to slow light effects.

I participated in the planning, I came up with the idea of having a small wedge on the cavity for frequency tuning. I did some simulation to understand the behavior of the light polarization while propagating through the $Pr^{3+}:Y_2SiO_5$ crystal in collaboration with Prof. Gerhard Kristensson in the department of Electromagnetic theory, Lund University. I was the main responsible for the experiments and wrote the manuscript as the corresponding author.

VI **Efficient Quantum Memory Using a Weakly Absorbing Sample**
M. Sabooni, Qian Li, S. Kröll, and L. Rippe.
Phys. Rev. Lett. **110**, 133604 (2013).

This paper contain the best storage and retrieval efficiency achieved based on the AFC protocol, which is presently the best multimode quantum state storage protocol. The experiment is carried out in a 2 mm long praseodymium-doped crystal ($0.05\,\%\,Pr^{3+}\!:Y_2SiO_5$) which could be considered as a weakly absorbing medium. The advantages of the cavity configuration is used by depositing a reflection coating directly onto the crystal surfaces. Efficient quantum memories in a weakly absorbing media, opens up the possibility of utilizing materials with low optical depth but good coherence properties (e.g. $Eu^{3+}\!:Y_2SiO_5$).
I participated in the planning, I came up with the idea of finding out the impedance-matching condition on the cavity, experimentally. I was the main responsible for the experiments and wrote the manuscript as a corresponding author.

ACKNOWLEDGEMENTS

I wish to express my sincere gratitude to all those who have supported me and made my PhD studies pleasant and interesting. I would like to take this opportunity to thank all of you and particularly the following people who have been especially helpful and important for my studies:

First, I would like to express my deepest gratitude to Stefan Kröll, my supervisor, for giving me the opportunity to explore my ideas, for his patience, and for always having the time for discussion. Your enthusiasm and positive attitude have meant a great deal to me. I am greatly indebted to you.

I would like to thank my co-supervisors: Hans Lundberg for all your help during my PhD., Lars Rippe, for our enlightening discussions, all the support you have given me, and for the pleasant coffee breaks, which were moments of creation of new ideas. Very efficient coffee break, Lars.

I would like to thank the current quantum information group members, Andreas Walther, Yan Ying, Jenny Karlsson, Iman Moaddel Haghighi, and Diana Serrano, for their help and for creating a friendly atmosphere, and especially Qian Li for a good team effort to get things done. I am also indebted to all former members of quantum information group, Atia Amari who helped me to get involved in the Lab activity, Huang Maomao for his yoga lessons, Axel Thuresson, Samuel Kometa, Felix Beaudoin, Nan Lin, Adam Wiman, Viktor Nordblom, Fredrik Nilsson, and Xingqin Zhao for all their fantastic team efforts.

Some part of the present work is the result of many international collaborations. Special thanks should be given to Huiliang Zhang and Philip Hemmer for an interesting collaboration on biological imaging. In addition, I would like to express my warm gratitude to Phillipe Goldner for his friendship and valuable discussions, Marko Lovrić, and Biagio Tumino for a pleasant collaboration on the ZEFOZ experiment.

I would like to thank the staff at the Division of Atomic Physics, especially Prof. Sune Svanberg, who creates such an enjoyable environment. Bertil Hermansson for all the times he spent making sure the computer system worked properly, Minna Ramkul,

Camilla Nilsson, and Harriett Lindahl for all their extensive administrative support.

Special thanks to Anders Persson for his valuable technical advises. The achievement of the present thesis would not have been possible without the special supports at Cryolab of Leif Magnusson, who provided me with liquid helium whenever I needed it.

Special thanks to Gerhard Kristensson from the Electromagnetic Theory Department who helped me to gain a deeper understanding of the light propagation effects in anisotropic media. Thanks to Ivan Maximov from the Solid State Physics Department for his assistance in removing the cavity coating.

I would like to thank all friends who helped me when I arrived to Sweden, particularly, Davood Shahsavani, Reza Yazdi, Mohsen Sadrossadat, Parisa Sehati. I am greatly indebted to all of you.

I need to further thank all my dear friends who shared their time with me, particularly, Hamzeh, Elnaz, Piotr, Mohammad Ali, Ghasem, Hengameh, Bahram, Keyvan, Farhad, Arefeh, Mohammad, Shabnam, Mehran, Behruz, Reza, and Mehrdad. In addition, I send my thanks also to all my friends who gave me the opportunity to play football every week.

I reserve my deepest gratitude for my beloved mother and father for their unconditional love and for my brother and sisters and my extended family in Iran for their encouragement. Special thanks to my cousin, Mostafa, for all the unlimited help and advice. Thanks to my mother-in-law, brother-in-law for all their moral support during these years. Also thanks to all my beloved relatives and friends in my life.

I would like to express my love and gratitude to my lovely wife, Elham. Her support, encouragement, quiet patience and unwavering love were undeniably the bedrock upon which the past six years of my life have been built. I love you.

REFERENCES

1. P. W. Shor. *Algorithms For Quantum Computation - Discrete Logarithms and Factoring.* 35th Annual Symposium On Foundations of Computer Science, Proceedings pages 124–134 (1994).

2. L. K. Grover. *A fast quantum mechanical algorithm for database search.* Proceedings of the twenty-eighth annual ACM symposium on theory of computing pages 211–219 (1996).

3. T. Thompson. *When silicon hits its limits, whats next?* Byte **21**, 45–& (1996).

4. M. A. Nielsen and I. L. Chuang. *Quantum computation and quantum information.* Cambridge University Press (2000).

5. K. Hammerer, A. S. Sorensen and E. S. Polzik. *Quantum interface between light and atomic ensembles.* Reviews of Modern Physics **82**, 1041–1093 (2010).

6. H. J. Briegel, W. Dur, J. I. Cirac and P. Zoller. *Quantum repeaters: The role of imperfect local operations in quantum communication.* Physical Review Letters **81**, 5932–5935 (1998).

7. L. M. Duan, M. D. Lukin, J. I. Cirac and P. Zoller. *Long-distance quantum communication with atomic ensembles and linear optics.* Nature **414**, 413–418 (2001).

8. N. Sangouard, C. Simon, B. Zhao, Y. A. Chen, H. de Riedmatten, J. W. Pan and N. Gisin. *Robust and efficient quantum repeaters with atomic ensembles and linear optics.* Physical Review A **77**, 062301 (2008).

9. W. J. Munro, A. M. Stephens, S. J. Devitt, K. A. Harrison and K. Nemoto. *Quantum communication without the necessity of quantum memories.* Nature Photonics **6**, 777–781 (2012).

10. P. W. Shor. *Scheme For Reducing Decoherence In Quantum Computer Memory.* Physical Review A **52**, R2493–R2496 (1995).

11. P. Kok, W. J. Munro, K. Nemoto, T. C. Ralph, J. P. Dowling and G. J. Milburn. *Linear optical quantum computing with photonic qubits.* Reviews of Modern Physics **79**, 135–174 (2007).

12. E. Knill, R. Laflamme and G. J. Milburn. *A scheme for efficient quantum computation with linear optics.* Nature **409**, 46–52 (2001).

13. J. Nunn, N. K. Langford, W. S. Kolthammer, T. F. M. Champion, M. R. Sprague, P. S. Michelberger, X. M. Jin, D. G. England and I. A. Walmsley. *Enhancing multiphoton rates with quantum memories.* arXiv:1208.1534v1 (2012).

14. S. Chen, Y. A. Chen, T. Strassel, Z. S. Yuan, B. Zhao, J. Schmiedmayer and J. W. Pan. *Deterministic and storable single-photon source based on a quantum memory.* Physical Review Letters **97**, 173004 (2006).

15. A. I. Lvovsky, B. C. Sanders and W. Tittel. *Optical quantum memory.* Nature Photonics **3**, 706–714 (2009).

16. M. Hosseini, B. M. Sparkes, G. Campbell, P. K. Lam and B. C. Buchler. *High efficiency coherent optical memory with warm rubidium vapour.* Nature Communications **2**, 174 (2011).

17. M. P. Hedges, J. J. Longdell, Y. Li and M. J. Sellars. *Efficient quantum memory for light.* Nature **465**, 1052–1056 (2010).

18. J. J. Longdell, E. Fraval, M. J. Sellars and N. B. Manson. *Stopped light with storage times greater than one second using electromagnetically induced transparency in a solid.* Physical Review Letters **95**, 063601 (2005).

19. Georg Heinze. et al. (to be published).

20. M. Bonarota, J. L. Le Gouët and T. Chanelière. *Highly multimode storage in a crystal.* New Journal of Physics **13**, 013013 (2011).

21. I. Usmani, M. Afzelius, H. de Riedmatten and N. Gisin. *Mapping multiple photonic qubits into and out of one solid-state atomic ensemble.* Nature Communications **1**, 12 (2010).

22. E. Saglamyurek, N. Sinclair, J. Jin, J. A. Slater, D. Oblak, F. Bussieres, M. George, R. Ricken, W. Sohler and W. Tittel. *Broadband waveguide quantum memory for entangled photons.* Nature **469**, 512–515 (2011).

23. R. W. Equall, Y. Sun, R. L. Cone and R. M. Macfarlane. *Ultraslow Optical Dephasing In* Eu^{3+} : $\mathrm{Y_2}Si\mathrm{O_5}$. Physical Review Letters **72**, 2179–2181 (1994).

24. Brian G. Wybourne. *Spectroscopic properties of rare-earths.* John Wiley (1965).

25. M. Nilsson, L. Rippe, N. Ohlsson, T. Christiansson and S. Kröll. *Initial experiments concerning quantum information processing in rare-earth-ion doped crystals.* Physica Scripta **T102**, 178–185 (2002).

26. N. Ohlsson, R. K. Mohan and S. Kröll. *Quantum computer hardware based on rare-earth-ion-doped inorganic crystals.* Optics Communications **201**, 71–77 (2002).

27. S. Svanberg. *Atomic and molecular spectroscopy.* Springer (2001).

28. W. T. Carnall, G. L. Goodman, K. Rajnak and R. S. Rana. *A Systematic Analysis of the Spectra of the Lanthanides Doped Into Single crystal* $\mathrm{L}a\mathrm{F_3}$. Journal of Chemical Physics **90**, 3443–3457 (1989).

29. Y. C. Sun. *Spectroscopic properties of rare-earths in optical materials, Chapter 7.* edited by G. Liu, and B. Jacquier. Springer Series in Material Science (2005).

30. F. Graf. Investigation of Spectral dynamics in rare earth ion doped crystals using high resolution laser techniques (1998).

31. C. J. Foot. *Atomic physics.* Oxford master series in atomic, optical and laser physics (2005).

32. R. M. Macfarlane and R. M. Shelby. *Coherent transient and holeburning spectroscopy of rare-earth ions in solids.* Elsevier Scientific Publisher (1987).

33. P. Radaelli. *Symmetry in crystallography: understanding the international tables.* Oxford University Press, New York (2011).

34. B. A. Maksimov, V. V. Ilyukhin, Yu. A. Kharitonov and N. V. Belov. *Crystal structure of Yttrium Oxyorthosilicate* $Y_2 0_3 Si G_2 = Y_2 Si O_5$ *dual function of yttrium.* Soviet Physics-Crystallography **15**, 806–812 (1971).

35. T. Bottger, C. W. Thiel, Y. Sun and R. L. Cone. *Optical decoherence and spectral diffusion at 1.5* μm *in* $Er^{3+} : Y_2 Si O_5$ *versus magnetic field, temperature, and* Er^{3+} *concentration.* Physical Review B **73**, 075101 (2006).

36. C. Li, C. Wyon and R. Moncorgé. *Spectroscopic Properties and Fluorescence Dynamics of* Er^{3+} *and* Yb^{3+} *In* $Y_2 Si O_5$. Ieee Journal of Quantum Electronics **28**, 1209–1221 (1992).

37. L. Allen and J. H. Eberly. *Optical resonance and two atoms.* Dover publications (1987).

38. Y. Sun, G. M. Wang, R. L. Cone, R. W. Equall and M. J. M. Leask. *Symmetry considerations regarding light propagation and light polarization for coherent interactions with ions in crystals.* Physical Review B **62**, 15443–15451 (2000).

39. Wikipedia. Periodic table (2013). URL `http://en.wikipedia.org/wiki/Periodic_table#Atomic_radii`.

40. Y. Sun, C. W. Thiel, R. L. Cone, R. W. Equall and R. L. Hutcheson. *Recent progress in developing new rare earth materials for hole burning and coherent transient applications.* Journal of Luminescence **98**, PII S0022–2313(02)00281–8 (2002).

41. R. M. Macfarlane, R. S. Meltzer and B. Z. Malkin. *Optical measurement of the isotope shifts and hyperfine and superhyperfine interactions of Nd in the solid state.* Physical Review B **58**, 5692–5700 (1998).

42. C. W. Thiel, T. Bottger and R. L. Cone. *Rare-earth-doped materials for applications in quantum information storage and signal processing.* Journal of Luminescence **131**, 353–361 (2011).

43. M. D. Levenson. *Introduction to nonlinear laser spectroscopy.* Academic Press, New York (1982).

44. Y. R. Shen. *The principles of nonlinear optics.* Wiley-interscience, New York (1984).

45. A. Szabo. *Laser-induced fluorescence-line narrowing in ruby.* Physical Review Letters **25**, 924–927 (1970).

46. A. Szabo. *Observation of hole burning and cross relaxation effects in ruby.* Physical Review B **11**, 4512–4517 (1975).

47. N. A. Kurnit, S. R. Hartmann and I. D. Abella. *Observation of photon echo.* Physical Review Letters **13**, 567–569 (1964).

48. A. Z. Genack, R. M. Macfarlane and R. G. Brewer. *Optical free-induction decay in* $LaF_3 : Pr^{3+}$. Physical Review Letters **37**, 1078–1080 (1976).

49. B. E. A. Saleh and M. C. Teich. *Fundamentals of photonics.* Wiley Series in Pure and Applied Optics (2007).

50. Y. Zhang and M. Xiao. *Multi-wave mixing processes.* Springer (2009).

51. R. M. Camacho. *Implementations of slow light using double-resonances.* PhD thesis Department of Physics and Astronomy The College Arts and Sciences University of Rochester, Rochester, New York (2008).

52. E. L. Hahn. *Spin echoes.* Physical Review **80**, 580–594 (1950).

53. P. R. Berman and W. E. Lamb. *Theory of collision effects on line shapes using a quantum-mechanical description of atomic center-of-mass motion-application to lasers .II. Pseudoclassical collision model and steady-state laser intensities.* Physical Review A **4**, 319–343 (1971).

54. P. R. Berman and V. S. Malinovsky. *Principles of laser spectroscopy and quantum optics.* Princeton University Press (2011).

55. R. W. Boyd. *Nonlinear optics.* Academic Press, New York (2003).

56. C. S. Cornish, W. R. Babbitt and L. Tsang. *Demonstration of highly efficient photon echoes.* Optics Letters **25**, 1276–1278 (2000).

57. T. Wang, C. Greiner and T. W. Mossberg. *Experimental observation of photon echoes and power-efficiency analysis in a cavity environment.* Optics Letters **23**, 1736–1738 (1998).

58. L. Tsang and C. S. Cornish. *Analytic solutions of the Maxwell-Bloch equations for high photon-echo efficiency of multiple pulse sequences.* Journal of the Optical Society of America B-optical Physics **20**, 379–390 (2003).

59. C. C. Gerry and P. L. Knight. *Introductory quantum optics.* Cambridge University Press (2005).

60. J. Ruggiero, J. L. Le Gouët, C. Simon and T. Chanelière. *Why the two-pulse photon echo is not a good quantum memory protocol.* Physical Review A **79**, 053851 (2009).

61. J. Ruggiero, T. Chanelière and J. L. Le Gouët. *Coherent response to optical excitation in a strongly absorbing rare-earth ion-doped crystal.* Journal of the Optical Society of America B-optical Physics **27**, 32–37 (2010).

62. N. Sangouard, C. Simon, J. Minár, M. Afzelius, T. Chanelière, N. Gisin, J.-L. Le Gouët, H. de Riedmatten and W. Tittel. *Impossibility of faithfully storing single photons with the three-pulse photon echo.* Physical Review A **81**, 062333 (2010).

63. B. Julsgaard, A. Walther, S. Kröll and L. Rippe. *Understanding laser stabilization using spectral hole burning.* Optics Express **15**, 11444–11465 (2007).

64. L. Rippe. *Quantum computing with naturally trapped sub-nanometre-spaced ions.* PhD thesis Division of Atomic Physics, Lund University (2006).

65. B. C. Young, F. C. Cruz, W. M. Itano and J. C. Bergquist. *Visible lasers with subhertz linewidths.* Physical Review Letters **82**, 3799–3802 (1999).

66. H. Stoehr, E. Mensing, J. Helmcke and U. Sterr. *Diode laser with 1* Hz *linewidth.* Optics Letters **31**, 736–738 (2006).

67. A. D. Ludlow, X. Huang, M. Notcutt, T. Zanon-Willette, S. M. Foreman, M. M. Boyd, S. Blatt and J. Ye. *Compact, thermal-noise-limited optical cavity for diode laser stabilization at 1 X* 10^{-15}. Optics Letters **32**, 641–643 (2007).

68. M. J. Thorpe, L. Rippe, T. M. Fortier, M. S. Kirchner and T. Rosenband. *Frequency stabilization to 6 x* 10^{-16} *via spectral-hole burning.* Nature Photonics **5**, 689–694 (2011).

69. D. R. Leibrandt, M. J. Thorpe, M. Notcutt, R. E. Drullinger, T. Rosenband and J. C. Bergquist. *Spherical reference cavities for frequency stabilization of lasers in non-laboratory environments.* Optics Express **19**, 3471–3482 (2011).

70. R. W. P. Drever, J. L. Hall, F. V. Kowalski, J. Hough, G. M. Ford, A. J. Munley and H. Ward. *Laser phase and frequency stabilization using an optical-resonator.* Applied Physics B-photophysics and Laser Chemistry **31**, 97–105 (1983).

71. M. Zhu and J. L. Hall. *Stabilization of optical-phase frequency of a laser system - Application to a commercial dye-laser with an external stabilizer.* Journal of the Optical Society of America B-optical Physics **10**, 802–816 (1993).

72. E. D. Black. *An introduction to Pound-Drever-Hall laser frequency stabilization.* American Journal of Physics **69**, 79–87 (2001).

73. P. B. Sellin, N. M. Strickland, T. Bottger, J. L. Carlsten and R. L. Cone. *Laser stabilization at 1536 nm using regenerative spectral hole burning.* Physical Review B **63**, 155111 (2001).

74. T. Bottger, Y. Sun, G. J. Pryde, G. Reinemer and R. L. Cone. *Diode laser frequency stabilization to transient spectral holes and spectral diffusion in* $\mathrm{Er}^{3+}:\mathrm{Y}_2Si\mathrm{O}_5$ *at 1536 nm.* Journal of Luminescence **94**, 565–568 (2001).

75. T. Bottger, G. J. Pryde and R. L. Cone. *Programmable laser frequency stabilization at 1523 nm by use of persistent spectral hole burning.* Optics Letters **28**, 200–202 (2003).

76. K. D. Merkel, R. D. Peters, P. B. Sellin, K. S. Repasky and W. R. Babbitt. *Accumulated programming of a complex spectral grating.* Optics Letters **25**, 1627–1629 (2000).

77. L. Rippe, B. Julsgaard, A. Walther and S. Kröll. *Laser stabilization using spectral hole burning.* arXiv:quant-ph/0611056v1 (2006).

78. A. Wiman. Laser stabilization to a low-expansion Fabry-Pérot cavity. Master's thesis Atomic Physics division, Lund University (2011).

79. A. E. Siegman. *Lasers.* University Science Books, Mill Valley, California (1985).

80. G. C. Bjorklund, M. D. Levenson, W. Lenth and C. Oritz. *Frequency-modulation (FM) spectroscopy - Theory of lineshapes and signal-to-noise analysis.* Applied Physics B-photophysics and Laser Chemistry **32**, 145–152 (1983).

81. S. Rikte, G. Kristensson and M. Andersson. *Propagation in bianisotropic media - reflection and transmission.* Ieee Proceedings-microwaves Antennas and Propagation **148**, 29–36 (2001).

82. H. Haug and S. W. Koch. *Quantum theory of the optical and electronic properties of semiconductors.* World Scientific (2004).

83. R. Beach, M. D. Shinn, L. Davis, R. W. Solart and W. F. Krupke. *Optical-absorption and stimulated-emission of neodymium in yttrium orthosilicate.* Ieee Journal of Quantum Electronics **26**, 1405–1412 (1990).

84. A. P. Lund and T. C. Ralph. *Nondeterministic gates for photonic single-rail quantum logic.* Physical Review A **66**, 032307 (2002).

85. I. Marcikic, H. de Riedmatten, W. Tittel, V. Scarani, H. Zbinden and N. Gisin. *Time-bin entangled qubits for quantum communication created by femtosecond pulses.* Physical Review A **66**, 062308 (2002).

86. M. D. Eisaman, J. Fan, A. Migdall and S. V. Polyakov. *Invited Review Article: Single-photon sources and detectors.* Review of Scientific Instruments **82**, 071101 (2011).

87. C. H. Bennett, G. Brassard, C. Crepeau, R. Jozsa, A. Peres and W. K. Wootters. *Teleporting an unknown quantum state via dual classical and Einstein-Podolsky-Rosen channels.* Physical Review Letters **70**, 1895–1899 (1993).

88. E. Waks, A. Zeevi and Y. Yamamoto. *Security of quantum key distribution with entangled photons against individual attacks.* Physical Review A **65**, 052310 (2002).

89. J. W. Pan, S. Gasparoni, R. Ursin, G. Weihs and A. Zeilinger. *Experimental entanglement purification of arbitrary unknown states.* Nature **423**, 417–422 (2003).

90. J. Appel, P. J. Windpassinger, D. Oblak, U. B. Hoff, N. Kjaergaard and E. S. Polzik. *Mesoscopic atomic entanglement for precision measurements beyond the standard quantum limit.* Proceedings of the National Academy of Sciences of the United States of America **106**, 10960–10965 (2009).

91. C. Simon, M. Afzelius, J. Appel, A. Boyer de la Giroday, S. J. Dewhurst, N. Gisin, C. Y. Hu, F. Jelezko, S. Kröll, J. H. Muller, J. Nunn, E. S. Polzik, J. G. Rarity, H. De Riedmatten, W. Rosenfeld, A. J. Shields, N. Skoeld, R. M. Stevenson, R. Thew, I. A. Walmsley, M. C. Weber, H. Weinfurter, J. Wrachtrup and R. J. Young. *Quantum memories.* European Physical Journal D **58**, 1–22 (2010).

92. K. Hammerer, M. M. Wolf, E. S. Polzik and J. I. Cirac. *Quantum benchmark for storage and transmission of coherent states.* Physical Review Letters **94**, 150503 (2005).

93. S. Massar and S. Popescu. *Optimal extraction of information from finite quantum ensembles.* Physical Review Letters **74**, 1259–1263 (1995).

94. N. Sangouard, C. Simon, M. Afzelius and N. Gisin. *Analysis of a quantum memory for photons based on controlled reversible inhomogeneous broadening.* Physical Review A **75**, 032327 (2007).

95. J. J. Longdell, G. Hétet, P. K. Lam and M. J. Sellars. *Analytic treatment of controlled reversible inhomogeneous broadening quantum memories for light using two-level atoms.* Physical Review A **78**, 032337 (2008).

96. S. A. Moiseev and S. Kröll. *Complete reconstruction of the quantum state of a single-photon wave packet absorbed by a Doppler-broadened transition.* Physical Review Letters **87**, 173601 (2001).

97. M. Nilsson and S. Kröll. *Solid state quantum memory using complete absorption and re-emission of photons by tailored and externally controlled inhomogeneous absorption profiles.* Optics Communications **247**, 393–403 (2005).

98. G. Hétet, J. J. Longdell, M. J. Sellars, P. K. Lam and B. C. Buchler. *Multimodal properties and dynamics of gradient echo quantum memory.* Physical Review Letters **101**, 203601 (2008).

99. N. Sangouard, C. Simon, H. de Riedmatten and N. Gisin. *Quantum repeaters based on atomic ensembles and linear optics.* Reviews of Modern Physics **83**, 33–80 (2011).

100. M. Afzelius, I. Usmani, A. Amari, B. Lauritzen, A. Walther, C. Simon, N. Sangouard, J. Minár, H. de Riedmatten, N. Gisin and S. Kröll. *Demonstration of atomic frequency comb memory for light with spin-wave storage.* Physical Review Letters **104**, 040503 (2010).

101. X. H. Bao, A. Reingruber, P. Dietrich, J. Rui, A. Dück, T. Strassel, L. Li, N. L. Liu, B. Zhao and J. W. Pan. *Efficient and long-lived quantum memory with cold atoms inside a ring cavity.* Nature Physics **8**, 517–521 (2012).

102. M. Steger, K. Saeedi, M. L. W. Thewalt, J. J. L. Morton, H. Riemann, N. V. Abrosimov, P. Becker and H. J. Pohl. *Quantum information storage for over 180 s using donor spins in a* ^{28}Si *"semiconductor vacuum".* Science **336**, 1280–1283 (2012).

103. P. C. Maurer, G. Kucsko, C. Latta, L. Jiang, N. Y. Yao, S. D. Bennett, F. Pastawski, D. Hunger, N. Chisholm, M. Markham, D. J. Twitchen, J. I. Cirac and M. D. Lukin. *Room-temperature quantum bit memory exceeding one second.* Science **336**, 1283–1286 (2012).

104. E. Fraval, M. J. Sellars and J. J. Longdell. *Dynamic decoherence control of a solid-state nuclear-quadrupole qubit.* Physical Review Letters **95**, 030506 (2005).

105. K. Holliday, M. Croci, E. Vauthey and U. P. Wild. *Spectral hole-burning and holography in an* $\mathrm{Y_2S}i\mathrm{O_5} : \mathrm{P}r^{3+}$ *crystal.* Physical Review B **47**, 14741–14752 (1993).

106. M. Yamaguchi, K. Koyama, T. Suemoto and M. Mitsunaga. *Perturbed ion sites in* $\mathrm{E}u^{3+} : \mathrm{YA}l\mathrm{O_3}$ *studied by optical-rf double-resonance spectroscopy.* Physical Review B **59**, 9126–9131 (1999).

107. N. Timoney, B. Lauritzen, I. Usmani, M. Afzelius and N. Gisin. *Atomic frequency comb memory with spin-wave storage in* $^{153}\mathrm{Eu}^{3+} : \mathrm{Y_2S}i\mathrm{O_5}$. Journal of Physics B-atomic Molecular and Optical Physics **45**, 124001 (2012).

108. L. Viola, E. Knill and S. Lloyd. *Dynamical decoupling of open quantum systems.* Physical Review Letters **82**, 2417–2421 (1999).

109. W. Yang, Z. Y. Wang and R. B. Liu. *Preserving qubit coherence by dynamical decoupling.* Frontiers of Physics **6**, 2–14 (2011).

110. A. M. Souza, G. A. Alvarez and D. Suter. *Robust dynamical decoupling.* Philosophical Transactions of the Royal Society A-mathematical Physical and Engineering Sciences **370**, 4748–4769 (2012).

111. E. Fraval, M. J. Sellars and J. J. Longdell. *Method of extending hyperfine coherence times in* $\mathrm{P}r^{3+} : \mathrm{Y_2S}i\mathrm{O_5}$. Physical Review Letters **92**, 077601 (2004).

112. C. Simon, H. de Riedmatten, M. Afzelius, N. Sangouard, H. Zbinden and N. Gisin. *Quantum repeaters with photon pair sources and multimode memories.* Physical Review Letters **98**, 190503 (2007).

113. M. Afzelius, C. Simon, H. de Riedmatten and N. Gisin. *Multimode quantum memory based on atomic frequency combs.* Physical Review A **79**, 052329 (2009).

114. J. Nunn, K. Reim, K. C. Lee, V. O. Lorenz, B. J. Sussman, I. A. Walmsley and D. Jaksch. *Multimode memories in atomic ensembles.* Physical Review Letters **101**, 260502 (2008).

115. B. Lauritzen, J. Minár, H. de Riedmatten, M. Afzelius, N. Sangouard, C. Simon and N. Gisin. *Telecommunication-wavelength solid-state memory at the single photon level.* Physical Review Letters **104**, 080502 (2010).

116. B. Lauritzen, J. Minár, M. de Riedmatten, H. Afzelius and N. Gisin. *Approaches for a quantum memory at telecommunication wavelengths.* Physical Review A **83**, 012318 (2011).

117. J. M. Raimond, M. Brune and S. Haroche. *Colloquium: Manipulating quantum entanglement with atoms and photons in a cavity.* Reviews of Modern Physics **73**, 565–582 (2001).

118. T. F. Gallagher. *Rydberg atoms.* Cambridge University Press (1994).

119. O. Landry, J. A. W. van Houwelingen, A. Beveratos, H. Zbinden and N. Gisin. *Quantum teleportation over the Swisscom telecommunication network.* Journal of the Optical Society of America B-optical Physics **24**, 398–403 (2007).

120. T. B. Pittman, B. C. Jacobs and J. D. Franson. *Single photons on pseudodemand from stored parametric down-conversion.* Physical Review A **66**, 042303 (2002).

121. X. Maitre, E. Hagley, G. Nogues, C. Wunderlich, P. Goy, M. Brune, J. M. Raimond and S. Haroche. *Quantum memory with a single photon in a cavity.* Physical Review Letters **79**, 769–772 (1997).

122. T. Tanabe, M. Notomi, H. Taniyama and E. Kuramochi. *Dynamic release of trapped light from an ultrahigh-Q nanocavity via adiabatic frequency tuning.* Physical Review Letters **102**, 043907 (2009).

123. H. P. Specht, C. Nolleke, A. Reiserer, M. Uphoff, E. Figueroa, S. Ritter and G. Rempe. *A single-atom quantum memory.* Nature **473**, 190–193 (2011).

124. A. D. Boozer, A. Boca, R. Miller, T. E. Northup and H. J. Kimble. *Reversible state transfer between light and a single trapped atom.* Physical Review Letters **98**, 193601 (2007).

125. B. B. Blinov, D. L. Moehring, L. M. Duan and C. Monroe. *Observation of entanglement between a single trapped atom and a single photon.* Nature **428**, 153–157 (2004).

126. B. Julsgaard, J. Sherson, J. I. Cirac, J. Fiurasek and E. S. Polzik. *Experimental demonstration of quantum memory for light.* Nature **432**, 482–486 (2004).

127. D. G. England, P. S. Michelberger, T. F. M. Champion, K. F. Reim, K. C. Lee, M. R. Sprague, X. M. Jin, N. K. Langford, W. Kolthammer, J. Nunn and I. A. Walmsley. *High-fidelity polarization storage in a gigahertz bandwidth quantum memory.* Journal of Physics B-atomic Molecular and Optical Physics **45**, 124008 (2012).

128. O. S. Mishina, N. V. Larionov, A. S. Sheremet, I. M. Sokolov and D. V. Kupriyanov. *Stimulated Raman process in a scattering medium applied to the quantum memory scheme.* Physical Review A **78**, 042313 (2008).

129. M. Fleischhauer and M. D. Lukin. *Dark-state polaritons in electromagnetically induced transparency.* Physical Review Letters **84**, 5094–5097 (2000).

130. S. E. Harris. *Electromagnetically induced transparency.* Physics Today **50**, 36–42 (1997).

131. M. D. Lukin. *Colloquium: Trapping and manipulating photon states in atomic ensembles.* Reviews of Modern Physics **75**, 457–472 (2003).

132. M. Fleischhauer, A. Imamoglu and J. P. Marangos. *Electromagnetically induced transparency: Optics in coherent media.* Reviews of Modern Physics **77**, 633–673 (2005).

133. B. Kraus, W. Tittel, N. Gisin, M. Nilsson, S. Kröll and J. I. Cirac. *Quantum memory for nonstationary light fields based on controlled reversible inhomogeneous broadening.* Physical Review A **73**, 020302 (2006).

134. A. L. Alexander, J. J. Longdell, M. J. Sellars and N. B. Manson. *Photon echoes produced by switching electric fields.* Physical Review Letters **96**, 043602 (2006).

135. M. Bonarota, J. Ruggiero, J. L. Le Gouët and T. Chanelière. *Efficiency optimization for atomic frequency comb storage.* Physical Review A **81**, 033803 (2010).

136. G. Hétet, J. J. Longdell, A. L. Alexander, P. K. Lam and M. J. Sellars. *Electro-optic quantum memory for light using two-level atoms.* Physical Review Letters **100**, 023601 (2008).

137. M. Hosseini, B. M. Sparkes, G. Hétet, J. J. Longdell, P. K. Lam and B. C. Buchler. *Coherent optical pulse sequencer for quantum applications.* Nature **461**, 241–245 (2009).

138. V. Damon, M. Bonarota, A. Louchet-Chauvet, T. Chanelière and J. . L. Le Gouët. *Revival of silenced echo and quantum memory for light.* New Journal of Physics **13**, 093031 (2011).

139. D. L. McAuslan, P. M. Ledingham, W. R. Naylor, S. E. Beavan, M. P. Hedges, M. J. Sellars and J. J. Longdell. *Photon-echo quantum memories in inhomogeneously broadened two-level atoms.* Physical Review A **84**, 022309 (2011).

140. S. E. Beavan, P. M. Ledingham, J. J. Longdell and M. J. Sellars. *Photon echo without a free induction decay in a double-Lambda system.* Optics Letters **36**, 1272–1274 (2011).

141. S. E. Beavan, M. P. Hedges and M. J. Sellars. *Demonstration of photon-echo rephasing of spontaneous emission.* Physical Review Letters **109**, 093603 (2012).

142. Y. Colombe, T. Steinmetz, G. Dubois, F. Linke, D. Hunger and J. Reichel. *Strong atom-field coupling for Bose-Einstein condensates in an optical cavity on a chip.* Nature **450**, 272–U9 (2007).

143. W. Nakagawa, P. C. Sun, C. H. Chen and Y. Fainman. *Wide-field-of-view narrow-band spectral filters based on photonic crystal nanocavities.* Optics Letters **27**, 191–193 (2002).

144. H. S. Rong, R. Jones, A. S. Liu, O. Cohen, D. Hak, A. Fang and M. Paniccia. *A continuous-wave Raman silicon laser.* Nature **433**, 725–728 (2005).

145. G. S. Pati, M. Salit, K. Salit and M. S. Shahriar. *Demonstration of a tunable-bandwidth white-light interferometer using anomalous dispersion in atomic vapor.* Physical Review Letters **99**, 133601 (2007).

146. A. V. Gorshkov, A. Andre, M. D. Lukin and A. S. Sorensen. *Photon storage in Lambda-type optically dense atomic media. II. Free-space model.* Physical Review A **76**, 033805 (2007).

147. A. V. Gorshkov, A. Andre, M. D. Lukin and A. S. Sorensen. *Photon storage in Lambda-type optically dense atomic media. I. Cavity model.* Physical Review A **76**, 033804 (2007).

148. A. V. Gorshkov, A. Andre, M. D. Lukin and A. S. Sorensen. *Photon storage in Lambda-type optically dense atomic media. III. Effects of inhomogeneous broadening.* Physical Review A **76**, 033806 (2007).

149. M. Afzelius and C. Simon. *Impedance-matched cavity quantum memory.* Physical Review A **82**, 022310 (2010).

150. S. A. Moiseev, S. N. Andrianov and F. F. Gubaidullin. *Efficient multimode quantum memory based on photon echo in an optimal QED cavity.* Physical Review A **82**, 022311 (2010).

151. C. C. Davis. *Lasers and electro-optics: fundamentals and engineering.* Cambridge University Press. (1996).

152. J. Zhang, G. Hernandez and Y. Zhu. *Slow light with cavity electromagnetically induced transparency.* Optics Letters **33**, 46–48 (2008).

153. L. Rippe, M. Nilsson, S. Kröll, R. Klieber and D. Suter. *Experimental demonstration of efficient and selective population transfer and qubit distillation in a rare-earth-metal-ion-doped crystal.* Physical Review A **71**, 062328 (2005).

154. M. S. Silver, R. I. Joseph, C. N. Chen, V. J. Sank and D. I. Hoult. *Selective-population inversion in NMR.* Nature **310**, 681–683 (1984).

155. I. Roos and K. Mølmer. *Quantum computing with an inhomogeneously broadened ensemble of ions: Suppression of errors from detuning variations by specially adapted pulses and coherent population trapping.* Physical Review A **69**, 022321 (2004).

156. L. V. Hau, S. E. Harris, Z. Dutton and C. H. Behroozi. *Light speed reduction to 17 metres per second in an ultracold atomic gas.* Nature **397**, 594–598 (1999).

157. D. F. Phillips, A. Fleischhauer, A. Mair, R. L. Walsworth and M. D. Lukin. *Storage of light in atomic vapor.* Physical Review Letters **86**, 783–786 (2001).

158. A. V. Turukhin, V. S. Sudarshanam, M. S. Shahriar, J. A. Musser, B. S. Ham and P. R. Hemmer. *Observation of ultraslow and stored light pulses in a solid.* Physical Review Letters **88**, 023602 (2002).

159. J. B. Khurgin and R. S. Tucker. *Slow light : science and application.* Boca Raton: CRC Press. (2009).

160. R. N. Shakhmuratov, A. Rebane, P. Megret and J. Odeurs. *Slow light with persistent hole burning.* Physical Review A **71**, 053811 (2005).

161. A. Walther, A. Amari, S. Kröll and A. Kalachev. *Experimental superradiance and slow-light effects for quantum memories.* Physical Review A **80**, 012317 (2009).(Correction: the expression for the group velocity needs to be corrected to $v_g = \frac{2\pi\Gamma}{\alpha}$ in subsection "IV.B. Slow light effects")).

162. R. Winston, W. T. Welford, J. C. Minano and P. Benýítez. *Nonimaging optics.* Academic, Boston, MA (2005).

163. Y. Li, H. Zhang, C. Kim, K. H. Wagner, P. Hemmer and L. V. Wang. *Pulsed ultrasound-modulated optical tomography using spectral-hole burning as a narrowband spectral filter.* Applied Physics Letters **93**, 011111 (2008).

164. H. Zhang, M. Sabooni, L. Rippe, C. Kim, S. Kröll, L. V. Wang and P. R. Hemmer. *Slow light for deep tissue imaging with ultrasound modulation.* Applied Physics Letters **100**, 131102 (2012).

165. D. Dalecki. *Mechanical bioeffects of ultrasound.* Annual Review of Biomedical Engineering **6**, 229–248 (2004).

166. S. Sakadzic and L. V. Wang. *Correlation transfer equation for multiply scattered light modulated by an ultrasonic pulse.* Journal of the Optical Society of America A-optics Image Science and Vision **24**, 2797–2806 (2007).

167. A. Louchet-Chauvet, R. Lauro, P. Goldner, F. Ramaz, T. Chaneliére and J. L. Le Gouët. *High resolution, large dynamic range spectral filtering at 800 nm using* Tm*:*YAG *crystals.* Advances In Photonics of Quantum Computing, Memory, and Communication IV **7948**, 794805 (2011).

PAPERS

PAPER I

Towards an efficient atomic frequency comb quantum memory

A. Amari, A. Walther, M. Sabooni, M. Huang, S. Kröll, M. Afzelius, I. Usmani, B. Lauritzen, N. Sangouard, H. de Riedmatten, N. Gisin.

Journal of Luminescence **130**, 1579–1585 (2010).

Journal of Luminescence 130 (2010) 1579–1585

Contents lists available at ScienceDirect

Journal of Luminescence

journal homepage: www.elsevier.com/locate/jlumin

Towards an efficient atomic frequency comb quantum memory

A. Amari [a,*], A. Walther [a], M. Sabooni [a], M. Huang [a], S. Kröll [a], M. Afzelius [b], I. Usmani [b], B. Lauritzen [b], N. Sangouard [b], H. de Riedmatten [b], N. Gisin [b]

[a] *Department of Physics, Lund University, P.O. Box 118, SE-22100 Lund, Sweden*
[b] *Group of Applied Physics, University of Geneva, CH-1211 Geneva 4, Switzerland*

ARTICLE INFO

Available online 1 February 2010

Keywords:
Quantum repeater
Quantum memory
Atomic frequency comb
Storage efficiency

ABSTRACT

We present an efficient photon-echo experiment based on atomic frequency combs [Phys. Rev. A 79 (2009) 052329]. Echoes containing an energy of up to 35% of that of the input pulse are observed in a Pr^{3+}-doped Y_2SiO_5 crystal. This material allows for the precise spectral holeburning needed to make a sharp and highly absorbing comb structure. We compare our results with a simple theoretical model with satisfactory agreement. Our results show that atomic frequency combs has the potential for high-efficiency storage of single photons as required in future long-distance communication based on quantum repeaters.

1. Introduction

The distribution of entanglement over long distances is a critical capability for future long-distance quantum communication (e.g. quantum cryptography) and more generally for quantum networks. This can be achieved via so-called quantum repeaters [1–4], which can overcome the exponential transmission losses in optical fiber networks. Quantum memories (QM) for photons [5–9] are key components in quantum repeaters, because the distribution of entanglement using photons is of probabilistic nature due to the transmission losses over long quantum channels. QMs enables storage of entanglement in one repeater segment until entanglement has also been established in the adjacent sections. For quantum repeaters a QM should be able to store single-photon states with high conditional fidelity F and with high storage and retrieval efficiency, η [4]. Further, it has recently been shown that in order to reach useful entanglement distribution rates in a repeater, QMs with multiplexing capacity (multimode QM) are necessary [3,10].

Significant progress have been achieved lately using atomic ensembles for manipulating the propagation and quantum state of an optical field, see Hammerer et al. [11] for a recent review. Storage of single photons using electromagnetically induced transparency (EIT) has been demonstrated with warm [7] and cold vapors [6,8] of alkali atoms. Storage of light at the single photon level has been demonstrated also in rare-earth-ion-doped crystals (REIC) [9]. REICs are characterized by large optical inhomogeneous broadening which enables storage and recall of coherent information by manipulating and controlling the inhomogeneous dephasing using echo techniques. Although traditional photon echoes cannot be used in the single-photon regime due to spontaneous-emission noise induced by the π-pulse [12], photon echo techniques avoiding this noise have been proposed; controlled reversible inhomogeneous broadening (CRIB) [13–17] and more recently atomic frequency combs (AFC) [18]. The AFC protocol may offer a breakthrough for the practical construction of quantum repeaters capable of achieving sufficient entanglement distribution rate, since the number of modes that can be stored in an AFC QM is independent of the memory material absorption depth. Since the proposal of the AFC scheme, storage of light pulses at the single photon level (so called weak coherent states) has been shown in Nd^{3+}:YVO_4 [9]. The fidelity of the storage was measured by storing a time-bin qubit and performing an interference measurement on the recalled qubit. The resulting interference fringe visibility was V=95%, which corresponds to a fidelity $F=(1+V)/2$ [19] of 97.5%. This shows that light at the single photon level can be stored and retrieved without introducing noise, and future experiments are likely to improve the fidelity further. The combined storage and retrieval efficiency, however, was only 0.5% in that experiment. A more recent experiment in Tm^{3+}:YAG [20] showed improved efficiency of 9%, also with weak coherent states. Finally, storage of 64 weak coherent states encoded in different temporal modes has been achieved in Nd^{3+}:Y_2SiO_5 [21], underlying the high multimode capacity of the AFC scheme. In view of these encouraging results in terms of fidelity and multimode storage, it is clear that increasing the efficiency is of great importance, particularly in the perspective future long-distance quantum repeaters where QM efficiencies of 90% are necessary with the architectures known today [4].

---

[*] Corresponding author. Tel.:+46 462229625.
E-mail address: atia.amari@fysik.lth.se (A. Amari).

0022-2313/$ - see front matter © 2010 Elsevier B.V. All rights reserved.
doi:10.1016/j.jlumin.2010.01.012

Here we report a photon-echo experiment based on an AFC in a Pr^{3+}-doped Y_2SiO_5 crystal. We measure echoes containing an energy of up to 35% of that of the input pulse, which is the highest AFC echo efficiencies measured so far. This shows that AFC-based schemes can be used for efficient light storage. This improvement is possible because of a good control of the procedure that creates the atomic frequency comb, via optical pumping techniques, and because of a storage medium with high optical depth. Combs with peaks of widths 100–300 kHz with peak absorption depths approaching 10 were created inside a transparent region created by optical pumping techniques in a part of the inhomogeneous profile in a $Pr^{3+}:Y_2SiO_5$ crystal. We also examine parameters related to the experimental optimization of the efficiency and compare to a theoretical model in order to understand how to further improve the efficiency of storage and retrieval from a memory using the AFC scheme.

The paper is organized in the following way. In Section 2 we give an overview of the theory of AFC. In Section 3 the experimental setup is described. Preparation of a narrow periodic series of absorption peaks is discussed in Section 4. In Section 5 experimental results of AFC echoes are presented and compared with the theoretical model. Conclusions are given in Section 6.

2. Theory of AFC

We consider an ensemble of atoms with a transition $|g\rangle - |e\rangle$ having a narrow homogeneous linewidth γ_h, but a large inhomogeneous broadening $\Gamma_{in} \gg \gamma_h$. There are thus many addressable spectral channels within the optical transition. We also assume that there is at least one more meta-stable ground state, $|aux\rangle$, having a long population lifetime. This allows a high-resolution spectral shaping of the $|g\rangle - |e\rangle$ transition by spectral hole burning, where $|aux\rangle$ is used as population storage reservoir. These properties are often found in rare-earth-ion-doped crystals [22,23], which are considered here. The detailed experimental procedure for precise spectral shaping depend on the particular system. In Section 4 we discuss the procedure for Praseodymium doped Y_2SiO_5 crystals.

We assume that the inhomogeneously broadened transition has been shaped into a periodic series of narrow peaks, called an atomic frequency comb, see Fig. 3. We further assume that the light pulse to be stored has a spectral bandwidth, γ_p, larger than the periodicity in the comb ($\gamma_p > \varDelta$), but smaller than the total comb structure. The interaction between the input pulse and a ground-state population grating versus frequency generally results in a photon echo emission after a time $1/\varDelta$, which is used in accumulated or spectrally programmed photon echoes [24–29]. The echo emission arises from the evolution of the atomic coherence induced by the input pulse, which periodically rephases due to the periodicity in the atomic population grating. In typical echo experiments only a small fraction of the input pulse is re-emitted in the echo and the storage time is not variable since it is set by the predetermined grating periodicity $\varDelta$. This is not useful for quantum repeaters where efficiencies close to 100% and on-demand read-out of the quantum memory is necessary [3]. Solutions to these issues were, however, recently proposed in Ref. [18].

In Ref. [18] it is shown theoretically that a comb-shaped grating consisting of sharp and strongly absorbing peaks could generate a very efficient echo. This can be understood in terms of the Fourier-transform of the grating function, which governs the evolution of the atomic coherence. The periodicity in frequency results in a periodic time evolution, with an overall decay given by the width of the peak in the comb. For a series of well-separated Gaussian peaks, with full width at half maximum (FWHM) γ, the decay (dephasing) is given by $e^{-t^2\tilde{\gamma}^2/2}$ where $\tilde{\gamma} = \gamma/\sqrt{8\ln 2}$. For the first echo emission at $t = 2\pi/\varDelta$ this dephasing factor becomes $e^{-(1/F^2)(\pi^2/4\ln 2)}$ (note that the factor applies to the field amplitude), where $F = \varDelta/\gamma$. From this observation it follows that a high-finesse grating strongly reduces the intrinsic dephasing. In general the dephasing factor (for the field amplitude) is given by the Fourier-transform of one peak in the comb.

Obtaining a high efficiency echo also requires a strong interaction between the ensemble of atoms and the field, which can be achieved by a high absorption depth, d. It is shown in Ref. [18] that the comb absorbs uniformly over the photon bandwidth, under the assumption that $\gamma_p > \varDelta$. The effective absorption $\tilde{d}$ depth depend on the exact shape of the peaks in the comb, but in general it decreases with increasing F for a given peak amplitude, since the total number of atoms decreases. For Gaussian peaks one finds that $\tilde{d} \approx d/F$, and the fraction of the input light that is transmitted through the AFC is given by [18]

$$T = e^{-\tilde{d}}, \tag{1}$$

while the absorption is simply given by $1 - T$. For an AFC consisting of peaks with Gaussian line shape the resulting echo efficiency is given by (see Ref. [18] for the derivation)

$$\eta = \tilde{d}^2 e^{-\tilde{d}} e^{-\frac{1}{F^2}\frac{\pi^2}{2\ln 2}}, \tag{2}$$

where qualitatively the first factor can be understood as the coherent response of the sample, the second factor the re-absorption of the echo and the last factor the previously mentioned dephasing. For a high finesse, F, and high peak absorption d, the efficiency tends to a maximum of 54% for an effective absorption depth $\tilde{d} = 2$, limited by re-absorption of the echo. Higher efficiency can be achieved using three-level storage and counter-propagating fields [18] (see below). In this work we show experimental efficiencies up to 35%, which is significantly higher than previous AFC experiments. This improvement results from our ability to make high finesse, high absorbing comb structures.

We also note that a solution to the predetermined storage time was proposed in Ref. [18] (see above). It is based on coherent transfer of the excited state amplitude to a long-lived ground state coherence, for instance a spin coherence, before the appearance of the echo. The memory can be read-out by transferring back the amplitude to the excited state, after a time determined by the user. This aspect of the proposal was recently demonstrated experimentally [30]. A three-level system and counterpropagating control pulses allows for a spatial reversal of the propagation of the echo (so called backward recall). In the absence of dephasing backward recall can reach 100% efficiency by cancelation of the re-absorption, as discussed in Refs. [13,15,18,31,32].

3. Experiment

The measurements were performed on the site 1 transition $^1D_2 - {}^3H_4$ at 605.977 nm in a $Pr^{3+}:Y_2SiO_5$ crystal immersed in liquid helium at a temperature close to 2.1 K. The sample was $20 \times 10 \times 10\,\text{mm}^3$ and had a Pr^{3+} concentration of 0.05% which gives an absorption depth in the range $60 < d < 80$ [33] at the center of the inhomogeneous profile. The high absorption was critical in order to obtain highly absorbing peaks (see Section 4).

A ring dye laser (Coherent699-21) using Rhodamine 6G pumped by $Nd:YVO_4$ laser (Coherent Verdi) is used to give 600 mW output power at $\lambda = 605.977$ nm. The laser is stabilized against a spectral hole in a second $Pr^{3+}:Y_2SiO_5$ crystal, yielding a coherence time $> 100\,\mu s$ and a frequency drift < 1 kHz/s [34]. In order to create the desired pulse shapes and to eliminate beam movement accompanying frequency shifts, the laser light was passed twice through a 200 MHz acousto-optic modulator (AOM) with a bandwidth of 100 MHz. A 1 GS/s arbitrary waveform generator (Tektronix AWG520) controlled the AOM, allowing direct control of the light pulse amplitude, phase, and frequency.

After the AOM, the light passed through a single mode optical fiber to clean up the spatial mode. A beam sampler removed a small percentage of the light before the cryostat to be used as a reference beam. The rest of the beam passed through a $\lambda/2$ plate, such that the light polarization could be aligned along the transition dipole moment direction to give maximum absorption. The beam was then focused to a 100 μm radius at the center of the sample, which gave Rabi frequencies of maximum 2 MHz for the strongest transitions.

The spectral structures were measured by scanning the light frequency across the spectral structure and recording the intensities of both the transmitted and the reference beams [35]. The signals from the detectors were divided to reduce the effect of laser amplitude fluctuations. The intensity of the probe pulses were chosen such that they did not affect the created spectral structures during the readout process. The scan rate was also set such that it had negligible effect on the resolution of the recorded spectra (see discussion below).

4. Preparation of AFC

Creating the atomic frequency comb structure, with good control of all necessary parameters, such as peak height, width, separation and number of peaks, can be challenging. Especially considering that the frequency comb structure also preferably should be well separated in frequency from all other absorbing atoms in the material. However, in rare-earth-metal-ion-doped crystals the inhomogeneous absorption profile can indeed be efficiently manipulated, providing the flexibility needed to meet all those requirements. This flexibility is useful not only for AFC, but also for many other similar experiments, such as electromagnetically induced transparency (EIT) [36], slow light [33] or quantum computing [37,38]. Since the precise control of the absorption structure is of particular concern for this paper, we will here make a detailed description of how to create a test platform for AFC experiments and essentially the same technique can be used also for the other listed experiments mentioned above.

4.1. Pit creation

The inhomogeneous $^1D_2-{}^3H_4$ absorption line in Pr^{3+} : Y$_2$SiO$_5$ is about 5 GHz and the homogeneous line width of a single Pr ion is about a kHz at temperatures below ~ 5 K. A chirped laser pulse applied somewhere within the inhomogeneous profile will create a spectral hole through optical pumping. The maximum width of the spectral hole burnt by such a scan is given by the specific level structure of the Pr^{3+} ion [39] (see Fig. 2). After relaxation from excited states the ion has to be in one of the three hyperfine ground levels, which have a total separation of 27.5 MHz, but the maximum spectral hole width is reduced by the hyperfine splitting of the excited state levels of 9.4 MHz, yielding a final spectral hole interval of 18.1 MHz. The scanned pulse will thus create a simple, wide spectral hole, henceforth called a *pit*, and is shown in Fig. 1a.

When light pulses are applied to perform operations inside the pit, they also have a probability to interact with the tails of the absorption profile of the ions outside the pit, and in particular with the ions immediately outside, forming the walls of the pit. Generally one would like to avoid such interactions and the simple pit in Fig. 1a then is not optimal. Fortunately, it is possible to shuffle many ions in the walls of the pit further away from the pit. This is illustrated in the top right part of Fig. 1. In this figure, a class of ions having the $|0\rangle \rightarrow |e1\rangle$ transition at some specific frequency just inside the pit and the transitions from the other two ground state levels outside the pit, is displayed. For this ion class, the simple burning pulse only targets the $|0\rangle$-state, so only this ground state will be emptied. However, it is clear that these

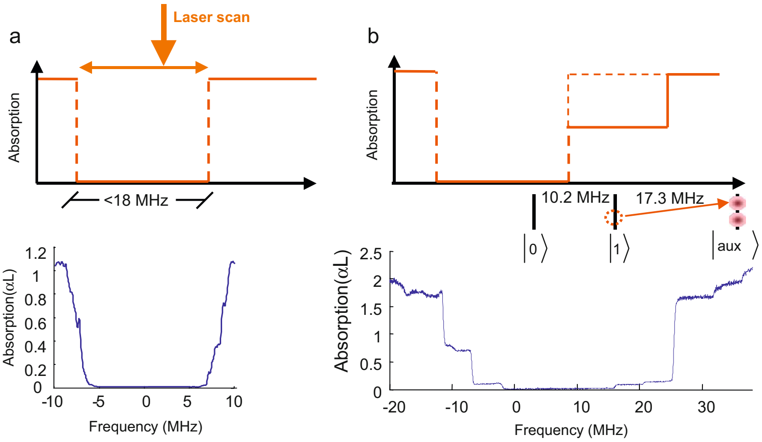

Fig. 1. (color online) In (a) a simple spectral pit created only by scanning a pulse across a specific interval <18 MHz is shown (upper part shows a schematic view and lower part shows actual experimental data). In (b) a more optimal pit is shown, where additional burning pulses on different frequency intervals have iteratively been applied to spectrally remove ions as far from the spectral pit as possible (see text). For an exact pulse sequence, see Appendix A. Note that the frequency scale in the two experimental figures is different.

ions do not have to be in the $|1\rangle$ state, in fact, it would be better if they could be further shifted outwards so that all end up in the $|aux\rangle$ state. This can be done by additional burning pulses at the $|1\rangle \rightarrow |e1\rangle$ transitions. This will cause some ions to go to the $|aux\rangle$-state but also cause some of the ions to fall back down into the pit, and thus, to get the optimal effect, one would have to iterate between the pulses burning at the center of the pit and the ones burning outside it to improve the walls. Similar techniques can be used on the lower frequency side of pit to obtain the final optimal pit, as shown in the lower part of Fig. 1b.

4.2. *Experimental implementation*

The exact sequence of pit burning pulses differ depending on the exact level structure of the ion used. Table 1 in Appendix A lists the explicit pulses used to create an optimal pit in $Pr^{3+}:Y_2SiO_5$ in this work, and the order in which we have applied those pulses is also listed in Appendix A. When working in other materials, essentially the same sequencing can be used, but of course, the actual frequencies have to be changed to match the transitions of the ion in question.

The different optical pumping *BurnPitX* pulses listed in Table 1 (see Appendix A) are repeated and iterated, as explained in the previous section, in order to create good shallow walls while maintaining no atoms inside the pit. The repetition sequence given at the end of the Appendix A is somewhat arbitrary. A higher number of repetitions reflects the fact that the primarily target transition has relatively low oscillator strength. The exact numbers can be changed a bit up or down without significant effect on the result. There is a 1 ms waiting time after every single *BurnPitX* pulse (see Appendix A), to give excited ions time to decay back to the ground state before the next pulse arrives. The excited state lifetime is $T_1 = 164\,\mu s$ [39].

4.3. *Peak creation*

After a suitable pit has been created, a narrow selection of ions is coherently burnt back into the pit. This narrow ensemble of ions now forms an absorption peak spectrally clearly separated from all other ions. The pulses used for this transfer are two complex hyperbolic secant pulses (sechyp for short). The first one targets the $|5/2g\rangle \rightarrow |5/2e\rangle$ transition, of ions having their $|1/2g\rangle \rightarrow |1/2e\rangle$ transition at frequency zero (0) MHz. The second pulse is applied immediately after the first, before the excited ions can decay spontaneously, on the $|5/2e\rangle \rightarrow |1/2g\rangle$ transition. One could imagine taking other routes to burn back a peak, but this particular route is advantageous because the first pulse targets the strongest transition, which means the exciting pulse power, and thus power broadening effects, can be kept at a minimum. The deexcitation pulse on the other hand then targets a weak transition, but since this transition is inside the pit and spectrally far away from other ions, the power can here be increased without any power broadening effects.

Fig. 2 briefly illustrates how to create such a peak structure, and also displays an experimentally created version. Creating a full atomic frequency comb from this situation, is now the relatively simple matter of adding additional coherent burn-back pulses, with appropriate frequency offsets, creating the additional peaks. The shape of the peaks, as well as width and absorption height, is determined by the burn-back pulses. Changing the spectral shape of these pulses will change the shape of the peaks, and increasing the pulse power will cause more ions to be transferred, which results in higher absorption peaks (as long as there is enough ions available in the crystal at that frequency). This yields a good control over all the essential parameters of the AFC.

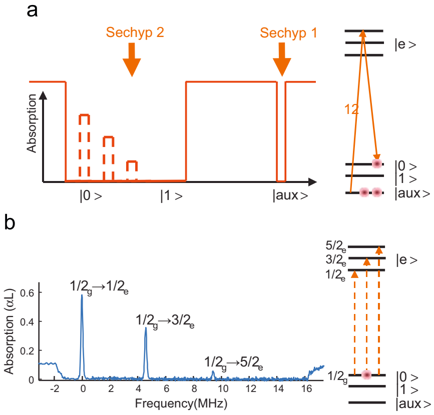

Fig. 2. (Color online) Top part shows the sequence and position of the pulses that burns back a narrow ensemble of ions into an empty spectral pit. The lower (b) part shows an experimental version of such a created peak structure. The difference in height of the three different transition from the $|0\rangle$ state, comes from the fact that these transitions have different oscillator strength.

4.4. *Comb structure measurement*

One of the goals of this work was to compare the observed AFC echo efficiency with the one predicted by the theoretical model discussed in Section 2. This requires a precise measurement of the AFC structure in order to determine the shape, width and height of the peaks. To do this the laser was slowly swept in frequency across the created AFC structure and the transmitted light intensity was detected after the sample. From this transmission profile of the structure, the absorption spectrum can be calculated. The intensity of the scan pulse was chosen such that it did not affect the created spectral structure. For most comb measurements we chose to scan the laser over one peak only and lowered the scan rate to a minimum. This is to reduce the effect of the scan rate on the measurement resolution [40,35]. By varying the rate we confirmed that the measured width was indeed independent of the scan rate.

The comb was created on the $|1/2g\rangle \rightarrow |1/2e\rangle$ transition in order to maximize the absorption. It is, however, very challenging to measure absorptions above d=3–4. In order to circumvent this problem we instead measured the comb structure on the weaker $|1/2g\rangle \rightarrow |5/2e\rangle$ transition, cf. Fig. 2. The ratio of these two transitions is known from previous work [41], thus the optical depth of the $|1/2g\rangle \rightarrow |1/2e\rangle$ transition is readily inferred from the measured absorption spectrum.

5. Results and discussion

The input pulse is stored on the $|1/2g\rangle \rightarrow |1/2e\rangle$ transition, which is the transition for ions in state $|1/2g\rangle$ with the highest oscillator strength. This results in a comb with high optical depth d. The bandwidth of the AFC is limited by the frequency separation between the excited states and in the present case this is about 4.6 MHz, as set by the $|1/2e\rangle$ and $|3/2e\rangle$ separation (cf. Fig. 2). Fig. 3 shows a comb containing four peaks, and where the width of each peak is about $\gamma = 150$ kHz. The separation between the peaks was set to $\Delta = 1.2$ MHz. The pulse to be stored has a Gaussian shape with duration 200 ns, resulting in a frequency power spectrum with FWHM 2 MHz (see Fig. 3).

A high-efficiency echo is shown in Fig. 4. The emitted echo is observed after 800 ns, as expected from the comb periodicity $\tau_s = 1/\Delta = 800$ ns. To be able to calculate the efficiency of the echo, first a reference input pulse is sent through the empty pit (no AFC prepared). This pulse is thus completely transmitted through the sample. The AFC is then prepared inside the pit and an identical pulse (the storage pulse) is sent in. This pulse is partially absorbed in the medium and produces an echo. The ratio between the area of the echo and the area of the reference pulse gives the storage efficiency. A small part of the reference pulse as well as the storage pulse is split off before they enter the cryostat so unintentional input power differences between the reference and storage pulses can be compensated for. For the data shown in Fig. 4 we measured an efficiency of 35%. To our knowledge this is the highest AFC echo efficiency observed up to date.

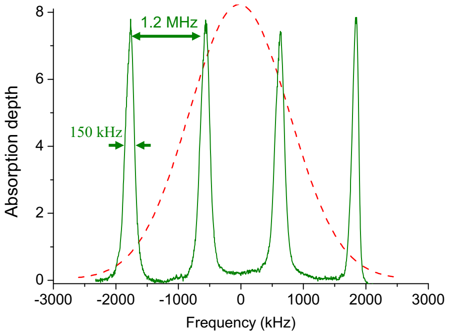

Fig. 3. (Color online) From the inhomogeneous absorption profile, four peaks with ions, all absorbing on the $|1/2g\rangle \rightarrow |1/2e\rangle$ transition are created. The peak width (FWHM) is $\gamma = 150$ kHz and they are separated by $\Delta = 1.2$ MHz. The input pulse has a Gaussian power spectrum with FWHM=2 MHz.

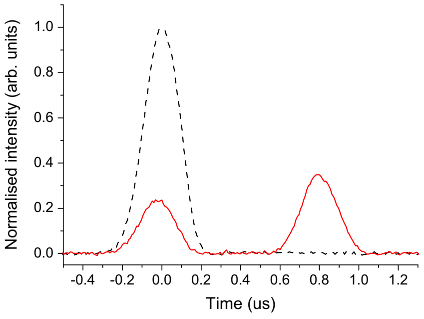

Fig. 4. (Color online) The dashed line shows the input pulse that is completely transmitted through the empty pit (no absorption). The solid line shows the partially transmitted input pulse and the subsequent echo emission with the AFC created in the pit (cf. Fig. 3). The echo efficiency is 35% of the input pulse (see text for details).

As discussed in Section 2 the efficiency depends strongly on the shape of the AFC. Our comb structure measurements show peaks that have near Gaussian shapes. This facilitates the theoretical modeling since we can use the simple model discussed in Section 2 and we need only then to measure two parameters; the peak absorption d and peak width γ (the finesse is calculated from the relationship $F = \Delta/\gamma$). In order to make a quantitative comparison with the model, we varied the peak absorption d and measured the resulting input pulse transmission and echo efficiency. This was done by increasing the power of the back burning pulses used in the peak creation (see Section 4.3). For each power setting we also measured the comb structure to find d and F. The width of the peaks could be varied by changing the chirp width of the sechyp pulses used for peak creation. We did measurements as a function of d for two settings of the chirp; 200 and 300 kHz. The measured peak widths for these two settings were 175 and 245 kHz, respectively, corresponding to F=6.9 and 4.9. With increasing back burning power (hence increasing d) the peaks were slightly broadened due to power broadening, but the observed increase was only 10–15% for the data considered here. The widths given above are averages over all back burning powers (hence d values).

In Fig. 5 we show measured transmission coefficients of the input pulse and the efficiencies of the echo for the two data sets. The data are plotted as a function of the measured peak

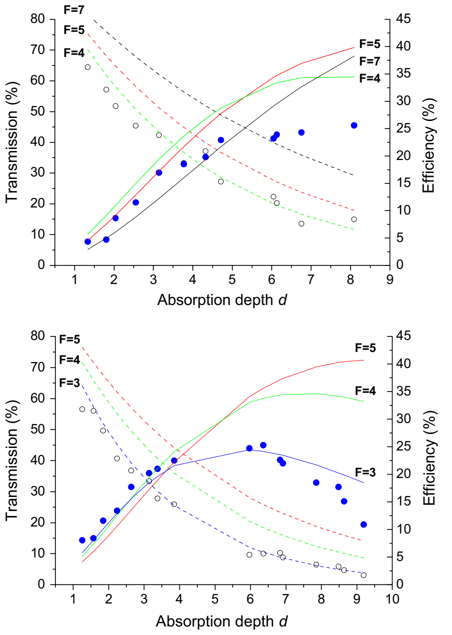

Fig. 5. (Color online) Measured transmission of the input pulse (open circles and left axis) and echo efficiency (closed circles and right axis) as a function of the measured optical depth for two different experimental values of the finesse, (a) F=6.9 and (b) F=4.9. The dashed lines are theoretically calculated transmission coefficients and solid lines are calculated efficiencies for (a) F=4,5 and 7, and for (b) F=3,4 and 5 (see text for details).

absorption d as extracted from the AFC spectra. Theoretical transmission and efficiency curves are also shown. These were calculated using the experimental d values, for different values of finesse. It is observed that the transmission coefficient is very sensitive to the finesse, whereas the efficiency is less sensitive up to $d=4-5$. In general the best agreement for the transmission is obtained for a finesse lower than the one measured from the comb spectra (see above). We can also see that the best-fit finesse is lower for the 300 kHz data set, than for the 200 kHz, which is to be expected. The echo efficiency shows a reasonably good agreement with all three values of the finesse up to $d=4-5$. But for $d \geq 5$ the discrepancy between the experimental and theoretical values becomes significant for $F=4$ and 5, while for $F=3$ it is still satisfactory.

The general trend, for both transmission and efficiency, is that our data fit better with a finesse lower than the measured one. This comparison is, however, made within the theoretical framework of Section 2 where a comb of Gaussian peaks was assumed. Both the transmission and echo efficiency are strongly dependent on the actual peak shape [18,20]. For instance, the same comparison with a Lorentzian model [20] yields very different best-fit values for the finesse. Although much effort was devoted to the precise measurement of the comb structure, it is still conceivable that the actual peak shape deviate from a pure Gaussian shape. Particularly since the sechyp pulses used for peak creation have power spectra with more super-Gaussian shape [35]. Another source of error could be imperfections in the peak creation pulses, where the high power needed to obtain high optical depth might generate an increase in the absorption background due to off-resonant excitation. Such an additional absorption will reduce both the experimental transmission and efficiency [9] compared to the theoretical model in Section 2 where such an absorption background is neglected. This would particularly affect the high d range, where indeed we observe a larger discrepancy.

6. Conclusions

We have in detail described optical pumping and preparation procedures for creating AFC structures in $Pr^{3+}:Y_2SiO_5$. We were able to make comb structures yielding $>30\%$ AFC echo efficiency, which are the most efficient AFC echoes observed up to date. We believe that further progress will be possible, by carefully optimizing the comb parameters. It should thus be possible to approach the theoretical limit of 54% used in the present forward-propagation configuration. In order to make a significant further progress, recall in the backward direction would be necessary, in which case 100% efficiency is theoretically possible in the absence of dephasing.

In this work we also compared the experimentally observed efficiencies to a theoretical model. Considerable care has been put into determining the line shape and line width of the generated AFC structure with good precision in order to be able to theoretically model the experimental efficiencies. Still, at high optical densities the finesse required to theoretically reproduce the experimental echo efficiency are lower than those measured experimentally. Nevertheless, the present results indeed show that high efficiency QMs can be created using the AFC technique.

Acknowledgments

This work was supported by the Swedish Research Council, the Knut and Alice Wallenberg Foundation, the Swiss NCCR Quantum Photonics, the European Commission through the integrated project QAP, and the ERC Advanced Grant QORE.

Appendix A

The optical pumping pulses used for creating the pit structure in Fig. 1b are presented in Table 1.

Table 1
List of pulses used for the pit burning sequence, with start and end frequencies.

Pulse	ν_{start} (MHz)	ν_{end} (MHz)	Ω_{rel}
BurnPit1	+31.85	+24.15	$3/2_g \rightarrow 1/2_e$
BurnPit2	+23.85	+16.15	$3/2_g \rightarrow 5/2_e$
BurnPit3	+15.95	+7.65	$3/2_g \rightarrow 5/2_e$
BurnPit4	+23.85	+16.15	$3/2_g \rightarrow 5/2_e$
BurnPit5	−16.85	−9.15	$5/2_g \rightarrow 5/2_e$
BurnPit6	−8.85	−1.15	$5/2_g \rightarrow 1/2_e$
BurnPit7	+15.95	+7.65	$3/2_g \rightarrow 5/2_e$
BurnPit8	+7.35	−1.10	$3/2_g \rightarrow 5/2_e$
BurnPit9	−1.10	+7.35	$5/2_g \rightarrow 1/2_e$
BurnPit10	+7.65	+15.95	$5/2_g \rightarrow 1/2_e$

This set of pulses will create the pit in Fig. 1b with zero absorption (no absorbing ions) from −1.2 up to 16.2 MHz. The frequency scale is defined by denoting the $|1/2g\rangle \rightarrow |1/2e\rangle$ transition, for an arbitrarily selected ion class, as zero MHz. The column Ω_{rel} lists the primary target transition of the scan for the purpose of knowing what light intensity to choose in order to match the Rabi frequency to the relative oscillator strength. Note that pulse numbers 2 and 4 are the same, as is pulses 3 and 7.

These pulses are then repeated in an iterative sequence in the following manner

(1) *Repeat* 60 *times*: BurnPit5, BurnPit6.
(2) *Repeat* 30 *times*: BurnPit1-4, BurnPit6-10.
(3) *Repeat* 20 *times*: BurnPit1-4, BurnPit6.
(4) *Repeat* 30 *times*: BurnPit7-10.

Finally yielding the pit in Fig. 1b.

References

[1] H.-J. Briegel, W. Dür, J.I. Cirac, P. Zoller, Phys. Rev. Lett. 81 (1998) 5932.
[2] L.M. Duan, M.D. Lukin, J.I. Cirac, P. Zoller, Nature 414 (2001) 413.
[3] C. Simon, H. de Riedmatten, M. Afzelius, N. Sangouard, Z. Zbinden, N. Gisin, Phys. Rev. Lett. 98 (2007) 190503.
[4] N. Sangouard, C. Simon, H. de Riedmatten, N. Gisin, Quantum repeaters based on atomic ensembles and linear optics, arXiv:0906.2699.
[5] B. Julsgaard, J. Sherson, J.I. Cirac, J. Fiurasek, E.S. Polzik, Nature 432 (2004) 482.
[6] T. Chanelière, D.N. Matsukevich, S.D. Jenkins, S.-Y. Lan, T.B. Kennedy, Nature 438 (2005) 833.
[7] M.D. Eisaman, A. Andre, F. Massou, M. Fleischhauer, A.S. Zibrov, M.D. Lukin, Nature 67 (2005) 452.
[8] K.S. Choi, H. Deng, J. Laurat, H.J. Kimble, Nature 452 (2008) 67.
[9] H. de Riedmatten, M. Afzelius, M.U. Staudt, C. Simon, N. Gisin, Nature 456 (2008) 773.
[10] O.A. Collins, S.D. Jenkins, A. Kuzmich, T.A.B. Kennedy, Phys. Rev. Lett. 98 (2007) 060502.
[11] K. Hammerer, A. Sorensen, E. Polzik, Quantum interface between light and atomic ensembles, arXiv:0807.3358.
[12] J. Ruggiero, J.L. Le Gouët, C. Simon, T. Chanelière, Phys. Rev. A 79 (2009) 053851.
[13] S.A. Moiseev, S. Kröll, Phys. Rev. Lett. 87 (2001) 173601.
[14] M. Nilsson, S. Kröll, Opt. Commun. 247 (2005) 393.
[15] B. Kraus, W. Tittel, N. Gisin, M. Nilsson, S. Kröll, J.I. Cirac, Phys. Rev. A 73 (2006) 020302 (R).
[16] A.L. Alexander, J.J. Longdell, M.J. Sellars, N.B. Manson, Phys. Rev. Lett. 96 (2006) 043602.
[17] W. Tittel, M. Afzelius, R.L. Cone, T. Chanelière, S. Kröll, S.A. Moiseev, M. Sellars, Photon-echo quantum memory, arXiv:0810.0172.
[18] M. Afzelius, C. Simon, H. Riedmatten, N. Gisin, Phys. Rev. A 79 (2009) 052329.
[19] M.U. Staudt, S.R. Hastings-Simon, M. Nilsson, M. Afzelius, V. Scarani, R. Ricken, H. Suche, W. Sohler, W. Tittel, N. Gisin, Phys. Rev. Lett. 98 (2007) 113601.
[20] T. Chaneliére, J. Ruggiero, M. Bonarota, M. Afzelius, J.L. Le Gouët, Efficient light storage in a crystal using an atomic frequency comb, arXiv:0902.2048.

[21] I. Usmani, M. Afzelius, H. de Riedmatten, N. Gisin, Mapping tens of photonic qubits onto one solid-state atomic ensemble, in preparation.
[22] R.M. Macfarlane, R.M. Shelby, Coherent transient and holeburning spectroscopy of rare earth ions in solids, in: A. Kaplyanskii, R. Macfarlane (Eds.), Modern Problems in Condensed Matter Sciences, North-Holland, Amsterdam, 1987.
[23] R.M. Macfarlane, J. Lumin. 100 (2002) 1.
[24] W.H. Hesselink, D.A. Wiersma, Phys. Rev. Lett. 43 (1979) 1991.
[25] N.W. Carlson, Y.S. Bai, W.R. Babbitt, T.W. Mossberg, Phys. Rev. A 30 (1984) 1572.
[26] M. Mitsunaga, R. Yano, N. Uesugi, Opt. Lett. 16 (1991) 264.
[27] R. Yano, M. Mitsunaga, N. Uesugi, J. Opt. Soc. Am. B 9 (1992) 992.
[28] K.D. Merkel, W.R. Babbitt, Opt. Lett. 21 (1996) 1102.
[29] M. Tian, J. Zhao, Z. Cole, R. Reibel, W.R. Babbitt, J. Opt. Soc. Am. B 18 (2001) 673.
[30] M. Afzelius, I. Usmani, A. Amari, B. Lauritzen, A. Walther, C. Simon, N. Sangouard, J. Minar, H. de Riedmatten, N. Gisin, S. Kröll, Demonstration of atomic frequency comb memory for light with spin-wave storage, Phys. Rev. Lett. 104 (2010) 040503.
[31] M. Nilsson, L. Rippe, S. Kröll, R. Klieber, D. Suter, Phys. Rev. B 70 (2004) 214116.
[32] N. Sangouard, C. Simon, M. Afzelius, N. Gisin, Phys. Rev. A 75 (2007) 032327.
[33] A. Walther, A. Amari, A. Kalachev, S. Kröll, Phys. Rev. A 80 (2009) 012317.
[34] B. Julsgaard, L. Rippe, A. Walther, S. Kröll, Opt. Express 15 (2007) 11444.
[35] L. Rippe, M. Nilsson, R. Klieber, D. Suter, S. Kröll, Phys. Rev. A 71 (2005) 062328.
[36] P. Goldner, O. Guillot-Noël, F. Beaudoux, Y.L. Du, J. Lejay, J.L. Le Gouët, T. Chanelière, L. Rippe, A. Amari, A. Walther, S. Kröll, Phys. Rev. A 79 (2009) 033809.
[37] J.J. Longdell, M.J. Sellars, Phys. Rev. A 69 (2004) 032307.
[38] L. Rippe, B. Julsgaard, A. Walther, Y. Ying, S. Kröll, Phys. Rev. A 77 (2008) 022307.
[39] R.W. Equall, R.L. Cone, R.M. Macfarlane, Phys. Rev. B 52 (1995) 3963.
[40] T. Chang, M.Z. Tian, R.K. Mohan, C. Renner, K.D. Merkel, W.R. Babbitt, Opt. Lett. 30 (2005) 1129.
[41] M. Nilsson, L. Rippe, R. Klieber, D. Suter, S. Kröll, Phys. Rev. B 70 (2004) 214116.

Paper II

Storage and Recall of Weak Coherent Optical Pulses with an Efficiency of 25%

M. Sabooni, F. Beaudoin, A. Walther, N. Lin, A. Amari, M. Huang, and S. Kröll.

Phys. Rev. Lett. **105**, 060501 (2010).

PRL **105,** 060501 (2010) PHYSICAL REVIEW LETTERS week ending 6 AUGUST 2010

Storage and Recall of Weak Coherent Optical Pulses with an Efficiency of 25%

M. Sabooni, F. Beaudoin, A. Walther, N. Lin, A. Amari, M. Huang, and S. Kröll
Department of Physics, Lund University, P.O. Box 118, SE-22100 Lund, Sweden

(Received 10 December 2009; published 2 August 2010)

We demonstrate experimentally an efficient coherent rephasing scheme for the storage and recall of weak coherent light pulses in an inhomogeneously broadened optical transition in a Pr^{3+}:YSO crystal at 2.1 K. Precise optical pumping using a frequency stable (≈1 kHz linewidth) laser is employed to create a highly controllable atomic frequency comb structure. We report single photon level storage and retrieval efficiencies of 25%, based on coherent photon-echo-type reemission in the forward direction. The high efficiency is mainly a product of our highly controllable and precise ensemble-shaping technique. The coherence property of the quantum memory is proved through interference between a super-Gaussian pulse and the emitted echo.

DOI: 10.1103/PhysRevLett.105.060501 PACS numbers: 03.67.Hk, 42.50.Ct, 42.50.Ex, 42.50.Md

Introduction.—Quantum information processing applications such as quantum networks require coherent and reversible mapping between light and matter [1,2]. Currently, this requirement is expected to be met by means of quantum repeaters, which allow temporal storage of quantum information in quantum memories and distribution of entanglement across long distances [3]. In the repeater protocol, the entanglement distribution has probabilistic behavior, and without quantum memories all probabilistic steps would have to succeed simultaneously. Quantum memories are therefore a key ingredient in any future long distance quantum communication scheme and have thus been subject to very active development in recent time. To be useful in actual processing applications, these devices must maintain fidelities close to 100% during storage times of the order of seconds and also ensure high recall output efficiency [4–6].

Quantum memory protocols [such as electromagnetically induced transparency (EIT) [7] based on stopped light [8], controlled reversible inhomogeneous broadening (CRIB) [9–11], and atomic frequency comb (AFC) [6,12], based on photon-echo experiments] use atomic ensembles to obtain the required control and strong coupling between the light field and the storage medium. These protocols can be adapted to the original Duan-Lukin-Cirac-Zoller protocol [1] to create entanglement generation via single photon detection. Therefore, it is important to demonstrate that quantum memories can be operated at the single photon level.

Protocols which enable storage of multiple temporal modes can increase the entanglement generation rate by a factor approximately equal to the number of temporal modes [13]. Storing many modes with high efficiency requires a high optical depth, which generally can be an experimental difficulty. Achieving efficient multimode storage at lower optical depth is therefore desirable. It has been shown [12,14] that the number of modes N_m that can be efficiently stored by using EIT scales as $N_m \approx \sqrt{\alpha L}$, where αL is the optical depth. CRIB offers a better scaling since $N_m \approx \alpha L$ (to double the number of modes, it is sufficient to double αL), but in the AFC protocol the number of temporal modes that can be stored with a given efficiency is independent of optical depth.

Based on EIT, storage and retrieval efficiency of 10% for 10 μs storage time in hot atomic vapor was published by Eisaman *et al.* [15]. With the same scheme, Choi *et al.* [16] achieved 17% for 1 μs in a cold atomic ensemble. Recently, Lauritzen *et al.* [17] published a storage and retrieval efficiency of 0.25% for 600 ns in an erbium-doped crystal by using the CRIB protocol. By using the AFC protocol, de Riedmatten *et al.* [6] obtained 0.5% storage and retrieval efficiency after 250 ns in Nd^{3+}:YVO_4, and

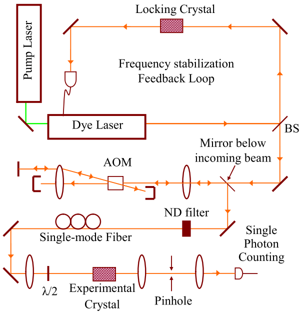

FIG. 1 (color online). Experimental setup. The frequency stabilization feedback system uses a Pr^{3+}:YSO crystal as a locking crystal. All pulses are created by using a double pass AOM. The incoming and outgoing beams in the AOM have different height, and a mirror below the incoming beam redirects the outgoing beam to the experiment. Absorptive neutral density filters stand for most of the attenuation such that the AOM can operate in a linear light intensity vs rf amplitude regime for adjusting the storage pulse intensity. After spatial cleaning in the single mode fiber, the light interacts with the Pr^{3+}:$\mathrm{Y}_2\mathrm{SiO}_5$ experimental crystal at 2.1 K. A 50 μm pinhole is used to select the center of the beam for the single photon counting detector.

0031-9007/10/105(6)/060501(4)

Chaneliére *et al.* [18] achieved 9% storage and retrieval efficiency for 1.5 μs in Tm^{3+}:YAG crystal.

In this Letter, we use the AFC protocol to store weak coherent pulses, with on the average 0.1 photons/pulse, up to 800 ns with 25% storage and retrieval efficiency in a Pr^{3+}:YSO crystal. Recently, in this material 96% transfer efficiency from an excited state to ground state spin level was achieved [19], and such transfer pulses were used to demonstrate an on-demand readout quantum memory based on a collective spin wave excitation in the hyperfine ground state levels of Pr:YSO [20]. The lifetime of such spin state storage has subsequently been extended to the 100 μs range [21]. Therefore, to achieve high efficiency on demand quantum memory operation, the key issue is to demonstrate high efficiency coherent rephasing in the low photon number regime which here is achieved through our highly controllable and precise ensemble-shaping technique.

Materials and methods.—The experimental setup is shown in Fig. 1. A 6-W Coherent Verdi-V6, 532 nm $Nd:YVO_4$ laser pumps a Coherent 699-21 dye laser, which emits approximately 500 mW light at 605.82 nm. This frequency matches the $^3H_4$-$^1D_2$ transition of praseodymium ions doped into yttrium silicate ($Pr^{3+}:Y_2SiO_5$). We use a frequency stabilization feedback system [22], based on a $Pr^{3+}:Y_2SiO_5$ crystal, which has a frequency drift below 1 kHz/s. This precise frequency control gives us ability to create and control the AFC structure and is the main reason for increasing the storage and retrieval efficiency. An acousto-optic modulator (AOM) with 200 MHz center frequency, in a double pass arrangement that cancels spatial movement when changing the frequency of the diffracted beam, controls phase, amplitude, and frequency of the light. The radio-frequency signal used to drive the AOM is created by a 1-GS/s arbitrary waveform generator (Tektronix AWG520). Two mechanisms for light attenuation to the single photon level are used. The light beam can be attenuated by reducing the amplitude of the radio-frequency field driving the AOM, but since rf amplitude versus light amplitude is highly nonlinear and difficult to calibrate due to low diffraction efficiency at low rf amplitudes, a shutter wheel with absorptive neutral density filters was added in the setup. The remaining control of the light amplitude was then handled through the AOM rf amplitude finally yielding about 0.1 photons per pulse at the sample. For cleaning up the spatial mode, after the AOM, the light was sent to a single mode fiber and then to a $\lambda/2$ plate such that the light polarization could be aligned along the transition dipole moment to yield maximum absorption. The sample is a $Pr^{3+}:Y_2SiO_5$ crystal with 0.05% doping concentration, and it has three perpendicular optical axes labeled $D1$, $D2$, and b, where the direction of light propagation was chosen along the b axis. The crystal dimensions are $10 \times 10 \times 20$ mm along the $D1 \times D2 \times b$ axis. The width of the Gaussian beam at the center of the crystal is about 100 μm, and it is imaged (1:1) onto a 50 μm pinhole. The pinhole gives us the opportunity to pick the light emitted by ions at the center of the beam that all have experienced roughly the same light intensity. To keep the optical coherence time (T_2) of the praseodymium >100 μs, the crystal was immersed in liquid helium at 2.1 K. After the sample crystal, a mechanical shutter was used to protect the detector from the intense AFC preparation pulses. A Hamamatsu single photon counting detector (model H8259-01) with a quantum efficiency of 7.5% and a minimum gating time of 100 ns was used.

Let us now describe (see Fig. 2) in more detail how to create an AFC [12], i.e., a periodic series of narrow (FWHM $= \gamma$) and highly absorbing (optical depth αL) peaks with a periodicity Δ as a frequency grating of ions in the $|1/2g\rangle$ state (see Fig. 2). By means of optical pumping, an 18 MHz zero absorption frequency region (see Ref. [23]) is created within the 5 GHz wide $Pr^{3+}:Y_2SiO_5$ inhomogeneous profile [24]. This nonabsorbing frequency region is hereafter referred to as a spectral pit. Optimal pit creation needs a series of explicit pulses [23]. Afterwards, a frequency-dependent absorption grating was created inside this spectral pit. Complex hyperbolic secant optical pulses were used to transfer some ions from $|5/2g\rangle$ to $|5/2e\rangle$ and then from the $|5/2e\rangle$ to the $|1/2g\rangle$ state [25]. Changing the center frequency of the complex hyperbolic secant pulses, by an amount Δ, is a simple technique to create a second peak inside the spectral pit. By repeating this procedure, it is possible to create an atomic frequency comb in the $|1/2g\rangle$ level with a periodicity Δ. The number of peaks (N) is limited by the

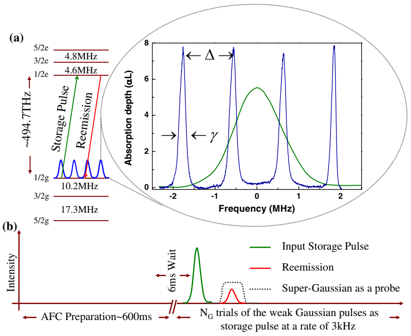

FIG. 2 (color online). (a) The $^3H_4$-$^1D_2$ transition of the $Pr^{3+}:Y_2SiO_5$ crystal is used for the experiment. An experimental AFC absorption profile with defined height (αL), peak separation (Δ), and FWHM (γ) with all ions in the state $|1/2g\rangle$ is created. A Gaussian pulse with center frequency set to the $|1/2g\rangle \rightarrow |1/2e\rangle$ transition is used as a storage pulse. (b) A sequence of pulses which can be divided into preparation and storage pulses of a total duration of approximately 1.1 s is sent into the sample. A super-Gaussian pulse is used as a probe pulse for interfering with the reemission (echo) and showing the phase preservation of the AFC interface.

$|1/2e\rangle \rightarrow |3/2e\rangle$ separation, $(\delta f_{|1/2e\rangle \rightarrow |3/2e\rangle})$, and Δ $[\Delta \times (N-1) < \delta f_{|1/2e\rangle \rightarrow |3/2e\rangle}]$.

Results and discussions.—First, we offer a brief theoretical background to the AFC quantum memory interface. A weak light pulse is sent as a coherent state ($|\alpha\rangle_L$), on the average containing less than a single photon, with a well-defined bandwidth ($1/\tau_p$), to an AFC structure with well-defined peak separation (Δ), peak width (γ), finesse $F = \Delta/\gamma$, and peak height (αL) consisting of N ions all in the $|1/2g\rangle$ state. The objective is to transfer all the energy of the weak coherent wave packet to the distribution of ions, $|g_1 \ldots g_N\rangle$, in the spectral grating with defined finesse ($F = \Delta/\gamma$). After the light-matter interaction, the initial state of the N atoms will develop into the state [12]:

$$|\alpha\rangle_A = |g_1 \ldots g_N\rangle + \sum_{j=1}^{N} c_j e^{i(2\pi\delta_j t - kz_j)} |g_1 \ldots e_j \ldots g_N\rangle, \quad (1)$$

where z_j is the spatial position of ion j, k is the wave number of the weak coherent wave packet, and c_j is an amplitude that depends on the absorption probability, the spatial position, and the absorption frequency of the ion. The AFC is a well-separated periodic structure with frequency detuning $\delta_j = m_j\Delta$ (m_j is an integer). Studying the time evolution of the superposition state in Eq. (1) shows that in this state the ions will start to dephase. But the key feature of the AFC structure, with its periodicity Δ, is that it gives rise to a constructive emission exactly after a time $t = 1/\Delta$. The storage and retrieval efficiency of the AFC protocol in the forward direction can be written [6] as

$$\eta = (\alpha L/F)^2 e^{-\alpha L/F} e^{-7/F^2}. \quad (2)$$

Because of the trade-off between the coherent response of the sample (first), reabsorption (second), and dephasing (third) factors, there is an optimum value for the finesse as discussed in Ref. [6].

In our measurements we have two sets of pulses. They correspond to the preparation pulses described in Ref. [23] and the storage pulses described below. The amplitude of the storage pulse was adjusted by taking into account attenuation factors due to windows, optical components, pinhole, and the quantum efficiency of the single photon detector until the mean number of photons per pulse was about $\tilde{n} \approx 0.1$ at the sample. To improve measurement statistics, weak Gaussian storage pulses were sent in 2000 times at a rate of 3 kHz. To measure the efficiency, the storage pulse, which had a 200 ns FWHM, was sent through the empty spectral pit. In the empty pit there are no ions absorbing the pulse; therefore this is a good reference to compare with the recall pulse. The photon counting results fitted to a Gaussian time distribution for the empty pit are shown (circles and dashed curve) in Fig. 3.

Next, an AFC structure with peak separation $\Delta = 1.2$ MHz, peak width $\gamma = 200$ kHz, and $\alpha L \approx 6$ is created and a Gaussian weak coherent storage pulse ($\tau_{\text{FWHM}} = 200$ ns) tuned to the $|1/2g\rangle \rightarrow |1/2e\rangle$ transition [Fig. 2(a)] is sent through the medium, which has a phase relaxation time much longer than the duration of the pulse. Reemission (the echo) occurs after 800 ns ($1/\Delta$) (solid curve in Fig. 3). The measured storage and retrieval efficiency is 25%, which means that the energy contained in the collective reemission (echo) pulse relative to the energy transmitted through empty pit (dashed curve) is 0.25. Based on our knowledge this is the highest AFC echo efficiency in the single photon regime observed so far, and it is the product of our high controllable and precise ensemble-shaping technique.

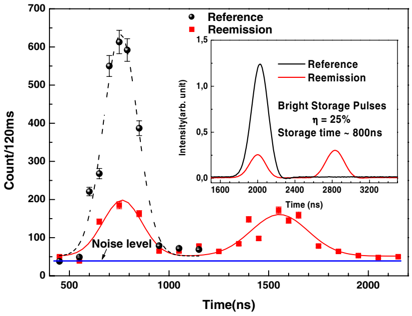

FIG. 3 (color online). Black circles (reference) are the single photon counts for the transmission of a 200 ns Gaussian storage pulse ($n = 0.1$ photon per pulse) sent through the transparent empty pit without any AFC grating. Red squares correspond to the counts for an identical storage pulse sent through the AFC spectral grating with $\Delta = 1.2$ MHz, $\gamma = 300$ kHz, and $\alpha L \approx 6$. The ratio of the areas below the echo and the reference after fitting with a simple Gaussian function and subtracting the noise level is 0.25. The same result is achieved with bright storage pulses which is shown in the inset.

So far, we have considered the efficiency properties of our interface, but for quantum memory applications it is vital that the interface also conserve the phase of the storage pulse with high fidelity. To show the phase preservation, a super-Gaussian ($n = 7$) pulse with controllable phase, overlapping the reemission pulse temporally, but with a 2.3 MHz frequency offset is prepared. This frequency offset allows us to send the super-Gaussian pulse through a transparent frequency window inside the pit between $|1/2g\rangle \rightarrow |1/2e\rangle$ and $|1/2g\rangle \rightarrow |3/2e\rangle$ transition peaks [23]. To have enough frequency space between these two transitions, the peak separation (Δ) is reduced to 1 MHz, but the rest of the AFC parameters are the same as before. In these measurements the τ_{FWHM} of the Gaussian pulse is 420 ns, whereas the super-Gaussian full width at half maximum is 840 ns.

Because of the interference between the two pulses, a beating pattern is expected at the detector at the time of the reemission (the echo) pulse (Fig. 4). The measured visibility after subtraction of the noise level is 83%. To show that the phase is conserved, the phase of the super-Gaussian pulse was changed by π and the beating pattern is reversed (Fig. 4).

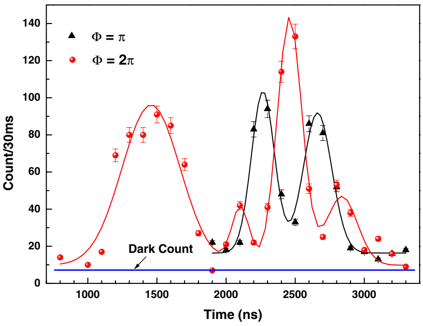

FIG. 4 (color online). Beating between reemission (echo) and the super-Gaussian ($n = 7$) pulses. The first pulse to the left is the transmitted part of the input storage pulse, which is independent of the phase of the super-Gaussian pulse. The visibility after subtracting the noise level is 83%. The interference patterns is inverted when the phase factor of the super-Gaussian pulse is changed by π, demonstrating phase conservation of the weak coherent storage pulse by the AFC spectral grating.

The 25% storage and retrieval efficiency obtained in this Letter is independent of the storage pulse intensity. Furthermore, all results with the bright storage pulses [23] are reproducible in the single photon regime. The experiment is based on coherent photon-echo-type reemission experiments in the forward direction. Theoretically, as discussed in Ref. [6], the maximum achievable efficiency for emission in the forward direction is 54%. This is basically limited by the reabsorption of the emitted echo. From an experimental point of view, the most critical issues for reaching this efficiency are first to have control over the AFC peak shape and second to obtain a high effective absorption ($\alpha L/F$). There is a good agreement between the effective absorption and obtained storage and recall efficiency which is discussed in Ref. [23]. To improve the efficiency beyond 54%, counterpropagating control fields [9] or external control of the ion frequency [26] could be used; alternatively, the crystal could be placed inside a cavity [27]. The efficiency could also be enhanced by using optimum input pulses [28–30].

This work was supported by the Swedish Research Council, the Knut and Alice Wallenberg Foundation, the Crafoord Foundation, and the European Commission through the integrated project QAP.

Note added in proof.—A quantum memory storage efficiency of 69% has been reported after the submission of this manuscript [31].

[1] L. M. Duan, M. D. Lukin, J. I. Cirac, and P. Zoller, Nature (London) **414**, 413 (2001).
[2] H. J. Kimble, Nature (London) **453**, 1023 (2008).
[3] H. J. Briegel, W. Dur, J. I. Cirac, and P. Zoller, Phys. Rev. Lett. **81**, 5932 (1998).
[4] W. Tittel, M. Afzelius, R. L. Cone, T. Chaneliére, S. Kröll, S. A. Moiseev, and M. Sellars, Laser Photon. Rev. **4**, 244 (2009).
[5] N. Sangouard, C. Simon, H. de Riedmatten, and N. Gisin, arXiv:0906.2699.
[6] H. de Riedmatten, M. Afzelius, M. U. Staudt, C. Simon, and N. Gisin, Nature (London) **456**, 773 (2008).
[7] S. E. Harris, Phys. Today **50**, No. 7, 36 (1997).
[8] J. J. Longdell, E. Fraval, M. J. Sellars, and N. B. Manson, Phys. Rev. Lett. **95**, 063601 (2005).
[9] S. A. Moiseev and S. Kröll, Phys. Rev. Lett. **87**, 173601 (2001).
[10] M. Nilsson and S. Kröll, Opt. Commun. **247**, 393 (2005).
[11] B. Kraus, W. Tittel, N. Gisin, M. Nilsson, S. Kröll, and J. I. Cirac, Phys. Rev. A **73**, 020302(R) (2006).
[12] M. Afzelius, C. Simon, H. de Riedmatten, and N. Gisin, Phys. Rev. A **79**, 052329 (2009).
[13] C. Simon, H. de Riedmatten, M. Afzelius, N. Sangouard, H. Zbinden, and N. Gisin, Phys. Rev. Lett. **98**, 190503 (2007).
[14] J. Nunn, K. Reim, K. C. Lee, V. O. Lorenz, B. J. Sussman, I. A. Walmsley, and D. Jaksch, Phys. Rev. Lett. **101**, 260502 (2008).
[15] M. D. Eisaman, A. Andre, F. Massou, M. Fleischhauer, A. S. Zibrov, and M. D. Lukin, Nature (London) **438**, 837 (2005).
[16] K. S. Choi, H. Deng, J. Laurat, and H. J. Kimble, Nature (London) **452**, 67 (2008).
[17] B. Lauritzen, J. Minár, H. de Riedmatten, M. Afzelius, N. Sangouard, C. Simon, and N. Gisin, Phys. Rev. Lett. **104**, 080502 (2010).
[18] T. Chaneliére, J. Ruggiero, M. Bonarota, M. Afzelius, and J. L. Le Gouët, New J. Phys. **12**, 023025 (2010).
[19] L. Rippe, B. Julsgaard, A. Walther, Y. Ying, and S. Kröll, Phys. Rev. A **77**, 022307 (2008).
[20] M. Afzelius, I. Usmani, A. Amari, B. Lauritzen, A. Walther, C. Simon, N. Sangouard, J. Minár, H. de Riedmatten, N. Gisin, and S. Kröll, Phys. Rev. Lett. **104**, 040503 (2010).
[21] L. Rippe *et al.* (to be published).
[22] B. Julsgaard, L. Rippe, A. Walther, and S. Kröll, Opt. Express **15**, 11 444 (2007).
[23] A. Amari, A. Walther, M. Sabooni, M. Huang, and S. Kröll, J. Lumin. **130**, 1579 (2010).
[24] R. W. Equall, R. L. Cone, and R. M. Macfarlane, Phys. Rev. B **52**, 3963 (1995).
[25] L. Rippe, M. Nilsson, S. Kröll, R. Klieber, and D. Suter, Phys. Rev. A **71**, 062328 (2005).
[26] A. Kalachev and S. Kröll, Phys. Rev. A **78**, 043808 (2008).
[27] M. Afzelius, in *Proceedings of the Workshop on Rare-Earth-Ion-doped Solids for Quantum Information* (Lund University, Lund, Sweden, 2009).
[28] A. Kalachev, Phys. Rev. A **76**, 043812 (2007).
[29] I. Novikova, A. V. Gorshkov, D. F. Phillips, A. S. Sørensen, M. D. Lukin, and R. L. Walsworth, Phys. Rev. Lett. **98**, 243602 (2007).
[30] N. B. Phillips, A. V. Gorshkov, and I. Novikova, Phys. Rev. A **78**, 023801 (2008).
[31] M. P. Hedges, J. J. Longdell, Y. Li, and M. Sellars, Nature (London) **465**, 1052 (2010).

Paper III

Hyperfine characterization and spin coherence lifetime extension in $Pr^{3+} : La_2(WO_4)_3$

M. Lovrić, P. Glasenapp, D. Suter, B. Tumino, A. Ferrier, P. Goldner,
M. Sabooni, L. Rippe, and S. Kröll.

Phys. Rev. B **84**, 104417 (2011).

PHYSICAL REVIEW B **84**, 104417 (2011)

Hyperfine characterization and spin coherence lifetime extension in Pr^{3+}:$La_2(WO_4)_3$

Marko Lovrić,[*] Philipp Glasenapp, and Dieter Suter
Technische Universität Dortmund, Fachbereich Physik, D-44221 Dortmund, Germany

Biagio Tumino, Alban Ferrier, and Philippe Goldner[†]
Chimie ParisTech ENSCP, Laboratoire de Chimie de la Matiére Condensée de Paris (LCMCP), F-75005 Paris, France UPMC Univ Paris 06, F-75005 Paris, France CNRS, UMR 7574, F-75005 Paris, France

Mahmood Sabooni, Lars Rippe, and Stefan Kröll
Department of Physics, Lund University, P.O. Box 118, S-221 00 Lund, Sweden

(Received 27 June 2011; revised manuscript received 11 August 2011; published 12 September 2011)

Rare-earth ions in dielectric crystals are interesting candidates for storing quantum states of photons. A limiting factor on the optical density and thus the conversion efficiency is the distortion introduced in the crystal by doping elements of one type into a crystal matrix of another type. Here we investigate the system Pr^{3+}:$La_2(WO_4)_3$, where the similarity of the ionic radii of Pr and La minimizes distortions due to doping. We characterize the praseodymium hyperfine interaction of the ground-state ($^3H_4$) and one excited state ($^1D_2$) and determine the spin Hamiltonian parameters by numerical analysis of Raman-heterodyne spectra, which were collected for a range of static external magnetic-field strengths and orientations. On the basis of a crystal-field analysis, we discuss the physical origin of the experimentally determined quadrupole and Zeeman tensor characteristics. We show the potential for quantum memory applications by measuring the spin coherence lifetime in a magnetic field that is chosen such that additional magnetic fields do not shift the transition frequency in first order. Experimental results demonstrate a spin coherence lifetime of 158 ms — almost 3 orders of magnitude longer than in zero field.

DOI: 10.1103/PhysRevB.84.104417 PACS number(s): 42.50.Md, 76.30.Kg, 76.70.Hb, 76.60.−k

I. INTRODUCTION

Rare-earth ion-doped crystals (REICs) have recently appeared as promising solid-state materials for quantum information processing. In the field of quantum computing, achieved milestones include controlled phase gates[1] and single-qubit arbitrary rotation.[2] While these experimental results were performed on single-qubit and two-qubit systems, scalable schemes have also been proposed.[3] In the field of quantum memories, devices able to faithfully store and release photonic quantum states have been proposed and implemented. Using several different storage-recall protocols,[4–7] high-efficiency,[8] multiple-photon storage with large bandwidth[9,10] and entanglement storage[11,12] were demonstrated in REICs. These results rely on the very long optical coherence lifetimes, e.g., 4.4 ms lifetimes have been observed in Er^{3+}:Y_2SiO_5.[13]

Even longer lifetimes have been reported for rare-earth ion hyperfine transitions and accordingly, the qubit in REIC-based quantum computing and memories is generally defined by selecting two ground-state hyperfine levels. Optical transitions are used to selectively address qubits or to transfer coherences from the optical to the rf domain and vice versa. Coherence lifetimes can be extended to 30 s for a ground-state hyperfine transition of Pr^{3+}:Y_2SiO_5 at liquid helium temperature.[14] This was achieved in two steps: First, an external magnetic field was applied to the sample in order to decouple one hyperfine transition from magnetic-field fluctuations due to host spin flips. As these are the main source of dephasing, the zero-field coherence lifetime of 500 μs was extended in this way to 82 ms[15] and later to 860 ms.[14] The decoupling was achieved by minimizing the transition energy dependence with respect to the magnetic field. This condition is referred as ZEFOZ, or zero-first-order Zeeman shift transitions.[16] The coherence lifetime was then further increased by rf decoupling pulses arranged in a Carr-Purcell sequence.[14]

Y_2SiO_5 is the most thoroughly studied host in REIC quantum information processing. It combines long coherence lifetimes, favored by its low-magnetic-moment density, mainly due to Y nuclear spins, and high oscillator strengths. A disadvantage of Y-based host material is that doping with Pr^{3+} or Eu^{3+} leads to relatively large inhomogeneous linewidths at high doping concentrations, which limits the maximal achievable optical depth. This is an important concern in high-efficiency quantum memories.[17] To overcome this limitation for Pr^{3+}, we proposed a La-based crystal, $La_2(WO_4)_3$. Pr^{3+} substitutes La^{3+} in this material, both having very similar ionic radii ($r_{La^{3+}} = 1.18$ Å, $r_{Pr^{3+}} = 1.14$ Å).[18] Compared to Y_2SiO_5 ($r_{Y^{3+}} = 1.02$ Å),[18] doping stress is reduced and the inhomogeneous linewidth is 15 times smaller for high Pr^{3+}concentrations. However, the magnetic moment of lanthanum (2.78 μ_B) is much higher than that of Y^{3+} (-0.14 μ_B), and the $La_2(WO_4)_3$ magnetic-moment density is 7.5 times higher than in Y_2SiO_5. It seems that this should be seriously detrimental to coherence lifetimes, but we measured a hyperfine lifetime of 250 μs,[19] which is only smaller by a factor of ≈2 compared to the value in Y_2SiO_5. This allowed us to measure narrow and efficient electromagnetically induced transparency in this material.[20] This result also suggested that REICs that could be useful for quantum information processing are not limited to the few crystals with very low-magnetic-moment density. However, since applications require T_2 values in the millisecond range, techniques for increasing the coherence lifetime should be used. In this paper we show that by using a ZEFOZ transition hyperfine T_2 can reach 158 ± 7 ms, corresponding to a 630-fold increase. It is therefore possible to strongly reduce the influence of host spin flips, even in the case of high-magnetic-moment density.

ZEFOZ transitions appear at specific magnetic field vectors, which can only be predicted if all parameters of the system Hamiltonian are known with high precision. In the present system, the $I = 5/2$ nuclear spin of ^{141}Pr (100% abundance) and the C_1 site symmetry result in a complicated hyperfine structure. We therefore used the approach of Ref. 21, which consists of determining the spin Hamiltonian parameters by coherent Raman scattering before numerically identifying ZEFOZ transitions. Finally, the coherence lifetimes of the hyperfine transitions were measured by optically detected Raman echoes.

II. MODEL FOR THE HYPERFINE INTERACTION

A good approximation for the Hamiltonian of many rare-earth-doped compounds is[22]

$$\mathcal{H}_0 = [\mathcal{H}_{\mathrm{FI}} + \mathcal{H}_{\mathrm{CF}}] + [\mathcal{H}_{\mathrm{HF}} + \mathcal{H}_Q + \mathcal{H}_Z + \mathcal{H}_z]. \qquad (1)$$

The first two terms, the free ion (including spin-orbit coupling), and the crystal-field Hamiltonians determine the energies of the electronic degrees of freedom. The terms in the second bracket, consisting of the hyperfine coupling, the nuclear quadrupole coupling, and the electronic and the nuclear Zeeman Hamiltonian, lift the degeneracy of the nuclear-spin states.

The site symmetry of our system is low enough that the electronic states are nondegenerate. As a result of this "quenching" of the electronic angular momentum, the electronic Zeeman $\mathcal{H}_Z$ and hyperfine interaction $\mathcal{H}_{\mathrm{HF}}$ contribute only as second-order perturbations. Utilizing this, the four last terms of Eq. (1) can be well approximated by a nuclear-spin Hamiltonian[22,23]:

$$\mathcal{H}_1 = \vec{B} \cdot \mathbf{M}_1 \cdot \vec{I} + \vec{I} \cdot \mathbf{Q}_1 \cdot \vec{I}, \qquad (2)$$

$$\mathbf{M}_1 = R_M \cdot \begin{bmatrix} g_x & 0 & 0 \\ 0 & g_y & 0 \\ 0 & 0 & g_z \end{bmatrix} \cdot R_M^T, \qquad (3)$$

$$\mathbf{Q}_1 = R_Q \cdot \begin{bmatrix} E - \frac{1}{3}D & 0 & 0 \\ 0 & -E - \frac{1}{3}D & 0 \\ 0 & 0 & \frac{2}{3}D \end{bmatrix} \cdot R_Q^T, \qquad (4)$$

where the $R_i = R(\alpha_i,\beta_i,\gamma_i)$ represent rotation matrices and Euler angles[24] (see Sec. II in Ref. 25), specifying the orientation of the effective Zeeman tensor **M** and the effective quadrupolar tensor **Q** principal axis system (PAS) $[(x',y',z')$ and (x'',y'',z''), respectively$]$ relative to the laboratory-based reference axis system (x,y,z) (see Sec. III). In general, the **M** and **Q** principal axes are not aligned and accordingly, the R_Q and R_M matrices are not identical.

In zero magnetic field, the quadrupole interaction results in a partial lifting of the nuclear-spin states degeneracy. The corresponding structures for lowest levels of the crystal-field multiplets $^3H_4$ and $^1D_2$ were determined by hole-burning experiments[19,26] and are shown in Fig. 1. We label the levels by their projections onto the z'' principal axes of the **Q** tensor, noting that these states are not eigenstates of the nuclear-spin Hamiltonian. Since the PAS of the **Q** tensors of different crystal-field levels do not coincide, their quantization axes are also different. For the small magnetic fields used to determine spin Hamiltonian parameters, the hyperfine structure remains close to the zero-field one, which allows us to identify resonance lines with transitions between zero-field states.

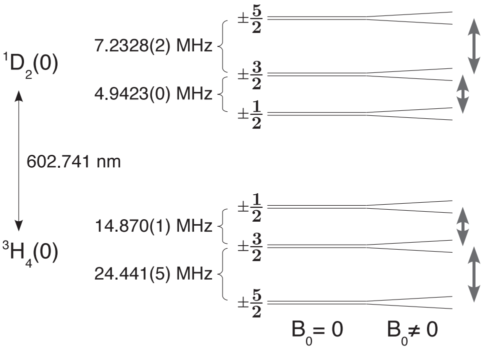

FIG. 1. Pr^{3+}:$La_2(WO_4)_3$ level structure of the lowest (0) $^3H_4$ and $^1D_2$ crystal-field manifolds, including their hyperfine structure. The order of the energy levels follows from previous work,[19] whereas the transition frequencies given above could be measured with higher precision utilizing zero-field Raman-heterodyne scattering within the present work. The arrows on the right indicate the range of hyperfine transitions excited by rf in the separate experiments.

Since Pr^{3+} occupies two different subsites in the crystal (see Sec. III), the Hamiltonian describing the second site includes different rotation matrices. Utilizing Eq. (2) of site 1 and the property that both sites are connected by a C_2 symmetry we write

$$\mathcal{H}_2 = \vec{B} \cdot \left(R_{C_2}\mathbf{M}_1 R_{C_2}^T\right) \cdot \vec{I} + \vec{I} \cdot \left(R_{C_2}\mathbf{Q}_1 R_{C_2}^T\right) \cdot \vec{I}. \qquad (5)$$

With

$$R_{C_2} = R_C^T \cdot R_\pi \cdot R_C,$$
$$R_C = R(\alpha_{C_2},\beta_{C_2},0), \quad R_\pi = R(180^\circ,0,0),$$

the angles α_{C_2} and β_{C_2} correspond to the spherical coordinates of the C_2 axis in the laboratory system. Therefore in this manuscript the complete nuclear-spin Hamiltonian of a given crystal-field level depends on 13 parameters: $D,E,\alpha_Q,\beta_Q,\gamma_Q,g_x,g_y,g_z,\alpha_M,\beta_M,\gamma_M,\alpha_{C_2},\beta_{C_2}$.

III. EXPERIMENT

We used a sample of high optical quality, grown by the Czochralski method, containing 0.2 at. % Pr^{3+}. The 5 × 5 × 5 mm crystal was mounted in an optical cryostat and cooled to liquid helium temperatures. $La_2(WO_4)_3$ forms a monoclinic crystal with a $C2/c$ space group, identical to that of Y_2SiO_5. The La^{3+} ions occupy only one crystallographic site of C_1 symmetry. In each unit cell (containing four formula units), this site appears at eight positions which are related by inversion, translation, and C_2 symmetries. The C_2 axes are identical to the C_2 crystal symmetry axis, also denoted by b in the following. The C_2 symmetry divides the La positions into two groups of four ions, which behave differently, unless the magnetic field is perpendicular or parallel to the b axis. These two groups are called subsites in the following. The crystal surfaces were polished perpendicular to the (X,Y,Z) principal axes of the optical indicatrix. Optical back reflection at the Z surface and mechanical alignment of the X and Y surfaces was used to align the crystal along our reference (x,y,z) axes, defined by the static magnetic-field coils (see below). Apart from alignment errors the (X,Y,Z) axes should be a replica of (x,y,z), the laser propagating along the z/Z and the b/Y axis expected to be closely aligned to the laboratory-frame y axis.

To obtain the hyperfine spectra of both the electronic ground-state and the electronically excited state, we used Raman-heterodyne scattering (RHS).[27,28] In this scheme a resonant rf field creates coherence between two hyperfine levels. Prior to this, the laser can be used to create initial population between those states. The laser further serves to transfer the hyperfine coherence into the optical transition and can simultaneously be used as the local oscillator for a heterodyne detection of the excited Raman field, as the latter is coherently emitted into the same optical mode.

A Coherent 899-21 dye laser, further stabilized by home-built electronics with respect to intensity and frequency (linewidth <20 kHz), served as the light source. It was tuned to the center of the $^3H_4(0) \leftrightarrow {}^1D_2(0)$ transition (see Fig. 1). The laser was focused, from a collimated beam of 1.5 mm diameter, with a 300-mm lens into the sample. We generated the optical pulses and frequency chirps by double-pass acousto-optic modulator setups.

The rf fields were applied to the sample by a ten-turn 6-mm-diameter coil. For continuous-wave experiments (ground-state), one side of the coil was terminated by a 50-Ω load, and the other was attached to an rf driver. For the exited state spectra, we used a pulsed RHS scheme. Here the coil was part of an appropriate tuned tank circuit. Figure 2 shows the sequences used for the two types of experiments.

The frequencies for the rf excitation and the shifting of the laser frequency were generated by 48-bit, 300-MHz direct digital synthesizers, yielding very precise frequencies. We controlled the timing of the pulses and frequency chirps by a word generator with a resolution of 4 ns. Detection of the heterodyne beat signal was accomplished by a 100-MHz balanced photo receiver (Femto HCA-S), a phase-sensitive quadrature-detection demodulation scheme, appropriate analog and digital filters, and a digital oscilloscope.

The static magnetic field was created by a set of three orthogonal Helmholtz coil pairs. They are mounted outside the cryostat and their coil diameters range from 20 to 40 cm, providing a homogeneous field over the sample volume in their center. With currents of about 10 A, each coil pair generates a magnetic field of about 8 mT. To control the field vector a computer control was set up for the current sources of the Helmholtz coils. To compensate nonlinearities and drifts, we used a set of three orthogonal Hall probes as sensors for a computer-based feedback loop. The absolute error of the field components is <0.06 mT, and the relative linear error for the static magnetic field is <0.3%. To minimize the effect of small background fields (e.g., earth magnetic field), a small compensation field was used, which minimized the observed zero-field RHS line splitting and also led to almost perfect destructive interference.[29,30] We used this compensation field as our zero-field reference in all measurements.

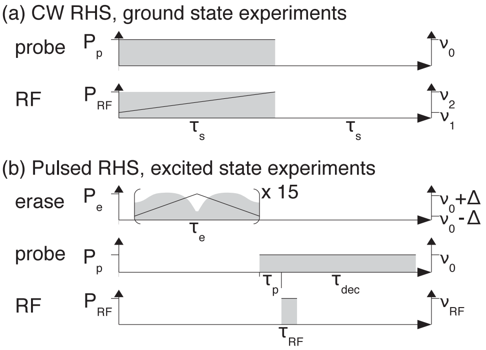

FIG. 2. RHS pulse sequences. Black lines indicate frequencies and gray areas the applied optical and rf powers. (a) Continuous-wave sequence for the ground-state measurements. A low-power laser probe ($P_p = 0.3$ mW) and a scanning frequency rf ($P_{\mathrm{RF}} \approx 1$ W, $\tau_s = 50$ ms, $\nu_1 = 7.4$, and $\nu_2 = 22.4$ MHz for $|\pm\frac{1}{2}\rangle \leftrightarrow |\pm\frac{3}{2}\rangle$ or, respectively, 17.1 and 32.1 MHz for $|\pm\frac{3}{2}\rangle \leftrightarrow |\pm\frac{5}{2}\rangle$) were applied to the sample. The optimum temperature of the cold finger for this scheme was 4.5 K, since still lower temperatures gave such slow hyperfine level relaxation rates that it would be necessary to repump the hyperfine level population. (b) Pulsed RHS sequence for the excited state. Probe and erase beam were overlapped in the sample at an angle of 0.6°. To allow for higher repetition rate the chirped erase laser ($\Delta = 64$ MHz, $\tau_e = 10$ ms, average power $P_e \approx 20$ mW) redistributed the populations. An initial population difference between hyperfine sublevels was created by the probe beam ($P_p = 1.2$ mW, $\tau_p = 100$ μs) and converted to coherences by an rf pulse ($\nu_{\mathrm{RF}} = 4.94/7.23$ MHz ($|\pm\frac{1}{2}\rangle \leftrightarrow |\pm\frac{3}{2}\rangle$ resp. $|\pm\frac{3}{2}\rangle \leftrightarrow |\pm\frac{5}{2}\rangle$), $P_{\mathrm{RF}} = 214/287$ W, $\tau_{\mathrm{RF}} = 4$ μs). For optical heterodyne detection the same probe beam was left active for an additional time τ_{dec}. The temperature of the cold finger for this scheme was 2.4 K.

For an optimal determination of the Hamiltonian parameters, it is important to sample different strengths and orientations of the magnetic field. In our experiments we used a spiral on the surface of an ellipsoid[21]:

$$\vec{B}(t) = \begin{pmatrix} B_x\sqrt{1-t^2}\cos(6\pi t) \\ B_y\sqrt{1-t^2}\sin(6\pi t) \\ B_z t \end{pmatrix}. \tag{6}$$

Here, we use

$$t = -1 + (N-1)\,\frac{2}{N_{\mathrm{tot}}-1}, \quad N = 1,2,\ldots,N_{\mathrm{tot}}$$

to represent the discrete coordinate along the trajectory. For the ground-state series, we measured $N_{\mathrm{tot}} = 101$ orientations, with magnetic-field amplitudes $[B_x,B_y,B_z] = [7,8,9]$ mT and for the excited state we used $N_{\mathrm{tot}} = 251$ and

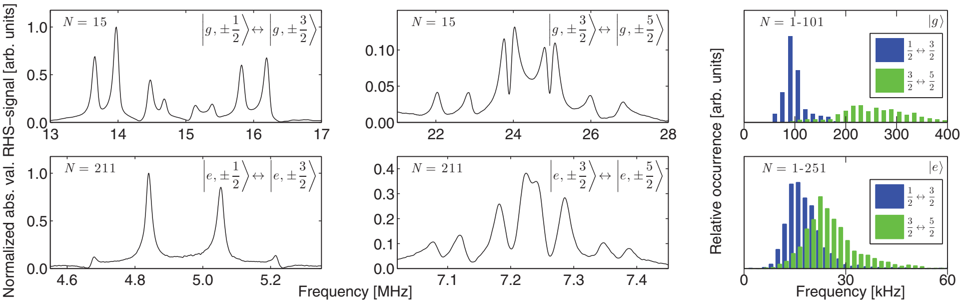

FIG. 3. (Color online) Representative ground- (cw) and exited-state (pulsed) RHS spectra. Both spectra from the ground-state ($|g,i \leftrightarrow j\rangle$) are recorded at $\vec{B} = (2.60,-5.27,-5.76)$ mT. For the excited state spectra, we used $\vec{B} = (4.62,1.19,4.42)$ mT. The normalization is relative to the largest line from ground- or excited state spectra, respectively. The $|g,i \leftrightarrow j\rangle$ spectra shown here resolve all 8 + 8 possible RHS transitions, while in the $|e,i \leftrightarrow j\rangle$ spectra not all lines are resolved. The histograms on the right show the distributions of fitted FWHM RHS linewidths for all recorded data (see Sec. IA in Ref. 25), plotted separately for the two hyperfine transitions ($|g/e,i \leftrightarrow j\rangle, i/j = \pm\frac{1}{2}/\pm\frac{3}{2}$ or $\pm\frac{3}{2}/\pm\frac{5}{2}$). For both the ground- and the excited state, the $\pm\frac{3}{2} \leftrightarrow \pm\frac{5}{2}$ linewidths are bigger (see Sec. V C). The mean linewidths are $|g,\pm\frac{1}{2} \leftrightarrow \pm\frac{3}{2}\rangle \approx 105$ kHz, $|g,\pm\frac{3}{2} \leftrightarrow \pm\frac{5}{2}\rangle \approx 301$ kHz, $|g,\text{all}\rangle \approx 196$ kHz and $|e,\pm\frac{1}{2} \leftrightarrow \pm\frac{3}{2}\rangle \approx 18.3$ kHz, $|e,\pm\frac{3}{2} \leftrightarrow \pm\frac{5}{2}\rangle \approx 26.3$ kHz, $|e,\text{all}\rangle \approx 22.3$ kHz.

$B_x = B_y = B_z = 6.5$ mT. Figure 3 shows some typical experimental spectra for the ground- and excited states.

IV. THE FITTING PROCEDURE

As described in Sec. II, 13 parameters are necessary to fully characterize the spin Hamiltonian in the laboratory. Using those it is possible to compute the line positions in the RHS spectra. By minimization of the the rms deviation [see Eq. (14) in Ref. 25] between calculated and experimental line positions, the spin Hamiltonian parameters can be derived. Due to the large number of parameters and their complicated interdependency, gradient-based algorithms are not efficient, as they tend to stick to local minima. In our case the combination of first running a probabilistic and then a direct search yielded the best convergence to the global minimum. As in the work of Longdell *et al.*,[16,21] we used simulated annealing[31] for the first step. It allows for robust convergence to a global minimum when using appropriate settings. The latter typically cause simulated annealing to converge relatively slowly, although being already close to the global minimum in advanced phases. Therefore we switch to a pattern search[32] algorithm in this situation. We provide additional details of the fitting procedure in the supplementary material.[25]

The underlying symmetry of the crystal-field and the structure of the spin Hamiltonian cause some ambiguity if only RHS spectra are used to determine the Hamiltonian parameters.[33] Important for our investigation is the fact that the RHS spectra do not depend on the signs of D, E, and the gyromagnetic factors g_x, g_y, and g_z. In addition, different sets of Euler angles correspond to the same tensor orientations. As a consequence, different runs with random initial values lead to apparently different solutions. We checked that these solutions are related by the symmetry operations mentioned above and thus verified that we really found a unique global minimum.

V. RESULTS

A. Electronic ground-state

Figure 4(a) shows the experimental data for $N_{\text{tot}} = 101$ different external magnetic fields. Several fit trails reliably led to the parameters shown in Table I and represented by the solid lines in Fig. 4(a). All quoted Euler angles are given in the "zyz" convention.[24]

With these parameters, the rms deviation between all accounted line positions and the fit is ≈32 kHz, significantly smaller than the average linewidth of the ground-state RHS lines of ≈196 kHz (see Fig. 3), indicating that it is dominated by statistical error. At the end of the fitting procedure, $L = 1218$ of the total 1221 experimental lines could be unambiguously assigned (see Sec. I B in Ref. 25) to calculated resonance line positions.

To estimate the uncertainty of the fitted parameters, we sampled the parameter space in the vicinity of the global minimum by repeating the probabilistic part of the fitting procedure using a fixed, low-temperature T_σ. Such a procedure can be shown to be rigorous if the only source of error is Gaussian noise in the line positions.[21,33] To estimate this noise we used the mean ratio of fitted linewidths σ_i to the individual signal-to-noise ratio (SNR_i) for all contributing RHS lines:

$$\nu_\sigma = \frac{1}{L}\sum_{i=1}^{L}\frac{\sigma_i}{SNR_i}.$$

For the ground-state data we found $\nu_\sigma = 1.4$ kHz. According to this we chose the fixed temperature T_σ, so that a single parameter change from its optimum value by T_{σ_i}(see Sec. I B in Ref. 25) resulted in an increase of the rms deviation by ν_σ. After 2×10^6 iterations the histograms of the accepted parameters all showed a Gaussian shape, whose 1σ widths are given as fit error in Table I.

Apart from the statistical error, we also consider systematic errors. The most important contribution is due to the calibration

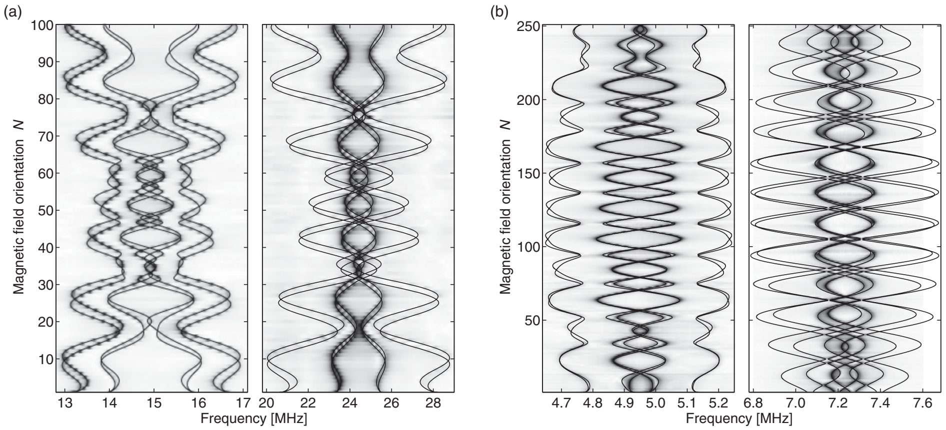

FIG. 4. RHS spectra of the $|\pm\frac{1}{2}\rangle \leftrightarrow |\pm\frac{3}{2}\rangle$ and $|\pm\frac{3}{2}\rangle \leftrightarrow |\pm\frac{5}{2}\rangle$ hyperfine transitions. (a) $^3H_4(0)$ ground-state cw RHS spectra. (b) $^1D_2(0)$ excited state pulsed RHS spectra. In both cases the solid lines represent the fit results and the shaded background the absolute value of the experimental spectra. For each field orientation, the spectrum was normalized to the maximum signal amplitude.

error of the magnetic field. We estimate its precision to $\approx$0.65%, which translates to the same fractional uncertainty of the gyromagnetic ratios g_x, g_y, and g_z. As the parameters are given in the laboratory-fixed reference frame (x,y,z), a misalignment of the crystal does not contribute to the error but is expressed by the α_{C_2} and β_{C_2} values not being exactly 90°. The only systematic contribution in the angles arises from the nonorthogonality of the coils, which is $<1^\circ$. The uncertainty of the alignment of the crystal relative to our reference (x,y,z) and that of the crystal surfaces to the optical indicatrix (X,Y,Z) results in an error of $\approx 5^\circ$ for the angles seen relative to the crystal axis system.

B. Excited state

With the optimal fit parameters, we found an rms deviation of 3.1 kHz between theoretical and experimental frequency values, using $L = 2345$ of the 2353 measured lines in $N_{\text{tot}} = 251$ spectra. Compared to the mean experimental full width at half maximum (FWHM) of 22.3 kHz, the rms deviation is even better than for the ground-state. We mainly attribute this to the higher quality of pulsed RHS spectra, with fewer line-shape artifacts. Figure 4(b) and Table II show the results.

For the determination of the fit errors here we found $\nu_\sigma = 136$ Hz. The systematic errors are again dominated by the calibration error of the magnetic field. We note that although the crystal was remounted between this and the ground-state experiments, the resulting orientation of the C_2 axis deviates less than our estimated alignment accuracy. As the Zeeman tensor is almost axially symmetric, $g_x \approx g_z$, its orientation relative to the quadrupole tensor or to the ground-state tensor orientations cannot be determined accurately.

C. Discussion

Examining Tables I and II, it appears that the principal values for the **Q** and **M** tensors are similar to those found in other hosts like Y_2SiO_5,[21] LaF_3, or $YAlO_3$.[22] Especially, the

TABLE I. Ground-state spin Hamiltonian parameters.

Parameter	Value	Fit error	Unit
D	−6.3114	0.0027	MHz
E	−0.8915	0.0021	MHz
α_Q	20.4	3.3	deg.
β_Q	147.7	1.4	deg.
γ_Q	10.2	1.4	deg.
g_x	−51.7	3.6	MHz/T
g_y	−23.5	1.1	MHz/T
g_z	−146.97	0.75	MHz/T
α_M	30.1	3.8	deg.
β_M	146.59	0.55	deg.
γ_M	13.09	0.69	deg.
α_{C_2}	88.34	0.47	deg.
β_{C_2}	92.45	0.31	deg.

TABLE II. Excited state spin Hamiltonian parameters.

Parameter	Value	Fit error	Unit
D	1.90705	0.00023	MHz
E	0.35665	0.00014	MHz
α_Q	−18.51	0.71	deg.
β_Q	73.83	0.48	deg.
γ_Q	−84.22	0.37	deg.
g_x	−17.22	0.27	MHz/T
g_y	−14.39	0.10	MHz/T
g_z	−18.37	0.14	MHz/T
α_M	−23.7	2.4	deg.
β_M	88.5	4.1	deg.
γ_M	−80.1	1.8	deg.
α_{C_2}	88.63	0.25	deg.
β_{C_2}	92.69	0.24	deg.

ground-state gyromagnetic tensor is anisotropic with one large component, in contrast to the excited state which also exhibits smaller values. To get some insight into these properties, we compared these results with calculations derived from crystal-field calculations.

In a previous work[34] we found that quadrupolar D and E values for ground- and excited states could be very well reproduced starting from electronic wave functions obtained by a crystal-field analysis. The latter was done assuming a C_{2v} site symmetry, which is higher than the actual one (C_1). In this higher symmetry, the **Q** tensors for different crystal-field levels are colinear, in clear contradiction with our results. Nevertheless, it seems that the additional crystal-field parameters of C_1 symmetry have little effect on the **Q** principal values. In the following we present the calculations of the **M** tensor principal values.

In C_{2v} orthorhombic symmetry, the spin Hamiltonian of Eq. (2), expressed in the (x_c,y_c,z_c) crystal-field axes, reads

$$\mathcal{H}'' = \sum_{i=x_c,y_c,z_c} B_i g_i I_i + D\left(I_{z_c}^2 - \frac{I(I+1)}{3}\right) + E\left(I_{x_c}^2 - I_{y_c}^2\right), \qquad (7)$$

where the g_i are related to a tensor $\mathbf{\Lambda}$[23]:

$$g_i = -2A_J g_J \mu_B \Lambda_{ii} - g_I \mu_N. \qquad (8)$$

The Λ tensor is given by

$$\Lambda_{\alpha\beta} = \sum_{n=1}^{2J+1} \frac{\langle 0|J_\alpha|n\rangle\langle n|J_\beta|0\rangle}{E_n - E_0} \qquad (9)$$

and can be calculated from the electronic wave functions $|n\rangle$. The latter were found using a free ion and crystal-field Hamiltonian whose parameters were fitted to experimentally determined crystal-field levels E_n.[34] In this calculation, we use arbitrary permutations of the (x_c,y_c,z_c) axes. This results in different sets of E and D values, which give the same hyperfine energy levels. We subsequently fix the choice of the axis system such that the convention $0 \leqslant 3E/D = \eta \leqslant 1$[35] is fulfilled, thereby resolving ambiguous sets of parameters, such as (in megahertz) $D = -1.8184$, $E = 3.6014$ and $D = -6.3114$, $E = -0.8915$, which describe identical ground-state zero-field hyperfine structures and correspond to an exchange of x_c with z_c. With this convention, we fix the permutation of the axes and thus the values for D and E for both electronic states. The crystal-field parameters we used and the corresponding E and D values for the ground- and excited states are listed in Table III.[36] The electronic wave function of the excited $^1D_2(1)$ level is used instead of that of $^1D_2(0)$ to take into account a wrong ordering in the calculated crystal-field levels of this multiplet.[34,37]

Comparing Tables I and II with Table III shows that a reasonable agreement is found between experimental and calculated principal values of ground- and excited state **M** tensors. Again, this suggests that additional parameters appearing in calculations using C_1 symmetry mainly determine the relative orientation between the different tensors. Calculated values especially reproduce the two features mentioned above: the very large value of g_z for the ground-state and the smaller g_i values for the excited state compared to the ground-state. A qualitative understanding of these properties can be obtained from the crystal-field analysis by looking at the different factors entering in Eq. (8) (see Table III). We first note that the isotropic and crystal-field independent nuclear Zeeman contribution to g_i equals –12.2 MHz/T. Differences in g_i values are mainly linked to the $\mathbf{\Lambda}$ tensors, since the products $A_J g_J$ vary by only 4% between ground- and excited states. The $\mathbf{\Lambda}$ tensors involve the $\vec{J}$ matrix elements and the energy differences appearing as denominators in Eq. (9). We first discuss the ground-state case. The electronic wave function of interest [^{3}H$_4$(0)] has the following form:

TABLE III. Crystal-field parameters B_{ij}, calculated **Q** and **M** tensor principal values, and second-order hyperfine interaction parameters.

B_{ij}	(cm^{-1})		Ground-state	Excited state	Unit
B_{20}	375	D	−6.1	2.0	MHz
B_{22}	−93	E	−0.63	0.30	MHz
B_{40}	768	g_{x_c}	−32	−18	MHz/T
B_{42}	445	g_{y_c}	−22	−4	MHz/T
B_{44}	1027	g_{z_c}	−151	−18	MHz/T
B_{60}	267	A_J	937	697	MHz
B_{62}	−402	g_J	0.81	1.03	
B_{64}	−61	$\Lambda_{x_c x_c}$	0.0280	0.0066	cm
B_{66}	−52	$\Lambda_{y_c y_c}$	0.0140	−0.0090	cm
		$\Lambda_{z_c z_c}$	0.2000	0.0069	cm

$$|0\rangle = -0.62|^3H_4,-4\rangle - 0.62|^3H_4,4\rangle - 0.4|^3H_4,0\rangle,$$

where brackets on the right-hand side are written as $|^{2S+1}L_J,M_J\rangle$ and only terms with a coefficient larger than 0.15 have been kept. The larger J_{z_c} matrix element is found between $|0\rangle$ and $|1\rangle$, since the latter is nearly only composed of $|^3H_4,\pm4\rangle$ states. The $|\langle 0|J_{z_c}|1\rangle|$ matrix element equals 3.6 close to the maximum value of $|\langle ^3H_4,\pm4|J_{z_c}|^3H_4,\pm4\rangle| = 4$. Moreover, this large matrix element is found for levels close in energy (65 cm^{-1} Ref. 34), resulting in a large $\Lambda_{z_c z_c}$. On the other hand, $|0\rangle$ couples to crystal-field levels containing $|^3H_4,\pm3\rangle$, $|^3H_4,\pm1\rangle$ by J_{x_c} or J_{y_c} operators. The corresponding matrix elements do not exceed 2.4 in absolute value. As expected, this is close to the average value of matrix elements of the form $\langle ^3H_4,\pm4|J_i|^3H_4,\pm3\rangle$ and $\langle ^3H_4,\pm1|J_i|^3H_4,\pm2\rangle$ (where $i = x_c$ or y_c), which is at most 1.9. The levels with the largest matrix elements are located at high energies ($E_3 = 143$ and $E_5 = 349$ cm^{-1} for J_{y_c} and J_{x_c}, respectively), resulting in low $\Lambda_{x_c x_c}$ and $\Lambda_{y_c y_c}$. This in turn explains the small values of g_{x_c} and g_{y_c} compared to g_{z_c}.

A similar analysis can be performed for the excited state. As mentioned above, the level of interest is $^1D_2(1)$ and is found to be equal to

$$|1\rangle = 0.67|^1D_2,-2\rangle - 0.67|^1D_2,2\rangle,$$

with the same convention as above. This state gives a J_{z_c} matrix element equal to 2 with the state $|4\rangle$, located 441 cm^{-1} higher than $|1\rangle$. Maximum average values for matrix elements of J_{x_c} and J_{y_c} can be estimated as above for levels containing $|^1D_2 \pm 1\rangle$ states, resulting in $|\langle 0|J_{x_c}|1\rangle| \approx |\langle 1|J_{x_c}|2\rangle| \approx 1$. The corresponding energies are

$E_0 - E_1 = -82$ cm^{-1} and $E_2 - E_1 = 113$ cm^{-1}. The combination of matrix elements and energy differences results in smaller values for Λ_{ii} compared to the ground-state. This can also partly explain the isotropy of the excited state g_i values, which are closer to the nuclear Zeeman contribution. As pointed out above, several Pr^{3+}-doped compounds exhibit the same behavior so that the discussion given above could also be applied to them.

We now turn to the principal axes of the spin Hamiltonian tensors. The oscillator strengths are assumed to be proportional to the square of the overlap of the nuclear wave functions,[22] the latter being given by the ground- and excited state Hamiltonians, which is reasonable since the hyperfine interactions are a small perturbation to the electronic wave functions. Thus we can check the relative oscillator strengths following from our $(\alpha_Q,\beta_Q,\gamma_Q,D,E)$ parameters against values from zero-field spectral tayloring experiments.[19] The results are gathered in Table IV. A good agreement is found, showing that indeed the orientation of the quadrupole tensors was determined correctly. In Pr^{3+}:Y$_2$SiO$_5$, significant discrepancies were found between calculated and experimental values.[38,39] This was tentatively attributed to additional selection rules due to superhyperfine coupling with Y ions. In our case, it seems that although superhyperfine coupling may also be observed (see Sec. V D), relative optical transition matrix elements can still be determined from the overlap of the nuclear wave functions.

Hyperfine transition linewidths were also determined during the fit procedure. The data show (see Fig. 3) that the transitions with the larger splittings also show the larger linewidths. For example, the ground-state $|\pm\frac{3}{2}\rangle \leftrightarrow |\pm\frac{5}{2}\rangle$ transitions at 24.44 MHz have an average linewidth of 301 kHz, whereas the $|\pm\frac{1}{2}\rangle \leftrightarrow |\pm\frac{3}{2}\rangle$ transitions at 14.87 MHz have a width of only 105 kHz. This becomes reasonable if we focus on the dominant part of the Hamiltonian (Eq. (7)), $\mathcal{H}'' \approx D[I_{z_c}^2 - I(I+1)/3]$. In this case, the transition energies become $|\frac{1}{2}\rangle \leftrightarrow |\frac{3}{2}\rangle \approx |2D|$ and $|\frac{3}{2}\rangle \leftrightarrow |\frac{5}{2}\rangle \approx |4D|$. Crystal-field variations from one ion position to another correspond to a distribution of crystal-field parameters and therefore of the D parameter. The hyperfine linewidths should then be proportional to the transition energies. This is qualitatively in agreement with the experimental values. The excited state linewidths are also smaller than the ground-state ones, which suggests that the D distribution width is also proportional to D.

TABLE IV. Relative optical oscillator strengths between $^3H_4(0)$ and $^1D_2(0)$ hyperfine levels. Experimental[19] and calculated values, using Tables I and II, are being compared. Rows correspond to transitions starting from the ground-state hyperfine levels and columns correspond to transitions to different excited state hyperfine levels (see Fig. 1).

		$\lvert e,\pm\frac{1}{2}\rangle$	$\lvert e,\pm\frac{3}{2}\rangle$	$\lvert e,\pm\frac{5}{2}\rangle$
$\langle g,\pm\frac{1}{2}\rvert$	Exp.	0.09 ± 0.01	0.28 ± 0.01	0.63 ± 0.01
	Calc.	0.08 ± 0.01	0.24 ± 0.02	0.67 ± 0.02
$\langle g,\pm\frac{3}{2}\rvert$	Exp.	0.33 ± 0.01	0.39 ± 0.01	0.28 ± 0.02
	Calc.	0.31 ± 0.02	0.45 ± 0.02	0.24 ± 0.02
$\langle g,\pm\frac{5}{2}\rvert$	Exp.	0.55 ± 0.01	0.36 ± 0.01	0.09 ± 0.01
	Calc.	0.60 ± 0.02	0.31 ± 0.02	0.09 ± 0.01

D. Experimental verification of a ZEFOZ transition

As mentioned earlier, the coherence times for ZEFOZ transitions are expected to be much longer than at zero or arbitrary magnetic field. To our best knowledge this was demonstrated experimentally only for Pr^{3+}:Y$_2$SiO$_5$.[14,15] To verify our hyperfine characterization and also the usefulness of the ZEFOZ technique for other compounds, we present experimental data of a ZEFOZ transition of Pr^{3+}:La$_2$(WO$_4$)$_3$ in the following. Using our ground-state parametrization we sought for magnetic-field configurations and transitions that satisfy the ZEFOZ conditions[15]:

$$\vec{S}^I(\vec{B}_{\text{opt}}) = \left(\frac{\partial\nu_i(\vec{B}_{\text{opt}})}{\partial B_x}, \frac{\partial\nu_i(\vec{B}_{\text{opt}})}{\partial B_y}, \frac{\partial\nu_i(\vec{B}_{\text{opt}})}{\partial B_z}\right) = \vec{0}.$$

We identified the points $\vec{B}_{\text{opt}}$ by numerical minimization of $|\vec{S}^I(\vec{B})|$ for all transitions ν_i within a magnetic-field grid. Several of the identified ZEFOZ transitions showed a low curvature, e.g., small second-order coefficients

$$S_{jk}^{II}(\vec{B}) = \left.\frac{\partial^2\nu_i(\vec{B})}{\partial B_j \partial B_k}\right|_{\vec{B}}. \tag{10}$$

We studied the ZEFOZ transition at $\nu_4 = 12.6$ MHz and $\vec{B}_{\text{opt}} = (57.5, 4.0, -36.1)$ mT. As the setup at TU Dortmund, described in Sec. III, was not designed for magnetic fields of more than 12 mT per axis, we carried out the ZEFOZ experiments at Lund University. This allowed for verification of the Hamiltonian parameters and predicted ZEFOZ points in an independent laboratory. The static magnetic-field vector was provided by a set of three orthogonal superconducting coils, suitable to generate the elevated field. Whereas the x and z coils could provide a resolution of ≈ 4 μT, the y-axis control was limited to a step size of 1 mT. To fit into the homogeneous region of the coils we cut the previously characterized crystal into a $5 \times 5 \times 1$ mm piece. This and the construction of the sample holder limited our alignment of the optical indicatrix to the coil frame to a precision of about 10° for the x and y axes. We could adjust the z axis much more precisely, aligning the reflection from the crystal surface normal to Z to be parallel with the incident laser. To find the ZEFOZ point experimentally we had to consider the alignment precision, the accuracy of the Hamiltonian parameters, and the calibration of the coils. In a first step we adjusted the magnetic field to get a good overlap between observed cw RHS spectra and the calculated line positions following from Table I and $\vec{B}_{\text{opt}}$. Close to the ZEFOZ condition, the transition frequency becomes an insensitive tuning parameter for the field. Thus, in a second step we fine tuned the magnetic-field components by looking at the achieved spin coherence lifetime directly. For this we used a Raman-echo sequence[40] and tuned the field in order to maximize the echo signal for long evolution times (rf pulse separations). Figure 5 shows the longest-lived Raman-echo decay curves we could achieve. These demonstrate hyperfine coherence times of up to $T_2(\vec{B}_{\text{opt}}) = 158 \pm 7$ ms, representing a 630-fold increase compared to the zero-magnetic-field situation.[20] The decay curves at magnetic fields slightly

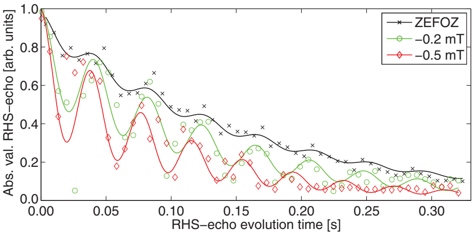

FIG. 5. (Color online) Raman-echo decays at the ZEFOZ point and with magnetic detunings of −0.2 and −0.5 mT for the z component.

detuned from the ZEFOZ point show slow modulations with a frequency of $\nu_M = 24.5 \pm 1.7$ Hz.[41] This could be due to a superhyperfine interaction with La nuclei, but a clear explanation is lacking at the present time. This point will be investigated in further experiments. As we moved the magnetic field away from the ZEFOZ point $\vec{B}_{\text{opt}}$ by -0.2 mT in the z component, this resulted in a decrease of the coherence time to $T_2(-0.2\text{ mT}) = 133 \pm 16$ ms and a shift by -0.5 mT resulted in $T_2(-0.5\text{ mT}) = 97 \pm 19$ ms.

In the following we will use this measured $T_2(\vec{B})$ values to estimate the magnetic-field fluctuation at the Pr^{3+} site. These fluctuations cause frequency shifts and thereby broaden the hyperfine transition. For this purpose, we expand the hyperfine transition frequency ν_i on a deviation B_{off} from a given field $\vec{B}$:

$$\nu_i|_{\vec{B}} = \nu_i(\vec{B}) + s_1\, B_{\text{off}} + \frac{s_2}{2}\, B_{\text{off}}^2.$$

For $\vec{B} = \vec{B}_{\text{opt}}$ the first derivative vanishes ($s_1 = 0$) and the frequency change due to small shifts is

$$\Delta\nu = \frac{s_2}{2} B_{\text{off}}^2. \tag{11}$$

If the offset from the ZEFOZ condition is due to some random field ΔB, this leads to a line broadening instead of a frequency shift. The linewidth may then be written as

$$T_2^{-1} = \frac{s_2}{2}(\Delta B)^2. \tag{12}$$

With the experimentally obtained value of $T_2 = 158$ ms and $s_2 \approx 12\text{ kHz/mT}^2$, calculated from the maximum eigenvalue of the derivative matrix Eq. (10), using the parameters from Table I we thus estimate the magnetic-field fluctuations as $\Delta B \approx 32\ \mu$T.In Pr^{3+}:Y_2SiO_5 $\Delta B = 14\ \mu\text{T}$[14,16] ($s_2 \approx 3{-}6\text{ kHz/mT}^2$) was found, representing the only ZEFOZ testbed experimentally investigated up to date. Thus both ΔB are of the same order and their values are compatible with the observed zero-field T_2 relaxation times [Pr^{3+}:$\text{La}_2(\text{WO}_4)_3\approx$ 250 μs vs Pr^{3+}:$\text{Y}_2\text{SiO}_5\approx$ 500 μs], noting that their g_i factors and thus their $s_1(B = 0)$ are comparable too.

When the deviation from $\vec{B}_{\text{opt}}$ becomes large compared to the fluctuations, $B_{\text{off}} \gg \Delta B$, Eq. (11) changes to

$$\Delta\nu = \frac{s_2}{2}\left(B_{\text{off}}^2 + 2\Delta B\, B_{\text{off}}\right). \tag{13}$$

The first term describes the line shift, the second a line broadening. For $\Delta B \approx 32\ \mu$T Eq. (13) yields a broadening corresponding to decay times $T_2(0.2\text{ mT}) \approx 13$ ms and $T_2(0.5\text{ mT}) \approx 5$ ms. Both T_2 values are significantly shorter than the experimental values. We account this to wrong assumptions for the model.

The most likely explanation for this discrepancy is that the relaxation at our reference field is not entirely due to magnetic-field fluctuations and that the reference field does not exactly fulfill the ZEFOZ condition. Both effects lead to additional contributions to the dephasing rate. We therefore write the total dephasing rate as

$$T_2^{-1} = T_{2,0}^{-1} + s_1\, \Delta B + s_2\, \Delta B\, B_{\text{off}}. \tag{14}$$

Here $T_{2,0}^{-1}$ describes those contributions that are not due to magnetic-field fluctuations, such as phonons, while $s_1\, \Delta B$ accounts for a possible deviation of the experimental $\vec{B}_{\text{opt}}$ from the exact ZEFOZ condition. Both terms are independent of B_{off} and are therefore indistinguishable in the available experimental data.

Using $s_2 \approx 8.2\text{ kHz/mT}^2$, which corresponds to the projection of Eq. (10) into the z direction, we now use Eq. (14) to estimate the magnetic-field fluctuations. The result of a linear fit of T_2^{-1} vs B_{off} yields $\Delta B \approx 1\ \mu$T. Applying the same analysis to the Pr^{3+}:Y_2SiO_5 data (estimated from Fig. 2 in Ref. 14) gives $\Delta B \approx 1.3\ \mu$T. This also reduces the estimate for ΔB by approximately 1 order of magnitude compared to the analysis where the minimum dephasing rate is assumed to originate entirely from the quadratic term of the magnetic-field fluctuations.[16]

For a complete analysis of all contributions to the relaxation, further measurements are necessary. Phononic contributions to T_2 could be determined from measurements at different temperatures, since s_1 and s_2 are independent of the latter. Measurements of T_2 at several deviations $\vec{B}_{\text{off}}$ could help to estimate the numerical value of $s_1\, \Delta B$.

VI. CONCLUSION

We characterized the spin Hamiltonian of Pr^{3+}:$\text{La}_2(\text{WO}_4)_3$ for the electronic ground-state and one electronically excited state utilizing RHS spectra. Using a crystal-field analysis, we indicated the reasons for the measured tensor principal values and orientations. The relative oscillator strengths between the $^3H_4(0)$ and $^1D_2(0)$ hyperfine levels derived from our data agree well with those measured in earlier work.[19] Using our characterization we could predict the magnetic-field value at which a ZEFOZ transition occurs. We verified this condition experimentally in a second laboratory. By investigating the coherence properties of the ZEFOZ transition we estimated the order of magnetic fluctuations at the Pr^{3+} site (ΔB) and found evidence that it is smaller than expected. Besides observing characteristics similar to superhyperfine interaction, we could achieve an up to 630-fold increase of the coherence lifetime compared to zero field. The demonstrated $T_2 = 158 \pm 7$ ms and the relatively low second-order Zeeman coefficient show that even crystal systems with high-magnetic-moment density can have a high potential for quantum memory and information applications.

ACKNOWLEDGMENTS

The authors are grateful to J. J. Longdell and M. J. Sellars for useful discussions in preparation of the ZEFOZ measurements. This work was supported by the Swedish Research Council, the Knut & Alice Wallenberg Foundation, the Crafoord Foundation, and the EC FP7, Contract Nos. 228334 and 247743 (QuRep).

---

[*] marko.lovric@tu-dortmund.de
[†] philippe-goldner@chimie-paristech.fr

[1] J. J. Longdell, M. J. Sellars, and N. B. Manson, Phys. Rev. Lett. **93**, 130503 (2004).

[2] L. Rippe, B. Julsgaard, A. Walther, Y. Ying, and S. Kröll, Phys. Rev. A **77**, 022307 (2008).

[3] J. H. Wesenberg, K. Mølmer, L. Rippe, and S. Kröll, Phys. Rev. A **75**, 012304 (2007).

[4] M. Nilsson and S. Kröll, Opt. Commun. **247**, 393 (2005).

[5] M. Afzelius, C. Simon, H. deRiedmatten, and N. Gisin, Phys. Rev. A **79**, 52329 (2009).

[6] G. Hétet, J. J. Longdell, A. L. Alexander, P. K. Lam, and M. J. Sellars, Phys. Rev. Lett. **100**, 023601 (2008).

[7] R. Lauro, T. Chanelière, and J.-L. LeGouët, Phys. Rev. A **79**, 53801 (2009).

[8] M. P. Hedges, J. J. Longdell, Y. Li, and M. J. Sellars, Nature **465**, 1052 (2010).

[9] I. Usmani, M. Afzelius, H. de Riedmatten, and N. Gisin, Nature Comm. **1**, 1 (2010).

[10] M. Bonarota, J.-L. Le Gouët, and T. Chanelière, New J. Phys. **13**, 013013 (2011).

[11] C. Clausen, I. Usmani, F. Bussieres, N. Sangouard, M. Afzelius, H. de Riedmatten, and N. Gisin, Nature **469**, 508 (2011).

[12] E. Saglamyurek, N. Sinclair, J. Jin, J. A. Slater, D. Oblak, F. Bussieres, M. George, R. Ricken, W. Sohler, and W. Tittel, Nature **469**, 512 (2011).

[13] T. Böttger, C. W. Thiel, R. L. Cone, and Y. Sun, Phys. Rev. B **79**, 115104 (2009).

[14] E. Fraval, M. J. Sellars, and J. J. Longdell, Phys. Rev. Lett. **95**, 030506 (2005).

[15] E. Fraval, M. J. Sellars, and J. J. Longdell, Phys. Rev. Lett. **92**, 077601 (2004).

[16] J. J. Longdell, A. L. Alexander, and M. J. Sellars, Phys. Rev. B **74**, 195101 (2006).

[17] W. Tittel, M. Afzelius, T. Chaneliére, R. L. Cone, S. Kröll, S. A. Moiseev, and M. Sellars, Laser Photonics Rev. **4**, 244 (2010).

[18] R. D. Shannon and C. T. Prewitt, Acta Crystallogr. Sect. B **25**, 925 (1969).

[19] O. Guillot-Noël, P. Goldner, F. Beaudoux, Y. LeDu, J. Lejay, A. Amari, A. Walther, L. Rippe, and S. Kröll, Phys. Rev. B **79**, 155119 (2009).

[20] P. Goldner, O. Guillot-Noël, F. Beaudoux, Y. LeDu, J. Lejay, T. Chanelière, J. L. LeGouët, L. Rippe, A. Amari, A. Walther, and S. Kröll, Phys. Rev. A **79**, 33809 (2009).

[21] J. J. Longdell, M. J. Sellars, and N. B. Manson, Phys. Rev. B **66**, 35101 (2002).

[22] R. M. Macfarlane and R. M. Shelby, in *Spectroscopy of Solids Containing Rare Earth Ions*, *Modern Problems in Condensed Matter Sciences*, edited by A. A. Kaplyanskii and R. M. Macfarlane (North Holland, Amsterdam, 1987), Vol. 21, pp. 51–184.

[23] M. A. Teplov, Sov. Phys. JETP **26**, 872 (1968).

[24] H. Goldstein, C. P. Poole, and J. L. Safko, *Classical Mechanics* (Addison Wesley, San Francisco, 2002) p. 638.

[25] See Supplemental Material at http://link.aps.org/supplemental/10.1103/10.1103/PhysRevB.84.104417 for more details on conventions and the fitting procedure.

[26] O. Guillot-Noël, P. Goldner, Y. LeDu, P. Loiseau, B. Julsgaard, L. Rippe, and S. Kröll, Phys. Rev. B **75**, 205110 (2007).

[27] J. Mlynek, N. C. Wong, R. G. DeVoe, E. S. Kintzer, and R. G. Brewer, Phys. Rev. Lett. **50**, 993 (1983).

[28] N. C. Wong, E. S. Kintzer, J. Mlynek, R. G. DeVoe, and R. G. Brewer, Phys. Rev. B **28**, 4993 (1983).

[29] M. Mitsunaga, E. S. Kintzer, and R. G. Brewer, Phys. Rev. Lett. **52**, 1484 (1984).

[30] M. Mitsunaga, E. S. Kintzer, and R. G. Brewer, Phys. Rev. B **31**, 6947 (1985).

[31] S. Kirkpatrick, C. D. Gelatt, and M. P. Vecchi, Science **220**, 671 (1983).

[32] C. Audet and J. E. Dennis, SIAM J. Optim. **13**, 889 (2003).

[33] J. J. Longdell, Ph.D. thesis, Australian National University, 2003.

[34] O. Guillot-Noël, Y. LeDu, F. Beaudoux, E. Antic-Fidancev, M. F. Reid, R. Marino, J. Lejay, A. Ferrier, and P. Goldner, J. Lumin. **130**, 1557 (2010).

[35] A. Abragam, *The Principles of Nuclear Magnetism* (Oxford University Press, Oxford, 1994), p. 599.

[36] These parameters differ from those of Ref. 34, which correspond to another assignment of crystal-field axes.

[37] L. Esterowitz, F. J. Bartoli, R. E. Allen, D. E. Wortman, C. A. Morrison, and R. P. Leavitt, Phys. Rev. B **19**, 6442 (1979).

[38] M. Nilsson, L. Rippe, S. Kröll, R. Klieber, and D. Suter, Phys. Rev. B **70**, 214116 (2004).

[39] M. Nilsson, L. Rippe, S. Kröll, R. Klieber, and D. Suter, Phys. Rev. B **71**, 149902(E) (2005).

[40] The rf power was $P \approx 3$ W, the pulse lengths were $\tau_p \approx 25$ and 50 μs, respectively, and the rf coil axis was aligned along the z axis.

[41] We fit the decay times with the function $f(t) = [A + M\cos(2\pi\nu_M t)]\exp(-t/T_2) + c$, where A is the exponentially decaying part, ν_M is the modulation frequency, T_2 the decay time, and c an offset.

Paper IV

Slow light for deep tissue imaging with ultrasound modulation

H. Zhang, M. Sabooni, L. Rippe, C. Kim, S. Kröll, L. V. Wang, and P. R. Hemmer.

Appl. Phys. Lett. **100**, 131102 (2012).

APPLIED PHYSICS LETTERS **100**, 131102 (2012)

Slow light for deep tissue imaging with ultrasound modulation

Huiliang Zhang,[1,a)] Mahmood Sabooni,[2] Lars Rippe,[2] Chulhong Kim,[3,b)] Stefan Kröll,[2]
Lihong V. Wang,[3] and Philip R. Hemmer[1,c)]
[1]*Department of Electrical and Computer Engineering, Texas A&M University, College Station, Texas 77843, USA*
[2]*Department of Physics, Lund University, Box 118, S-221 00 Lund, Sweden*
[3]*Department of Biomedical Engineering, Washington University in St. Louis, St. Louis, Missouri 63130, USA*

(Received 6 February 2012; accepted 5 March 2012; published online 26 March 2012)

Slow light has been extensively studied for applications ranging from optical delay lines to single photon quantum storage. Here, we show that the time delay of slow-light significantly improves the performance of the narrowband spectral filters needed to optically detect ultrasound from deep inside highly scattering tissue. We demonstrate this capability with a 9 cm thick tissue phantom, having 10 cm^{-1} reduced scattering coefficient, and achieve an unprecedented background-free signal. Based on the data, we project real time imaging at video rates in even thicker phantoms and possibly deep enough into real tissue for clinical applications like early cancer detection. © *2012 American Institute of Physics*. [http://dx.doi.org/10.1063/1.3696307]

Optical imaging deep inside highly scattering materials can be accomplished using ultrasound to selectively modify or “tag” the light that is scattered by the object of interest, for example a tumor surrounded by healthy tissue.[1] This approach maintains the advantages of optical imaging, like sensitivity to color and texture which provides information on chemical content and biological function, but the resolution is determined by the ultrasound which is far less degraded by the scatter in the surrounding material.[2] Yet, to see small objects buried deep inside a scattering medium, an efficient filtering technique is required to remove the substantial noise due to background scattered light. In the case of ultrasound modulation, this can be accomplished by selectively filtering out light at the ultrasound modulated frequencies. However due to the highly diffuse nature of the scattered light, most optical filtering techniques do not perform well enough to allow small objects buried deep inside larger ones to be detected. This has so far prevented ultrasound modulated optical tomography from finding clinical applications. Here, we show that using slow light[3] in addition to a high performance spectral hole burning type filter[4] can finally reach this elusive goal. In particular, we show that ultrasound modulated light coming from deep inside an unprecedented 9 cm thick tissue phantom can be seen without detectable background. From this data and measurements made in real tissue, we show that straightforward improvements in the experimental setup would allow video rate imaging in even thicker tissue such as the breast or brain. This unique application of slow light and ultrasound opens the door to eventual clinical applications of ultrasound modulated optical tomography as well as numerous commercial and military applications like optical imaging through clouds, underwater, and in harsh manufacturing environments.

Optical imaging is normally the preferred technique for examining biological tissues and many other objects of interest in commercial, military, and scientific applications. In addition to the selectivity to color and texture, it has the potential for remote detection, and non-invasive imaging. Ultrasound imaging can give high resolution where optical imaging cannot, such as for highly scattering objects when a high depth to resolution ratio is required, but ultrasound images are mainly limited to mechanical contrast,[5] which do not give nearly as much chemical or biological information, and are subject to speckle artifacts.

To overcome the limitations of ultrasound imaging, a number of techniques involving optically generated and detected ultrasound have been developed. These techniques seek to keep the advantages of optical imaging even in highly diffuse media while maintaining the resolution of ultrasound imaging. For example, optical detection of ultrasound is routinely used for quality monitoring in harsh manufacturing environments,[6] and it has been demonstrated for remote environmental hazard monitoring.[7] When the optical detection of ultrasound is applied to biological imaging, it is known as ultrasound optical tomography (UOT) or acousto-optic tomography (AOT).[2] Compared to conventional ultrasound imaging, UOT images can have both optical and mechanical contrast in addition to being free of ultrasound speckle artifacts.[8] Likewise, the optical generation of ultrasound has led to powerful applications like photoacoustic spectroscopy for trace chemical detection which has multiple commercial and military uses.[9] When applied to biological imaging, this is known as photoacoustic tomography (PAT) and has shown great promise for imaging inside highly scattering tissue.[10] UOT and PAT can be viewed as complementary technologies because UOT produces images by the optical detection of ultrasound whereas PAT produces images by the optical generation of ultrasound.[1]

The basic physics of optically detected ultrasound is illustrated in Figure 1(a). Briefly, ultrasound produces high and low pressure regions inside the scattering medium which changes the local density of optical scattering centers and also

---

[a)] Now at Department of Physics, Harvard University, Cambridge, Massachusetts 02138, USA.
[b)] Now at Department of Biomedical Engineering, University at Buffalo, The State University of New York, Buffalo, New York 14260-2050, USA.
[c)] Author to whom correspondence should be addressed. Electronic mail: prhemmer@ece.tamu.edu.

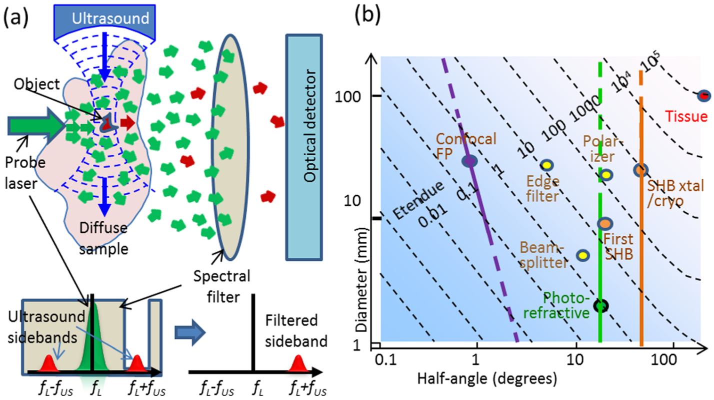

FIG. 1. (a) Optically detected ultrasound imaging inside a highly scattering medium. The probe light is modulated in the ultrasound region, for example at the location of the embedded object. This creates modulation sidebands on the probe light at plus and minus the ultrasound frequency. Since the sideband power depends on the optical and acoustic properties of the object, the image includes both optical and acoustic contrast. The spectral filter passes only one sideband with high discrimination. For demanding applications, a modulated signal of only a few photons will be produced even using Watts of illumination power. (b) Contour plot of units of steradians-mm^2 vs diameter and half angle. Solid lines show reasonable ranges for the three leading techniques, confocal FP, photorefractive, and SHB. Dots show particular cases discussed in text.

the refractive index via the acousto optic effect. This causes amplitude and phase modulation of the probe light at the ultrasound frequency, producing new optical frequencies, or sidebands, shifted from the original by +/- the ultrasound frequency, as illustrated in Figure 1(a). Monitoring the intensity of this ultrasound "tagged" light while scanning the ultrasound focus produces an image of the interior of the object.

The main technical challenge arises when applying ultrasound enhanced optical imaging to highly scattering objects as in deep tissue UOT. Here the ultrasound tagged

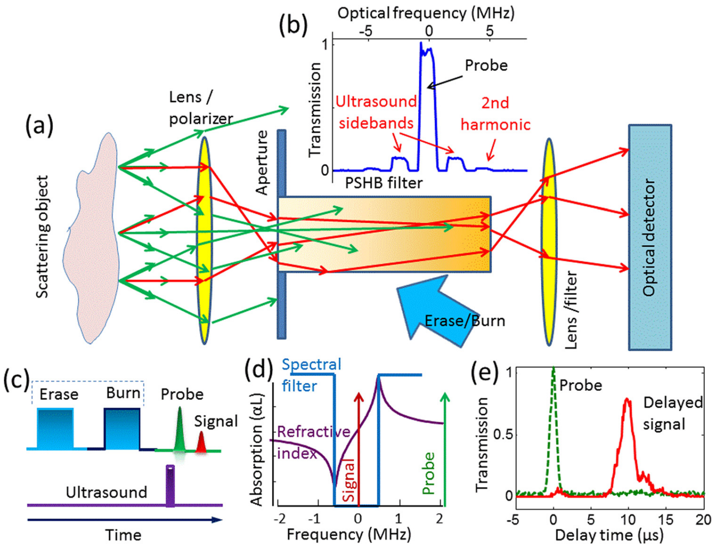

FIG. 2. (a) Schematic of spectral hole and slow light filtering setup. Scattered light from the sample is collected by a lens and passed through a persistent spectral hole burning (PSHB) filter. The filtered sideband (tagged) light is then sent through a fluorescence filter and imaged onto a sensitive photodetector. (b) Convolution of the spectral filter and ultrasound modulation spectrum for a 2.5 cm thick tissue phantom. The spectral filtering hole has a square shape, which was chosen to give the largest dynamic range. (c) Conceptual diagram of the optical and ultrasound pulse sequence. The spectral hole is created by first initializing, or erasing, any previous spectral holes. The desired hole is then engraved using a precise pulse sequence (denoted "Burn"). The ultrasound is applied and optically probed after some propagation delay. (d) A deep spectral hole also has a steep refractive index dispersion at its center, which gives a slow group velocity for the tagged light signal. (e) For a sufficiently short optical probe pulse, slow light gives complete temporal discrimination between the tagged and untagged light.

light is typically many orders of magnitude weaker than the background "untagged" light.[11] This is caused by the low light intensity deep inside tissue[2] and the small focused ultrasound volume used to get high resolution. The key task is then to efficiently extract this weak tagged light from the much stronger background or more precisely from the noise produced by the background. In Figure 1(a), this is illustrated by a spectral filter that absorbs the untagged light while allowing tagged light to pass with minimal attenuation. Another option is heterodyne detection, but this is most applicable to non-scattering objects. To collect as much of the tagged light as possible, the etendue, defined by the product of the light solid angle and area,[12] of the optical system should be as high as possible.

To quantify how etendue and other filter metrics limit tissue imaging depth, consider that the goal is to reach a signal to noise ratio (SNR) that is good enough to reliably identify an embedded object. From Rose's criteria,[13] this is possible if the $\mathrm{SNR} > 5$. Assuming sufficiently advanced classical noise suppression techniques are used, the SNR will eventually be limited by quantum statistics or shot noise. Considering only tagged light shot noise, the required SNR can be achieved by collecting at least 25 photons per image pixel, assuming a high contrast embedded object. If background light is present then its shot noise must also be considered. Assuming a signal to background ratio (SBR) that is independent of laser illumination intensity, the result is that a factor of 1/SBR more tagged (signal) photons are required to overcome background noise, assuming $\mathrm{SBR} \ll 1$. Thus to get sufficient SNR for weak signals, the optical filter must strongly suppress untagged light to increase the SBR, yet it must not attenuate the tagged light and therefore should have as high etendue as possible.

In Figure 1(b), the etendue of the leading UOT filtering techniques is compared to that of biological tissue. As seen, the lowest etendue filter is the confocal Fabry-Perot (FP) filter,[14] even though this technology has demonstrated the deepest tissue imaging until now. To achieve this, a very high laser power was used to give more tagged photons. The next higher etendue is the photorefractive (PR) filter.[15] This technology is based on real time holography which is like a high-etendue version of heterodyne detection. By far, the highest reported etendue is a Tm:YAG spectral hole burning (SHB) filter[16] since the SHB crystal itself has a maximal 90° acceptance half-angle.

Here, we make use of a persistent spectral hole burning (PSHB) optical filter which is a special class of SHB materials that have a long hole lifetime, seconds or longer. This long lifetime allows the use of complex hole burning pulse sequences that can give unprecedented performance as a spectral filter; for example using a carefully selected spatial geometry, 140 dB discrimination has been demonstrated in praseodymium doped yttrium silicate (Pr:YSO),[17] for collimated laser light, with better than 50% transmission in the passband.

The basic experimental setup for deep tissue UOT with PSHB filtering is shown in Figure 2(a). Diffuse light from the object of interest is collected by a high numerical aperture (NA) lens and funneled into the front face of the hole burning crystal. Once inside the crystal, the light is guided to the exit face via total internal reflection. Since this waveguiding is independent of crystal length, very long crystals can be used to achieve a high optical absorption of untagged light. The filtered tagged light exiting the crystal is then collected by another high NA lens and imaged onto a sensitive optical detector, for example a photon counter.

To demonstrate deep tissue imaging with slow light enhanced spectral hole filtering, experiments were performed on tissue-mimicking phantoms and real tissue (chicken breast), as illustrated in Figure 3. Here, Figure 3(a) shows a typical 1D image in the ultrasound propagation direction (A-line) for two absorbing objects buried inside a 4.5 cm thick (in the laser propagation direction) tissue phantom, having a reduced scattering coefficient of $10\,\mathrm{cm}^{-1}$. As seen a high contrast image of the absorbing objects is produced, but there is significant untagged background light.

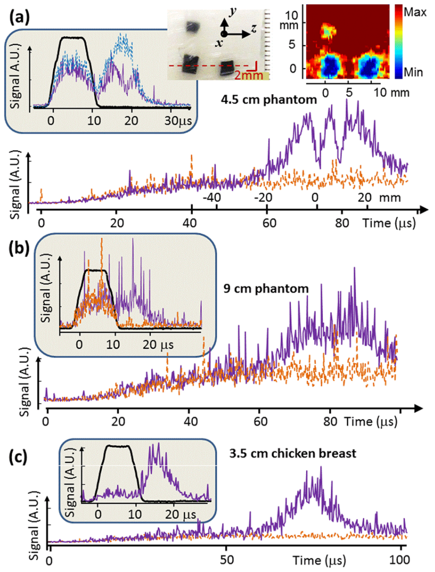

FIG. 3. (a) Images of buried (optically absorbing) objects in a 4.5 cm thick (x-direction) tissue phantom. The plotted data show a 1-D A-line image, and a 2-D image (B-mode tomogram) is shown above, along with a cutaway photo of the embedded objects. The smaller 2 mm object in the B-mode shows reduced contrast and hence this is the resolution limit. The upper (solid) A-line data is with ultrasound present and the lower (dashed) plot without. Both images are 50 trace accumulations, and the B-mode is interpolated and median filtered. The inset shows A-line imaging with slow light. The delayed light shows a high contrast dip when 3.5 mm thick absorbing object is present (solid). The data without an absorber (dashed) is superimposed, for comparison. (b) Ultrasound tagged light (A-traces) from a 9 cm thick tissue-mimicking phantom with ultrasound applied(upper solid line) and without (lower dashed line). These A-lines are 500 accumulations. The inset shows additional slow light filtering. Here, a significant delayed component is seen with ultrasound present (solid line) but only detector dark noise is seen at the same delay time without ultrasound (dashed line). The dark line shows the input laser pulse. (c) Ultrasound tagged light detected in 3.5 cm thick chicken breast tissue, with ultrasound (upper solid line) and without (lower dashed line). The inset shows additional filtering with slow light. The dark line shows the reference optical pulse. These A-lines were averaged 500 times.

TABLE I. Projections for ultimate imaging depth in tissue phantoms assuming real-time video rate imaging. Here video rate is defined as a frame rate of 35 frames/s for a 2D image with 30 lines.

Parameter		Present setup	Best possible	Unit	Improvement factor
Laser energy	Power	0.1	240	W	2400
	Duration	10	10	μs	1
Ultrasound	Pressure	4	4	Mpa	1
	Duration	2	2	cycle	1
Filter etendue		3	900	sr-mm^2	300
Passband transmission		0.3	0.3		1
Detector quantum efficiency		0.07	0.8		10
Tagged photo-counts/0.5 μs_pixel/shot		0.04	290 K	Photo-counts	7 M
dB above (25 counts/pixel)		−28	+40	dB	+68 dB
Single shot depth (4.4 dB/cm)		3	18	cm	+15 cm

To remove this background, slow light was used to selectively delay the tagged light, as shown by the A-line images in the inset of Figure 3(a). Slow light naturally arises from the steep refractive index dispersion in the passband of a deep spectral hole (see Figure 2(d)).[4,18] Conversely, since the dispersion is relatively flat in the absorbing region several hole widths away, any untagged light leaking through the crystal is not significantly slowed. For an optical pulse whose spectral width is matched to that of the spectral hole passband, the delay measured in pulse widths will be proportional to the optical density in the surrounding absorbing region.[4] The quality of the data that can be obtained strongly depends on the filter characteristics (transmission, suppression, steepness, etc.) and extensive work has been investigated in optical pumping techniques important for the filter creation.[19] For our 2.3 MHz ultrasound frequency, a 2 cycle pulse is about 1 μs long, and a light pulse of this length is easily delayed many pulse widths as seen in Figure 2(e). In the inset of Figure 3(a)), a much longer probe pulse was used so as to image an entire buried object in one A-line, but a full pulse-width delay can still be achieved.

Figure 3(b) illustrates the limits of persistent spectral filtering with and without slow light, using a much thicker 9 cm tissue phantom. Again both long and short optical illumination pulses are used to illustrate the advantage of slow light delay. As seen in the inset of Figure 3(b), the delayed ultrasound tagged light is well separated from the untagged light background, and furthermore, data taken without ultrasound present show no visible untagged light at the relevant delay times (i.e., it is indistinguishable from detector dark noise). From this data, we estimate a lower limit of 16 for the signal to background ratio. Such a large SBR is unprecedented for so thick a phantom and clearly shows the multiplicative filtering capability of slow light, as the untagged background has already been suppressed 30 dB by the spectral hole filter in the long pulse illumination case.

Figure 3(c) (inset) shows that slow light also effectively separates tagged light from the untagged background in real tissue (chicken breast). Here, a much thinner sample, 3.5 cm thick, was needed as the 606 nm illumination was more strongly absorbed than in the phantom.

It is of interest to estimate the thickest tissue sample that can be imaged in real time (video rate) using slow light enhanced spectral hole burning filters. In the current setup, there are too few signal photons to acquire real time images from the 9 cm thick phantom since the tagged light amounts to only about 4 photon counts per 100 ns data bin with a 500 trace accumulation. However, by increasing the laser illumination intensity to 1/10 of the 2.4 kW laser safety limit,[20] increasing the etendue up to the limit imposed by the cryostat for the present crystal diameter, and using a higher quantum efficiency photon counter, we project ∼290 k photo-counts per image pixel for a single shot A-line with a pixel width of 500 ns (1 cycle of ultrasound). Since only 25 counts are needed to satisfy Rose's criteria for a high contrast object, there would be 14 000 times more photo-counts than needed for video rate imaging at this 9 cm depth. These extra photons could be used to see even deeper into tissue, as illustrated in Table I. In this table, the surplus photo-counts are converted into additional tissue thickness using the measured 4.4 dB/cm signal attenuation to arrive at the 18 cm thickness projection for single-shot A-lines in phantoms.

Note that the projections in Table I neglect the effects of background which would reduce the ultimate imaging depth. From Figure 3(b), it is seen that the SBR ∼ 1 for the 9 cm tissue phantom using spectral hole filtering alone. Since the PSHB spectral filtering discrimination is already degraded to 30 dB for diffuse light, it is expected that the extra SBR enhancement provided by slow light will be essential for achieving the goal deep tissue imaging at video rates.

Clearly, video rate imaging at such tissue depths is approaching that needed for clinical applications if it can be extended to real tissue. The validity of using tissue phantoms to model imaging performance in real tissue was recently demonstrated at 1.06 μm, where both real tissue and phantoms of the same thickness showed similar image quality.[14] While no candidate PSHB materials exist at 1.06 μm, Tm:YAG operating at 793 nm is still within the therapeutic window has shown to be capable of persistent spectral holes with up to 30 s lifetimes[21] and could eventually realize the elusive goal of deep tissue imaging for certain clinical applications.

S.K. was sponsored in part by the Swedish Research Council, the Knut & Alice Wallenberg Foundation, the Crafoord Foundation and the EC FP7 Contract No. 247743 (QuRep). L.V.W. was sponsored in part by National Institutes of Health grants R01 EB000712 and U54 CA136398.

[1] C. Kim, K. H. Song, and L. V. Wang, J. Biomed. Opt. **13**(2), 020507 (2008).

[2] L. V. Wang and Hsin-i Wu, *Biomedical Optics: Principles And Imaging* (Wiley, Hoboken, NJ, 2007).

[3] L. V. Hau, S. E. Harris, Z. Dutton, and C. H. Behroozi, Nature **397**(6720), 594 (1999); F. Morichetti, C. Ferrari, A. Canciamilla, and A. Melloni, Laser Photonics Rev. **6**(1), 74 (2012); K. F. Reim, P. Michelberger, K. C. Lee, J. Nunn, N. K. Langford, and I. A. Walmsley, Phys. Rev. Lett. **107**(5), 053603 (2011); M. Salit and M. S. Shahriar, J. Opt. **12**(10), 11 (2010).

[4] R. N. Shakhmuratov, A. Rebane, P. Mégret, and J. Odeurs, Phys. Rev. A **71**(5), 053811 (2005).

[5] L. V. Wang, *Photoacoustic Imaging and Spectroscopy* (CRC, Boca Raton, 2009).

[6] R. J. Dewhurst and Q. Shan, Meas. Sci. Technol. **10**(11), R139 (1999).

[7] C. E. Brown and M. F. Fingas, Mar. Pollution Bull. **47**(9-12), 485 (2003).

[8] X. Xu, H. Zhang, P. Hemmer, De-kui Qing, C. Kim, and L. V. Wang, Opt. Lett. **32**(6), 656 (2007).

[9] M. W. Sigrist, *Air Monitoring by Spectroscopic Techniques* (Wiley, New York, 1994).

[10] L. V. Wang, Nat. Photonics **3**(9), 503 (2009).

[11] M. Kempe, M. Larionov, D. Zaslavsky, and A. Z. Genack, J. Opt. Soc. Am. A **14**(5), 1151 (1997).

[12] R. Winston, W. T. Welford, J. C. Miñano, and P. Benítez, *Nonimaging Optics* (Academic, Boston, MA, 2005).

[13] J. T. Bushberg, *The Essential Physics of Medical Imaging*, 2nd ed. (Lippincott Williams & Wilkins, Philadelphia, 2002).

[14] G. Rousseau, A. Blouin, and J.-P. Monchalin, Opt. Lett. **34**(21), 3445 (2009).

[15] F. Ramaz, B. Forget, M. Atlan, A. C. Boccara, M. Gross, P. Delaye, and G. Roosen, Opt. Express **12**(22), 5469 (2004).

[16] Y. Li, H. Zhang, C. Kim, K. H. Wagner, P. Hemmer, and L. V. Wang, Appl. Phys. Lett. **93**(1), 011111 (2008); Y. Li, P. Hemmer, C. Kim, H. Zhang, and L. V. Wang, Opt. Express **16** (19), 14862 (2008).

[17] M. P. Hedges, J. J. Longdell, Y. Li, and M. J. Sellars, Nature **465**(7301), 1052 (2010).

[18] A. Walther, A. Amari, S. Kröll, and A. Kalachev, Phys. Rev. A **80**(1), 012317 (2009).

[19] M. Nilsson, L. Rippe, S. Kröll, R. Klieber, and D. Suter, Phys. Rev. B **70**(21), 214116 (2004); L. Rippe, M. Nilsson, S. Kröll, R. Klieber, and D. Suter, Phys. Rev. A **71**(6), 062328 (2005); M. Nilsson, L. Rippe, N. Ohlsson, T. Christiansson, and S. Kröll, Phys. Scr. **2002**(T102), 178 (2002); A. Amari, A. Walther, M. Sabooni, M. Huang, S. Kröll, M. Afzelius, I. Usmani, B. Lauritzen, N. Sangouard, H. de Riedmatten *et al.*, J. Lumin. **130**(9), 1579 (2010).

[20] American National Standard for the Safe Use of Lasers, Standard Z136.1-2000 (ANSI, Inc., New York, 2000).

[21] N. Ohlsson, M. Nilsson, S. Kröll, and R. Krishna Mohan, Opt. Lett. **28**(6), 450 (2003).

Paper V

Cavity enhanced storage-preparing for high efficiency quantum memories

M. Sabooni, S. T. Kometa, A. Thuresson, S. Kröll, and L. Rippe.

New Journal of Physics **15**, 035025 (2013).

Cavity-enhanced storage—preparing for high-efficiency quantum memories

2013 New J. Phys. 15 035025

(http://iopscience.iop.org/1367-2630/15/3/035025)

New Journal of Physics
The open access journal for physics

Cavity-enhanced storage—preparing for high-efficiency quantum memories

M Sabooni[1], S Tornibue Kometa, A Thuresson, S Kröll and L Rippe
Department of Physics, Lund University, PO Box 118, SE-22100 Lund, Sweden
E-mail: mahmood.sabooni@fysik.lth.se

New Journal of Physics **15** (2013) 035025 (12pp)
Received 30 November 2012
Published 25 March 2013
Online at http://www.njp.org/
doi:10.1088/1367-2630/15/3/035025

Abstract. Cavity-assisted quantum memory storage has been proposed for creating efficient (close to unity) quantum memories using weakly absorbing materials. Using this approach, we experimentally demonstrate a significant (∼20-fold) enhancement in quantum memory efficiency compared to the no cavity case. A strong dispersion originating from absorption engineering inside the cavity was observed, which directly affects the cavity line width. A more than three orders of magnitude reduction of cavity mode spacing and cavity line width from GHz to MHz was observed. We are not aware of any previous observation of several orders of magnitude cavity mode spacing and cavity line width reduction due to slow light effects.

Contents

---

[1] Author to whom any correspondence should be addressed.

New Journal of Physics **15** (2013) 035025
1367-2630/13/035025+12$33.00

1. Introduction

Coherent and reversible mapping of a quantum state between light and matter, as a flying and stationary qubit, is an essential step toward scalability of quantum information processing [1, 2]. Such an optical quantum memory would be important for storing and synchronizing the output quantum states of several quantum gates in quantum computation protocols [3]. In addition, quantum memories may also play a crucial role in enabling long-distance (>150 km) quantum communication [4] and in other applications [5]. Most ensemble-based optical quantum memory protocols [5, 6] belong to one of two main groups: one where the protocols are based on electromagnetically induced transparency [7–9] and one where they are based on the coherent rephasing (echo) effect [10] such as controlled reversible inhomogeneous broadening [11, 12], atomic frequency comb (AFC) [13–18], gradient echo memory [19–21] and revival of silenced echo [22].

There are specific criteria for assessing quantum memory performance based on the application in mind, but generally we could list the following key parameters: efficiency, fidelity, storage time, multi-mode storage capacity and operational wavelength [5]. The scope of this paper is mainly to demonstrate how to improve the memory efficiency of weakly absorbing materials. The memory efficiency is here defined as the energy of the pulse recalled from the memory divided by the energy of the pulse sent in for storage in the memory. At the quantum level (weak coherent pulses), storage efficiency basically corresponds to the probability that the stored information is retrieved. Fidelity is simply defined as the overlap of the quantum state wavefunction of the recalled photon with that of the one originally sent in for storage. In the optimum fidelity case, the wave-functions for the input and output photons are identical. An alternative definition is conditional fidelity, i.e. the overlap conditional on that the photon was emitted by the memory [5]. Based on the application, there will also be requirements on longer storage time [7, 23–25] and on-demand retrieval. The capacity to store several photons (modes) at the same time in the memory is called multi-mode storage capability. Multi-mode storage is crucial in probabilistic applications to boost the occurrence rate of events [16, 26, 27] and the AFC concept has been shown to be particularly suitable for multi-mode applications [28].

In the AFC protocol, which is employed in this paper, the combination of photon-echo and spin-wave storage allows on-demand storage. However, the present experiment does not include spin storage. The principle of the AFC protocol preparation is shown in figure 1. A sequence of narrow peaks, equidistant in frequency, with a peak optical absorption depth d and background absorption d_0 is created by optical pumping and/or targeted state-to-state transfer pulses. The input field for storage, with a spectral distribution larger than the peak separation Δ in figure 1 and narrower than the AFC bandwidth, could be totally absorbed by a sequence of narrow peaks. Afterwards, the input field will excite all the atoms in the AFC structure coherently. The collective coherent state distributed over AFC peaks separated by Δ will rapidly dephase into a non-collective state. Well-separated equidistance AFC peaks will rephase and lead to a collective emission after a time $1/\Delta$.

For high-efficiency quantum state storage, one basic requirement is to have enough absorption depth to fully transfer all the input pulse energy to the atomic media. However, in strongly absorbing media one also needs to eliminate the reabsorption of the emitted echo in the medium. This can be done by shifting the absorber using the linear Stark effect with an electric field gradient where the output field will be emitted in the backward [11] or forward [20] direction. On the other hand, the strong absorption requirement will clearly

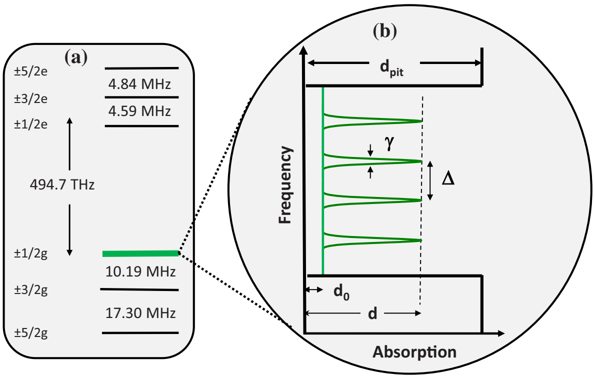

Figure 1. (a) The hyperfine splitting of ${}^3H_4$–${}^1D_2$ transition of the site I Pr^{3+}:Y_2SiO_5 is shown [29, 30]. (b) The Pr absorption engineering based on AFC protocol. d_{pit} is the absorption depth outside the AFC structure spectral region, which is situated in what is called a spectral pit, d is the peak optical depth, while d_0 is the background absorption. Δ is the AFC peak separation and γ is the full-width at half-maximum (FWHM) of the AFC peaks. The finesse of the AFC structure will be $F_{\mathrm{AFC}} = \frac{\Delta}{\gamma}$. The effective absorption of the AFC structure is defined as $\tilde{d} = \frac{d-d_0}{F_{\mathrm{AFC}}}$.

pose some limitations on the material used. Thus, it would be very important to enhance the absorption of materials with long coherence time but low absorption (e.g. europium).

Interestingly, complete absorption of the input pulse can also be obtained for weakly absorbing materials (that, for example, could have longer coherence time, such as Eu^{3+}:Y_2SiO5 [31]) if they are inserted in a cavity [32, 33]. This cavity should satisfy the impedance-matched condition for achieving complete absorption of the input pulse. To do this, the absorption during one round trip of the cavity should be exactly equal to the transmission of the input coupling mirror and also there should be no other losses during the cavity round trip. Obtaining this (impedance-matched) condition is a vital step toward efficient quantum memories using weakly absorbing media. In this work, we employed a cavity configuration around our absorber material and demonstrate more than one order of magnitude improvement in memory efficiency compared to that obtained without the cavity. The praseodymium absorption line in Pr^{3+}:Y_2SiO_5 was tailored based on the AFC protocol [13] and an impedance-matched cavity configuration [32] is employed to mainly enhance the quantum memory efficiency. On-demand recall as well as longer quantum memory storage time could be achievable via spin-wave storage [14, 23] but this is beyond the scope of the present paper. Cavity-enhanced spin wave-to-photon conversion efficiency results have, for example, been demonstrated in atomic gases [34, 35].

The paper is organized in the following way. In section 2, we give an overview of the experimental setup, in particular as regards the cavity design. In section 3, the effect of having an absorbing quantum memory material inside the cavity is discussed. In section 4, we show

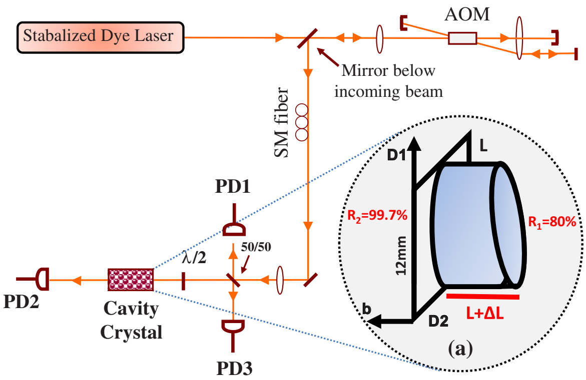

Figure 2. Experimental setup. A double-pass acousto-optic modulator (AOM) is employed to tailor the optical pulses which come from a narrow (kHz) line width laser. A photo diode (PD1) monitors the input light to the cavity. Two other photo diodes monitor the transmitted (PD2) and reflected (PD3) light from the cavity. The cavity crystal was designed to have a small wedge, such that the length L differs by about $\Delta L = 200$ nm. In practice, the wedged surface is not completely flat, see figure 3. (a) The input and output facets of the crystal have 80 and 99.7% reflectivity, respectively.

quantum memory efficiency results following the preparation steps toward the AFC memory demonstration, and in section 5, a further discussion about the strong dispersion and cavity free spectral range effect is included. The conclusions are presented in section 6.

2. Experimental setup

This section discusses the experimental setup and is divided into two main parts. The first part describes the stabilized laser source and the modulator setup which generates the pulses, while the second part outlines the cavity crystal design as shown in figure 2(a). A 6 W Nd:YVO$_4$ Coherent Verdi-V6 laser at 532 nm pumps a Coherent 699-21 dye laser, which generates ∼500 mW laser radiation at 605.977 nm. This wavelength matches the $^3H_4$–$^1D_2$ transition of praseodymium ions doped into yttrium silicate (Pr^{3+}:Y$_2$SiO$_5$) [29, 30].

The laser stabilization system, which uses hole-burning in a Pr^{3+}:Y$_2$SiO$_5$ crystal in a separate cryostat as the frequency reference, improves the frequency stability of the laser to ≈1 kHz line width [36]. Good frequency stability is crucial for coherent interaction experiments such as the ones described here. The $^3H_4$–$^1D_2$ transition in Pr^{3+}:Y$_2$SiO$_5$ has an excited state coherence time (T_2) of 152 μs [29]. A double pass acousto-optic modulator (AA opto-electronics St.200/B100/A0.5-VIS, AOM) with 200 MHz center frequency is employed to tailor the laser light amplitude, phase and frequency and to carry out the required pulse shaping in the experiment. An extensive MATLAB code calculates the pulse shapes and a 1 GS s^{-1} arbitrary waveform generator (Tektronix AWG520) generates the RF signal that drives the

AOM that modulates the light. The spatial laser mode is cleaned by passing light through a single-mode fiber and then a 50/50 beam splitter is used to obtain the reference signal at the photo diode (PD1) before the cavity crystal. The transmitted light through the cavity will be detected at PD2 in figure 2. The reflected light from the cavity will be detected by the third photo diode (PD3) in figure 2. The PD1 and PD3 are PDB150A photo detectors from Thorlabs, while PD2 is a Hamamatsu S5973 photo diode which is connected directly to a Femto DHP CA-100 transimpedance amplifier. The beam diameter at the cavity crystal position is set to about 80 μm. The crystal was immersed in liquid helium at 2.1 K to ensure that the optical coherence time (T_2) of the praseodymium is not shortened by phonon interaction. A $\lambda/2$ plate was used in front of the crystal to control the light polarization direction with respect to the crystal axes and the Pr transition dipole moment direction [37].

The cavity crystal is made of 0.05% praseodymium ions doped into yttrium silicate (Pr^{3+}:Y_2SiO_5). It has 12 mm diameter and is (except for the small wedge) cut along the $D_1 \times D_2$ plane with a thickness of 2 mm as shown in figure 2(a). The cavity mirrors are created by coating the 12 mm diameter crystal surfaces. Multiple layer stacks of SiO_2 and ZrO_2 are designed and applied for these coating surfaces by Optida. The light propagation direction is selected to be along the crystal b-axis as shown in figure 2. The input and output cavity facets are designed to have reflectivities of $R_1 = 80\%$ and $R_2 = 99.7\%$, respectively. The losses because of the Pr ion absorption through the double pass of the cavity should be adjusted to compensate for the unequal cavity surface coating to achieve the impedance-matched cavity condition [32, 33]. The impedance-matched cavity condition occurs when the directly reflected field and a transmitted field coming from the field circulating inside the cavity cancel each other at the input surface and consequently the reflected intensity vanishes.

3. Cavity without and with an absorber

The calculated cold cavity (i.e. neglecting any Pr absorption effects) transmission frequency spacing ($\frac{c}{2nL}$) for this crystal with $n = 1.8$ and $L = 2$ mm is 41.6 GHz. The theoretical finesse of this cavity based on the mentioned mirror reflectivities is $\approx$25 which corresponds to a spectral line width of 1.5 GHz. Scanning the laser light across the cold cavity (off-resonance with the Pr ion absorption line) shows a cavity transmission line width of about 2.5 GHz, which corresponds to a finesse of about $\approx$16. Part of the reduction could be related to the wedge design, causing a small beam walk-off as the light bounces between the mirrors.

To spectrally match the cavity transmission profile to the inhomogeneous absorption line of Pr [29], the crystal was designed to have a small wedge as shown in figure 2(a), such that the length L differs by about 200 nm. In this way the cavity transmission spectrum could be translated well over one free spectral range. To accurately match the cavity transmission peak to the Pr absorption line, a translation stage with sub-μm accuracy (Attocube system, ANCz150) is employed to translate the crystal perpendicular to the input beam.

The parallelism of the cavity surfaces is determined by an interference experiment. A collimated coherent beam ($\lambda = 606$ nm) with diameter $>$12 mm impinged almost perpendicularly on the crystal surface and the reflected pattern was monitored. Figure 3 shows the non-uniform interference pattern before coating the cavity surface. One could estimate the cavity parallelism in figure 3, as the change in the cavity length is $\lambda_{\text{material}}/2$ between two bright or dark fringes in the cavity. Since figure 3 shows the light reflected from the cavity, the dark fringes are the areas of larger transmission.

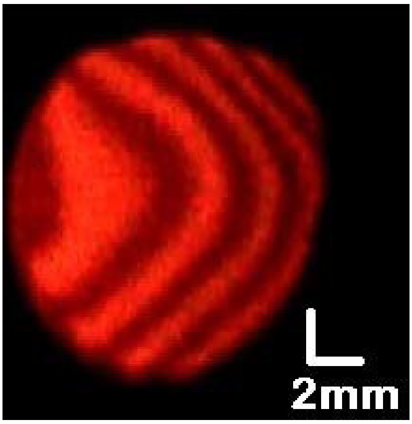

Figure 3. An interference experiment is used to investigate the parallelism of the cavity surfaces. A collimated laser beam at $\lambda = 606$ nm was impinging perpendicularly to the 12 mm diameter cavity crystal surface. The figure shows the reflected light from the cavity surface displayed on a screen.

For quantum state storage, the AFC protocol [13] is chosen for engineering the absorption profile of the inhomogeneously broadened Pr ion. The heart of the AFC protocol is using a spectrally periodic medium for enhancing the storage capacity. Using a frequency domain interpretation, the periodic structure shown in figure 1(b) can be viewed as a spectral grating. The storage pulse tuned to the AFC structure is diffracted in time and produces an echo [38]. Based on a time domain interpretation, this will be interpreted as a rephasing of a set of dipoles in time [13]. The storage pulse will be absorbed by AFC peaks well separated in frequency (Δ in figure 1(b)). The collective emission of AFC peaks will be in phase after time $1/\Delta$ generating an echo of the input pulse.

The first step toward this preparation is to make a zero absorption window within the inhomogeneous Pr ion absorption profile. A series of optical pumping pulses is employed to create an 18 MHz transmission window (spectral pit) within the $\approx$9 GHz inhomogeneous profile of Pr^{3+}:Y_2SiO_5. A detailed discussion about what pulses can be used to create the transmission window is presented in [17]. This transmission window is called the spectral pit in [30], which we will use afterwards.

It turns out that a spectral transmission window (spectral pit) might change the cavity mode spacing by several orders of magnitude due to slow light effects. This will now be briefly explained by considering a dispersive medium inside a cavity as follows (see equation (11.58), p 437 of [39]):

$$\Delta\nu_{\text{mode}} = \nu_{q+1} - \nu_q = \frac{1}{2L}\frac{c_0}{n_g(\nu)} = \frac{v_g}{2L}, \tag{1}$$

$$n_g(\nu) = \frac{c_0}{v_g} = \frac{\partial(\nu n_r(\nu))}{\partial\nu} = n_r(\nu) + \nu\frac{dn_r(\nu)}{d\nu}, \tag{2}$$

where q is an integer, L is the cavity length, c_0 is the speed of light in vacuum, $n_{\mathrm{g}}(\nu)$ is the refractive index for the group velocity, $n_{\mathrm{r}}(\nu)$ is the real part of the refractive index for the phase velocity and v_{g} is the group velocity. It is important to note that the index of refraction in equation (1) is not the index of refraction for the phase velocity, n, but the index of refraction of the group velocity, n_{g}. This is sometimes overlooked, but in a low dispersion medium the two indices of refraction are the same ($n \approx n_{\mathrm{g}}$), so often the dispersion is not important. The real and imaginary parts of the susceptibility are connected via the Kramers–Kronig relation as follows:

$$\mathrm{Re}\,(\chi(\nu)) = \frac{2}{\pi}\int_0^{\infty} \frac{\nu'\mathrm{Im}(\chi(\nu'))}{\nu'^2-\nu^2}\,\mathrm{d}\nu', \tag{3}$$

$$\mathrm{Im}\,(\chi(\nu)) = \frac{2}{\pi}\int_0^{\infty} \frac{\nu'\mathrm{Re}(\chi(\nu'))}{\nu'^2-\nu^2}\,\mathrm{d}\nu'. \tag{4}$$

Therefore, by measuring the absorption spectrum $\alpha(\nu)$ which is directly related to $\mathrm{Im}\,(\chi(\nu))$ and using this as an input to equation (3), one can calculate $\mathrm{Re}\,(\chi(\nu))$ which is proportional to $n_{\mathrm{r}}(\nu)$ and then calculate the dispersion ($\frac{\mathrm{d}n_{\mathrm{r}}(\nu)}{\mathrm{d}\nu}$). In the cold cavity case where there is no absorption and consequently also no dispersion, the $n_{\mathrm{r}}(\nu) \gg \nu\frac{\mathrm{d}n_{\mathrm{r}}(\nu)}{\mathrm{d}\nu}$ regime holds, while in the case of a spectral pit we have $n_{\mathrm{r}}(\nu) \ll \nu\frac{\mathrm{d}n_{\mathrm{r}}(\nu)}{\mathrm{d}\nu}$. Actually, using the experimentally recorded absorption $\alpha(\nu)$ as the input to equation (3) gives a dispersion term ($\nu\frac{\mathrm{d}n_{\mathrm{r}}(\nu)}{\mathrm{d}\nu}$) in equation (2) which is three to four orders of magnitude larger than $n_{\mathrm{r}}(\nu)$. This means that the mode spacing for frequencies inside the spectral transmission window now is only of the order of 10 MHz.

To experimentally monitor the created transmission window, a weak minimally disturbing pulse was frequency chirped at a rate of 1 MHz μs across the corresponding frequency region. In the absence of a cavity this procedure typically displays an ≈18 MHz spectral pit (see, e.g., figure 1 in [40][2]). For the cavity case, only a much narrower transmission line (≈2 MHz) inside the spectral region was observed. This sharp transmission line turns out to be about three orders of magnitude narrower than the cold cavity transmission peaks. The cavity finesse (F_{cav}) is primarily determined by the mirror reflectivity. Therefore, F_{cav} should be independent of the spectral pit (transmission window) properties provided that the possible residual absorption in the spectral pit is small. Based on the assumption of a constant cavity finesse, the ratio between the cavity free spectral range ($\Delta\nu$) and δ will be constant. Thereby, it follows from equation (1) that the cavity transmission line width is proportional to the group velocity (v_{g}). Thus, the 2 MHz transmission peak is largely consistent with the obtained results based on the theoretical calculation above. Two cavity transmission peaks that are translated by changing the cavity length are shown in figure 4. The cavity transmission peaks were translated by moving the slightly wedged crystal perpendicular to the beam propagation direction. The reduction of the cavity transmission line width is also due to the strong dispersion that is created by the spectral pit inside the cavity.

In fact, although there are experimental observations of changes in the cavity mode spacing in active media of more than an order of magnitude [41, 42], we are not aware of any effects as large as the three to four orders of magnitude observed here. Details of this effect are, however, beyond the scope of the present paper and will be addressed in a separate publication [43].

---

[2] Correction: the expression for the group velocity needs to be corrected to $v_{\mathrm{g}} = \frac{2\pi\Gamma}{\alpha}$ in the subsection ‘IVB slow light effects’.

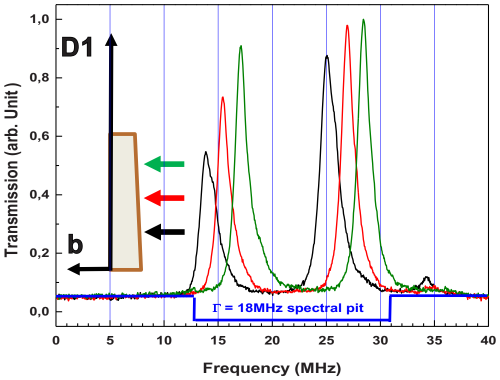

Figure 4. Three cavity transmission spectra taken at different positions through the crystal as indicated by the arrows are shown. The cavity crystal had about 2 mm length and 80 and 99.7% mirror reflectivity while the Pr absorption line was tailored to create a ≈18 MHz spectral pit within the cavity. The spectral pit is responsible for the three orders of magnitude cavity mode reduction from GHz to MHz. The maximum difference in the cavity transmission spectrum as the beam was translated at the input surface is about 3 MHz, which corresponds to about 40 nm cavity length changes. The designed wedge on the crystal surface gives us enough freedom to translate the cavity transmission between two cavity modes, which is ≈11 MHz here.

4. Atomic frequency comb preparation and memory efficiency

Each AFC peak shown in figure 1(b) is prepared within the created transmission window (spectral pit) by employing two consecutive complex hyperbolic secant [30] pulses to optically pump Pr ions from $|\pm\frac{5}{2}g\rangle \rightarrow |\pm\frac{5}{2}e\rangle$ and $|\pm\frac{5}{2}e\rangle \rightarrow |\pm\frac{1}{2}g\rangle$ (see figure 1(a)). This procedure is carried out four times, each time with a new center frequency shifted by Δ to create an AFC structure as shown in figure 1(b). In this way the AFC structure is engraved in the $|\pm\frac{1}{2}g\rangle$ state. To be able to use the cavity configuration and improve the storage efficiency, the AFC structure needs to be engraved within the cavity transmission window. Therefore, the cavity transmission line width (δ) needs to be optimized to cover the whole AFC structure bandwidth. As discussed in [40] the group velocity can be written as $v_g = \frac{2\pi\Gamma}{\alpha}$, where Γ and α are the spectral pit width and the absorption coefficient outside the spectral pit, respectively. It was, therefore, concluded that in 0.05% Pr:YSO, where the maximum spectral pit window width (Γ) is limited to 18 MHz and at the line center absorption coefficient (α) is about 2000 m^{-1}, the only possibility for the cavity transmission line of width δ to cover the AFC bandwidth was to obtain a smaller α by moving the whole spectral pit to a part of the inhomogeneous profile where the absorption was lower than at the inhomogeneous line center. The created spectral pit and the AFC peaks will affect the dispersion and finally the cavity mode structure (see equation (1)). Therefore, the

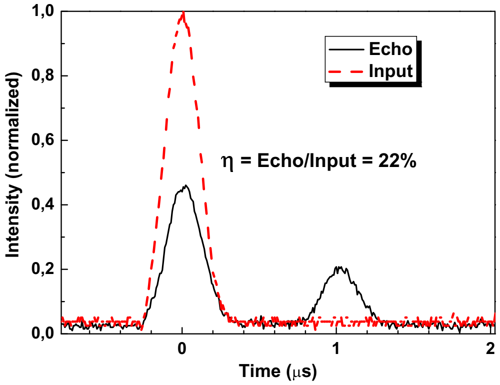

Figure 5. Storage efficiency measurement. A 250 ns FWHM Gaussian pulse tuned to an AFC structure with four peaks separated by $\Delta = 1$ MHz. 22% of the input energy (red dashed line) was retrieved in the echo (black solid line) after 1 μs.

shape of the spectrum is a combination of the effect from the AFC absorption pattern and the cavity dispersion effect.

The next step after the AFC preparation is to send the storage pulse tuned to the AFC structure center frequency through mirror R_1 (see figure 2). For this purpose, a Gaussian pulse with $\tau_{\mathrm{FWHM}} = 250$ ns was employed. For an AFC structure with peak separation Δ, there will be a rephasing after a delay $1/\Delta$ [13]. The black solid trace in figure 5 is the signal when the storage pulse is tuned to the AFC structure center frequency and impinged onto mirror R_1. We define the memory efficiency as the ratio of the output (echo) energy divided by the input pulse energy. To obtain a reference signal, for the input energy to the memory, the cavity was turned $\sim 180^\circ$ such that the input Gaussian storage pulse impinged on the mirror with reflectivity R_2 (nearly 100% reflection) and the reflection was detected at the reflection detector (PD3). This signal represents the input signal shown by the (red) dashed line in figure 5 and corresponds to the signal strength that would be observed if the memory efficiency were 100%. The reference detector PD1 was employed to compensate for the measurements for laser fluctuation from one measurement to another. 22% of the input energy was retrieved in the echo after 1 μs as shown in figure 5.

5. Strong dispersion and the cavity free spectral range

Finally, an interesting observation is that the requirement of matching the absorption with the mirror reflectance, in combination with the slow light effect when creating the spectral pit and the AFC structure, may put restrictions on the system performance as shown by the following calculation. According to equation (1) the mode spacing of a cavity with length L is given by

$\Delta\nu = \frac{v_g}{2L}$ and from $v_g = \frac{2\pi\Gamma L}{d_{\text{pit}}}$ [40, 44] the cavity line width, δ, could be written as

$$\delta = \frac{\Delta\nu}{F_{\text{cav}}} = \frac{\pi\Gamma}{F_{\text{cav}} d_{\text{pit}}}, \tag{5}$$

where F_{cav} is the cavity finesse. Therefore, as a general statement, the ratio $\frac{\delta}{\Gamma} = \frac{\pi}{F_{\text{cav}} d_{\text{pit}}}$. To explore the cavity condition on the AFC preparation, one could write the cavity finesse

$$F_{\text{cav}} = \frac{\pi R^{1/4}}{1 - \sqrt{R}}, \tag{6}$$

where the mirror reflectance (R) should satisfy the impedance matching condition ($R = \exp(-2\tilde{d})$) and $\tilde{d} = \frac{d}{F_{\text{AFC}}}$. $\tilde{d}$ is the effective absorption ($d_0 = 0$) according to figure 1. Considering $2\tilde{d} \ll 1$, we could simplify equation (6) as

$$F_{\text{cav}} \approx \frac{\pi}{\tilde{d}}. \tag{7}$$

Now we can rewrite the cavity line width as

$$\delta = \Gamma \frac{\tilde{d}}{d_{\text{pit}}} = \frac{\Gamma}{F_{\text{AFC}}}. \tag{8}$$

Therefore, the cavity line width for a matched cavity to first order just depends on the spectral pit width and the finesse of the AFC structure. This may cause complications because, to minimize the memory loss due to dephasing, F_{AFC} should be as high as possible and Γ is limited by the hyperfine splitting in the material and cannot easily be varied freely.

This can affect the fitting of the AFC structure under the cavity line width since the cavity line width might not be wide enough. But, practically, we do not expect this limitation to become important until one gets into the high-efficiency ($\eta > 90\%$) regime where it is important to suppress memory loss due to the dephasing factor ($\exp(\frac{-7}{F_{\text{AFC}}^2})$ in equation (9)) by choosing higher AFC finesse ($F_{\text{AFC}} > 9$). Even in this case, the cavity line width will readily still be close to the excited state hyperfine transition separation, which is the bandwidth limitation of the AFC protocol as discussed in [13]. On the other hand, the AFC peaks themselves are very narrow absorption structures and consequently will create strong dispersion effects. The effects will modify the transmission structure and this may offer further possibilities; however, as previously stated, a detailed analysis is beyond the scope of this paper.

To estimate the enhancement in storage efficiency attained by employing the cavity configuration, we calculate what signal would have been expected if the end faces were uncoated. The AFC storage efficiency, η, is given by [45]

$$\eta = \tilde{d}^2 \exp(-\tilde{d}) \exp\left(\frac{-7}{F_{\text{AFC}}^2}\right) \exp(-d_0), \tag{9}$$

where $\tilde{d} = \frac{d - d_0}{F_{\text{AFC}}}$ is the effective absorption, d_0 is the background absorption and $F_{\text{AFC}} = \frac{\Delta}{\gamma}$ as shown in figure 1(b). This equation has been shown to agree very well with experiment in [15, 17]. According to equation (5), we can estimate the ratio between the absorption depth of the pit at the spectral position where the quantum memory was prepared, $d_{\text{pit}}^{\text{QM}}$, and the absorption depth of the pit at the line center, $d_{\text{pit}}^{\text{c}}$ (see figure 1(b)) as follows:

$$\frac{d_{\text{pit}}^{\text{QM}}}{d_{\text{pit}}^{\text{c}}} = \frac{\delta_{\text{c}}}{\delta_{\text{QM}}}, \tag{10}$$

where δ_{QM} and δ_{c} are the cavity line width at the quantum memory preparation spectral position and the line center, respectively (with the assumption that Γ and F_{cav} are similar in these two cases). For the present setup, it turns out that we have $\delta_c = 1.5\,\mathrm{MHz}$, $\delta_{\mathrm{QM}} = 8\,\mathrm{MHz}$ and $d^{\mathrm{c}}_{\mathrm{pit}} = 4$, which gives $d^{\mathrm{QM}}_{\mathrm{pit}} = 0.75$. To our knowledge $d < d^{\mathrm{QM}}_{\mathrm{pit}}$ in all the papers published so far; thus we might chose the actual optical depth of the AFC structure $d = 0.75$. From equation (9), considering negligible background absorption d_0, and $F_{\mathrm{AFC}} = 7$ (which is our best guess for the present work) we get an efficiency of $<1\%$. Thus the estimate is that we have at least observed a 20-fold enhancement using the cavity.

The main experimental limitations in the present setup for achieving unity storage and retrieval efficiency, which is predicted theoretically [32, 33], are the following. Firstly, as shown by the black solid trace in figure 5, about 50% of the input pulse is reflected directly at time $t = 0$. Therefore, to improve the storage efficiency one needs to increase the input pulse absorption. Limited absorption means, then, that the impedance-matched condition is not fulfilled. This is partly related to poor spatial mode matching. However, it is also possible that the impedance-matching condition in our cavity crystal could be improved by locking the laser further from the Pr line center (>5 GHz) where the absorption is lower. This could, however, not be fully tested in the present setup since it is difficult to select the laser frequency stabilization point far from the line center for the stabilization setup based on a spectral hole [36]. Secondly, after optimizing the absorption, improving the retrieval part of the memory may be possible by improving the finesse of the prepared AFC structure (F_{AFC}).

6. Conclusion

In conclusion, we demonstrate a ∼20-fold enhancement in quantum memory efficiency for cavity-assisted quantum memories compared to the no cavity case. This is a proof of principle for achieving high quantum memory efficiency using weakly absorbing media. In addition, we demonstrate a ∼3 order decrease in cavity mode spacing using slow light effects in a dispersive medium. We are not aware of any previous observations of cavity mode spacing changes of this order of magnitude due to slow light effects.

Acknowledgments

This work was supported by the Swedish Research Council, the Knut and Alice Wallenberg Foundation, the Crafoord Foundation and EC FP7 contract no. 247743 (QuRep). We are grateful to Dr Mikael Afzelius for several valuable discussions.

References

[1] Kimble H J 2008 *Nature* **453** 1023–30
[2] Ritter S, Nolleke C, Hahn C, Reiserer A, Neuzner A, Uphoff M, Mucke M, Figueroa E, Bochmann J and Rempe G 2012 *Nature* **484** 195–201
[3] Nunn J, Langford N K, Kolthammer W S, Champion T F M, Sprague M R, Michelberger P S, Jin X M, England D G and Walmsley I A 2012 arXiv:1208.1534v1
[4] Duan L M, Lukin M D, Cirac J I and Zoller P 2001 *Nature* **414** 413–8
[5] Simon C *et al* 2010 *Eur. Phys. J.* D **58** 1–22

Paper VI

Efficient Quantum Memory Using a Weakly Absorbing Sample

M. Sabooni, Qian Li, S. Kröll, and L. Rippe.

Phys. Rev. Lett. **110**, 133604 (2013).

PRL **110,** 133604 (2013) PHYSICAL REVIEW LETTERS week ending 29 MARCH 2013

Efficient Quantum Memory Using a Weakly Absorbing Sample

Mahmood Sabooni, Qian Li, Stefan Kröll, and Lars Rippe
Department of Physics, Lund University, P. O. Box 118, SE-22100 Lund, Sweden

(Received 29 December 2012; published 26 March 2013)

A light-storage experiment with a total (storage and retrieval) efficiency $\eta = 56\%$ is carried out by enclosing a sample, with a single-pass absorption of 10%, in an impedance-matched cavity. The experiment is carried out using the atomic frequency comb (AFC) technique in a praseodymium-doped crystal ($0.05\%\mathrm{Pr}^{3+}$:$\mathrm{Y_2SiO_5}$) and the cavity is created by depositing reflection coatings directly onto the crystal surfaces. The AFC technique has previously by far demonstrated the highest multimode capacity of all quantum memory concepts tested experimentally. We claim that the present work shows that it is realistic to create efficient, on-demand, long storage time AFC memories.

DOI: 10.1103/PhysRevLett.110.133604 PACS numbers: 42.50.Ct, 03.67.Hk, 42.50.Gy, 42.50.Md

A quantum memory that has the ability to map onto, store in, and later retrieve the quantum state of light from matter is an important building block in quantum information processing [1]. Quantum memories are expected to become vital elements for long distance quantum key distribution [2,3]. Quantum computing based on linear optics schemes [4], signal synchronization in optical quantum processing [5,6], the implementation of a deterministic single-photon source [7], and precision measurements based on mapping of the quantum properties of an optical state to an atomic ensemble [8] are other applications of quantum memories. For most of the applications mentioned, high performance will be required in terms of high efficiency [9,10], on-demand readout, long storage time [11,12], multimode storage capacity [13,14], and broad bandwidth [15].

Many protocols have been proposed to realize an efficient quantum memory; these include electromagnetically induced transparency (EIT) [16], off-resonant Raman interactions [17], controlled reversible inhomogeneous broadening (CRIB) [18–20], gradient echo memory (GEM) [21], and atomic frequency combs (AFC) [22]. The most impressive storage and retrieval efficiencies so far, 87% [9] and 69% [10], were achieved in hot atomic vapor and rare-earth doped crystals, respectively, using the GEM technique. Additionally, 43% storage and retrieval efficiency using EIT in a hot Rb vapor [23] and 35% using AFC in a rare-earth doped crystal [24] were attained.

The AFC technique [22] is employed in this Letter because the number of (temporal) modes that can be stored in a sample is independent of the optical depth (d) of the storage material, in contrast to other quantum memory approaches. An AFC structure consists of a set of (artificially created) narrow absorbing peaks with equidistant frequency spacing Δ and uniform peak width γ (see the inset in Fig. 3). An input (storage) field (at time $t = 0$) that spectrally overlaps the AFC structure will be absorbed and leave the absorbers (in our case the Pr ions) in a superposition state [22]. If the coherence time is long compared to $1/\Delta$, a collective emission due to constructive interference (similar as for the modes in a mode-locked laser) will occur at time $t_{\mathrm{echo}} = 1/\Delta$.

High storage and retrieval efficiency is one of the main targets of quantum memories and this relies on strong coupling between light and matter [1]. One approach for studying light-matter interaction is based on the high finesse cavity-enhanced interaction of light with a single atom [25,26]. Another alternative for increasing the coupling efficiency of a quantum interface between light and matter is using an optically thick free space atomic ensemble [1]. In this Letter, we combine the advantages of both approaches to implement an efficient quantum interface in a weakly absorbing solid state medium [27]. Within the ensemble approach several experimental realizations from room-temperature alkali gases [28], to alkali atoms cooled and trapped at temperature of a few tens or hundreds of microkelvin [29] have been investigated. Among the ensemble-based approaches impurity centers in a solid state crystal is a powerful alternative for quantum memories because of the absence of atomic movement.

The objective of this Letter is to demonstrate a quantum memory with high storage and retrieval efficiency, with the added benefit of being achievable in a weakly absorbing medium. Another benefit is the short crystal length (2 mm), and small physical storage volume ($\ll \mathrm{mm}^3$). This can simplify the implementation of long-term storage in the hyperfine levels, as will be further discussed at the end of the Letter. For an AFC memory with no cavity and with emission in the forward direction, the maximum theoretical efficiency is limited to 54% [22]. Our work is based on the proposals in Refs. [30,31], where it is shown that close to unity storage and retrieval efficiency can be obtained, using an atomic ensemble in an impedance-matched cavity. A cavity can be impedance matched, by having the absorption per cavity round trip ($1 - e^{-2\alpha L}$) equal to the transmission of the input coupling mirror ($1 - R1$), while the back mirror is 100% reflecting, which gives $R1 = e^{-2\alpha L}$, where α is the absorption coefficient and L is the length of the optical memory material. For this impedance-matching condition, all light sent to the cavity will be absorbed in the absorbing sample inside the cavity and no light is reflected.

The storage cavity is made up of a 2 mm long 0.05% Pr^{3+}:Y_2SiO_5 crystal; see Fig. 1. To reduce the complexity of the alignment and reduce losses, the crystal surfaces are reflection coated directly, rather than using separate mirrors. The two cavity crystal surfaces are not exactly parallel as shown in Fig. 1 ($\theta \approx 10$ arcsec). Part of the incoming field $\vec{E}_{\rm in}$ will be reflected ($\vec{E}_{\rm refl}$) at the first mirror surface ($R1$), see Fig. 1. The field leaking out through $R1$ from the cavity, $\vec{E}_{\rm leak}$, is coherently added to $\vec{E}_{\rm refl}$ such that $\vec{E}_{\rm out} = \vec{E}_{\rm refl} + \vec{E}_{\rm leak}$. At the impedance-matched condition, $\vec{E}_{\rm refl}$ and $\vec{E}_{\rm leak}$ differ in phase by π and have the same amplitude $|\vec{E}_{\rm refl}| = |\vec{E}_{\rm leak}|$. This means that the light intensity at the reflection detector (PD3) should ideally vanishes if this condition is satisfied.

The cavity crystal (impedance matching) was first tested without memory preparation. The effective cavity length can be optimized by translating the cavity perpendicular to the beam propagation direction. Here a sub-μm accuracy (Attocube system, ANCz150) translation stage was used. Then, a weak Gaussian pulse ($\tau_{\rm FWHM} = 250$ ns) with a small pulse area and repetition rate of 10 Hz was injected into the cavity while the laser frequency was slowly scanned during $\sim$6 s across the inhomogeneous Pr ion absorption line. To find the best impedance-matched point, the cavity crystal was translated in small steps perpendicular to the beam direction. For each step a 18 GHz laser scan was carried out. The calibrated reflected part of the input pulse (PD3/PD1) is plotted versus the frequency offset from the Pr^{3+}:Y_2SiO_5 inhomogeneous line center in Fig. 2, for the position where the highest absorption was obtained. This measurement shows that a maximum of about 84% of the input energy could be absorbed. This occurred about 45 GHz above the inhomogeneous broadening center frequency. This will set an upper limit for the achievable storage and retrieval efficiency in the present setup. Due to the absorption tailoring during the memory preparation (to be discussed below), the impedance-matching condition will be fulfilled closer to the inhomogeneous line center in the actual storage experiment, but the measurement establish the losses caused by spatial mode mismatching. In addition, in the present setup the dye laser is frequency stabilized against a Fabry-Pérot cavity using the Pound-Drever-Hall (PDH) locking technique [32,33]. This provide more freedom for locking the laser frequency further away from the inhomogeneous profile center compared to our earlier work [34] where stabilization based on hole burning was used. This has a

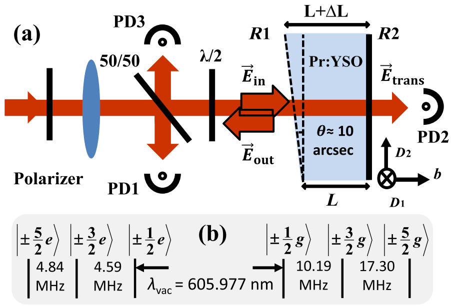

FIG. 1 (color online). (a) Part of the experimental setup. A frequency stabilized (< 1 kHz linewidth) dye laser at $\lambda_{\rm vac} = 605.977$ nm is employed as light source. A 50/50 beam splitter splits off part of the input light onto a photo diode (PD1), to calibrate against variations in the input light intensity. Two other photo diodes monitor the transmitted (PD2) and the reflected (PD3) light from the cavity. The cavity length along the b axis is $L = 2$ mm and the crystal diameter in the (D_1, D_2) plane is 12 mm. b, D_1, and D_2 are principal axes of the crystal [46]. A beam waist of about 100 μm is created at the crystal center via a lens with $f = 400$ mm. A half-wave plate ($\lambda/2$) is employed to align the polarization direction to a principal axis of the cavity crystal, which is immersed in liquid helium at 2.1 K. The input and output facet of the crystal has $R1 = 80\%$ and $R2 = 99.7\%$ reflectivity. A small part of the cavity crystal is left uncoated for measurements without a cavity effect. (b) The hyperfine splitting of the ground $|g\rangle$ and excited $|e\rangle$ state of the ${}^3H_4 - {}^1D_2$ transition of site I in Pr^{3+}:Y_2SiO_5 [38].

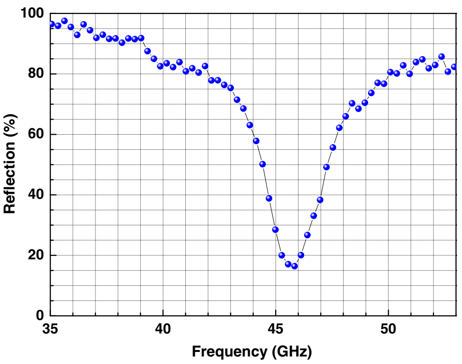

FIG. 2 (color online). The normalized reflected signal (PD3/PD1) is plotted against the frequency offset from the Pr^{3+}:Y_2SiO_5 inhomogeneous line center. The crystal was translated perpendicular to the input beam (see Fig. 1) and the graph is a frequency scan for the position that gave the best impedance matching. At the impedance-matching condition the reflected light detected at PD3 should vanish. The best impedance-matched condition without memory preparation (i.e., spectral manipulation by the absorption profile, see text) was a reflection of 16% (84% absorption), which was measured about 45 GHz above the inhomogeneous broadening center frequency that is located at 0 GHz in this figure.

large influence on improving the impedance-matching condition.

To demonstrate a quantum memory based on the AFC protocol, first, a transparent (nonabsorbing) spectral transmission window within the Pr ion absorption profile was created using optical pumping. An accurate description of the pulse sequences required for creating such a transparency window, which henceforth is called a spectral pit, is given in Ref. [24]. Because of the strong dispersion created by the spectral pit [35], the cavity free spectral range (FSR) and the cavity linewidth are reduced by 3–4 orders of magnitude [36]. The reduction can be understood as follows. The cavity FSR is $\Delta\nu_{\text{mode}} = \frac{c_0}{2L}\frac{1}{n_g}$ [37] where c_0 is speed of light in the vacuum, L is the cavity length, and n_g is the group refractive index. $n_g = n_r(\nu) + \nu\frac{dn_r(\nu)}{d\nu}$ and $n_r(\nu)$ is the real refractive index as a function of frequency ν. In case of no or constant absorption, the dispersion term is negligible compared to the real refractive index $(n_r(\nu) \gg \nu\frac{dn_r(\nu)}{d\nu})$. The FSR of this cavity with no absorbing material is about 40 GHz. In the presence of sharp transmission structures $(n_r(\nu) \ll \nu\frac{dn_r(\nu)}{d\nu})$ a dramatic reduction of the cavity FSR and the cavity linewidth can occur. In our case $\nu\frac{dn_r(\nu)}{d\nu} > 1000 n_r(\nu)$ and the reduction is >3 orders of magnitude at the center of the inhomogeneous line. A more detailed description of the cavity FSR reduction is given in Refs. [34,36]. Translating the crystal perpendicular to the beam propagation direction will move the cavity transmission within the spectral pit due to the small wedge on the crystal.

After preparing the transparent (nonabsorbing) spectral transmission window, each AFC peak is created using a complex hyperbolic secant pulse (sechyp for short) with chirp width $f_{\text{width}} = 70$ kHz [38] and temporal width $t_{\text{FWHM}} = 16.8$ μs [38]. This pulse excites ions from $|\pm\frac{1}{2}g\rangle \mapsto |\pm\frac{5}{2}e\rangle$ state [see Fig. 1(a)]. From the $|\pm\frac{5}{2}e\rangle$ state, Pr ions will decay mostly to the $|\pm\frac{5}{2}g\rangle$ due to the high branching ratio for the $|\pm\frac{5}{2}e\rangle \mapsto |\pm\frac{5}{2}g\rangle$ transition [39]. This pulse is repeated several (~ 50) times with a waiting time of 500 μs between each pulse. This process creates one AFC peak. Repeating this procedure with a consecutive change of center frequency of the sechyp pulse by Δ will create the other AFC peaks. The finesse of the AFC structure with peak width γ and peak separation Δ will be $F_{\text{AFC}} = \frac{\Delta}{\gamma}$.

As we discussed earlier, the absorption engineering of the Pr ions inside the cavity will directly affect the cavity modes via strong dispersion. Therefore, measuring the AFC structure properties in the cavity case is challenging. In order to at least to some extent estimate the AFC structure properties, the coating of a small part of the cavity crystal is removed, and the same preparation as for the memory is performed in this part. The remaining coating could affect the precision of this measurement through the cavity dispersion effect. The trace in Fig. 3 is recorded using a weak readout beam that is frequency chirped at a rate of 10 kHz/μs across the frequency region of the AFC structure. The overall spectral structure is complicated and a detailed discussion of the spectrum is beyond the scope of the present Letter. The inset in Fig. 3 shows the spectral content of the storage pulse relative to the four AFC peaks. The cavity transmission linewidth is tuned to be at least as wide as the whole prepared AFC structure [34]. In this case it was ≈ 11 MHz wide.

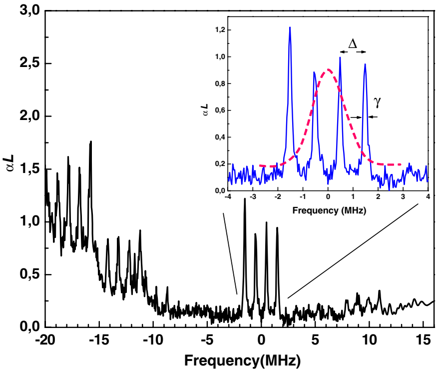

FIG. 3 (color online). The absorption profile created through the optical pumping process is shown. This measurement is done in a small part of the cavity crystal where the coating was removed. From the Pr inhomogeneous absorption profile, four AFC peaks, all absorbing on the $|\pm\frac{5}{2}g\rangle \mapsto |\pm\frac{5}{2}e\rangle$ transition, are created. The spectral content of the storage pulse is shown schematically in the inset by the red dashed line across the AFC structure, which has peak width γ and peak separation Δ. The finesse of the AFC structure is $F_{\text{AFC}} = \frac{\Delta}{\gamma}$.

The input pulse is stored using the $|\pm\frac{5}{2}g\rangle \mapsto |\pm\frac{5}{2}e\rangle$ transition for ions initially in state $|\pm\frac{5}{2}g\rangle$. A Gaussian pulse with a duration of $\tau_{\text{FWHM}} = 250$ ns and small pulse area is employed as a storage pulse. The frequency of the storage pulse is tuned to the center frequency of an AFC structure with a peak separation $\Delta = 0.9$ MHz. The retrieved echo pulse is detected at detector PD3 after 1.1 μs as shown with black solid line in Fig. 4. In addition, multiple echoes are detected at times 2.2 μs and 3.3 μs which are probably due to multiple rephasing of the ensemble.

In order to assess the storage and retrieval efficiency, the intensity of the input storage pulse at the cavity crystal should be measured. To this end, the cavity crystal was turned $\sim 180°$ such that the input storage pulse impinged on the $R2 = 99.7\%$ mirror, with no pit and peak creation active. In this way the input storage pulse is (almost completely) reflected and the signal on PD3, after calibrating using PD1, can be used as a reference value for the storage pulse input intensity, as shown by a red dashed line in Fig. 4. The pulse area of the first echo at ≈ 1.1 μs

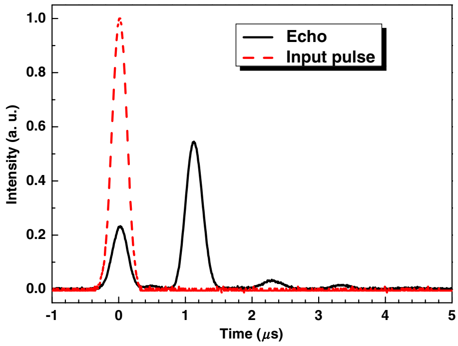

FIG. 4 (color online). The input storage pulse as a reference detected at PD3 (see text) is shown as a red dashed line. The retrieved echo pulse is detected at detector PD3 after 1.1 μs as shown with the black solid line. The area of the echo pulse at 1.1 μs divided by the reference signal pulse area gives a storage and retrieval efficiency of the memory of $\eta = 56\%$.

divided by the reference signal pulse area gives a storage and retrieval efficiency of the memory of $\eta = 56\%$ (four independent measurements gave values ranging from 55.5% to 56.8%). The leakage through the cavity detected on PD2 (see Fig. 1) during the storage is almost negligible ($\approx 1\%$ of the storage pulse).

The present result is lower than the best storage and retrieval efficiency achieved elsewhere [9,10]; however, it is the highest storage and retrieval efficiency based on the AFC protocol, which is presently the best multimode quantum state storage protocol [40], also in the cavity configuration [31]. The source of losses in the current setup can be estimated as about 16% related to the impedance mismatching, 5% associated with the multiple echoes, about 1% from transmission through the cavity, about 10% linked to the AFC finesse dephasing factor, and the rest possibly related to the crystal background absorption. By addressing these losses the efficiency could be improved. We estimate that the efficiency under the same conditions as in this experiment for a crystal in a single-pass configuration would be $<1\%$ [34]. Therefore the cavity configuration shows a significant enhancement compared to the bare crystal.

In order to obtain on-demand and long-term storage based on the AFC protocol [22], the ground-excited state superposition should be transferred to, and then brought back from, a spin-level superposition between two of the ground states [41]. The dephasing due to the spin state inhomogeneous broadening can be suppressed using radio-frequency (rf) spin-echo techniques. In addition, even longer (> 60s) storage time is possible by utilizing zero first-order Zeeman (ZEFOZ) shift [42] and spin-echo techniques to suppress slow variations of the spin transition frequencies [11,12]. Quantum memories in a smaller physical volumes requires significantly lower rf power. Although the present result is 13% lower than the highest rare-earth crystal efficiency results so far [10], it is obtained in a crystal that is 10 times shorter. This may in practice significantly simplify long time, high efficiency spin storage, since too large volumes will require excessive rf powers to compensate for the spin inhomogeneous broadening. In addition, efficient quantum memories in a weakly absorbing media opens up the possibility of utilizing materials with low optical depth but good coherence properties (e.g., Eu^{3+}:Y_2SiO_5 [43]).

In summary, we have demonstrated a quantum memory with $\eta = 56\%$ storage and retrieval efficiency based on the AFC protocol. This is done in a weakly absorbing medium and short crystal length (2 mm) by utilizing an impedance-matched cavity configuration. This achievement, in addition to the storage and recall of weak coherent optical pulses [14,44], spin-wave storage demonstration [41], the best multimode quantum memory [13,14], and storage of entanglement [15,45] increases the possibility of creating an efficient, on-demand, long storage time, and multimode quantum memory based on the AFC protocol in the future.

This work was supported by the Swedish Research Council, the Knut & Alice Wallenberg Foundation, the Maja & Erik Lindqvists forskningsstiftelse, the Crafoord Foundation, and the EC FP7 Contract No. 247743 (QuRep) and (Marie Curie Action) REA Grant No. 287252 (CIPRIS).

[1] K. Hammerer, A. S. Sorensen, and E. S. Polzik, Rev. Mod. Phys. **82**, 1041 (2010).

[2] L. M. Duan, M. D. Lukin, J. I. Cirac, and P. Zoller, Nature (London) **414**, 413 (2001).

[3] N. Sangouard, C. Simon, B. Zhao, Y. A. Chen, H. de Riedmatten, J. W. Pan, and N. Gisin, Phys. Rev. A **77**, 062301 (2008).

[4] P. Kok, W. J. Munro, K. Nemoto, T. C. Ralph, J. P. Dowling, and G. J. Milburn, Rev. Mod. Phys. **79**, 135 (2007).

[5] E. Knill, R. Laflamme, and G. J. Milburn, Nature (London) **409**, 46 (2001).

[6] J. Nunn, N. K. Langford, W. S. Kolthammer, T. F. M. Champion, M. R. Sprague, P. S. Michelberger, X. M. Jin, D. G. England, and I. A. Walmsley, arXiv:1208.1534v1 [Phys. Rev. Lett. (to be published)].

[7] S. Chen, Y.-A. Chen, T. Strassel, Z.-S. Yuan, B. Zhao, J. Schmiedmayer, and J.-W. Pan, Phys. Rev. Lett. **97**, 173004 (2006).

[8] A. I. Lvovsky, B. C. Sanders, and W. Tittel, Nat. Photonics **3**, 706 (2009).

[9] M. Hosseini, B. M. Sparkes, G. Campbell, P. K. Lam, and B. C. Buchler, Nat. Commun. **2**, 174 (2011).

[10] M. P. Hedges, J. J. Longdell, Y. Li, and M. J. Sellars, Nature (London) **465**, 1052 (2010).

[11] J. J. Longdell, E. Fraval, M. J. Sellars, and N. B. Manson, Phys. Rev. Lett. **95**, 063601 (2005).

[12] G. Heinze *et al.* (to be published).

[13] M. Bonarota, J. L. Le Gouët, and T. Chanelière, New J. Phys. **13**, 013013 (2011).
[14] I. Usmani, M. Afzelius, H. de Riedmatten, and N. Gisin, Nat. Commun. **1**, 12 (2010).
[15] E. Saglamyurek, N. Sinclair, J. Jin, J. A. Slater, D. Oblak, F. Bussieres, M. George, R. Ricken, W. Sohler, and W. Tittel, Nature (London) **469**, 512 (2011).
[16] M. Fleischhauer and M. D. Lukin, Phys. Rev. Lett. **84**, 5094 (2000).
[17] K. F. Reim, J. Nunn, V. O. Lorenz, B. J. Sussman, K. C. Lee, N. K. Langford, D. Jaksch, and I. A. Walmsley, Nat. Photonics **4**, 218 (2010).
[18] S. A. Moiseev and S. Kröll, Phys. Rev. Lett. **87**, 173601 (2001).
[19] M. Nilsson and S. Kröll, Opt. Commun. **247**, 393 (2005).
[20] B. Kraus, W. Tittel, N. Gisin, M. Nilsson, S. Kröll, and J. I. Cirac, Phys. Rev. A **73**, 020302 (2006).
[21] G. Hetet, J. J. Longdell, M. J. Sellars, P. K. Lam, and B. C. Buchler, Phys. Rev. Lett. **101**, 203601 (2008).
[22] M. Afzelius, C. Simon, H. de Riedmatten, and N. Gisin, Phys. Rev. A **79**, 052329 (2009).
[23] N. B. Phillips, A. V. Gorshkov, and I. Novikova, Phys. Rev. A **78**, 023801 (2008).
[24] A. Amari, A. Walther, M. Sabooni, M. Huang, S. Kröll, M. Afzelius, I. Usmani, B. Lauritzen, N. Sangouard, H. de Riedmatten, and N. Gisin, J. Lumin. **130**, 1579 (2010).
[25] J. M. Raimond, M. Brune, and S. Haroche, Rev. Mod. Phys. **73**, 565 (2001).
[26] Y. Colombe, T. Steinmetz, G. Dubois, F. Linke, D. Hunger, and J. Reichel, Nature (London) **450**, 272 (2007).
[27] A. V. Gorshkov, A. Andre, M. D. Lukin, and A. S. Sorensen, Phys. Rev. A **76**, 033804 (2007).
[28] B. Julsgaard, J. Sherson, J. I. Cirac, J. Fiurasek, and E. S. Polzik, Nature (London) **432**, 482 (2004).
[29] J. Simon, H. Tanji, J. K. Thompson, and V. Vuletic, Phys. Rev. Lett. **98**, 183601 (2007).
[30] M. Afzelius and C. Simon, Phys. Rev. A **82**, 022310 (2010).
[31] S. A. Moiseev, S. N. Andrianov, and F. F. Gubaidullin, Phys. Rev. A **82**, 022311 (2010).
[32] R. W. P. Drever, J. L. Hall, F. V. Kowalski, J. Hough, G. M. Ford, A. J. Munley, and H. Ward, Appl. Phys. B **31**, 97 (1983).
[33] D. R. Leibrandt, M. J. Thorpe, M. Notcutt, R. E. Drullinger, T. Rosenband, and J. C. Bergquist, Opt. Express **19**, 3471 (2011).
[34] M. Sabooni, S. T. Kometa, S. Thuresson, A. Kröll, and L. Rippe, arXiv:1212.3774 [New J. Phys. (to be published)].
[35] A. Walther, A. Amari, S. Kröll, and A. Kalachev, Phys. Rev. A **80**, 012317 (2009); Correction: the expression for the group velocity needs to be corrected to $v_g = \frac{2\pi\Gamma}{\alpha}$ in subsection "IV.B. Slow light effects."
[36] M. Sabooni *et al.* (in preparation).
[37] A. E. Siegman, *Lasers* (University Science Books, Mill Valley, California, 1985).
[38] L. Rippe, M. Nilsson, S. Kröll, R. Klieber, and D. Suter, Phys. Rev. A **71**, 062328 (2005).
[39] M. Nilsson, L. Rippe, S. Kröll, R. Klieber, and D. Suter, Phys. Rev. B **70**, 214116 (2004); M. Nilsson, L. Rippe, S. Kröll, R. Klieber, and D. Suter, Phys. Rev. B **71**, 149902 (E) (2005).
[40] J. Nunn, K. Reim, K. C. Lee, V. O. Lorenz, B. J. Sussman, I. A. Walmsley, and D. Jaksch, Phys. Rev. Lett. **101**, 260502 (2008).
[41] M. Afzelius, I. Usmani, A. Amari, B. Lauritzen, A. Walther, C. Simon, N. Sangouard, J. Minar, H. de Riedmatten, N. Gisin, and S. Kröll, Phys. Rev. Lett. **104**, 040503 (2010).
[42] M. Lovric, P. Glasenapp, D. Suter, B. Tumino, A. Ferrier, P. Goldner, M. Sabooni, L. Rippe, and S. Kröll, Phys. Rev. B **84**, 104417 (2011).
[43] B. Lauritzen, N. Timoney, N. Gisin, M. Afzelius, H. de Riedmatten, Y. Sun, R. M. Macfarlane, and R. L. Cone, Phys. Rev. B **85**, 115111 (2012).
[44] M. Sabooni, F. Beaudoin, A. Walther, N. Lin, A. Amari, M. Huang, and S. Kröll, Phys. Rev. Lett. **105**, 060501 (2010).
[45] C. Clausen, I. Usmani, F. Bussieres, N. Sangouard, M. Afzelius, H. de Riedmatten, and N. Gisin, Nature (London) **469**, 508 (2011).
[46] Y. C. Sun, *Spectroscopic Properties of Rare-Earths in Optical Materials* edited by G. Liu and B. Jacquier, Springer Series in Material Science (Springer, Berlin Heidelberg, 2005), Chap. 7.